DEPARTMENT OF AEROSPACE ENGINEERING
COLLEGE OF ENGINEERING & TECHNOLOGY
OLD DOMINION UNIVERSITY
NORFOLK, VIRGINIA 23529

# PREDICTION AND CONTROL OF VORTEX-DOMINATED AND VORTEX-WAKE FLOWS

By

Osama Kandil, Principal Investigator

Progress Report
For the period December 1, 1992 to November 30, 1993

Prepared for
National Aeronautics and Space Administration
Langley Research Center
Hampton, VA 23681-0001

Under
**Research Grant NAG-1-994**
Dr. Chen-Huei Liu, Technical Monitor
FLDMD-Theoretical Flow Physics Branch

**Submitted by the**
**Old Dominion University Research Foundation**
**P.O. Box 6369**
**Norfolk, Virginia 23508-0369**

December 1993

# PREDICTION AND CONTROL OF VORTEX-DOMINATED AND VORTEX-WAKE FLOWS

**Osama A. Kandil**[*]
**Aerospace Engineering Department**

## Accomplishments (December 1, 1992–Novemer 30, 1993)

This section documents the accomplishments which have been achieved in the present year covering the period from December 1, 1992 until November 30, 1993. These accomplishments include publications, national and international presentations, NASA presentations and the research group supported under this grant.

## I. Conference Papers, Proceedings and Journal Publications:

1. Kandil, O. A., Kandil, H. A. and Liu, C. H., "Shock-Vortex Interaction Over a 65 Degree Delta Wing in Transonic Flows," AIAA 93–2973, AIAA 24th Fluid Dynamics Conference, Orlando, Florida, July 5–7, 1993.
2. Kandil, O. A., Sharaf, H. H. and Liu, C. H., "Active Control of Asymmetric Conical Flow Using Spinning and Rotatory Oscillation," AIAA 93–2958, AIAA 24th Fluid Dynamics Conference, Orlando, Florida, July 5–7, 1993.
3. Kandil, O. A., Kandil, H. A., and Liu, C. H., "Three-Dimensional Supersonic Vortex Breakdown," AIAA 93–0526, AIAA 31st Aerospace Scienes Meeting, Reno, Nevada, January 1993.
4. Kandil, H. A., Kandil, O. A. and Liu, C. H., "Supersonic Vortex Breakdown Over a Delta Wing in Transonic Flow," AIAA-93-3472-CP, AIAA 11th Applied Aerodynamics Conference, Monterey, CA, August 1993, pp. 582–596.
5. Kandil, O. A., "Active Control of Vortical Flows Around Wings and Bodies Using CFD," III PAN American Congress of Applied Mechanics, São Paulo, Brazil, Proceedings pp. 29–32, January 4–8, 1993 (Invited).
6. Liu, C. H., Kandil, O. A. and Kandil, H. A., "Numerical Simulation and Physical Aspects of Supersonic Vortex Breakdown," Journal of Computers and Fluids, Vol. 22, No. 4/5, pp. 607–622, May 1993.

---

[*] Professor, Eminent Scholar and Chairman

7. Liu, C. H., Wong, T. C. and Kandil, O. A., "Prediction of Asymmetric Vortical Flows Around Slender Bodies Using Navier-Stokes Equations," Japanese Journal of Fluid Dynamics Research, Vol. 10, pp. 409–450, December 1992.
8. Kandil, O. A. and Liu, C. H., "Three-Dimensional Asymmetric Flows Around Cones," NAS Technical Summaries," December 1992, p. 73.

## II. Ph.D. Dissertation Produced:

"Navier-Stokes Simulation of Quasi-Axisymmetric and Three-Dimensional Supersonic Vortex Breakdown" by H. A. Kandil, Old Dominion University, May 1993. Most of the work is supported under this grant, and part of the work is supported under a grant from AFOSR, Bolling AFB, D.C. Director: Prof. Osama A. Kandil.

## III. National and International Presentations:

1. "Computation of Vortex Wake Flow and Fluid/Dynamics Interaction of a Generator/Follower Configuration," Computational Aerodynamics Branch, NASA Langley Research Center, Hampton, VA, November 23, 1993. Prof. Kandil gave the presentation.
2. "Supersonic Vortex Breakdown Over a Delta Wing in Transonic Flow," AIAA 11th Applied Aerodynamics Conference, Monterey, CA, August 1993. Prof. Kandil gave the presentation.
3. "Computation of Vortex Flow and Dynamics Interaction of a 747/747 Generator/Follower Configuration," Flight Vehicle Research Branch, NASA Langley, July 20, 1993. Prof. Kandil gave the presentation.
4. "Unsteady Vortex Aerodynamics," Presentation to P.R. China Visitors, ODU, June 20, 1993. Prof. Kandil gave the presentation.
5. "Active Control of Asymmetric Conical Flow Using Spinning and Rotatory Oscillation," AIAA 24th Fluid Dynamics Conference, Orlando, FL, July 6–9, 1993. Prof. Kandil gave the presentation.
6. "Shock-Vortex Interaction Over a 65–Degree Delta Wing in Transonic Flow," AIAA 24th Fluid Dynamics Conference, Orlando, FL, July 6–9, 1993. Prof. Kandil gave the presentation.
7. "Three-Dimensional Supersonic Vortex Breakdown," AIAA 31st Aerospace Sciences Meeting, Reno, Nevada, January 9–13, 1993. Prof. Kandil gave the presentation.
8. "Supersonic Vortex Breakdown," Division Review of Computational Aerodynamics Branch, NASA Langley Research Center, February 4, 1993. Dr. Liu and Prof. Kandil gave the presentation.

## IV. Papers Submitted or Accepted for Presentation:

1. Kandil, O. A., Wong, T.-C. and Liu, C. H., "Turbulent Flow Over a 747/747 Generator/Follower Configuration and Its Dynamics Response," submitted for presentation at the AIAA 25th Fluid Dynamics Conference, Colorado Springs, Colorado, June 20–23, 1994.
2. Kandil, O. A., Kandil, H. A. and Liu, C. H., "Supersonic Vortex Breakdown Over a Delta Wing in Transonic Flow," submitted for publication in the Journal of Aircraft.
3. Kandil, O. A., Kandil, H. A. and Liu, C. H., "Three-Dimensional Supersonic Vortex Breakdown," submitted for publication in the AIAA Journal.
4. Kandil, O. A., Sharaf, El-Din, H. H. and Liu, C. H., "Active Control of Asymmetric Conical Flow Using Spinning and Rotatory Oscillation," submitted for publication in the Journal of Aircraft.

## V. Research Group:

The Principal Investigator has been assisted by the following persons in the research group:

1. Dr. T. C. Wong, Research Associate, Aerospace Engineering Department, Old Dominion University, Vortex-Wake Flows
2. Dr. Hamdy A. Kandil, Research Assistant Professor, Aerospace Engineering Department, Old Dominion University, Vortex-Breakdown Flows.
3. Mr. Hazem H. Sharaf El-Din, Ph. D. Candidate, Aerospace Engineering Department, Old Dominion University, Passive and Active Control of Asymmetric Flows.

[illegible]

93A 43152

15P

# AIAA-93-2958

# ACTIVE CONTROL OF ASYMMETRIC CONICAL FLOW USING SPINNING AND ROTATORY OSCILLATION

Osama A. Kandil and Hazem H. Sharaf El-Din
Old Dominion University, Norfolk, VA 23529

C. H. Liu
NASA Langley Research Center, Hampton, VA 23681

**AIAA 24th**
**Fluid Dynamics Conference**
**July 6-9, 1993/Orlando, FL**

For permission to copy or republish, contact the American Institute of Aeronautics and Astronautics
370 L'Enfant Promenade, S.W., Washington, D.C. 20024

# ACTIVE CONTROL OF ASYMMETRIC CONICAL FLOW USING SPINNING AND ROTATORY OSCILLATIONS

**Osama A. Kandil*** **and Hazem H. Sharaf El-Din****
**Old Dominion University, Norfolk, VA 23529**

**C. H. Liu*****
**NASA Langley Research Center, Hampton, VA 23681**

## ABSTRACT

The effectiveness of active control on asymmetric flows around circular cones is investigated computationally using cone spinning and rotatory oscillation around its axis. The investigation uses the time-accurate solution of the unsteady, compressible, full Navier-Stokes equations with the implicit, upwind, flux-difference splitting, finite-volume scheme. The present solutions are obtained under the locally-conical-flow assumption in order to understand the flow physics using very fine grids for reasonable flow resolution at low computational cost. For all the computational solutions, a grid of $241 \times 81 \times 2$ points in the wrap-around, normal and axial directions, respectively, is used. The grid is spinning or oscillating rigidly with the cone according to its motion and the kinematical and dynamical boundary conditions are modified accordingly. The computational applications include the effects of uniform spinning rates and periodic rotatory oscillations at different amplitudes and frequencies on the flow asymmetry.

## INTRODUCTION

The problems of prediction, analysis and control of asymmetric vortical flows around slender pointed bodies are of vital importance to the dynamic stability and controllability of missiles and fighter aircraft. The onset of flow asymmetry occurs when the relative incidence (ratio of angle of attack to nose semi-apex angle) of pointed forebodies exceeds certain critical values. In addition to the relative incidence as one of the influential parameters for the onset of flow asymmetry, the freestream Mach number, Reynolds number and shape of the body-cross sectional area are also important parameters.

Substantial research efforts have recently been devoted for eliminating or alleviating flow asymmetry and its corresponding side force. In the experimental area, several passive-control methods[1–3] and active-control methods[4–8] have been investigated. Computational simulations have also been used to investigate the effectiveness of several passive-control methods[9] and active-control methods[7, 10, 11]. Various methods of passive control were demonstrated in the above references which include the use of vertical fins along the leeward plane of geometric symmetry, thin and thick side strakes with different orientations, and rotatable forebody tips which have variable cross section (from a circular shape at its base to an elliptic shape at its tip). It was shown by Kandil et al.[9] that side-strake control is more practical than vertical-fin control since the former was more effective over a wide range of angle of attack than the latter. Moreover, side-strake control provided an additional lifting force. However, the effectiveness of side-strake control terminated at very high angles of attack for the considered strake geometry and flow conditions.

Various active-control methods have been used which include forebody blowing and movable forebody strakes. The forebody blowing methods include forward blowing, normal blowing, aft blowing and tangential blowing. The main purposes of forebody blowing are to control flow separation on the forebody and to create yawing forces and moments which can be utilized in controlling the body.

In Ref. 12, the authors investigated the effectiveness of two methods of active control which include flow injection and surface heating. The study of flow-injection control covered normal and tangential injection. Moreover, a hybrid method of flow control which combined surface heating and normal injection methods was also investigated. These active control methods were directed at either rendering the asymmetric vortical flow symmetric or rendering the surface-pressure distribution symmetric.

Active control of asymmetric flows around slender pointed bodies using body spinning about its axis has

---

* Professor, Eminent Scholar and Chairman of Aerospace Engineering Department, Associate Fellow AIAA

** Graduate Research Assistant, Aerospace Engineering Department, Member AIAA

*** Senior Research Scientist, Computational Aerodynamics Branch, Associate Fellow AIAA

Copyright © 1993 by Osama Kandil Published by The American Institute of Aeronautics and Astronautics, Inc with permission

recently been investigated experimentally. Kruse[13] investigated the effects of several spinning rates on the side force of a 10° half apex-angle cone. The results were presented for spin tests at 58-60° angle of attack, 0.6 Mach number and $1 \times 10^6$ Reynolds number (based on diameter). For the 58° angle of attack, the side force versus the roll angle was shown for four spin rates which varied from 60 rpm (revolution per minute) to 400 rpm. For all values of spin rates, the side force changed direction in an irregular manner within each revolution of the cone and it was repeatable from one revolution to the next. Moreover, the side-force variation within each revolution showed roughly three cycles, and there was an evidence that the amplitude of the side force decreases with the increase of spin rate.

Fidler[14] used spinning of the nose, nose tip and a band of the body surface as active-control methods for alleviating asymmetric vortex effects on a tangent-ogive configuration. By rotating the nose, nose tip and a band of the body just aft of the nose, the wake pattern and the associated side forces and moments were cyclically altered. For the nose and nose-tip rotations, the peak-to-peak variations of the side force were decreased as the spin rate was increased. The results also showed that the average side force was constant throughout the spin range. However, by using the nose tip with three axial grit strips, the mean side force was brought to zero.

Experimental and computational studies on the effects of rotation and rotatory oscillations on the vortex shedding behind circular cylinders have recently been conducted by several researchers[15-17]. Coutanceau and Ménard[15] reviewed earlier work and conducted experimental investigation on a circular cylinder undergoing steady rotatory and rectilinear motion. They concluded that if the ratio of rotational velocity to rectilinear velocity is greater than 2, then the Kármán vortex street disappears. Taneda[16] showed that if the cylinder is forced to undergo a harmonic rotatory oscillations at large values of amplitude and frequency then vortex shedding is eliminated and a symmetric flow can be generated. Chen[17] et al. integrated the velocity/vorticity formulation using an explicit finite-difference/pseudo-spectral technique and the Biot-Savart law to study the temporal development of two-dimensional incompressible, viscous flow around a circular cylinder undergoing steady rotatory and rectilinear motion. Their computational results showed that rotation does not suppress vortex shedding for large values of the ratio of rotational velocity to rectilinear velocity. This conclusion is not in agreement with that of Cautanceau and Ménard.

In the present paper, we investigate the effectiveness of spinning and rotatory oscillation as active control methods to eliminate or alleviate the side forces due to vortex asymmetry for a 5°-semi-apex angle, circular cone. The investigation uses the time-accurate solution of the unsteady, compressible, full Navier-Stokes (NS) equations. The locally, conical-flow assumption is used to obtain all the present solutions since it provides excellent flow physics at substantially lower computational cost in comparison with that required for the corresponding three-dimensional flow cases.

## FORMULATION

### Governing Equations:

The vector form of the governing equations is developed in terms of an inertial frame of reference, and hence there are no source terms on the right-hand side of the equations. Hence, the components of the flow-field vector $[\rho, \rho\bar{V}, \rho e]^t$ are absolute quantities. This is unlike the earlier development of the governing equations by the principal author of this paper (Ref. 18), where the equations are developed in terms of a non-inertial frame of reference (translating and rotation frame of reference) and source terms appear on the right-hand side of the equations.

The conservative form of the dimensionless, unsteady, compressible, full NS equations in terms of time-dependent, body-conformed coordinates $\xi^1, \xi^2$ and $\xi^3$ is given by

$$\frac{\partial \bar{Q}}{\partial t} + \frac{\partial \bar{E}_m}{\partial \xi^m} - \frac{\partial (\bar{E}_v)_s}{\partial \xi^s} = 0; m = 1-3, s = 1-3 \tag{1}$$

where

$$\xi^m = \xi^m(x_1, x_2, x_3, t) \tag{2}$$

$$\bar{Q} = \frac{\hat{q}}{J} = \frac{1}{J}[\rho, \rho u_1, \rho u_2, \rho u_3, \rho e]^t \tag{3}$$

$$\begin{aligned}\bar{E}_m &\equiv \mathit{inviscid\ flux\ in\ } \xi^m \mathit{\ direction}\\ &= \frac{1}{J}\left[\partial_k \xi^m \hat{E}_k + \frac{\partial \xi^m}{\partial t}\hat{q}\right]^t\\ &= \frac{1}{J}\Big[\rho U_m, \rho u_1 U_m + \partial_1 \xi^m p, \rho u_2 U_m\\ &+ \partial_2 \xi^m p, \rho u_3 U_m + \partial_3 \xi^m p, (\rho e + p) U_m\\ &- \frac{\partial \xi^m}{\partial t} p\Big]^t\end{aligned} \tag{4}$$

$$(\bar{E}_v)_s \equiv \textit{viscous and heat–conduction flux in } \xi^3 \textit{ direction}$$
$$= \frac{1}{J}[0, \partial_k\xi^s\tau_{k1}, \partial_k\xi^s\tau_{k2}, \partial_k\xi^s\tau_{k3}, \partial_k\xi^s(u_n\tau_{kn} - q_k)]^t; \quad k = 1-3,\ n = 1-3 \qquad (5)$$

$$U_m = \partial_k\xi^m u_k + \frac{\partial\xi^m}{\partial t} \qquad (6)$$

and $\frac{\partial\xi^m}{\partial t}$ is the grid speed. The three momentum elements of Eq. (5) are given by

$$\partial_k\xi^s\tau_{kj} = \frac{M_\infty\mu}{Re}\left[\left(\partial_k\xi^s\partial_j\xi^n - \frac{2}{3}\partial_j\xi^s\partial_k\xi^n\right)\frac{\partial u_k}{\partial\xi^n} + \partial_k\xi^s\partial_k\xi^n\frac{\partial u_j}{\partial\xi^s}\right]; \quad j = 1-3 \qquad (7)$$

The last element of Eq. (5) is given by

$$\partial_k\xi^s(u_p\tau_{kp} - q_k) \equiv \frac{M_\infty\mu}{Re}\left[\left(\partial_k\xi^s\partial_p\xi^n - \frac{2}{3}\partial_p\xi^s\partial_k\xi^n\right)u_p\frac{\partial u_k}{\partial\xi^n} + \partial_k\xi^s\partial_k\xi^n u_p\frac{\partial u_p}{\partial\xi^n} + \frac{1}{(\gamma-1)P_r}\partial_k\xi^s\frac{\partial(a^2)}{\partial\xi^n}\right]; p = 1-3 \qquad (8)$$

The reference parameters for the dimensionless form of the equations are $L, a_\infty, L/a_\infty, \rho_\infty$ and $\mu_\infty$ for the length, velocity, time, density and molecular viscosity, respectively. The Reynolds number is defined as $Re = \rho_\infty V_\infty L/\mu_\infty$, where $L$ is the cone length. The pressure, $p$, is related to the total energy per unit mass, $e$, and density, $\rho$, by the gas equation

$$p = (\gamma - 1)\rho\left(e - \frac{1}{2}u_n u_n\right). \qquad (9)$$

The viscosity, $\mu$, is calculated from the Sutherland law

$$\mu = T^{3/2}\left(\frac{1+C}{T+C}\right), \quad C = 0.4317, \qquad (10)$$

and the Prandtl number Pr = 0.72.

In Eqs. (1)-(10), the indicial notation is used for convenience. The subscripts $j$, $k$ and $n$ are summation indices, the superscript or subscript $s$ is a summation index and the superscript or subscript $m$ is a free index. The range of $j$, $k$, $n$, $s$ and $m$ is 1-3, and $\partial_k \equiv \partial/\partial x_k$. In Eqs. (1)-(10), $u_n$ is the Cartesian velocity component, $U_m$ the contravariant velocity component, $\tau_m$ the Cartesian component of the shear stress tensor, $q_k$ the Cartesian component of heat flux vector, $a$ the local speed of sound and $M_\infty$ the freestream Mach number.

## Boundary and Initial Conditions and Grid Motion:

Boundary conditions are explicitly implemented. They include inflow-outflow conditions, solid-boundary conditions and plane of geometric symmetry conditions. At the plane of geometric symmetry, periodic conditions are enforced. Since we are dealing with a supersonic flow, at the far-field inflow boundaries, freestream conditions are specified and all the five flow variables are extrapolated from the exterior values according to the Riemann-invariant characteristic conditions. The conical shock is captured as part of the solution. At the far-field outflow boundaries, first-order extrapolation from the interior point is used.

Since the cone is undergoing spinning or rotatory-oscillation motion at an angular velocity of $\omega\hat{e}_x$ around the x-axis, where $\hat{e}_x$ is a unit vector along the x-axis and $\omega$ is either uniform (for spinning motion) or time dependent (for rotatory oscillation), the grid is moved with the same angular velocity as that of the body. The grid speed, $\frac{\partial\xi^m}{\partial t}$, and the metric coefficient, $\frac{\partial\xi^m}{\partial x_n}$, are computed at each time step of the computational scheme. Consequently, the kinematical boundary conditions at the inflow-outflow boundaries and at the cone surface are expressed in terms of the relative velocities. For the dynamical boundary condition, $\frac{\partial p}{\partial n}$ at the cone surface is no longer equal to zero. This condition for the present rotating cone is modified as

$$\left.\frac{\partial p}{\partial n}\right|_{cone} = -\rho\bar{a}_c\cdot\hat{n} = \rho r_c\omega^2 = \rho\left(\frac{\partial\xi^2}{\partial t}\right)^2_{cone}/r_c \qquad (11)$$

where $r_c$ is the cone radius and $\bar{a}_c$ is the acceleration of the cone surface. It should be noted that the other tangential acceleration does not contribute to the right-hand side of Eq. (13) since its scalar product with $\hat{n}$ is zero. Finally, the boundary condition for the temperature is obtained from the adiabatic boundary condition, $\left.\frac{\partial T}{\partial n}\right|_{cone} = 0$.

The initial conditions correspond to the asymmetric flow solution without the cone rotation.

## COMPUTATIONAL SCHEME

The implicit, upwind, flux-difference splitting, finite-volume scheme is used to solve the unsteady, compressible, full Navier-Stokes equations. The scheme uses the flux-difference splitting of Roe. The smooth flux limiter is used to eliminate oscillations at locations of large flow gradients. The viscous- and heat-flux terms are linearized in time and the cross-derivative terms are eliminated in the implicit operator and retained in the explicit terms. The viscous terms are differenced using second-order accurate central differencing. The resulting difference equation is approximately factored and is solved in three sweeps in the $\xi^1, \xi^2$ and $\xi^3$ directions. The computational scheme is coded in the computer program "FTNS3D".

For the locally-conical flow solutions, an axial station of $x_1 = 1.0$ is selected and the components of the flowfield vector are forced to be equal between this axial station and another axial station in close proximity. This ensures that the flow variables are locally independent of the axial direction at $x_1 = 1.0$.

The method of solution consists of two steps. In the first step, the problem is solved for the asymmetric flow without rotating the cone. This solution represents the initial conditions for the second step. In the second step, the cone spinning rate or rotatory oscillation is specified and the NS equations are solved accurately in time. At each time step, the body and the grid are rotated through an angle corresponding to the cone rotational velocity. The metric coefficients and the grid speed are computed and the Roe flux-difference splitting scheme is used to obtain the solution. The computations proceed until periodic responses are obtained.

## COMPUTATIONAL APPLICATIONS

A $5°$ semi-apex angle circular cone is used for the present applications. The freestream Mach number is 1.8 and the Reynolds number based on the cone length is $10^5$. A grid of $241 \times 81 \times 2$ grid points in the wrap-around, normal and axial directions, respectively, is used for all the computational applications. The minimum grid size, $\Delta\xi^3$, at the cone surface is of order $10^{-4}$.

### Initial Conditions, Cone at $\alpha = 20°$, $\frac{\partial \xi^2}{\partial t} = 0$:

The cone is set at an angle of attack, $\alpha$, of 20° and the spinning rate, $\frac{\partial \xi^2}{\partial t}$, is set equal to zero. Figure 1 shows the total-pressure-loss (TPL) contours, surface-pressure (SP) coefficient versus angle $\theta$ (measured from the windward plane of geometric symmetry) and streamlines for the locally-conical flow solution after 13,000 time steps. The solution is obtained using time-accurate stepping with $\Delta t = 0.001$. The solution shows that the flow is steady and asymmetric. This solution serves as initial conditions for the next applications with different spinning rates.

### Uniform Spinning Rate:

There are several basic ideas behind the use of spinning to alleviate or possibly eliminate the asymmetry of vortices and their subsequent result of producing a side force on the cone. One of the ideas can be explained by considering the asymmetric solution of Fig. 1, which represents the initial condition. By spinning the cone in the counter-clockwise direction, the speed of boundary-layer flow on the right-hand side of the cone is enhanced for resisting flow separation while the speed of the boundary-layer flow on the left-hand side of the cone is retarded for producing early flow separation. Moreover, the spinning motion is adding either positive or negative vorticity in the flowfield. Hence, by selecting the appropriate spinning rate, the asymmetric vortices might be rendered symmetric. This is the first effect of spinning. The second effect of spinning is the increase of the pressure gradient normal to the body $\left(\frac{\partial P}{\partial n}\big|_{cone} = \rho\omega^2 r_{cone}\right)$. For small values of $\omega$, the effect of the pressure gradient will not be pronounced. However, for large values of $\omega$, the effect of the pressure gradient will be pronounced. the other idea behind using spinning as an active control method is based on the experimental data where Kruse[13] and Fidler[14] found that spinning produced oscillatory side-force response. If the mean of the side force is zero then the average side force will be zero. In the next applications, we present the effects of constant spinning at tangential velocities, $\frac{\partial \xi^2}{\partial t}$, of ±0.06 and ±0.2 which correspond to spinning rates, $\Omega$, of ±2,292 rpm and ±7,639 rpm for a cone of one meter long, respectively.

### 1. Uniform Spinning at ±0.06:

Figures 2 and 3 show the results for uniform counter-clockwise (CCW) spinning at $\frac{\partial \xi^2}{\partial t} = 0.06$, and Figures 4 and 5 show the results for uniform clockwise (CW) spinning at $\frac{\partial \xi^2}{\partial t} = -0.06$. All spinning cases start at the time step n = 13,001 and the solutions are obtained with $\Delta t = 0.001$. With the present surface speed of 0.06, the cone rotates one revolution in 9.163 dimensionless time, which corresponds to 9,163 time steps. Figure 2 shows the side-force and lift coefficients ($C_Y$ and $C_L$) versus the number of time steps. It is observed that the force coefficients reach a periodic response very quickly and the period of oscillation is 9.163 dimensionless time, which is equal to the time required to rotate the cone one revolution. The $C_Y$ curve oscillates between −0.00069 and −0.00053 with a mean value of

–0.00061. The magnitude of the mean $C_Y$ is less than the magnitude of $C_Y$ without spinning which is equal to 0.00065. Thus, the CCW spinning reduces the magnitude of the side force on the average. The $C_L$-coefficient curve shows small-amplitude periodic response. In Fig. 3, snapshots of the TPL contours, SP coefficient and streamlines are shown at five instants covering one cycle of periodic side-force response. They are marked by the numbers 1, 2, 3, 4 and 5 on Figs. 2 and 3. The snapshots show that the right and left vortices heights, lateral positions, strengthens and separation points oscillate slightly. Consequently, the corresponding surface pressures oscillate slightly too. The CCW spinning delays flow separation on the right side and expedites flow separation on the left side.

With the CW spinning of –0.06, the $C_Y$ and $C_L$ curves of Fig. 4 show that their periodic response is also reached very quickly. The $C_Y$ curve oscillates between –0.00077 and –0.00055 with a mean value of –0.00066. The magnitude of the mean $C_Y$ is slightly higher than the magnitude of $C_Y$ without spinning. Thus, the CW spinning does not reduce the mean value of side force. Figure 5 shows snapshots of the TPL contours, SP coefficients and streamlines at four instants (marked by 1, 2, 3 and 4 in Figs. 3 and 4) during one cycle of periodic response. The CW spinning increases flow separation on the right side and delays flow separation on the left side. Comparisons of the snapshots of Fig. 5 with the corresponding snapshots of Fig. 3, show that the vortex on the right-hand side of Fig. 5 (snapshot 1) moves more to the right while the vortex on the right-hand side of Fig. 3 (snapshot 1) moves more to the left. Similar motions are observed for the vortex on the left side of Figs. 5 and 3 (snapshot 1). Hence, the side force at point 1 of the CW spinning will be of higher magnitude than the side force at point 1 of the CCW spinning.

### 2. Uniform Spinning at ±0.2:

Next, the uniform spinning is increased to 0.2. The results of the CCW spinning are shown in Figs. 6 and 7 and the results of the CW spinning are shown in Fig. 8. With the surface speed of 0.2, the cone rotates one revolution in 2.749 dimensionless time, which corresponds to 2,749 time steps. Figure 6 shows that the $C_Y$ and $C_L$ curves reach a periodic response very quickly and the period of oscillation is 2.749 dimensionless time. The $C_Y$ curve oscillates between –0.00089 and –0.000050 with a mean value of –0.00047. The magnitude of the mean $C_Y$ is substantially lower than the magnitude of $C_Y$ without spinning. Thus, the high CCW spinning does reduce the mean value of side force. It should be noticed that the amplitude of oscillation of the $C_L$ curve is higher than that of Fig. 2. Three snapshots of the TPL contours, SP coefficient and streamlines during a half-cycle of the periodic $C_Y$ curve (marked by 1, 2 and 3 in Figs. 6 and 7) are shown in Fig. 7. It is noticed that the CCW spinning substantially increases the flow separation on the left side and delays the flow separation on the right side. Also, it is noticed that the right-hand side vortex moves more in the downward and leftward directions than that of Fig. 3. The left-hand side vortex moves more in the leftward direction than that of Fig. 3.

Figure 8 shows the $C_Y$ and $C_L$ periodic responses for the CW spinning case at –0.2. The $C_Y$ curve oscillates between –0.00102 and –0.00021 with a mean value of –0.00615. The magnitude of the mean $C_Y$ is lower than the magnitude of $C_Y$ without spinning but it is substantially higher than the mean value of the CCW spinning of Fig. 6. A snapshot of the TPL contours, SP coefficient and streamlines is shown in Fig. 8. The CW spinning is observed to increase the flow separation on the right side and the left-hand side vortex moves more to the right.

### 3. Uniform Spinning at +0.6:

The uniform spinning is increased to 0.6 and the results of the CCW spinning are shown in Fig. 9. With the speed of 0.6, the cone rotates one revolution in 0.916 dimensionless time. The $C_Y$ curve shows the periodic response which oscillates between –0.005 and +0.0038 with a mean value of –0.0006. With this high value of CCW spinning, the side-force coefficient is oscillating between positive and negative values and the vortices on the left and right sides are changing heights periodically. It is noticed that the boundary layer at certain instants will become a free-shear-layer band around the body (e.g. Fig. 9-snapshot 1). Although the mean value of side force is not zero, this test tells that there is a certain CCW spinning value at which the mean side force will be zero.

## Rotatory Oscillations:

In this section, we investigate the effect of periodic rotatory oscillation of the cone on the flow asymmetry and the side force. The form of the surface speed is given by

$$\frac{\partial \xi^2}{\partial t} = V_s \cos \frac{2\pi}{\tau} t \qquad (12)$$

where $V_s$ is the surface-speed amplitude and $\tau$ is the period of oscillation. Substituting Eq. (12) into the relation $\frac{d\theta}{dt} = \frac{\partial\xi^2}{\partial t}/r_c$ and integrating the result one obtains the corresponding equation for the angular motion, $\theta$, which is

$$\theta = \theta_a \sin \frac{2\pi}{\tau} t \qquad (13)$$

where $\theta_a = \frac{V_s\tau}{2\pi r_c}$. By specifying $V_s$ and $\tau$, one can obtain the amplitude of the angular motion, $\theta_a$, for a certain value of the cone radius, $r_c$. Next, we present the results for different values of $V_s$ and $\tau$ of the periodic rotatory oscillation.

### 1. Rotatory Oscillation; $V_s$=0.06, $\tau$=7.2, $\theta_a$=45°:

The corresponding frequency of this motion is 0.873. The results of this case are given in Fig. 10. The period of the $C_Y$ response is observed to be 7.2 which is the same as that of the motion. The $C_Y$ curve oscillates between –0.00077 and –0.00054 with a mean value of –0.000655, which is between the mean values of CCW and CW spinning cases of Figs. 2 and 4. Hence, these values of $V_s, \tau$ and $\theta_a$ for the rotatory oscillation do not reduce the mean value of $C_Y$.

### 2. Rotatory Oscillation; $V_s$ = 0.2, $\tau$ = 4.3, $\theta_a$ = 90°:

The corresponding frequency of this motion is 1.461. The results of this case are given in Fig. 11. The period of the $C_Y$ response is observed to be 4.3 which is the same as that of the motion. The $C_Y$ curve oscillates between –0.00105 and –0.0002 with a mean value of –0.000625. This mean value of the $C_Y$ is higher than that of the CCW spinning case of Fig. 6 and is slightly higher than that of the CW spinning case of Fig. 8. Hence, these values of $V_s, \tau$ and $\theta_a$ for the rotatory oscillation do not reduce the mean value of $C_Y$.

### 3. Rotatory Oscillation; $V_s$ = 0.5, $\tau$ = 7.2, $\theta_a$ = 375°:

The corresponding frequency of this motion is 0.873. which is the same as that of the case of Fig. 10. However. the amplitudes of the surface velocity and angular motion are one order of magnitude higher than those of the case of Fig. 10. The results of this case are given in Fig. 12. Although the $C_Y$ response is periodic with the same period as that of the motion, there are several peaks within each period. The $C_Y$ changes sign from positive to negative and the mean value of the $C_Y$ is zero. This shows that the values of $V_s, \tau$ and $\theta_a$ for the rotatory oscillation eliminate the $C_Y$ on the average. It should be emphasized here that both the amplitudes of surface velocity and angular motion are one order of magnitude higher than that of the case of Fig. 10.

### 4. $V_s$ = 0.5, $\tau$ = 4.3, $\theta_a$ = 225°:

The corresponding frequency of this motion is 1.461, which is the same as that of the case of Fig. 11. However, the amplitudes of the surface velocity and angular motion are 2.5 times as those of the case of Fig. 11. The results of this case are given in Fig. 13. The $C_Y$ response is periodic with the same period as that of the motion, but with several peaks within each period. Here again the $C_Y$ changes sign from positive to negative and the mean value of the $C_Y$ is –0.00015, which is better than that of any of the uniform spinning cases or the rotatory oscillations of Figs. 10 and 11. However, it is higher than that of the previous case. The only differences between this case and the previous case is the period of oscillation and the amplitude of angular motion. Although the magnitude of the mean $C_Y$ is higher than that of the case of Fig. 12, the peak values of $C_Y$ of the present case are substantially lower than those of the previous case. It seems that the best $C_Y$ response (zero mean and small amplitude) can be achieved by using the higher $\theta_a$ and the lower $\tau$ of the present case and the previous case. Optimal control laws should be developed to effectively investigate this problem.

## CONCLUDING REMARKS

In the present study, the effectiveness of uniform spinning and rotary oscillation as active control methods for alleviating the flow asymmetry and the side force has been investigated computationally. It has been shown that a large value of uniform CCW spinning rate is very effective in substantially reducing the side force on the average for the given initial case of asymmetric flow. The CCW spinning increases flow separation on the left side and delays it on the right side. which produces equal positive and negative side forces within each cycle of the side-force response. The rotatory oscillation with large surface-velocity amplitude, large angular-motion amplitude and small period of oscillation (high frequency) is much more effective than the uniform CCW spinning for the same surface velocity because it does not only eliminate the mean side force but it also reduces the amplitude of the side force substantially. Moreover, the effectiveness of the rotatory oscillation control does not require certain initial shape of the vortex asymmetry.

Work is currently underway to study the effectiveness of the rotatory oscillation control on asymmetric flow cases with periodic vortex shedding at high angles of attack. Optimal control laws should be developed for investigating this problem.

## ACKNOWLEDGEMENT

For the first two authors, this research work has been supported under grant No. NAG-1-994 from the NASA Langley Research Center. The authors would like also to thank Dr. Tin-Chee Wong for validating some of the results using a different version of the FTNS3D code. The authors would like also to acknowledge the computer resources provided by the NAS facilities at Ames and the NASA Langley Research Center.

## REFERENCES

1. Stahl, W., "Suppression of Asymmetry of Vortex Flow Behind a Circular Cone at High Incidence," Proceedings of the AIAA Atmospheric Flight Mechanics Conference, Boston, MA, AIAA 39-3372–CP, pp. 231–236, 1989.
2. Ng, T. T., "On Leading Edge Vortex and Its Control," Proceedings of the AIAA Atmospheric Flight Mechanics Conference, Boston, MA, AIAA 89–3346-CP, pp. 1–15, 1989.
3. Moskovitz, C., Hall, R. and DeJarnette, "Experimental Investigation of a New Device to Control the Asymmetric Flowfield on Forebodies at Large Angles of Attack," AIAA 90–0069, 1990.
4. Skow, A. M. and Peake, D. J., "Control of the Forebody Vortex Orientation by Asymmetric Air Injection, (Part B) — Details of the Flow Structure," AGARD-LS-121, High Angle-of-Attack Aerodynamics, pp. 10.1–10.22, 1982.
5. Ng, T. T., Suarez, C. J. and Malcolm, N., "Forebody Vortex Control Using Slot Blowing," Proceedings of the AIAA 9th Applied Aerodynamics Conference, Baltimore, Maryland, AIAA 91–3254–CP, pp. 412–421, 1991.
6. Gittner, M. N. and Chokani, N., "An Experimental Study of the Effects of Aft Blowing on a 3.0 Caliber Tangent Ogive Body at High Angles of Attack," Proceedings of the AIAA 9th Applied Aerodynamics Conference, Baltimore, Maryland, AIAA 91–3252–CP, pp. 390–399, 1991.
7. Font, G. I., Celik, Z. Z. and Roberts, L., "A Numberical and Experimental Study of Tangential Jet Blowing Applied to Bodies at High Angles of Attack," Proceedings of the AIAA 9th Applied Aerodynamics Conference, Baltimore, Maryland, AIAA 91–3253–CP, pp. 400–411, 1991.
8. Ng, T. T., "Aerodynamic Control of NASP-Type Vehicles Through Vortex Manipulation," AIAA 90–0594, 1990.
9. Kandil, O. A., Wong, T-C., Kandil, H., A. and Liu, C. H., "Computation and Control of Asymmetric Vortex Flow Around Circular Cones Using Navier-Stokes Equations," ICAS Paper No. 3.5.3, Vol. 2, Stockholm, Sweden, pp. 883–893, 1990.
10. Tavella, D. A., Schiff, L. B. and Cummings, R. M., "Pneumatic Vortical Flow Control at High Angles of Attack," AIAA 90-0098, 1990.
11. Gee, K., Tavella, D. and Schiff, L. S., "Computational Optimization of a Pneumatic Forebody Flow Control Concept," Proceedings of the AIAA 9th Applied Aerodynamics Conference, Baltimore, Maryland, AIAA 91–3249–CP, pp. 370–380, 1991.
12. Kandil, O. A., Sheraf, H. H. and Liu, C. H., "Active Control of Asymmetric Vortical Flows around Cones Using Injection and Heating," AIAA 92–4426–CP, August 1992.
13. Kruse, R.L., "Influence of Spin Rate on Side Force of an Axisymmetric Body," AIAA Journal, Vol. 16, No. 4, April 1974, pp. 415–416.
14. Fidler, J.E., "Active Control of Asymmetric Vortex Effects," J. of Aircraft, Vol. 18, No. 4, April 1981, pp. 267–272.
15. Coutanceau, M. and Ménard, C., "Influence of Rotation on the Near-Wake Development behind an Impulsively Started Circular Cylinder," Journal of Fluid Mechanics, Vol. 158, 1985, pp. 399–446.
16. Taneda, S., "Visual Observations of the Flow Past a Circular Cylinder Performing Rotatory Oscillation," Journal of Physical Society of Japan, Vol. 45, 1978, pp. 1038–1043.
17. Chen, Y-M, Ou, Y-R and Pearlstein, A. J-., "Development of the Wake Behind a Circular Cylinder Impulsively Started Into Rotatory and Rectilinear Motion: Intermediate Rotation Rates," ICASE Report No. 91-10, NASA Research Center, January 1991.
18. Kandil, O.A. and Chuang, H.A., "Unsteady Navier-Stokes Computations Past Oscillating Delta Wing at High Incidence," AIAA-89–0081, January 1989. Also AIAA Journal, Vol. 28, No. 9, September 1990, pp. 1565–1572.

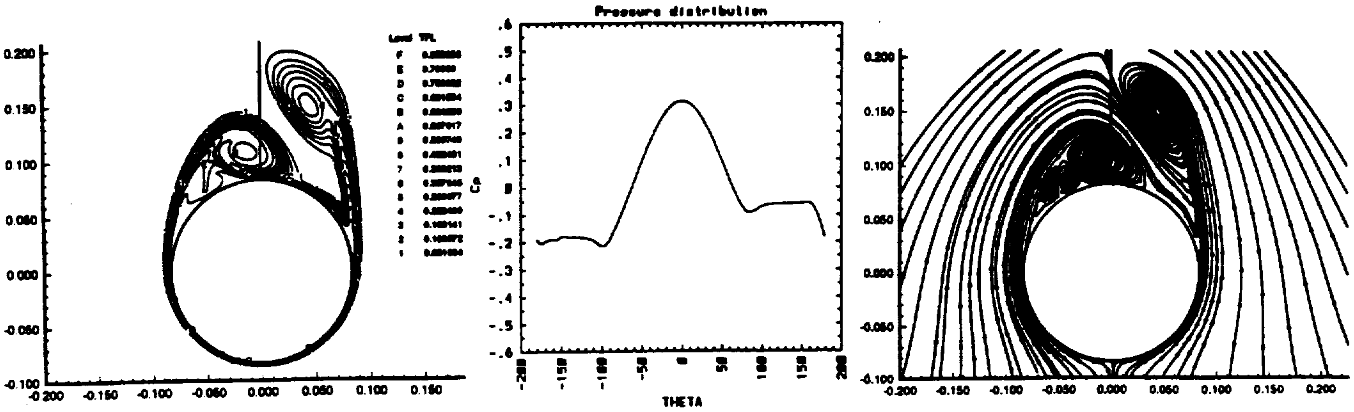

Fig. 1 Asymmetric solution without spinning, $\alpha = 20°$. $M_\infty = 1.8$. $R_e = 10^5$.

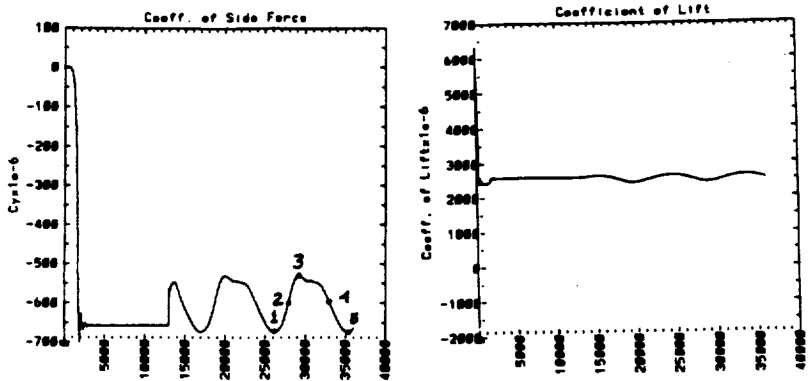

Fig. 2 Side-force and lift coefficients vz number of time steps, $\frac{\partial \xi^2}{\partial t} = 0.06$ (CCW spinning), $\alpha = 20°$. $M_\infty = 1.8$. $R_e = 10^5$. $\tau = 9.163$.

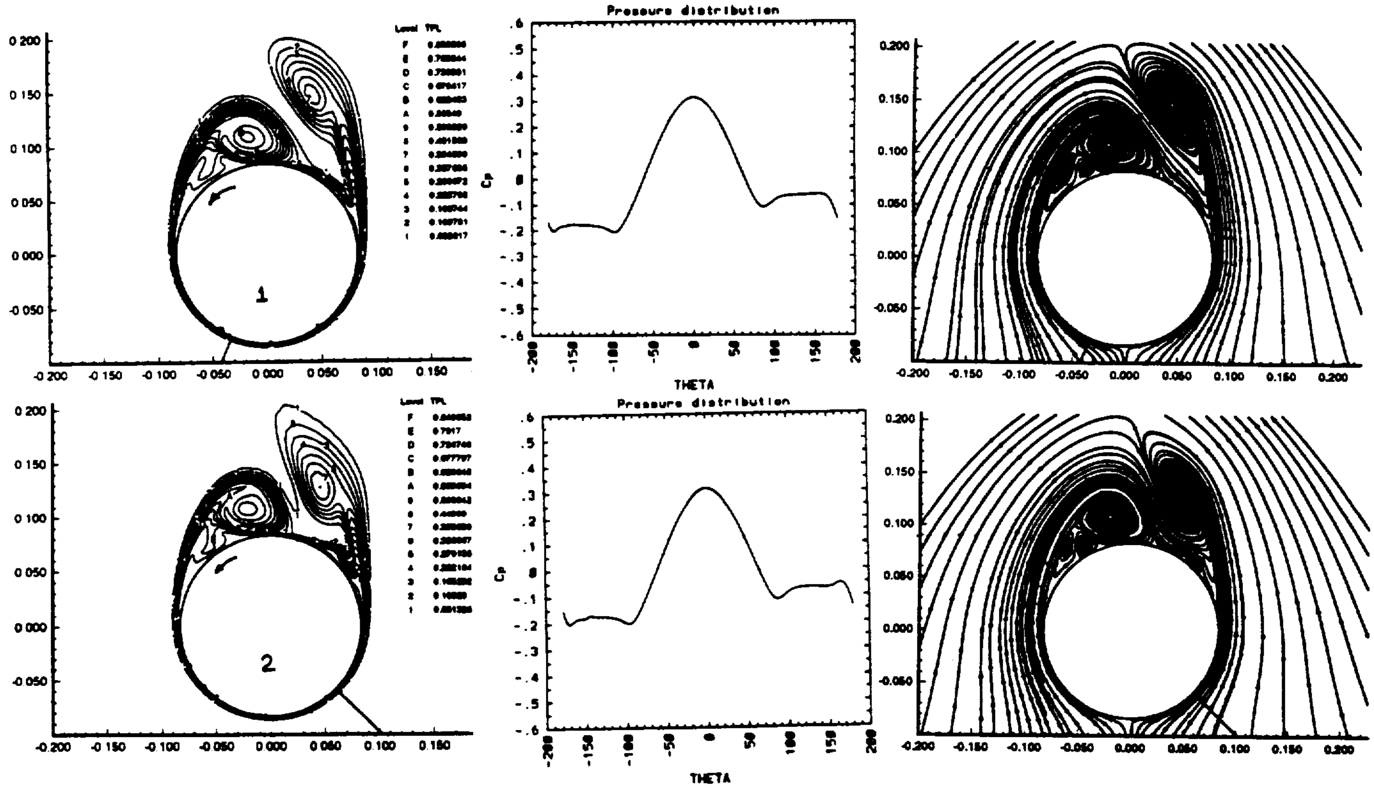

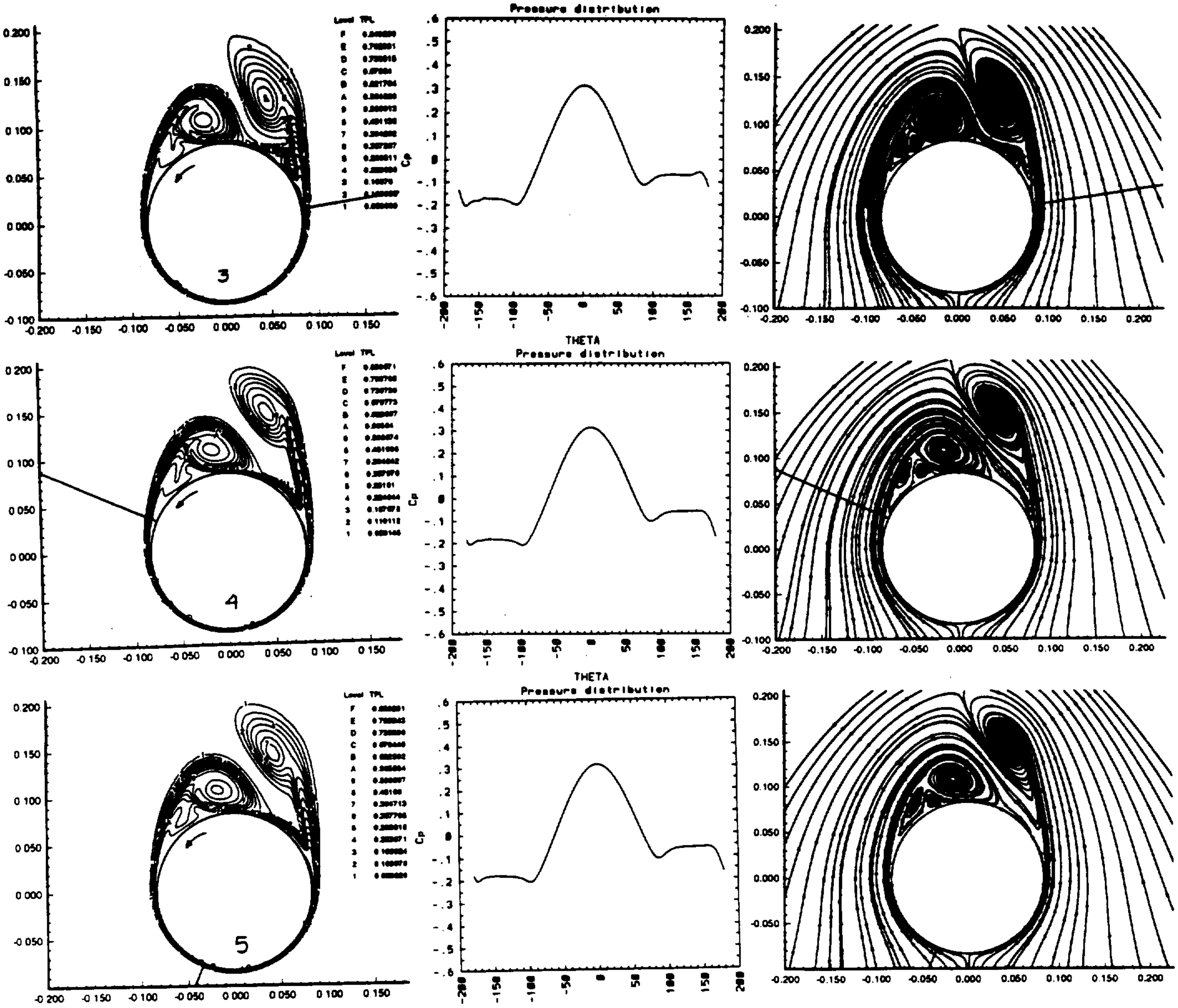

Fig. 3 Snapshots of TPL contours, Cp and streamlines covering one cycle, $\frac{\partial \xi^2}{\partial t} = 0.06$ (CCW spinning), $\alpha = 20^\circ$, $M_\infty = 1.8$, $R_e = 10^5$, $\tau = 9.163$.

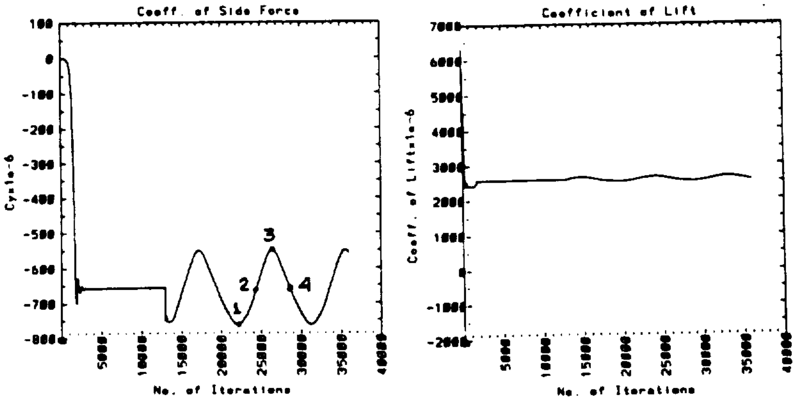

Fig. 4 Side-force and lift coefficients vz number of time steps, $\frac{\partial \xi^2}{\partial t} = -0.06$ (CW spinning), $\alpha = 20^\circ$, $M_\infty = 1.8$, $R_e = 10^5$, $\tau = 9.163$.

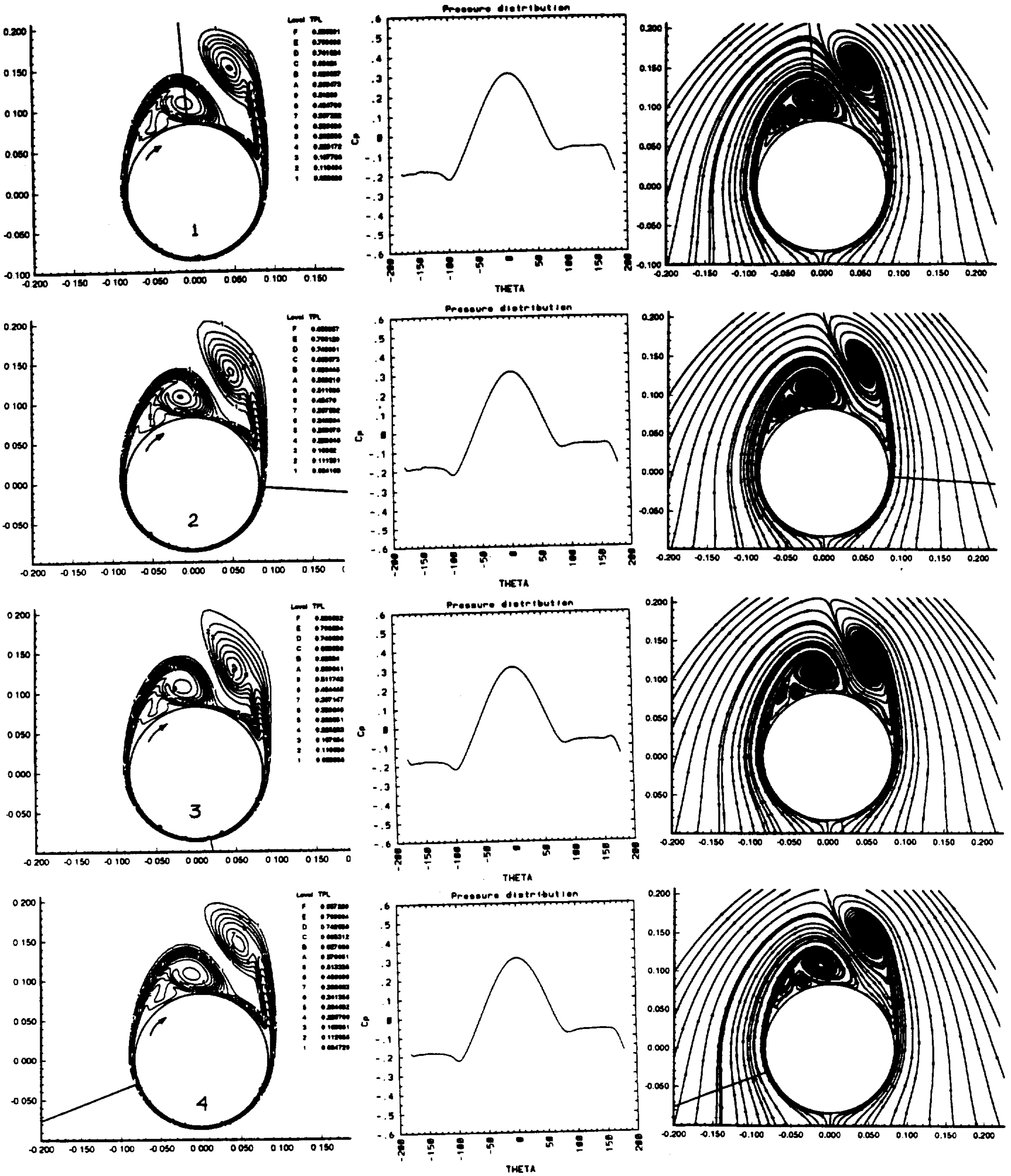

Fig. 5 Snapshots of TPL contours, Cp and streamlines within one cycle, $\frac{\partial \xi^2}{\partial t} = -0.06$ (CW spinning), $\alpha = 20^\circ$. $M_\infty = 1.8$. $R_e = 10^5$. $\tau = 9.163$.

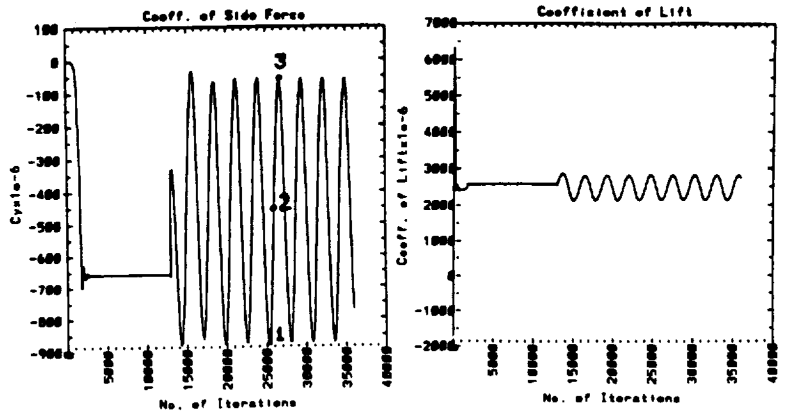

Fig. 6 Side-force and lift coefficients vz number of time steps, $\frac{\partial\xi^2}{\partial t} = 0.2$ (CCW spinning), $\alpha = 20^o$, $M_\infty = 1.8$, $R_e = 10^5$, $\tau = 2.749$.

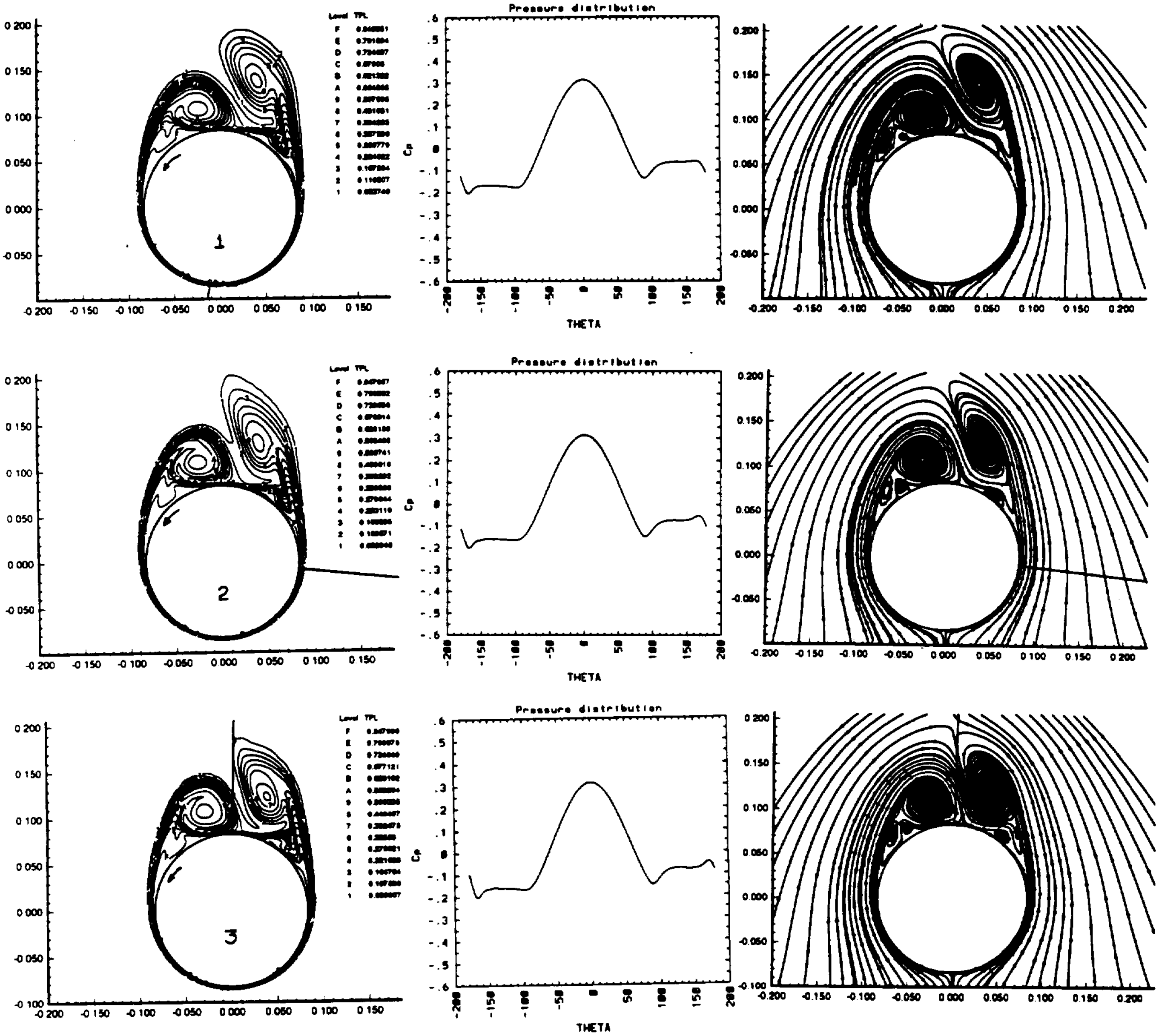

Fig. 7 Snapshots of TPL contours, Cp and streamlines within one cycle, $\frac{\partial\xi^2}{\partial t} = 0.2$ (CCW spinning), $\alpha = 20^o$, $M_\infty = 1.8$, $R_e = 10^5$, $\tau = 2.749$.

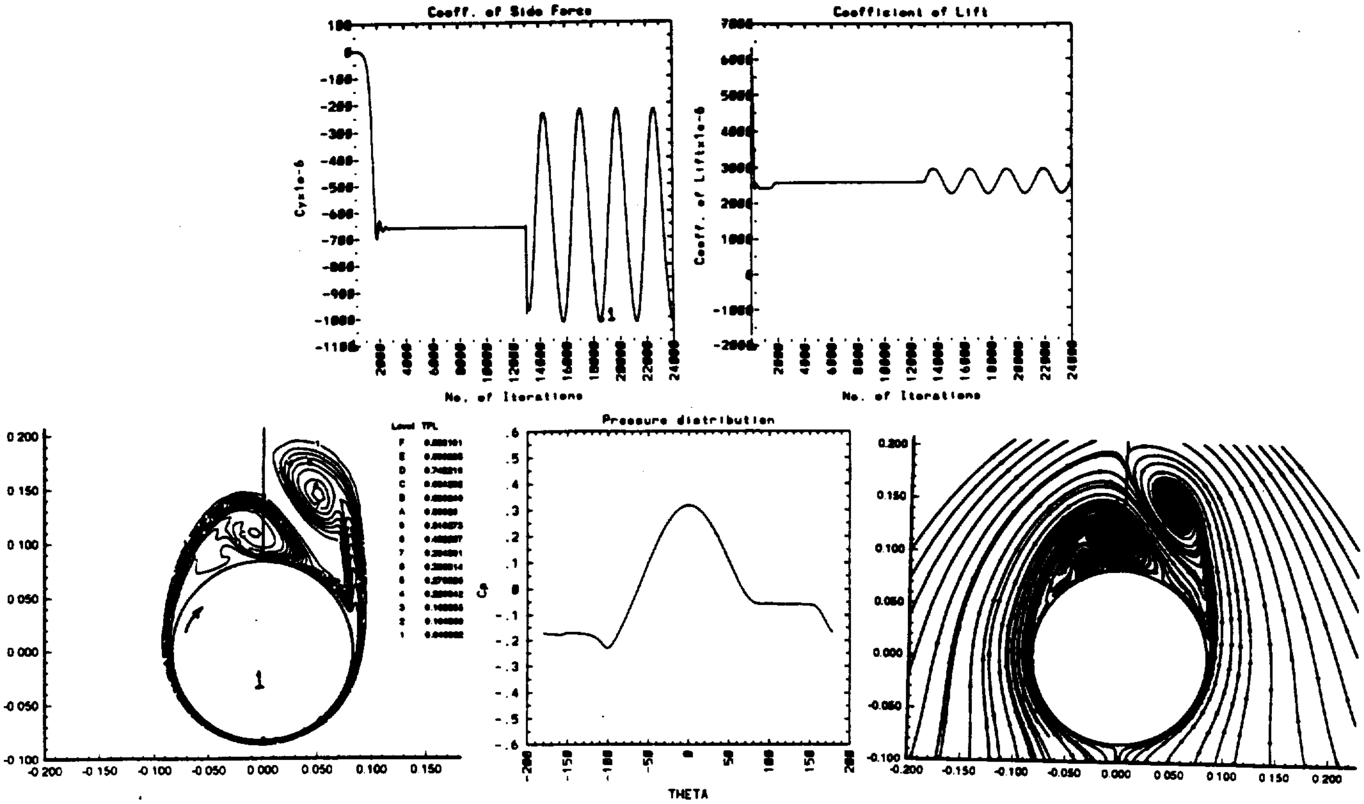

Fig. 8 Side-force and lift coefficients and TPL contours, Cp and streamlines, $\frac{\partial \xi^2}{\partial t} = -0.2$ (CW spinning), $\alpha = 20^\circ$, $M_\infty = 1.8$, $R_e = 10^5$, $\tau = 2.749$.

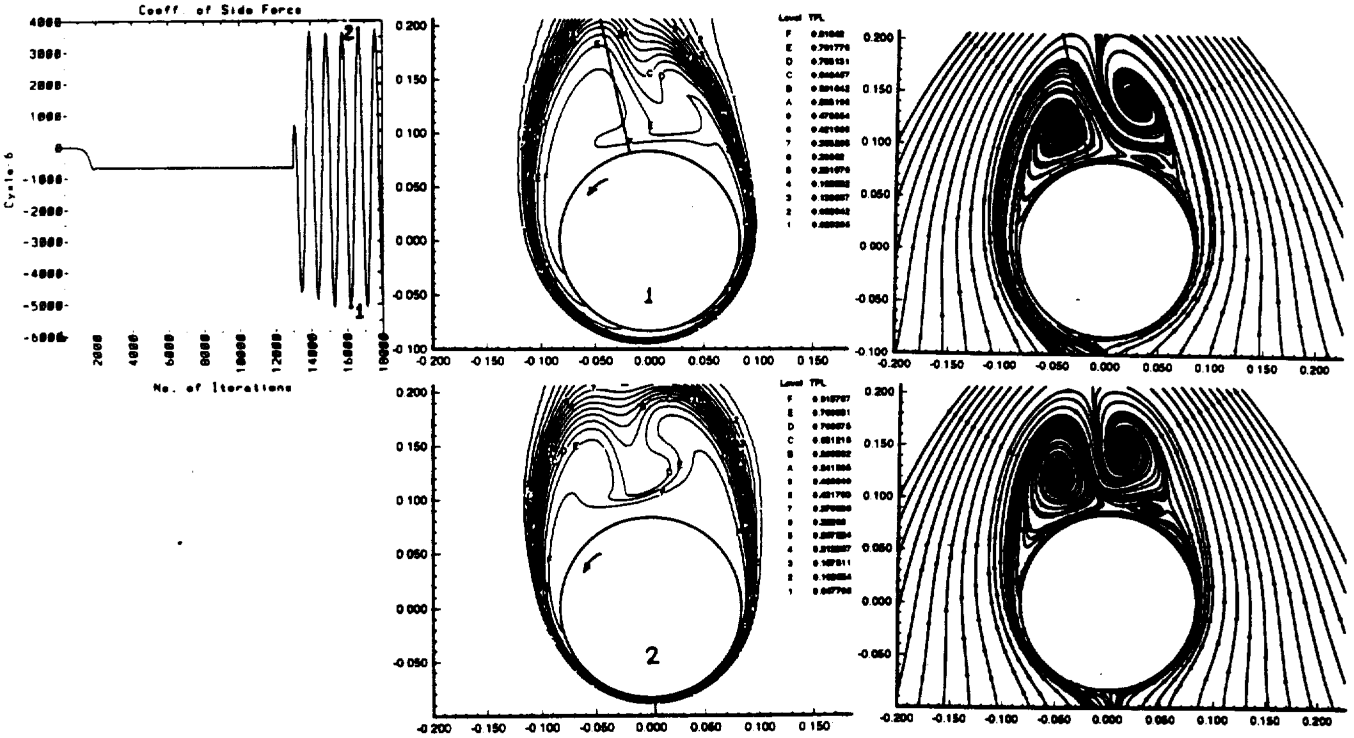

Fig. 9 Side-force coefficient, TPL contours, Cp and streamlines, $\frac{\partial \xi^2}{\partial t} = 0.6$ (CCW spinning), $\alpha = 20^\circ$, $M_\infty = 1.8$, $R_e = 10^5$, $\tau = 0.916$.

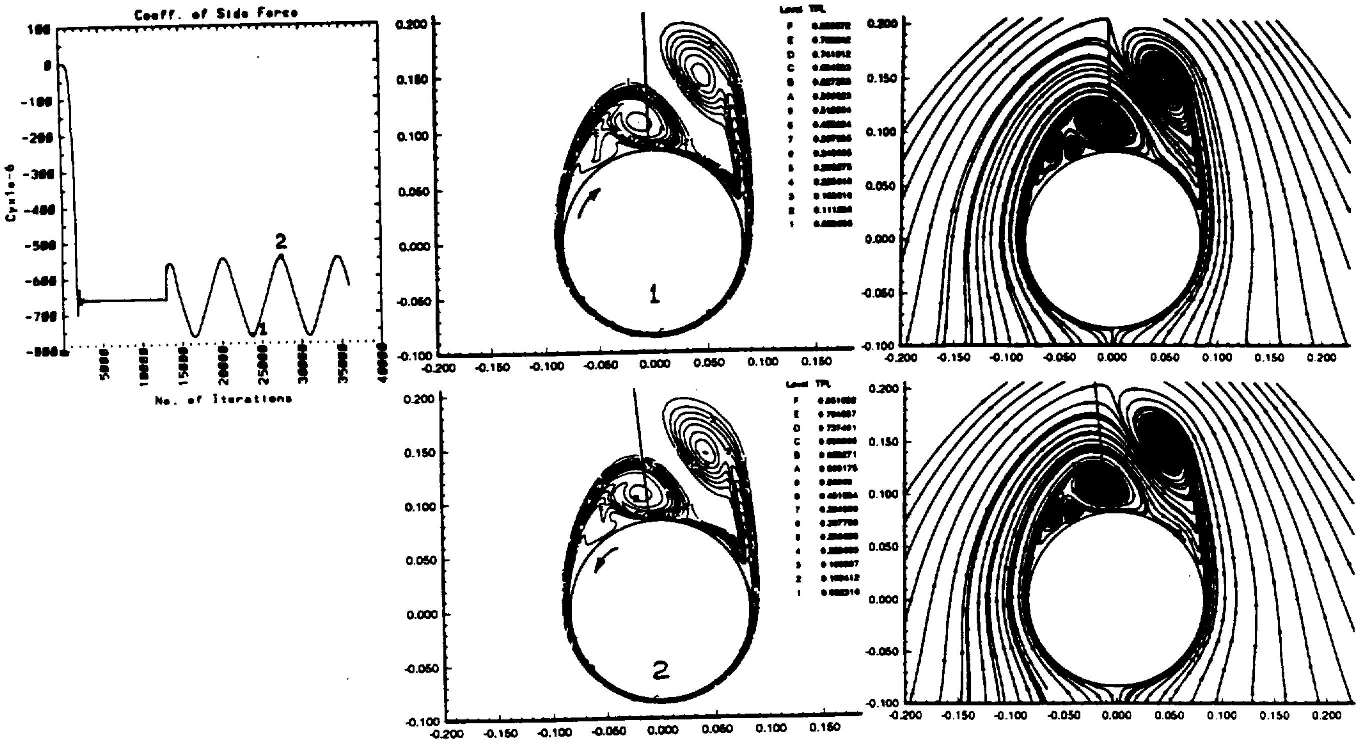

Fig. 10 Side-force coefficient, TPL contours, Cp and streamlines, $\frac{\partial \xi^2}{\partial t} = 0.06 \cos \frac{2\pi}{\tau} t$ (rotatory oscillation), $\tau = 7.2$, $\theta_a = 45^\circ$, $\alpha = 20^\circ$, $M_\infty = 1.8$, $R_e = 10^5$.

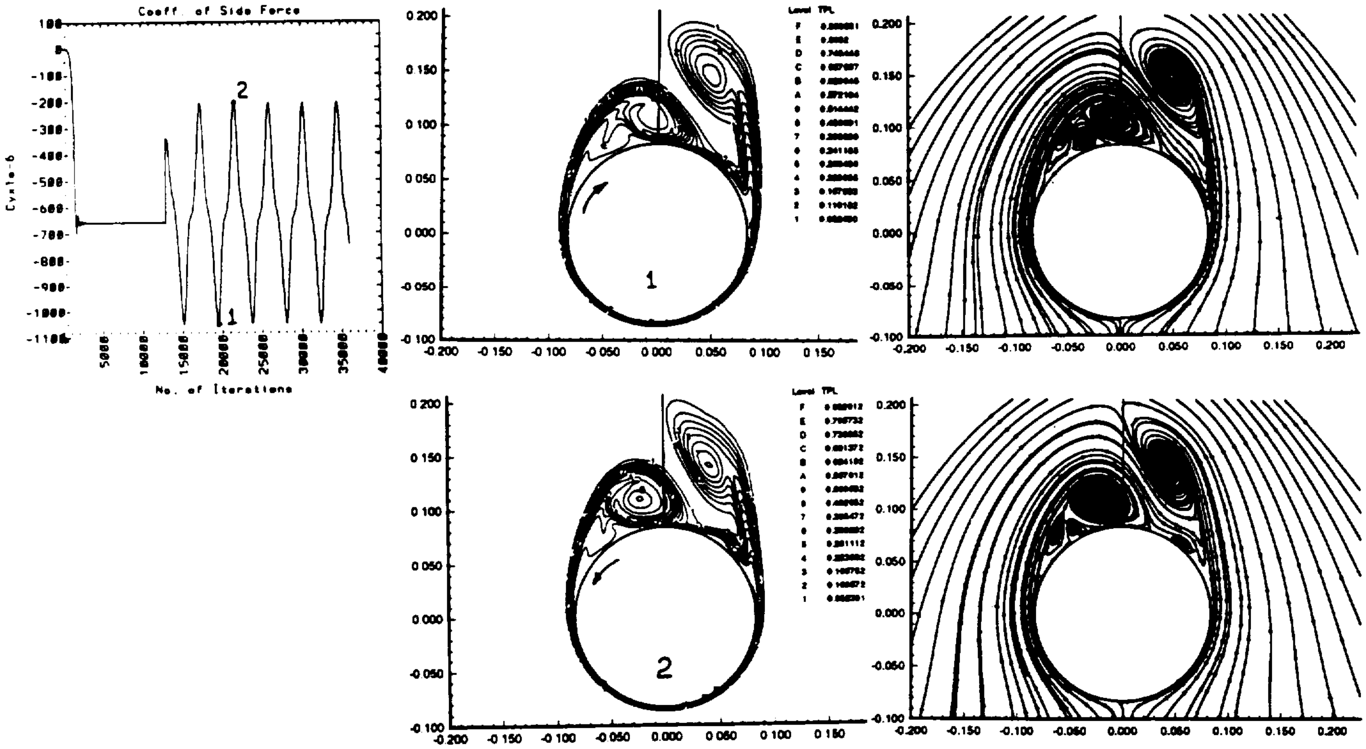

Fig. 11 Side-force coefficient, TPL contours, Cp and streamlines, $\frac{\partial \xi^2}{\partial t} = 0.2 \cos \frac{2\pi}{\tau} t$ (rotatory oscillation), $\tau = 4.3$, $\theta_a = 90^\circ$, $\alpha = 20^\circ$, $M_\infty = 1.8$, $R_e = 10^5$.

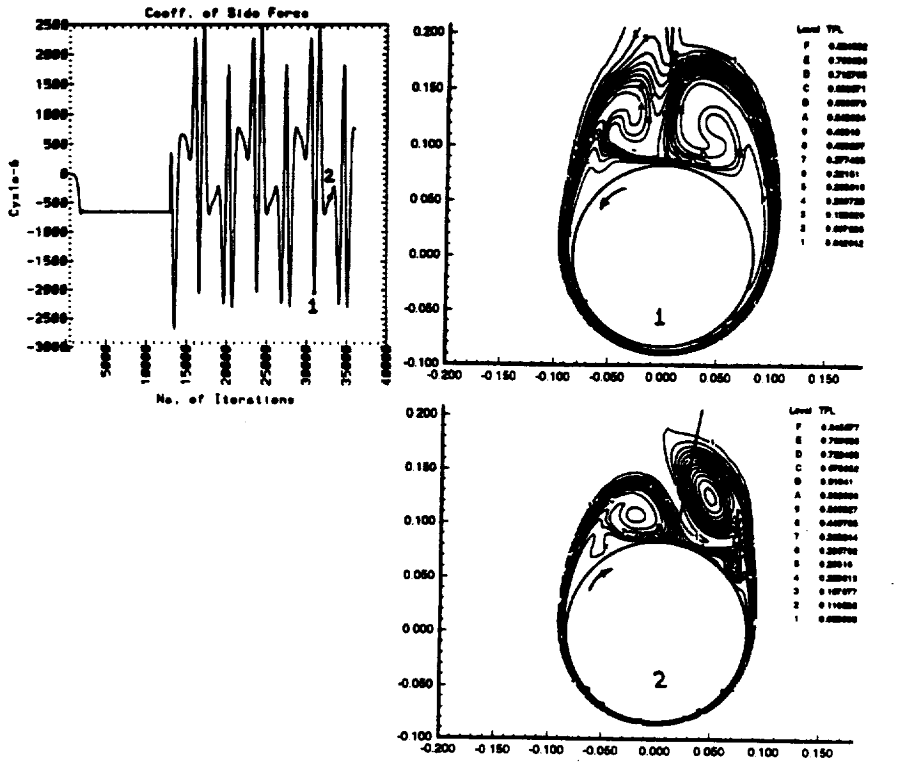

Fig. 12 Side-force coefficient and TPL contours, $\frac{\partial \xi^2}{\partial t} = 0.5 \cos\frac{2\pi}{\tau}t$ (rotatory oscillation), $\tau = 7.2$, $\theta_a = 375°$, $\alpha = 20°$, $M_\infty = 1.8$, $R_e = 10^5$.

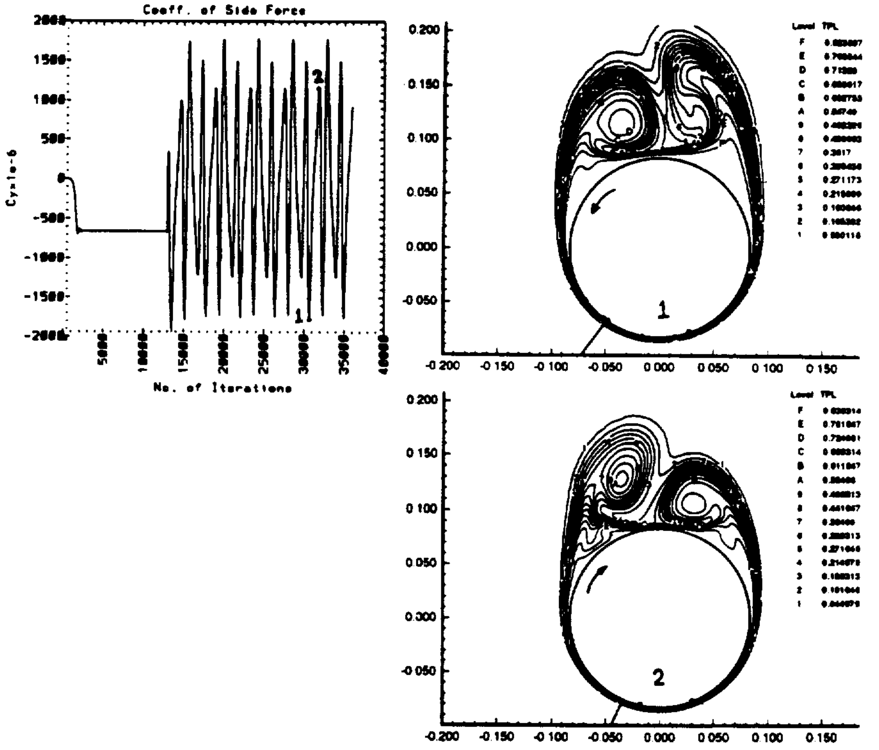

Fig. 13 Side-force coefficient and TPL contours, $\frac{\partial \xi^2}{\partial t} = 0.5 \cos\frac{2\pi}{\tau}t$ (rotatory oscillation), $\tau = 4.3$, $\theta_a = 225°$, $\alpha = 20°$, $M_\infty = 1.8$, $R_e = 10^5$.

92A[illegible]

16P

# AIAA-93-3472

# Supersonic Vortex Breakdown Over a Delta Wing in Transonic Flow

H. Kandil and O. Kandil
Old Dominion University
Norfolk, VA

C. Liu
NASA Langley Research Center
Hampton, VA

**AIAA Applied Aerodynamics Conference**
August 9-11, 1993 / Monterey, CA

For permission to copy or republish, contact the American Institute of Aeronautics and Astronautics
370 L'Enfant Promenade, S.W., Washington, D.C. 20024

AIAA-93-3472-CP

# SUPERSONIC VORTEX BREAKDOWN OVER A DELTA WING IN TRANSONIC FLOW

**Hamdy A. Kandil[*] and Osama A. Kandil[**]**
**Old Dominion University, Norfolk, VA 23529**
**and**
**C. H. Liu[***]**
**NASA Langley Research Center, Hampton, VA 23681**

## ABSTRACT

The effects of freestream Mach number and angle of attack on the leading-edge vortex breakdown due to the terminating shock on a 65–degree, sharp-edged, cropped delta wing are investigated computationally. The computational investigation uses the time-accurate solution of the laminar, unsteady, compressible, full Navier-Stokes equations with the implicit, upwind, flux-difference splitting, finite-volume scheme. A fine O-H grid consisting of $125 \times 85 \times 84$ points in the wrap-around, normal and axial directions, respectively, is used for all the flow cases. Keeping the Reynolds number fixed at $3.23 \times 10^6$, the Mach number is varied from 0.85 to 0.9 and the angle of attack is varied from 20° to 24°. The results show that at 20° angle of attack, the increase of the Mach number from 0.85 to 0.9 results in moving the location of the terminating shock downstream. The results also show that at 0.85 Mach number, the increase of the angle of attack from 20° to 24° results in moving the location of the terminating shock upstream. The results are in good agreement with the experimental data.

## INTRODUCTION

The literature shows that vortical flows around delta wings in the low-speed regime have received a substantial volume of experimental[1–4] and computational[5–9] research work. In the high angle of attack range, vortical flows in the low-speed regime are characterized with three types of boundary-layer separation, namely; primary, secondary and tertiary separations. The primary separated flow rolls up into a strong primary vortex core which produces a strong suction-pressure peak on the wing surface. The spanwise adverse-pressure gradient of the primary vortex causes the spanwise, outboard-moving, boundary-layer flow to separate forming a secondary vortex with opposite sense of rotation to and smaller strength than that of the primary vortex. The spanwise adverse-pressure gradient of the secondary vortex causes the spanwise, inboard-moving, boundary-layer flow to separate forming a tertiary vortex with same sense of rotation as and substantially small strength than that of the primary vortex. The spanwise surface-pressure curves are characterized with three suction-pressure peaks which varies in strength corresponding to the locations of the primary, secondary and tertiary vortices. When the angle of attack reaches a critical value, the axial-pressure gradient and the high swirl ratio of the primary vortex produce a stagnation point along the path line of the primary-vortex core, and vortex breakdown of the primary core develops. Depending on the swirl ratio, axial pressure gradient and Reynolds number, the primary-core vortex-breakdown mode might be a bubble type, a spiral type or a bubble-spiral type.

As the freestream Mach number increases, the vortical flow around the delta wing changes substantially due to the compressibility effects. In the supersonic flow regime, shock waves appear beneath or above the primary vortex, depending on the freestream normal Mach number and normal angle of attack. Experimental data[10, 11] and the computational results[12–14] have shown these types of vortical-flow structures. The foot print of these shock waves runs along a ray line from the wing vertex. If the shock wave is beneath the primary vortex, it interacts with the spanwise, outboard-moving, boundary-layer flow and causes, in addition to the adverse pressure gradient produced by the primary vortex, secondary-flow separation. If the shock wave is above the primary vortex, it flattens the primary vortex and the spanwise surface pressure curve. Comparison of the surface pressure distribution over a delta wing in low-speed and supersonic-speed regimes, shows that the suction-pressure peak corresponding to the primary vortex is lower for the supersonic flow than that for the low-speed flow.

In the transonic-flow regime, research work on vortical flows around delta wings was given adequate attention only recently. Understanding the steady and unsteady, transonic, vortical-flow structures around delta wings in the moderate-high angle of attack range is important for increasing the performance quality of the new generation of supermaneuver aircraft (e.g. YF22). Recent experimental measurements of transonic flows around a 65° cropped delta wing[15–21] show that a complex shock-wave system appears over the upper wing surface. The shock-wave system consists of a ray shock wave beneath the leading-edge primary vortex and a transverse, time-dependent[16], normal-shock wave (known as a terminating shock) which runs from the plane of symmetry to the wing leading edge. The terminating shock wave interacts

---

[*] Research Associate, Dept. of Aerospace Engineering, Member AIAA.

[**] Professor, Eminent Scholar and Chairman of Dept. of Aerospace Engineering, Associate Fellow AIAA.

[***] Senior Research Scientist, Computational Aerodynamic Branch, Associate Fellow AIAA.

Copyright © 1993 by Osama Kandil. Published by The American Institute of Aeronautics and Astronautics, Inc. with permission.

PRECEDING PAGE BLANK NOT FILMED

with the primary-vortex core causing it to breakdown at an angle of attack as low as 18°. Such a critical angle of attack is substantially smaller than the critical angle of attack of vortex breakdown in the low-speed regime. Reference 21 contains extensive flow measurements for the 65° cropped delta wing with and without leading-edge extension (LEX). A complete reconstruction of the three-dimensional flow field at and behind the terminating shock was not possible experimentally.

Computational simulations for transonic delta-wing flows have been developed on a very limited scale by using the Euler equations[20, 22] and the thin-layer Navier-Stokes equations[23]. The Euler-equations solutions were not capable of fully resolving the flow in the terminating shock region and the thin-layer Navier-Stokes-equations solutions did not address that region. In Ref. 24 by the present authors, the laminar, unsteady, compressible, full Navier-Stokes equations are integrated time accurately using the implicit, upwind, flux-difference splitting, finite-volume scheme to study and construct the flow field structure of a transonic flow around a 65° sharp-edged, cropped-delta wing at 20° angle to attack, 0.85 Mach number and $3.23 \times 10^6$ Reynolds number. A fine O-H grid consisting of $125 \times 85 \times 84$ points in the wrap-around, normal and axial directions, respectively, is used for the computational solution. A $\lambda$-shock system, which consists of a ray shock under the primary vortex core and a transverse terminating shock, has been captured. Behind the terminating shock, the leading-edge vortex core breaks down into a two-bubble cell type. The terminating shock and the vortex breakdown region behind it are time dependent and appear to be oscillatory. The flow field ahead of the terminating shock is steady and includes a supersonic pocket which is surrounded by the ray shock and the terminating shock. The flow inside the pocket does not change due to changes in the flow downstream. This is consistent with the fact that the supersonic pocket along with the terminating shock do not allow disturbances to propagate upstream. These results have been validated using the available experimental data and they are in good agreement. This work gives a complete construction of the flow field over the wing surface and in particular the structure of the flow at the terminating shock and behind it.

In this paper, a parametric study is carried out to investigate the effects of freestream Mach number and angle of attack on the terminating shock and the leading-edge, primary-vortex breakdown for the same 65° sharp-edged, cropped delta wing. The computational investigation uses the same equations, computational scheme and grid of Ref. 24. Keeping the Reynolds number fixed at $3.23 \times 10^6$, the Mach number is changed from 0.85 to 0.9 while the angle of attack is fixed at 20°, and the angle of attack is changed from 20° to 24° while the Mach number is fixed at 0.85.

## HIGHLIGHTS OF FORMULATION AND COMPUTATIONAL SCHEME

The conservative form of the dimensionless, unsteady, compressible, full Navier-Stokes equations is used for the formulation of the problem. The equations are written in terms of the time-independent, body-conformed coordinates $\xi^1, \xi^2$ and $\xi^3$ (Ref. 25).

The implicit, upwind, flux-difference splitting, finite-volume scheme is used to solve the unsteady, compressible, full Navier-Stokes equations. The scheme uses the flux-difference splitting scheme of Roe which is based on the solution of the approximate one-dimensional, Riemann problem. In the Roe scheme, the inviscid flux difference at the interface of computational cells is split into two parts; left and right flux differences. The splitting is accomplished according to the signs of the eigenvalues of the Roe averaged-Jacobian matrix of the inviscid fluxes at the cell interface. The smooth flux limiter is used to eliminate oscillations at locations of large flow gradients. The viscous- and heat-flux terms are linearized in time and the cross-derivative terms are neglected in the implicit operator and retained in the explicit terms. The viscous terms are differenced using a second-order accurate central differencing. The resulting difference equation is approximately factored and is solved in three sweeps in the $\xi^1, \xi^2$ and $\xi^3$ directions. The computational scheme is coded in the computer program "FTNS3D" which is a modified version of the CFL3D-code.

## COMPUTATIONAL RESULTS

A 65° swept-back, sharp-edged, cropped delta wing of zero thickness is considered for the computational solutions. The cropping ratio (tip length/root-chord length) is 0.15. An O-H grid of $125 \times 85 \times 84$ in the wrap-around, normal and axial directions, respectively, is used. The computational domain extends two-chord length forward and five-chord length backward from the wing trailing edge. The radius of the computational domain is four-chord length. The minimum grid size normal to the wing surface is $5 \times 10^{-4}$ from the leading edge to the plane of symmetry. Figure 1 shows a three-dimensional shape of the grid and a cross-flow plane.

Time-accurate integration of the laminar, unsteady, compressible, full Navier-Stokes equations has been carried out with $\Delta t = 0.0002$. Three flow conditions are used to study the effect of increasing the Mach number while the angle of attack is kept constant and the effect of increasing the angle of attack while the Mach number is kept constant. In all the three cases, the Reynolds number, $R_e$, is $3.23 \times 10^6$ based on the root-chord length.

### Case I ($M_\infty = 0.85$, $\alpha = 20°$)

For this case, the freestream Mach number, $M_\infty$, and angle of attack, $\alpha$, are 0.85 and 20°, respectively. Figure 2 shows a comparison of the computed, spanwise, surface-pressure coefficient ($C_p$) at different chord stations (x =

0.3, 0.6 and 0.8) with the experimental data of Erickson[21] ($R_c = 3.23\times10^6$) and Hartmann[17] ($R_c = 2.38\times10^6$ and $4.57\times10^6$). The computational results show the correct location and level of the suction-pressure peak corresponding to the primary vortex in comparison with the experimental data. They also show a smaller suction-pressure peak corresponding to the secondary vortex. The computational results are in fair to good agreement with the experimental data. For the chord station x = 0.9, the $C_p$-curve shows a rapid increase in the pressure coefficient (a decrease in the suction-pressure coefficient). For example, the suction-pressure-peak coefficient increases from a value of –1.4 at x = 0.8 to a value of –1.15 at x = 0.9. Figure 3 shows the total-Mach contours and streamlines at the chord stations of x = 0.60, 0.90 and 0.97. At x = 0.60, the Mach contours show an oblique shock beneath the primary vortex and a subsonic, separated region to its right. The streamlines show a secondary separated flow and the corresponding secondary vortex. This separation is due to the shock interaction with the surface boundary-layer flow and is also due to the adverse, spanwise pressure gradient created by the primary vortex. At x = 0.90, the shock beneath the primary vortex becomes weak and the primary-vortex size increases. At x = 0.97, the shock beneath the primary vortex disappears and the primary vortex diffuses and reduces to a repelling focus, as shown by the streamlines. The details of the flow structure at x = 0.90 and 0.97 in addition to the spanwise, pressure-distribution curve at x = 0.90 clearly indicate that the primary vortex is experiencing a vortex breakdown due to a transverse shock (terminating shock) which is located between x = 0.80 and x = 0.90.

Figure 4 shows the static pressure contours on the wing and symmetry planes. The contours clearly show the location, shape and strength of the terminating shock. A substantial supersonic pocket which is bounded by the terminating shock and the ray shocks (shocks beneath the primary-vortex cores) is observed on the wing plane. The terminating shock is located at x = 0.83 at the plane of symmetry, which is in good agreement with the experimental data[21], where the shock is located at x = 0.84 at the plane of symmetry. Figure 5 shows the position of ray lines from the wing vertex (which are marked by the letters A-H) and the static-pressure variation along these lines. The static-pressure curves give several points to generate the foot-print line of the terminating shock. The terminating shock is found to extend from the plane of symmetry to the wing leading edge. It reaches its highest strength at the location of the primary vortex (lines E-G). Figure 6 shows the total-Mach contours and streamlines on a vertical ray plane at the 0.68 spanwise location which passes through the vortex breakdown. Blow-ups of the velocity vectors and streamlines on this ray plane are also shown in Fig. 6. The streamlines conclusively show a two-bubble cell vortex breakdown. It is a typical three-dimensional vortex breakdown mode which consists of an attracting saddle point (front), a repelling saddle point (rear), an attracting focus (top), and a repelling focus (bottom). Such a breakdown mode is similar to the one which was captured for an isolated supersonic vortex in an unbounded domain in Refs. 26 and 27. The location of the attracting saddle point is at 0.97 along the ray line which corresponds to a location of 0.87 along the axial direction. The Mach contours show that the front surface of the vortex-breakdown bubbles is enclosed by a hemispherical shape-like shock surface. In Fig. 18, the details of the flow structure on the wing and symmetry planes are shown.

Having established the flow structure of this case, the Mach number is increased to 0.9 while the angle of attack is kept fixed at 20°.

### Case II ($M_\infty = 0.90$, $\alpha = 20°$)

The results of this case are given in Figs. 7-11 and 19. Figure 7 shows the computational spanwise, surface-pressure coefficient at different chord stations along with the experimental data of Erickson[21]. The computational results are in good agreement with the experimental data at x = 0.3 and 0.6. At x = 0.8, the computational results underestimates the pressure coefficient of the experimental data. The locations of the primary and secondary vortex cores are in good agreement with those of the experimental data. It is noticed that the levels of $C_p$ for the present case are lower than those of Case I (Fig. 2). Again, the pressure level decreases rapidly at x = 0.90. Figure 8 shows the total-Mach contours and streamlines in cross-flow planes at x = 0.60, 0.90 and 0.97. The shock beneath the primary vortex is observed in the Figures at x = 0.60 and x = 0.90. For x = 0.90, the shock beneath the primary vortex is still strong in comparison with that of Case I (Fig. 3). At x = 0.97, the repelling focus is observed indicating that vortex breakdown has occurred. Figure 9 shows that the terminating shock in the cross-flow plane is located at x = 0.93 within the boundary-layer, which is in good comparison with the experimentally measured shock of Ref. 21, where it is located at x = 0.95. The static-pressure contours on the wing plane show that the terminating shock for Case II (Fig. 9) is closer to the trailing edge that of Case I (Fig. 4). It should be noted here that the terminating-shock location in the outer flow is ahead of its location in the boundary-layer flow. The static-pressure variations along the ray lines of Fig. 10 clearly show that the terminating-shock foot print is located between x = 0.925 and x = 0.95, and that it extends from the plane of symmetry to the wing leading edge. Figure 11 shows the Mach contours and streamlines on a vertical ray plane passing through the vortex breakdown. It is noticed that the vortex breakdown shape is different from and smaller than that of Case I (Fig. 6). The attracting saddle point, attracting focus and repelling saddle point are clearly observed. The repelling focus is very small. This indicates that the terminating shock becomes smaller in strength than that of Case I. Figure 19 shows the details of this flow case on the wing and symmetry planes.

It is concluded that as the freestream Mach number increases slightly from 0.85 to 0.9, the terminating shock strength decreases and its location moves downstream from x = 0.84 to x = 0.93. Moreover, the surface pressure levels become smaller than those of Case I.

Next, the Mach number is kept fixed at 0.85 and the angle of attack is increased to 24°.

### Case III ($M_\infty = 0.85$, $\alpha = 24°$)

The results of this case are given in Figs. 12–17 and 20. The computational surface-pressure result at x = 0.3 (Fig. 12) is in good agreement with the experimental data of Erickson[21]. However, the computational results, at x = 0.6 and 0.8 are either overpredicting or underpredicting the experimental data. Figures 13, 14 and 15 show that the terminating shock moves upstream to x = 0.753 in the boundary-layer flow at the plane of symmetry. This is in good agreement with the experimental data of Ref. 21, where the shock is located at x = 0.75 in the boundary layer flow. The terminating-shock location in the outer flow is ahead of its location in the boundary layer. Figure 16 shows that the vortex-breakdown region is larger than those of Cases I and II. Moreover, the attracting and repelling foci are smaller than those of Case I. Figure 20 shows the details of this case on the wing and symmetry planes.

Thus, it is seen that as the angle of attack increases from 20° to 24° while the Mach number is kept fixed at 0.85, the terminating shock moves upstream and the vortex-breakdown region becomes large. Moreover, the surface pressure levels become larger than those of Case I.

The computational results show that the flow at the terminating shock and behind it is time dependent and it indicates oscillatory motion (The computations have not been carried out beyond t = 6.0 or 30,000 time steps with $\Delta t = 0.0002$). In Fig. 17, we show snapshots of the streamlines and their blow-ups on a ray plane passing through the vortex-breakdown region. The snapshots are shown at t = 4.22, 5.16 and 5.52. It is clearly seen that the vortex breakdown moves upstream showing different modes. In the same time, the terminating shock is also moving upstream and slows down to reverse its direction of motion. This is in complete agreement with the experimental observations of Bannik and Houtmann[16].

## CONCLUDING REMARKS

The laminar, unsteady, compressible, full Navier-Stokes equations are integrated time accurately using the implicit, upwind, flux-difference splitting finite-volume scheme to study the transonic flow field around a 65° sharp-edged, cropped delta wing. First, the flow field has been constructed for a Reynolds number of $3.23 \times 10^6$, a Mach number of 0.85 and an angle of attack of 20° (Case I). A $\lambda$-shock system consisting of a ray shock beneath the primary vortex core and a transverse terminating shock has been captured. Behind the terminating shock, the leading-edge vortex core breaks down. Keeping the Reynolds number constant and the angle of attack fixed at 20°, the Mach number is increased to 0.90. The results of this case (Case II) show that the terminating shock moves downstream and the vortex-breakdown region becomes smaller than that of Case I. Keeping the Reynolds number constant and the Mach number fixed at 0.85, the angle of attack is increased to 20°. The results of this case (Case III) show that the terminating shock moves upstream and the vortex-breakdown region becomes larger than that of Case I. The computational results are in good agreement with the experimental data. However, it must be emphasized that the flow at the terminating shock and behind it is time dependent while the flow ahead of the terminating shock is steady. The present paper shows the structure of the flow field behind the terminating shock for the first time.

## ACKNOWLEDGEMENT

For the first two authors, this work is supported by the NASA-Langley Research Center under grant No. NAG-1-994 along with a partial support from the AFOSR. The Computational Resources provided by the NAS Center at Ames and the NASA Langley Research Center are acknowledged and appreciated.

## REFERENCES

1. Marsden, D. J., Simpson, R. W. and Rainbird, W. J., "The Flow Over Delta Wings at Low Speeds with Leading Edge Separation," College of Aeronautics, Cranfield, Rep. CoA-114, 1957.

2. Lambourne, N. C. and Bryer, D. W., "Some Measurements in the Vortex Flow Generated by a Sharp Leading Edge Having 65 Degrees of Sweep," Aeronautical Research Council, CP No. 477, 1960.

3. Hummel, O., "On the Vortex Formation Over a Slender Wing at Large Angles of Incidences," AGARD CP-247, January 1979, pp. 15.1–15.7.

4. Verhaagen, N. G., "An Experimental Investigation of the Vortex Flow Over Delta and Double Delta Wings at Low Speed," AGARD CP-342, April 1983, pp. 7.1–7.16.

5. Kandil, O. A., "Numerical Prediction of Vortex Cores from the Leading and Trailing Edges of Delta Wings," ICAS Paper No. 14.2, 12th Congress of the International Council of Aeronautical Sciences, Munich, Germany, October 1980.

6. Hoeijmakers, H. W. M., "Aerodynamics of Vortical Type Flows in Three Dimensions," AGARD CP-342, July 1983, pp. 18.1–18.35.

7. Newsome, R. W. and Kandil, O. A., "Vortical Flow Aerodynamics-Physical Aspects and Numerical Simulation," AIAA Paper 87–0205, January 1987.

8. Thomas, J. L., Taylor, S. L. and Anderson, K., "Navier-Stokes Computations of Vortical Flows Over Low Aspect Wings," AIAA Paper 87–0207, January 1987.

9. Kandil, O. A. and Chuang, H. A., "Computation of Vortex-Dominated Flow for a Delta Wing Undergoing Pitching Oscillation," AIAA Journal, Vol. 28, No. 9, September 1990, pp. 1589–1595.

10. Stanbrook, A. and Squire, L. C., "Possible Types of Flow at Swept Leading Edges," Aeronautical Quarterly, Vol. XV, Feb. 1964.

11. Miller, D. S. and Wood, R. W., "Lee-Side Flow Over Delta Wings at Supersonic Speeds," NASA TP 2430, 1985.

12. Kandil, O. A. and Chuang, A. H., "Influence of Numerical Dissipation on Computational Euler Equations for Vortex-Dominated Flows," AIAA Journal, Vol. 25, No. 11, November 1987, pp. 1426–1434.

13. Newsome, R. W. and Thomas, J. L., "Computation of Leading-Edge Vortex Flows," NACA CP-2416, October 1985, pp. 305–330.

14. Murman, E. M., Goodsell, A., Powell, K. and Landahl, M., "Leading Edge Vortex Solutions with Large Total Pressure Loss," AIAA Paper 87–0039, January 1987.

15. Boersen, S. J. and Elsenaar, A., "Tests on the AFWAL 65° Delta Wing at NLR: A Study of Vortex Flow Development Between Mach = 0.4 and 4," Proceedings of Symposium on International Vortex Flow Experiment on Euler Code Validation, Stockholm, Sweden, October 1-3, 1986, pp. 23–36.

16. Bannik, W. J. and Houtman, E. M., "Experiments on the Transonic Flow Over a Delta Wing at High Angles of Attack," Proceedings of Symposium on International Vortex Flow Experiment on Euler Code Validation, Stockholm, Sweden, October 1-3, 1986, pp. 37–46.

17. Hartmann, K., "Force and Pressure Measurements Including Surface Flow Visualization on a Cropped Delta Wing," Proceedings of Symposium on International Vortex Flow Experiment on Euler Code Validation, Stockholm, Sweden, October 1–3, 1986, pp. 63–87.

18. Bütefisch, K. A., Pallek, D. and Sauerland, K. H., "International Vortex Flow Experiment-Results of Three Component LDA Measurements on a 65° Delta Wing," DFVLR IB 222–87 A 34, 1987.

19. Elsenaar, A., Hjelmberg, L., Bütefisch, K. and Bannink, W. J., "The International Vortex Flow Experiment," AGARD-CP-437, Lison, Portugal, May 1988, Vol. 1., pp. 9.1–9.23.

20. Bannink, W. J. and Houtman, E. M., "Experimental and Computational Study of the Vortical Flow Over a Delta wing at High Angles of Attack," IUTAM Symposium on Fluid Dynamics of High Angle of Attack, University of Japan, Tokyo, Japan, September 14–17, 1992.

21. Erickson, G. E., "Wind Tunnel Investigation of The Interaction and Breakdown Characteristics of Slender-Wing Vortices at Subsonic, Transonic and Supersonic Speeds," NASA Tech. paper 3114, November 1991.

22. Hitzel, S. M., "Wing Vortex-Flows Up into Vortex-Breakdown-A Numerical Simulation," AIAA 88-2518-CP, 1988, pp. 73–83.

23. Laine, S., Siikonen, T. and Kaurinkoski, P-, "Calculation of Transonic Viscous Flow Around a Delta Wing," ICAS 92–4.2.1, Beijing, PRC, September 22-25, 1992, pp. 286–295.

24. Kandil, O. A., Kandil, H. A. and Liu, C. H., "Shock-Vortex Interaction Over a 65-Degree Delta Wing in Transonic Flow," AIAA Paper 93–2973, AIAA 24th Fluid Dynamics Conference, Orlando, FL, July 6–9, 1993.

25. Kandil, O. A., Kandil, H. A. and Liu, C. H., "Supersonic Quasi-Axisymmetric Vortex Breakdown," AIAA 91–3311–CP, September 1991, pp. 851–863.

26. Kandil, O. A., Kandil, H. A. and Liu, C. H., "Three-Dimensional Supersonic Vortex Breakdown," AIAA 93–0526, January 11–14, 1993.

27. Kandil, H. A., "Navier-Stokes Simulation of Quasi-Axisymmetry and Three-Dimensional Supersonic Vortex-Breakdown," Ph.D. Dissertation, Dept. of Mechanical Engineering and Mechanics, Old Dominion University, Norfolk, VA, May 1993.

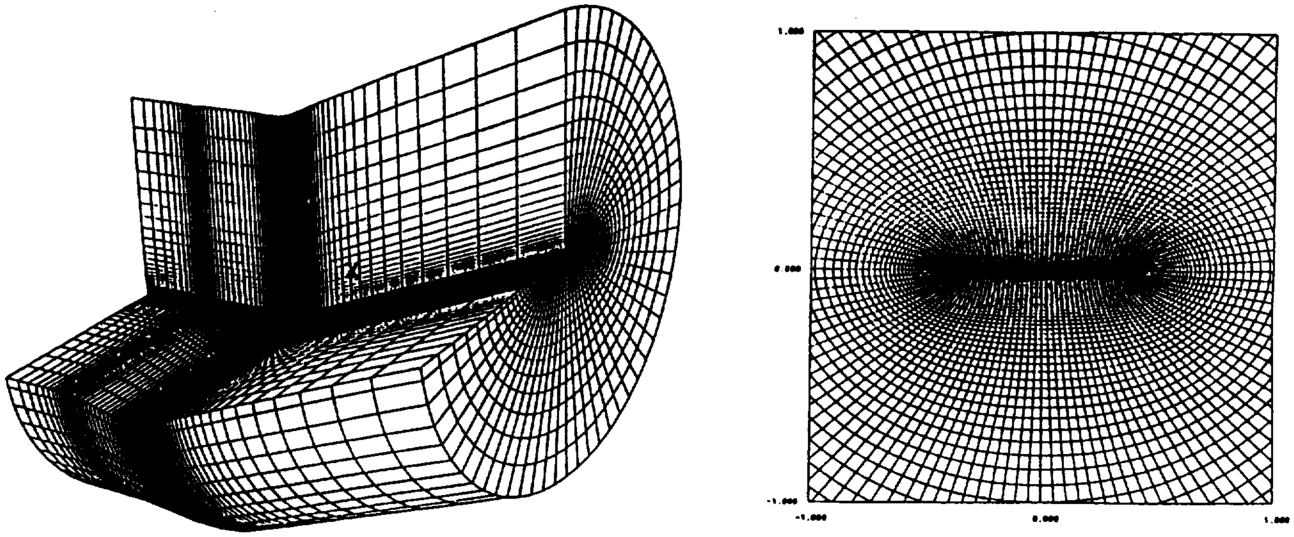

Fig. 1 Three-dimensional shape and cross-flow plane of a fine grid, 125×85×84.

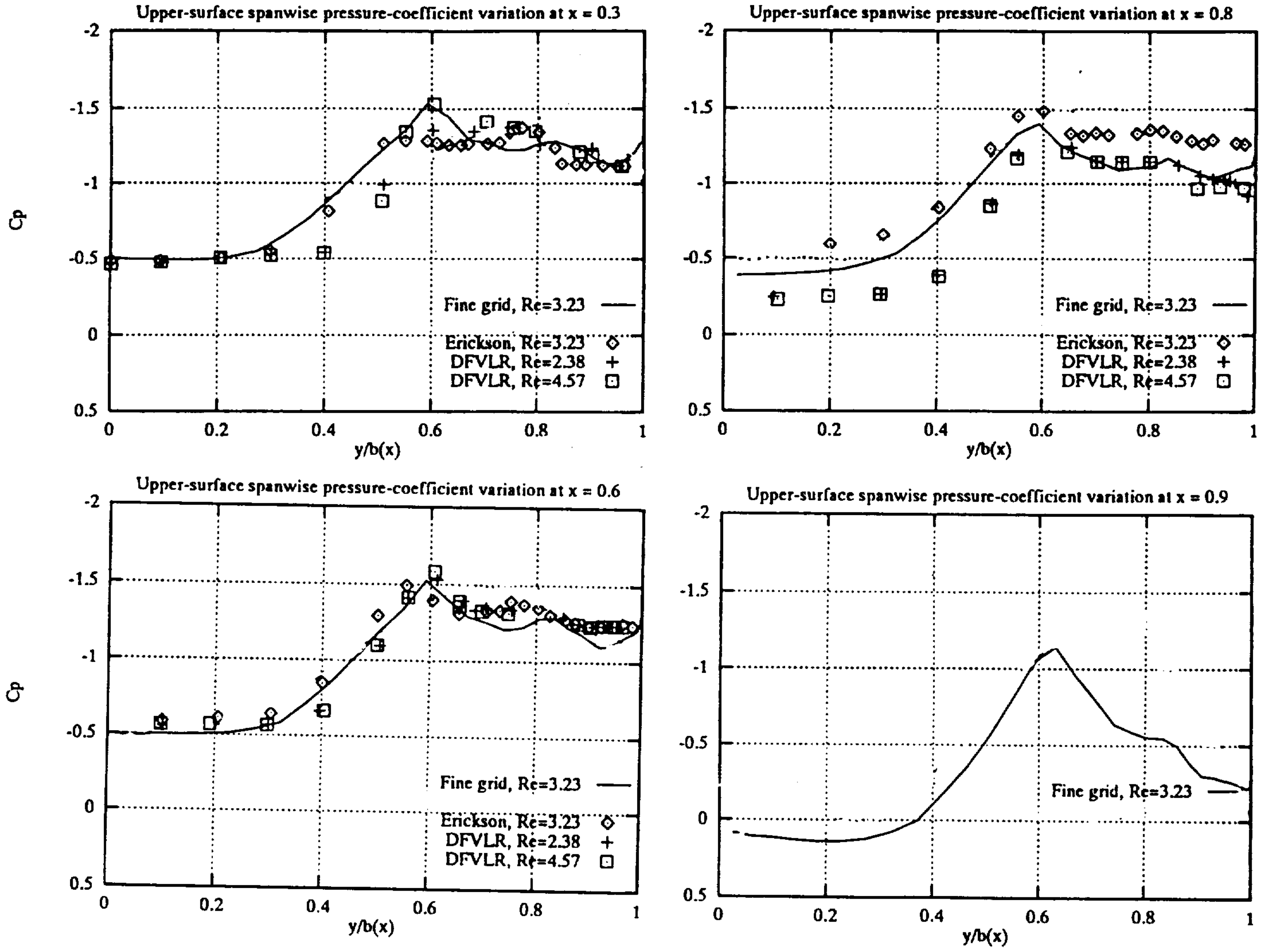
Upper-surface spanwise pressure-coefficient variation at x = 0.3

Upper-surface spanwise pressure-coefficient variation at x = 0.8

Upper-surface spanwise pressure-coefficient variation at x = 0.6

Upper-surface spanwise pressure-coefficient variation at x = 0.9

Fig. 2 Comparison of the computed and experimental spanwise, surface-pressure coefficient at different chord stations; $M_\infty = 0.85$, $\alpha = 20°$.

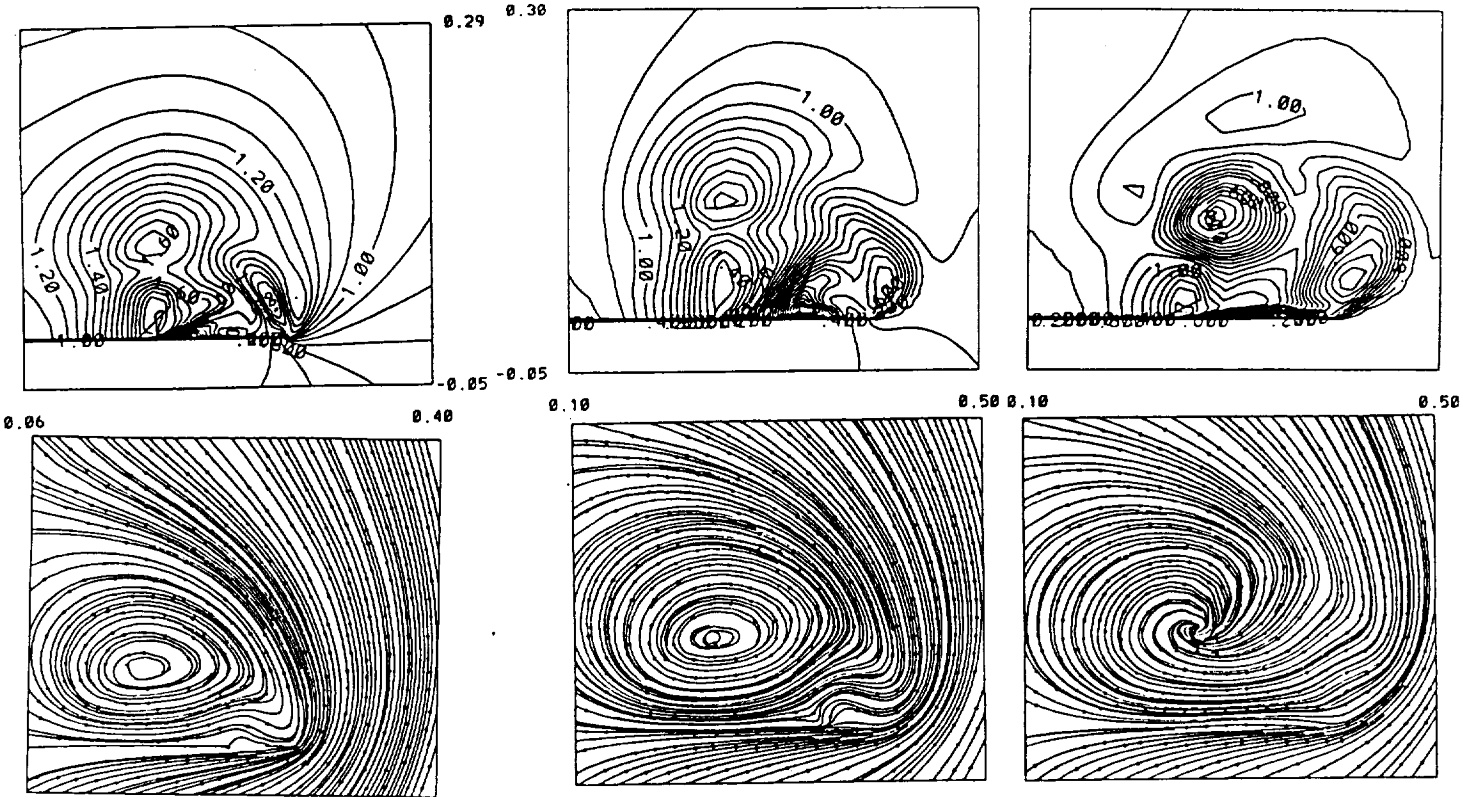

x = 0.60 x = 0.90 x = 0.97

Fig. 3 Total-Mach contours and streamlines in cross-flow planes; $M_\infty = 0.85$, $\alpha = 20°$.

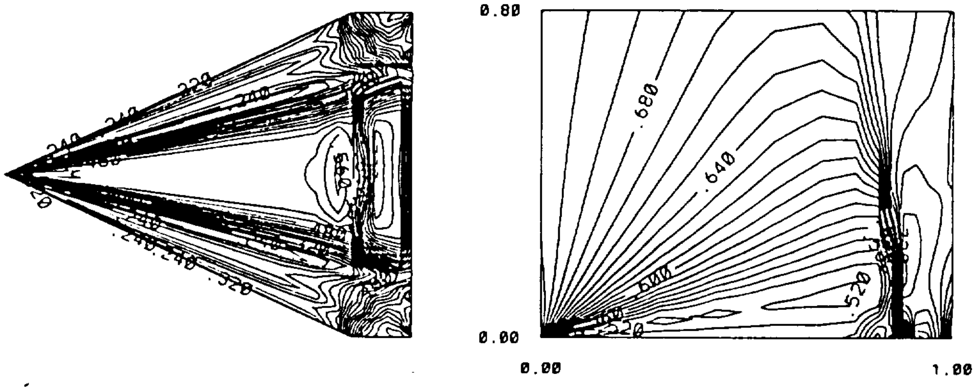

PRESSURE CONTOURS ON THE WING SURFACE PRESS. CONTOURS ON THE PLANE OF SYMMTRY

Fig. 4 Static-pressure contours on the wing and symmetry planes; $M_\infty = 0.85$, $\alpha = 20°$.

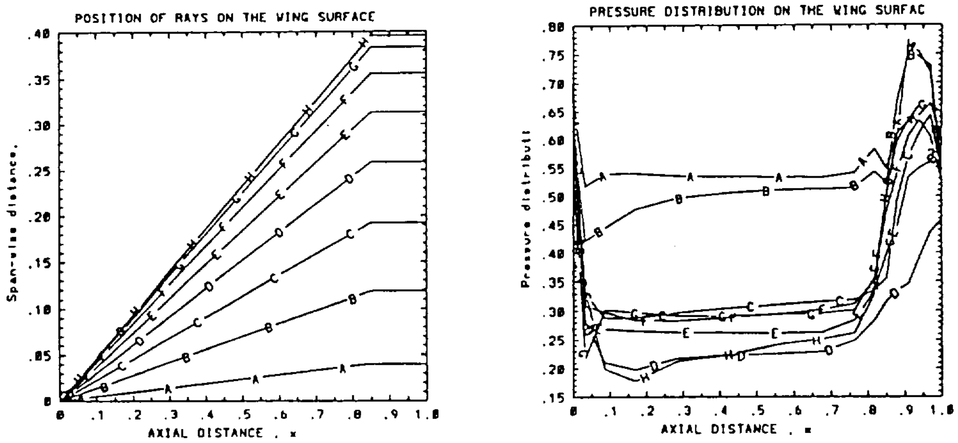

Fig. 5 Ray lines on the wing surface and the static-pressure variation along them; $M_\infty = 0.85$, $\alpha = 20°$.

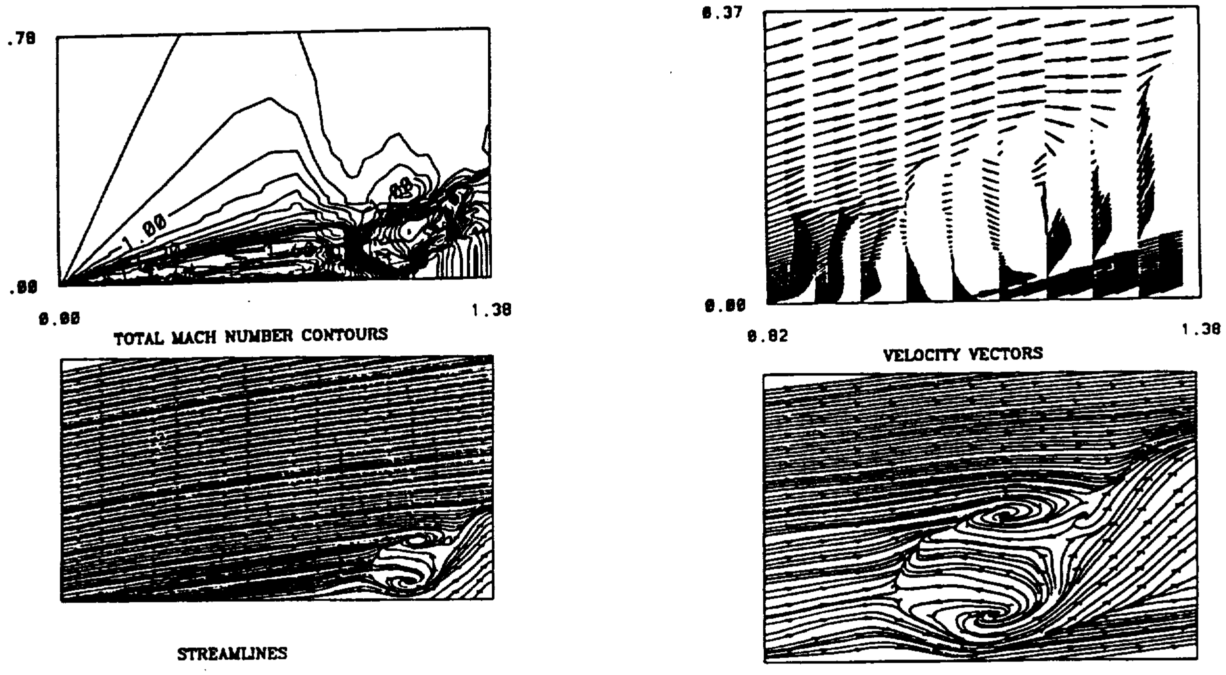

Fig. 6 Total-Mach contours, streamlines and velocity vectors on a ray plane passing through the vortex breakdown; $M_\infty = 0.85$, $\alpha = 20°$.

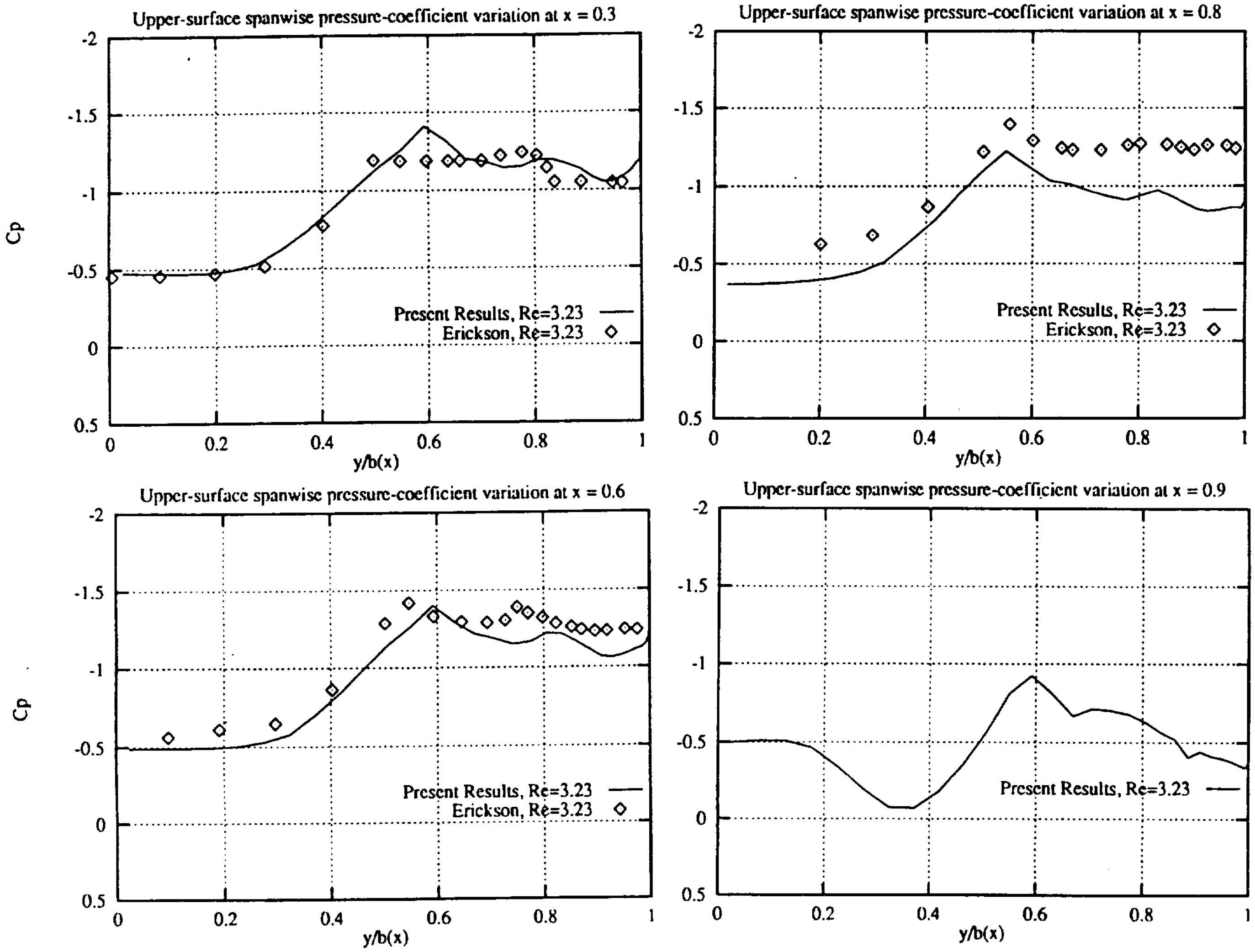

Fig. 7 Comparison of the computed and experimental spanwise, surface-pressure coefficient at different chord stations; $M_\infty = 0.90$, $\alpha = 20°$.

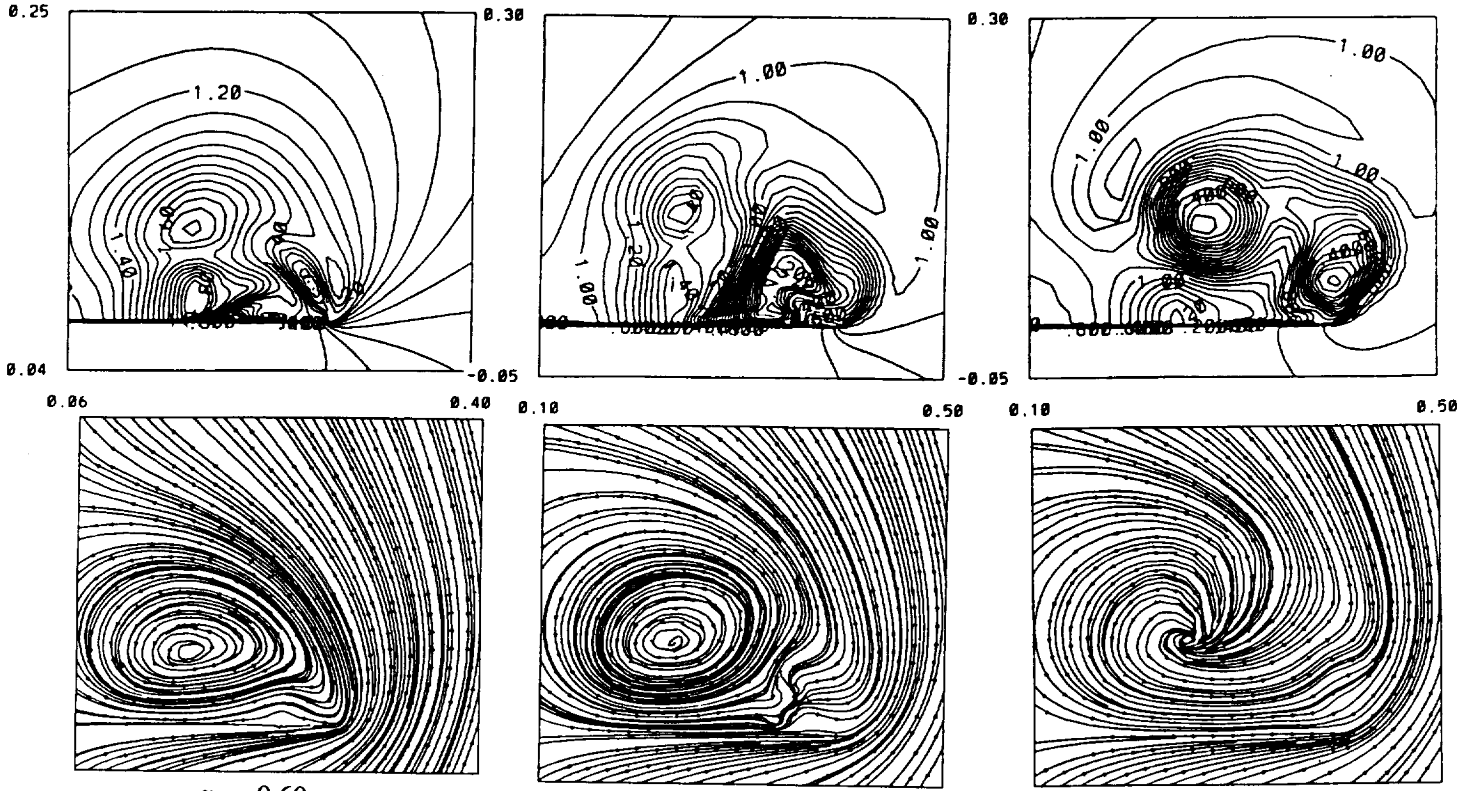

x = 0.60 x = 0.90 x = 0.97

Fig. 8 Total-Mach contours and streamlines in cross-flow planes; $M_\infty$ = 0.90, $\alpha$ = 20°.

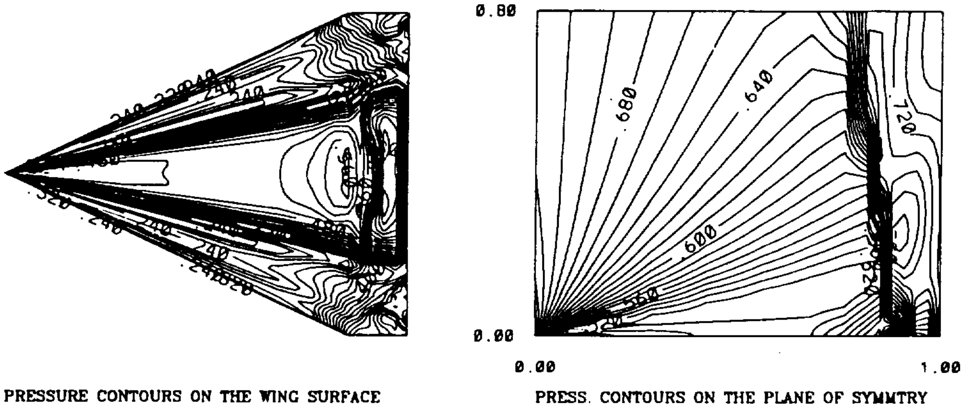

PRESSURE CONTOURS ON THE WING SURFACE PRESS. CONTOURS ON THE PLANE OF SYMMTRY

Fig. 9 Static-pressure contours on the wing and symmetry planes; $M_\infty$ = 0.90, $\alpha$ = 20°.

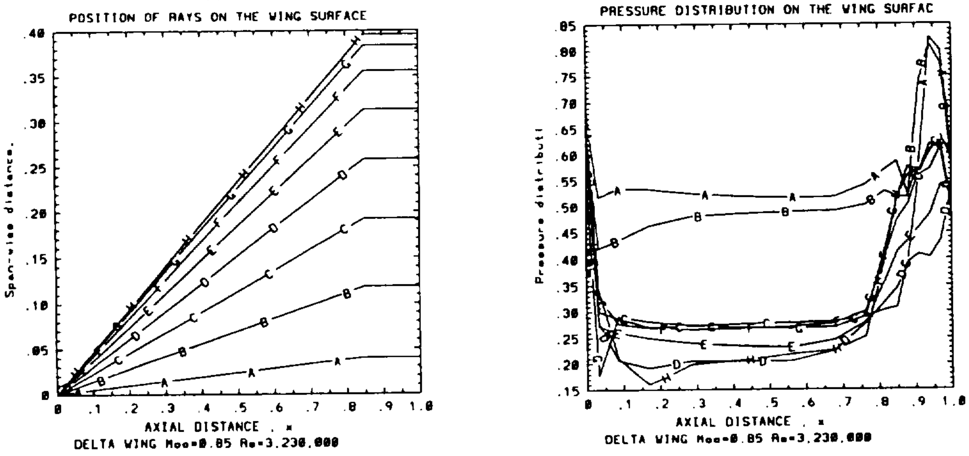

Fig. 10 Ray lines on the wing surface and the static-pressure variation along them; $M_\infty$ = 0.90, $\alpha$ = 20°.

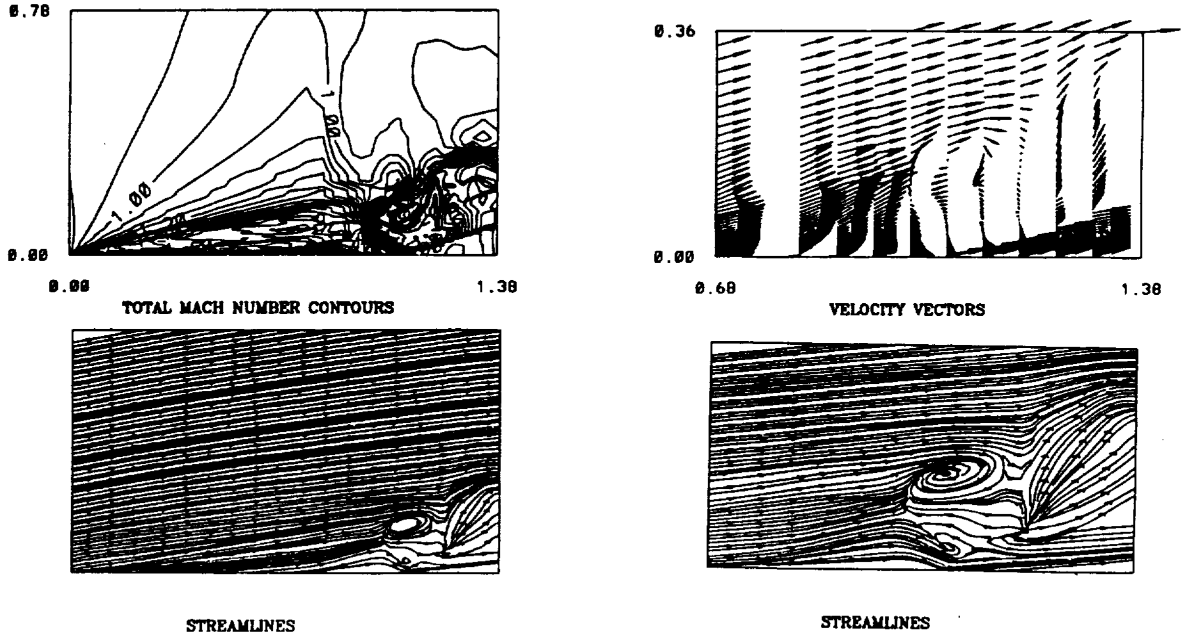

Fig. 11 Total-Mach contours, streamlines and velocity vectors on a ray plane passing through the vortex breakdown; $M_\infty = 0.9$, $\alpha = 20°$.

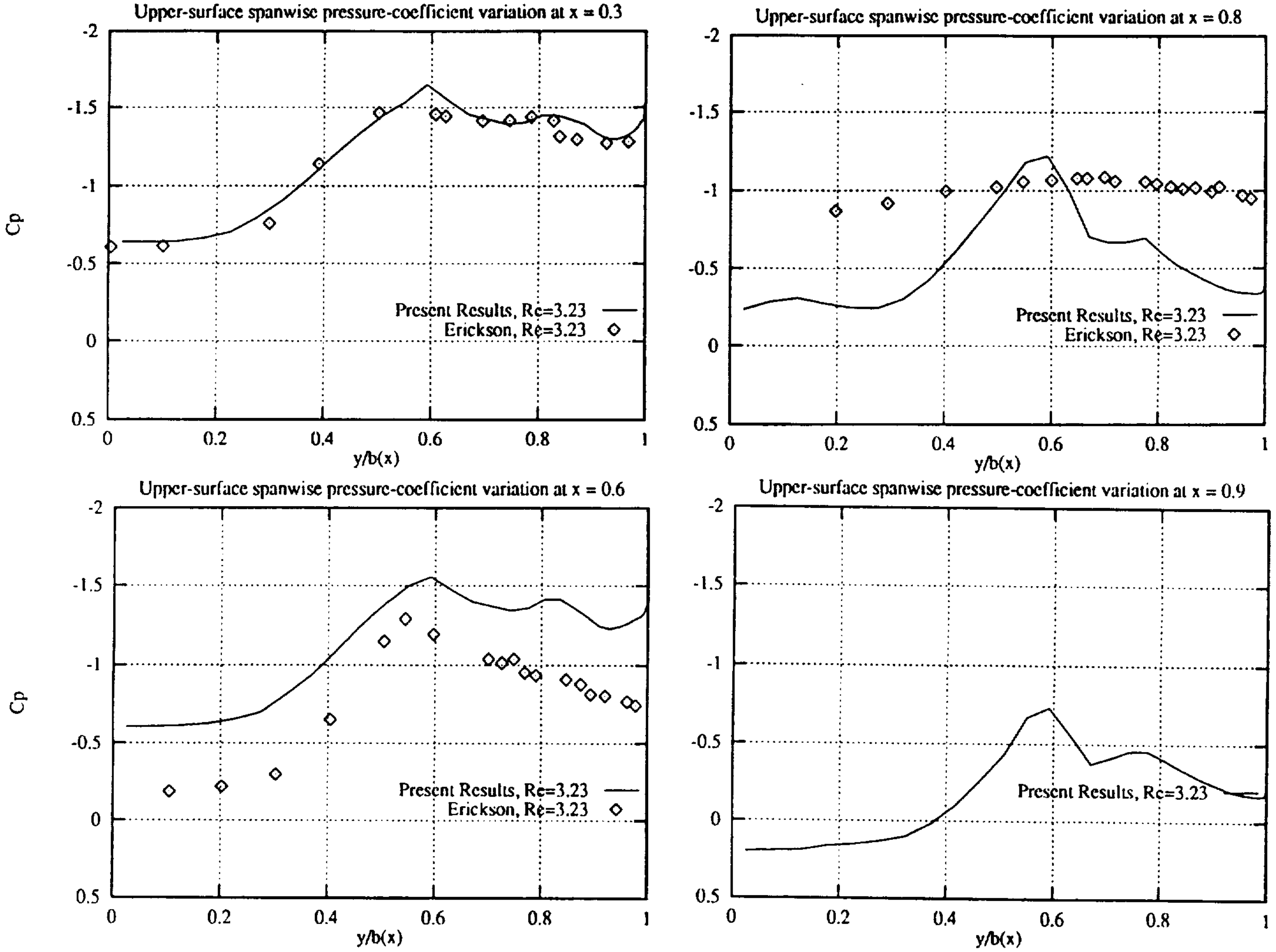

Fig. 12 Comparison of the computed and experimental spanwise, surface-pressure coefficient at different chord stations; $M_\infty = 0.85$, $\alpha = 24°$.

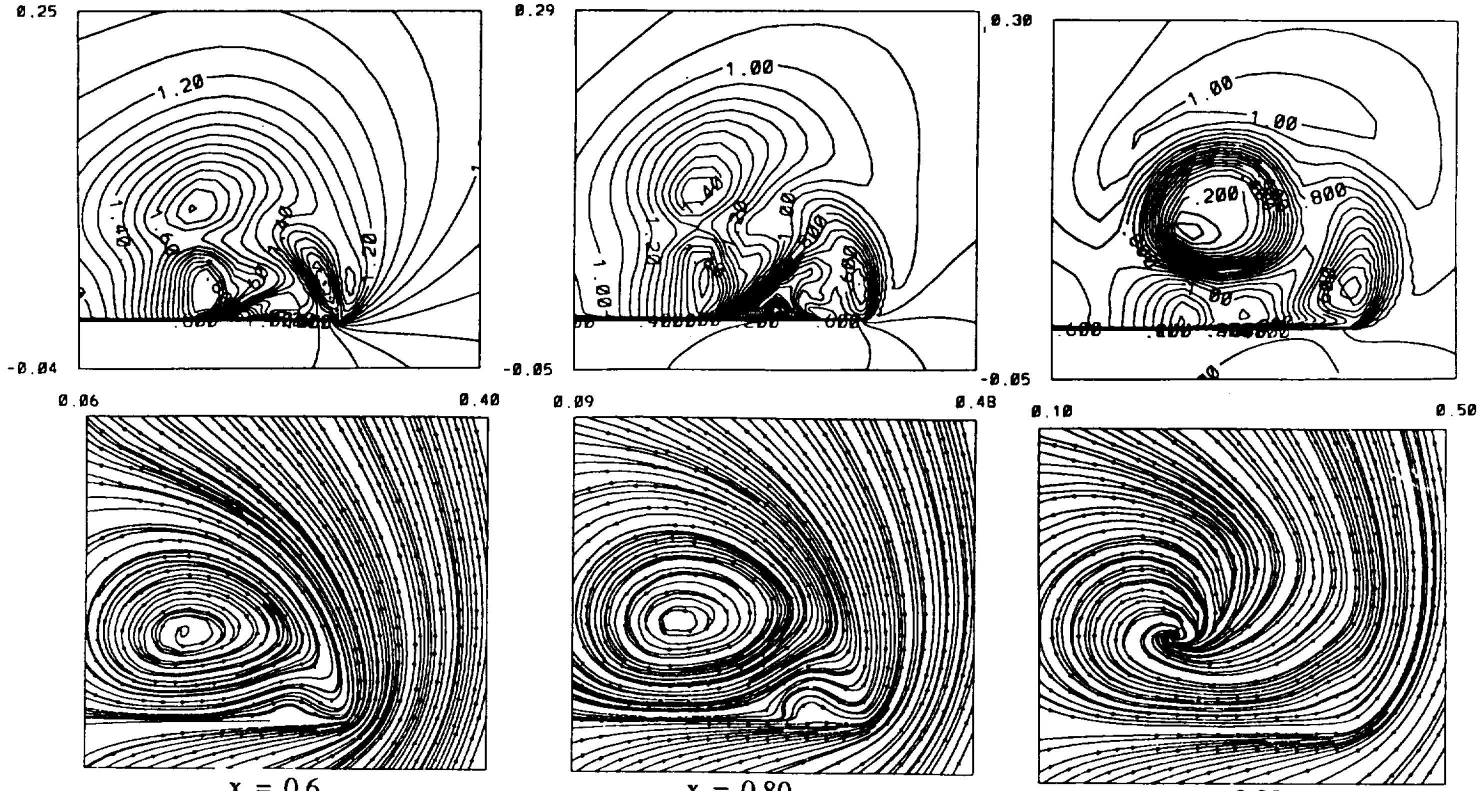

x = 0.6

x = 0.80

x = 0.88

Fig. 13 Total-Mach contours and streamlines in cross-flow planes; $M_\infty$ = 0.85, $\alpha$ = 24°.

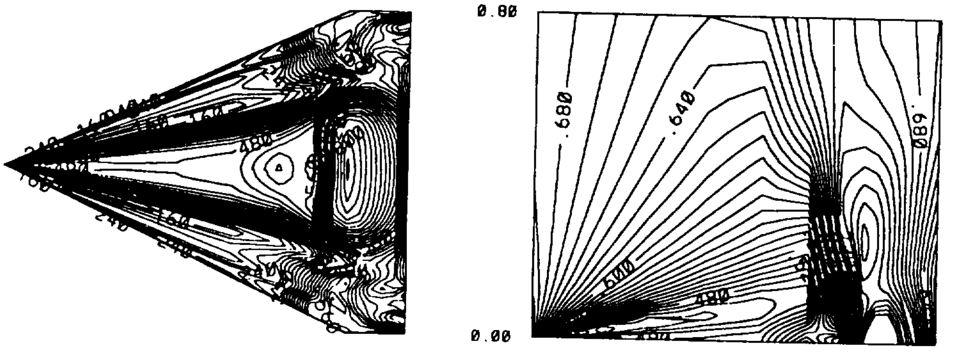

PRESSURE CONTOURS ON THE WING SURFACE

PRESS. CONTOURS ON THE PLANE OF SYMMETRY

Fig. 14 Static-pressure contours on the wing and symmetry planes; $M_\infty$ = 0.85, $\alpha$ = 24°.

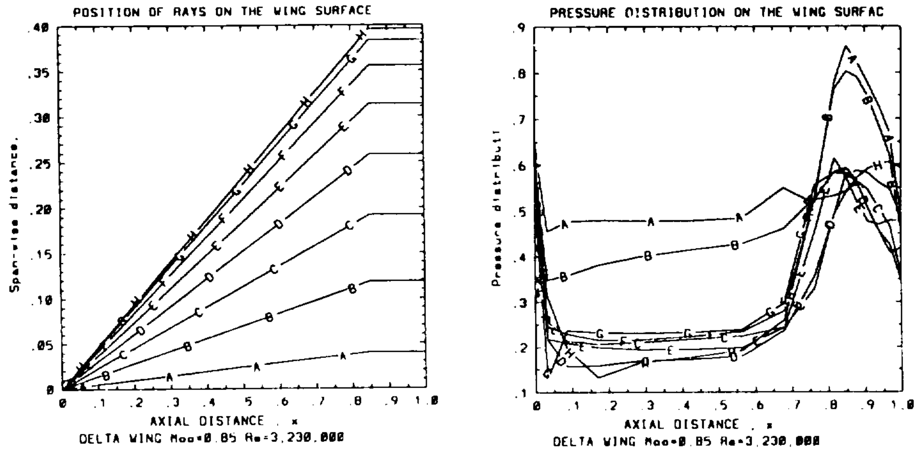

Fig. 15 Ray lines on the wing surface and the static-pressure variation along them; $M_\infty$ = 0.85, $\alpha$ = 24°.

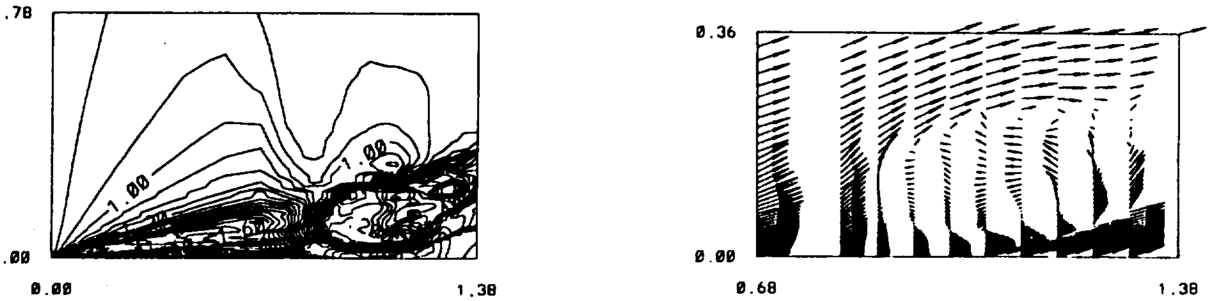

TOTAL MACH NUMBER CONTOURS

VELOCITY VECTORS

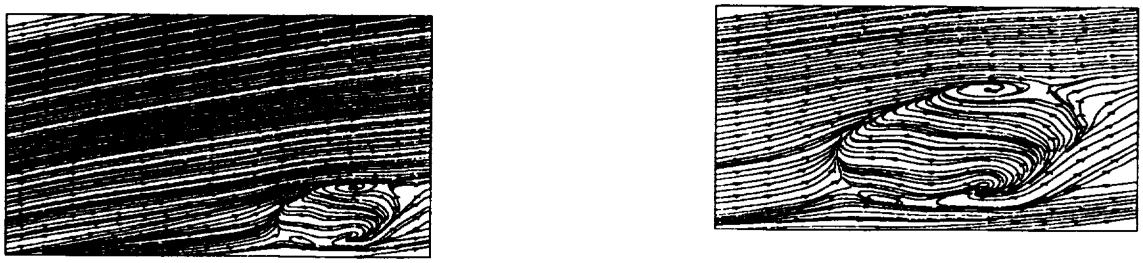

STREAMLINES

STREAMLINES

Fig. 16 Total-Mach contours, streamlines and velocity vectors on a ray plane passing through the vortex breakdown; $M_\infty = 0.85$, $\alpha = 24°$.

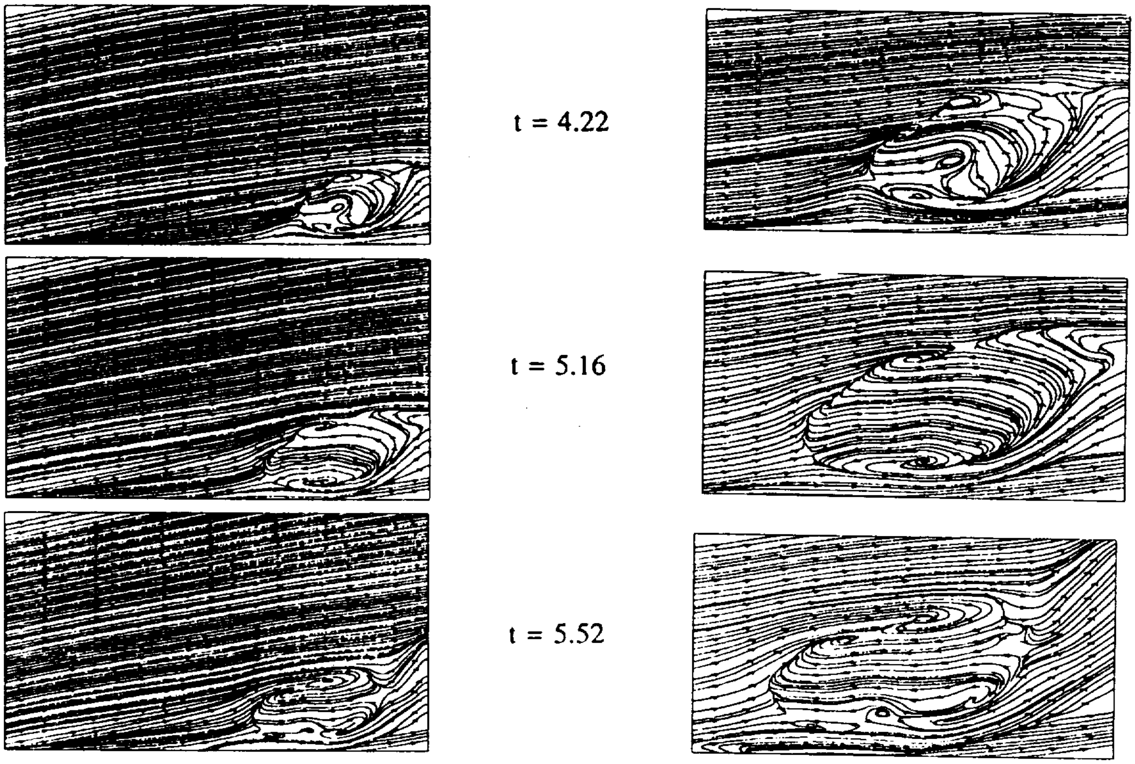

Fig. 17 Streamlines and blow-up on a ray plane passing through the vortex breakdown at different time levels; $M_\infty = 0.85$, $\alpha = 24°$.

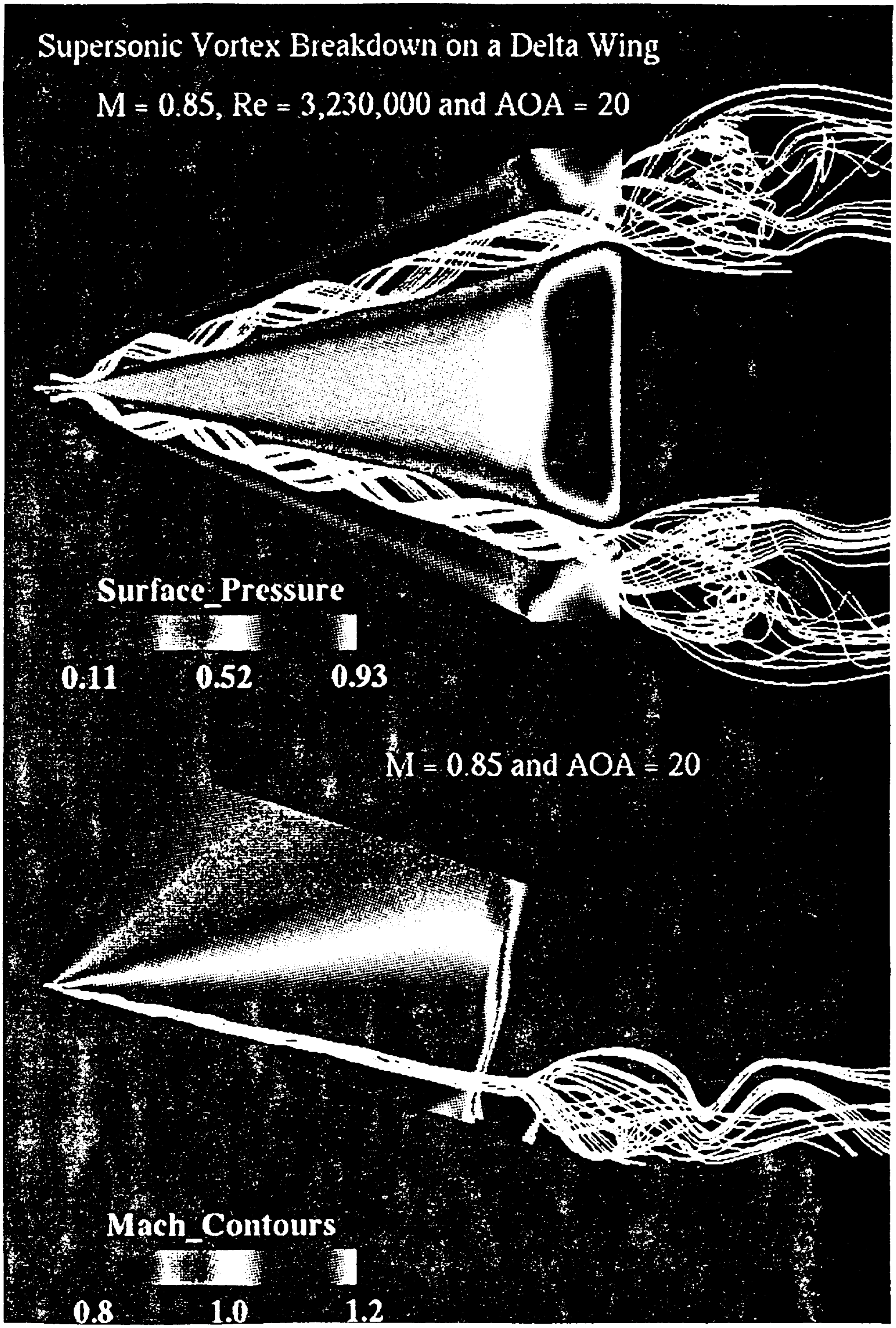
Supersonic Vortex Breakdown on a Delta Wing
M = 0.85, Re = 3,230,000 and AOA = 20
Surface_Pressure
0.11
0.52
0.93
M = 0.85 and AOA = 20
Mach_Contours
0.8
1.0
1.2

Fig. 18 Surface-pressure and Mach contours and particle trace on wing and symmetry planes; $M_\infty = 0.85$, $\alpha = 20°$.

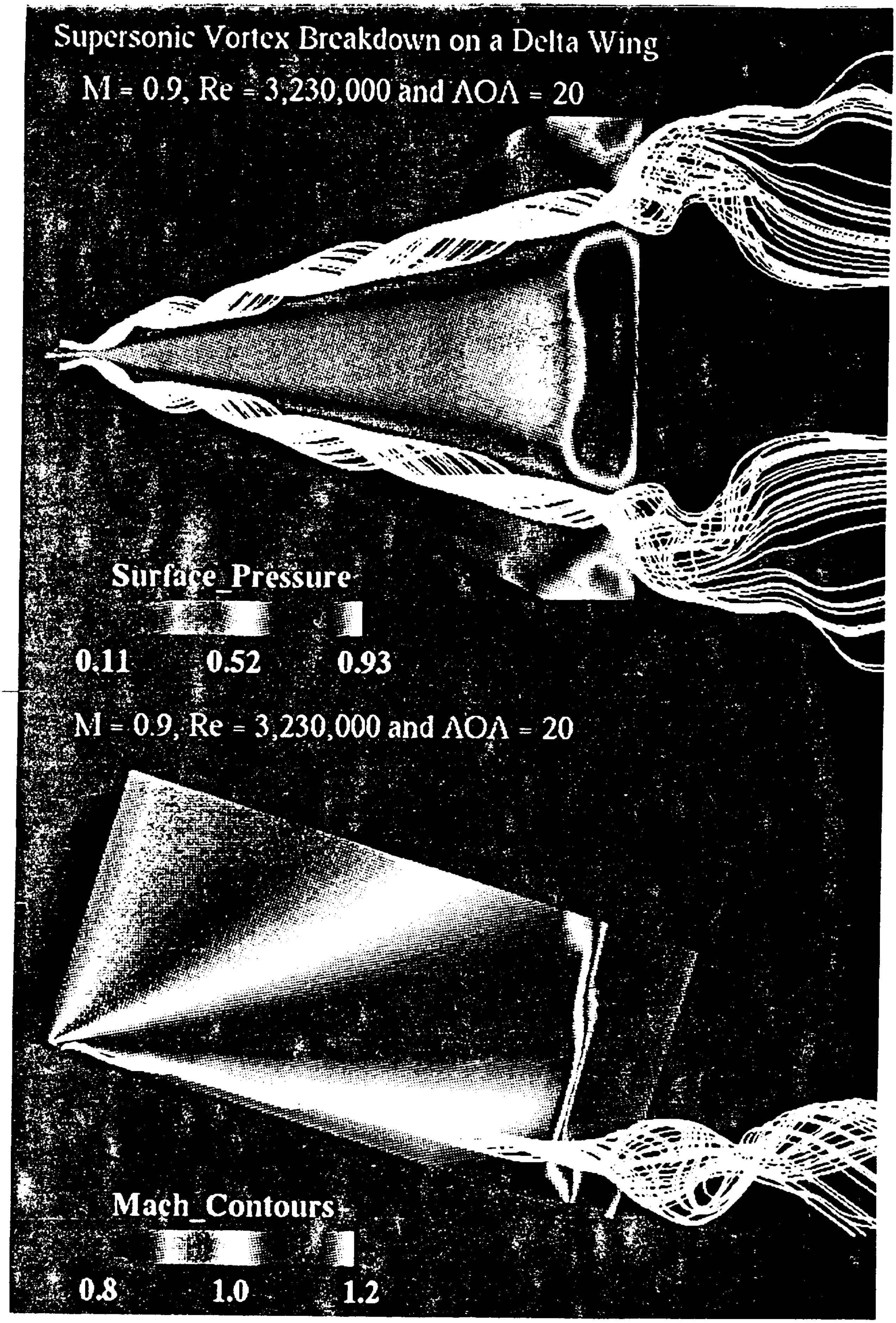
Supersonic Vortex Breakdown on a Delta Wing
M = 0.9, Re = 3,230,000 and AOA = 20
Surface_Pressure
0.11
0.52
0.93
M = 0.9, Re = 3,230,000 and AOA = 20
Mach_Contours
0.8
1.0
1.2

Fig. 19 Surface-pressure and Mach contours and particle trace on wing and symmetry planes: $M_\infty = 0.90$, $\alpha = 20°$

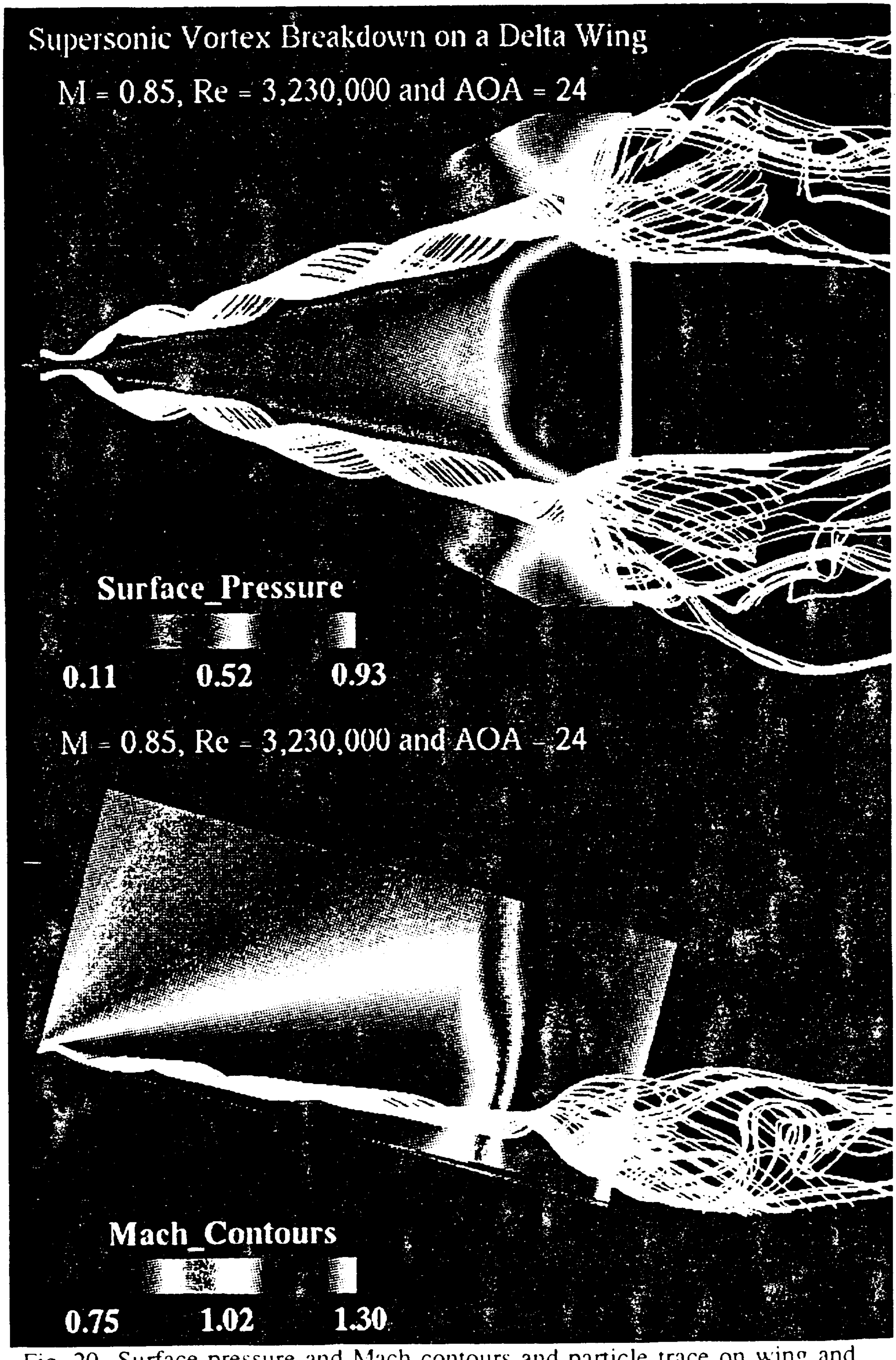

Fig. 20 Surface-pressure and Mach contours and particle trace on wing and symmetry planes: $M_\infty = 0.85$, $\alpha = 24°$.

[illegible]

[illegible]

14P

AIAA

AIAA-93-2973

# SHOCK-VORTEX INTERACTION OVER A 65-DEGREE DELTA WING IN TRANSONIC FLOW

Osama A. Kandil and Hamdy A. Kandil
Old Dominion University, Norfolk, VA 23529

C. H. Liu
NASA Langley Research Center, Hampton, VA 23681

**AIAA 24th**
**Fluid Dynamics Conference**
July 6-9, 1993 / Orlando, FL

For permission to copy or republish, contact the American Institute of Aeronautics and Astronautics
370 L'Enfant Promenade, S.W., Washington, D.C. 20024

# SHOCK-VORTEX INTERACTION OVER A 65–DEGREE DELTA WING IN TRANSONIC FLOW

**Osama A. Kandil* and Hamdy A. Kandil****
**Old Dominion University, Norfolk, Virginia 23529**
**and**
**C. H. Liu*****
**NASA Langley Research Center, Hampton, VA 23681**

## ABSTRACT

Transonic flow over a 65–degree swept-back, sharp-edged, cropped delta wing is investigated computationally using the time-accurate solution of the unsteady, compressible, full Navier-Stokes equations with an implicit, upwind, flux-difference splitting, finite-volume scheme. Coarse and fine O-H grids are used to obtain the solution. The grid consists of 125×85×84 points in the wrap-around, normal and axial directions, respectively. The results are presented for an angle of attack of 20°, March number of 0.85 and Reynolds number of $3.23 \times 10^6$ (based on the wing chord length). With the fine grid, the results show that a system of shocks has been captured over the upper wing surface, and that the leading-edge vortex core experiences an unsteady, supersonic vortex breakdown after passing through a spanwise shock (terminating shock) near the wing trailing edge. The computed results at a certain time are in good agreement with the experimental data. Topological aspects of the vortex-breakdown flowfield are also presented and discussed.

## INTRODUCTION

At sufficiently high angles of attack, vortex breakdown for incompressible flows around delta wings has been observed along the leading-edge primary vortex cores. Two distinct forms of vortex breakdown have been documented experimentally[1]. The first form is the bubble type and the second form is the spiral type. The bubble type shows an almost axisymmetric sudden swelling of the vortex core into a bubble, while the spiral type shows an asymmetric, spiral, vortex filament followed by a rapidly spreading turbulent flow. Both types are characterized by an axial stagnation point and a limited region of reversed axial flow. Much of our knowledge of incompressible vortex breakdown has been obtained from experimental studies of pipe flows where both types of breakdown and other types as well were generated and documented[2–4].

The major effort of computational study of vortex breakdown flows has also been focused on isolated swirling flows. For incompressible flows, quasi-axisymmetric, bubble-type, vortex-breakdown flows were computed using the Navier-Stokes equations[5–8]. Three-dimensional bubble and spiral vortex-breakdown flows were also computed for isolated swirling flows using the three-dimensional Navier-Stokes equations in the vorticity-velocity form or the primitive variables form[9–11].

Interaction between a longitudinal vortex and a transverse shock wave occurs in several flow applications which include transonic and supersonic flows over a delta wing or a strake-wing configuration at moderate to high angles of attack, a supersonic inlet ingesting a vortex, and a supersonic combustor where fuel is injected in a swirling jet to enhance fuel-air mixing[13–14]. For delta wings and strake-wing configurations, vortex breakdown is an undesirable phenomenon since it produces wing stall. Therefore, its occurrence needs to be delayed with passive or active control methods in order to increase the wing performance at large angles of attack. For a supersonic combustor, vortex breakdown is desirable since it enhances mixing of air and fuel and stabilizes the flame[15,16]. Therefore its occurrence needs to be enhanced and controlled.

For supersonic flows, quasi-axisymmetric bubble-type vortex-breakdown[17–19] and three-dimensional bubble-type and spiral-type vortex breakdown[20] for isolated swirling flows have been recently computed by the present authors. Using compatible, inlet boundary conditions, the time-accurate solutions of the unsteady, compressible, full Navier-Stokes equations were obtained to study the effects of Reynolds number, Mach number, swirl ratio, type of exit-boundary conditions and grid fineness and distribution on the vortex-breakdown modes for internal and external flows. Several modes of vortex breakdown which include transient single-bubble, transient multi-bubble, periodic multi-frequency multi-bubble, quasi-steady two-bubble cell and spiral-type vortex breakdowns have been obtained[21]. For three-dimensional vortex-breakdown flows in a swirling, supersonic jet flow, topological aspects of the critical points in the vortex-breakdown region have been studied and compared with the available experimental incompressible vortex-breakdown topology.

Recent experimental measurements[22–26] of transonic

---

* Professor, Eminent Scholar and Chairman of Aerospace Engineering Department, Associate Fellow AIAA.

** Research Associate, Aerospace Engineering Department, Member AIAA.

*** Senior Research Scientist, Computational Aerodynamics Branch, Associate Fellow AIAA.

Copyright © 1993 by Osama Kandil. Published by The American Institute of Aeronautics and Astronautics, Inc. with permission.

flows around a 65° swept-back, cropped delta wing show that shock wave formation is likely to occur underneath the leading-edge primary vortex core. In cross-flow planes perpendicular to the wing, the cross-flow beneath the primary vortex reaches supersonic speeds and a cross-flow shock develops beneath the primary vortex similar to the supersonic flow in a convergent-divergent nozzle. These measurements also show that a transverse shock "terminating shock" which might cause primary-vortex-core breakdown could develop in an analogous manner to the shock that terminates the two-dimensional supersonic pocket on an airfoil. A complete reconstruction of the three-dimensional flow field on the delta wing in this region was not possible experimentally[22-26]. Computational simulations for transonic delta-wing flows have been developed by using the Euler equations[27, 28] and the thin-layer, Navier-Stokes equations[29]. The Euler-equations solutions were not capable of fully resolving the flow in the terminating shock region and the thin-layer, Navier-Stokes solution did not address that region.

In the present paper, we consider the transonic flow around a 65° sharp-edged, cropped delta wing at an angle of attack of 20°, a Mach number of 0.85 and a Reynolds number of $3.23\times10^6$. The purpose of the present numerical simulation and study is to construct the flow field over the wing with particular emphasis of the vortex core-terminating shock interaction region. The laminar, unsteady, compressible, full Navier-Stokes equations are solved accurately in time with an implicit, flux-difference splitting, finite-volume scheme. The computations are carried out with time-accurate stepping on two O-H grids; a coarse grid and a fine grid. Both grids consist of $125\times85\times84$ points in the wrap-around, normal and axial directions, respectively. The main difference between the coarse and fine grids is the distribution of the grid points normal to the wing surface within the thin viscous layer (to be discussed later on).

## HIGHLIGHTS OF FORMULATION AND COMPUTATIONAL SCHEME

The conservative form of the dimensionless, unsteady, compressible, full Navier-Stokes equations is used for the formulation of the problem. The equations are written in terms of the time-independent, body-conformed coordinates $\xi^1,\xi^2$ and $\xi^3$ (Ref. 18).

The implicit, upwind, flux-difference splitting, finite-volume scheme is used to solve the unsteady, compressible, full Navier-Stokes equations. The scheme uses the flux-difference splitting scheme of Roe which is based on the solution of the approximate one-dimensional, Riemann problem. In the Roe scheme, the inviscid flux difference at the interface of computational cells is split into two parts; left and right flux differences. The splitting is accomplished according to the signs of the eigenvalues of the Roe averaged-Jacobian matrix of the inviscid fluxes at the cell interface. The smooth flux limiter is used to eliminate oscillations at locations of large flow gradients. The viscous- and heat-flux terms are linearized in time and the cross-derivative terms are neglected in the implicit operator and retained in the explicit terms. The viscous terms are differenced using a second-order accurate central differencing. The resulting difference equation is approximately factored and is solved in three sweeps in the $\xi^1,\xi^2$ and $\xi^3$ directions. The computational scheme is coded in the computer program "FTNS3D" which is a modified version of the CFL3D-code.

## COMPUTATIONAL RESULTS

A 65° swept-back, sharp-edged, cropped delta wing with zero thickness is considered for the computational solutions. The cropping ratio (tip length/root-chord length) is 0.15. The wing angle of attack is 20°, and the freestream Mach number and Reynolds number (based on the root-chord length) are 0.85 and $3.23\times10^6$, respectively. The reason behind the present, selected flow conditions is because of the uncertainty of the existing experimental data[22-26] about the structure of the downstream flow field of the leading-edge vortex core. The experimental data shows that a supersonic flow region appears on the upper wing surface near the plane of symmetry. This flow region is terminated by a transverse shock (known as a terminating shock) in a similar way to the shock that terminates a supersonic pocket on a supercritical airfoil[23].

### Grid:

An O-H grid of $125\times85\times84$ in the wrap-around, normal and axial directions, respectively, is used for the computational simulation. The computational domain extends two-chord length forward and five-chord length backward from the wing trailing edge. The radius of the computational domain is four-chord length. Two grids have been constructed using the same number of grid points. The first is called the coarse grid and the second is called the fine grid. For the coarse grid, the grid points in the cross flow planes have been distributed using a Joukowski transformation which produces a minimum grid size, normal to the wing surface, that varies from $5\times10^{-4}$ at the leading edge to $3\times10^{-2}$ at the plane of symmetry. For the fine grid, the elliptical grid lines in the cross-flow planes have been constructed such that the minimum grid size normal to the wing surface, stays constant at $5\times10^{-4}$ from the leading edge to the plane of symmetry. Figures 1 and 2 show three-dimensional shape of the coarse and fine grids and a cross-flow plane along with its blow-ups.

Time-accurate integration of the laminar, unsteady, compressible, full Navier-Stokes equations has been carried out with $\Delta t = 0.001$ for the coarse grid and $\Delta t = 0.0002$ for the fine grid. The results showed that the leading-edge vortex core passes through a terminating shock which causes the vortex core to breakdown. Moreover, it is shown that the flow becomes unsteady behind the terminating shock.

## Validation of Surface Pressure:

Figure 3 shows a comparison of the computed, spanwise surface-pressure coefficient ($C_p$) at different chord stations for the fine and coarse grids with the experimental data of Erickson[30] ($R_e = 3.23 \times 10^6$) and Hartmann[24] ($R_e = 2.38 \times 10^6$ and $4.57 \times 10^6$). The computed results are selected at t = 3.6. Obviously, the coarse-grid $C_p$-curves do not show the suction-pressure peak corresponding to the secondary vortex and the correct location of the suction-pressure peak corresponding to the primary vortex. The coarse-grid $C_p$-curves are similar to those of the Euler-equations solution. Therefore, they are discarded in this paper. The fine-grid $C_p$-curves show the correct location of the suction-pressure peak corresponding to the primary vortex and the suction-pressure peak corresponding to the secondary vortex. The fine-grid $C_p$-curves at x = 0.3, 0.6 and 0.8 are in fair to good agreement with the experimental data. For x = 0.9, the fine-grid $C_p$-curve shows a substantial, rapid increase in the pressure coefficient (a decrease in the suction pressure). Figure 4 shows the total-Mach contours and the streamlines in cross-flow planes at the chord stations of x = 0.3, 0.6, 0.8, 0.9, 0.97 and 1.0. At x = 0.3, 0.6 and 0.8, the total-Mach contours show an oblique shock under the primary vortex and a small subsonic region to the right of the shock. The streamlines show the secondary separation to the right of the shock. This separation is due to the shock interaction with the surface boundary-layer flow and is also due to the adverse, spanwise pressure gradient created by the primary vortex. At x = 0.9, the shock under the primary vortex becomes weak as observed in the total-Mach contours and the primary-vortex size increases. At x = 0.97, the shock under the primary vortex disappears and the primary vortex diffuses and reduces to a repelling focus as shown by the streamlines. At x = 1.0, the repelling focus becomes a repelling line. The details of the flow structure shown at x = 0.9, 0.97 and 1.0 indicate that the primary vortex is going through a breakdown mode which is caused by a transverse shock (terminating shock) between x = 0.8 and x = 0.9.

## Terminating Shock:

To show that a terminating, transverse shock exists and has been captured computationally, the static-pressure contours and total-Mach-contours on two planes are computed and displayed in Fig. 5. In this figure, the static-pressure contours are shown on the wing surface and the plane of symmetry, and the total-Mach contours are shown on the third plane (k = 3) above the wing (in the viscous layer) and on the plane of symmetry. The plane of symmetry contours clearly show the location, shape and strength of the terminating shock. Moreover, the Mach contours show that a substantial supersonic pocket (bounded by the sonic line and terminating shock) extends from the wing vertex to the shock location of x = 0.83, which is in good agreement with the experimental data[30], where the shock is located at x = 0.84. The computed results show that the shock is a normal shock with a height of 0.4 which is equal to one-half the wing span. In the spanwise direction, the shock foot print (shown on the Mach contours at k = 3) extends beyond the primary-vortex location. A $\lambda$-type shape of the shock-system foot print, which on one side of the wing, consists of the terminating shock and the shock under the primary vortex that runs along a ray plane from the wing vertex, is seen on the Mach contours at k = 3.

Figure 6 shows the position of the ray lines from the wing vertex (which are marked by the letters A-H) and the static-pressure curves along these lines. The static-pressure curves show the spanwise locations of several points on the foot-print line of the terminating shock. The terminating shock is clearly seen to run in the spanwise direction from the plane of symmetry to the wing leading edge. It reaches its highest strength from the location of the primary vortex to the wing leading edge (from line E to line H).

## Vortex-Breakdown Structure:

Having established the shock system that consists of the shock under the primary vortex and the terminating shock, the focus is directed on the structure of the flow behind the terminating shock. In Fig. 7, we show the total-Mach contours and streamlines on a ray plane at the 0.658 spanwise location, which passes through the leading-edge vortex core. Blow-ups of the velocity vectors and streamlines on this vertical plane are also shown in Fig. 7. The streamlines figures clearly show a two-bubble cell vortex breakdown. This is a typical three-dimensional vortex-breakdown mode which consists of an attracting saddle point (front) a repelling saddle point (rear), an attracting focus (top) and a repelling focus (bottom). Such a breakdown mode is similar to the one which was captured for an isolated supersonic vortex in an unbounded domain in Refs. 20 and 21. The location of the attracting saddle point is at 0.97 along the ray line, which corresponds to 0.87 along the axial direction. The attracting focus point is characterized with spiralling-in streamlines and the repelling focus point is characterized with spiralling-out streamlines. The Mach contours show that the front surface of the vortex-breakdown bubbles is enclosed by a hemi-spherical shape-like shock surface. Figures 12 and 13 show details of the flow structure on the wing plan view, on the plane of symmetry and on the ray plane at the 0.658 spanwise location (marked as J = 16 on Fig. 13). These figures and discussion give a complete construction of the flow structure including the shock system and its interaction with the leading-edge vortex core which produces vortex-breakdown of the two-bubble-cell mode.

## Unsteadiness of the Vortex-Breakdown:

The computations have been carried out with time-accurate stepping beyond t = 3.6. Figures 8–11 show the results at t = 5.52. These results show that the terminating shock moves in the upstream direction and so is the two-bubble-cell vortex breakdown behind the terminating shock. Figure 8 shows that the repelling focus is at x = 0.88 instead of x = 0.97 (Fig. 4). Figure 9 shows that the terminating shock in the plane of symmetry is at x = 0.685 instead of x = 0.83 (Fig. 5). The shock decreases in height and its thickness increases. Figure 10 shows that the size of the two-bubble cell vortex-breakdown region increases in comparison with the size at t = 3.6 (Fig. 7). Upstream of the terminating shock the flow stayed steady without any change.

Beyond the time t = 5.52, the upstream shock motion stopped and the motion reversed its direction to the downstream. The computations were not carried out beyond this instant due to its impeding cost. The unsteadiness of the terminating shock and the vortex-breakdown region behind it have also been observed experimentally by Bannik and Houtmann[23]. They also observed that the flow upstream of the terminating shock stayed steady without any change. These experimental observations undoubtedly support and validate our computational results.

## CONCLUDING REMARKS

The laminar, unsteady, compressible, full Navier-Stokes equations are integrated time accurately using the implicit, upwind, flux-difference splitting, finite-volume scheme to study and construct the flow field structure of a transonic flow around a 65° sharp-edged, cropped-delta wing. A $\lambda$-shock system, which consists of a ray shock under the primary vortex core and a transverse terminating shock, has been captured. Behind the terminating shock, the leading-edge vortex core breaks down into a two-bubble cell type. The terminating shock and the vortex breakdown region behind it is time dependent and appears to be oscillatory. The flow field ahead of the terminating shock stays steady without any change. This is consistent with the fact that the supersonic pocket along with the terminating shock do not allow disturbances to propagate upstream. The present results have been validated using the available experimental data and they are in good agreement. The present paper gives a complete construction of the flow field over the wing surface and in particular the structure of the flow at the terminating shock and behind it.

## ACKNOWLEDGEMENT

For the first two authors, this work is supported by the NASA-Langley Research Center under grant No. NAG-1-994 along with a partial support from the AFOSR. The Computational Resources provided by the NAS Center at Ames and the NASA Langley Research Center are acknowledged and appreciated.

## REFERENCES

1. Lambourne, N. C. and Bryer, D. W., "Bursting of Leading-Edge Vortices: Some Observations and Discussion of the Phenomenon," Aeronautical Research Council, R&M 3282, 1961.
2. Sarpkaya, T., "Effect of The Adverse Pressure Gradient on Vortex Breakdown," AIAA Journal, Vol. 12, No. 12, Dec. 1974, pp. 602–607.
3. Escudier, M. P. and Zender, N., "Vortex Flow Regimes," Journal of Fluid Mechanics, Vol. 115, 1982, pp. 105–122.
4. Leibovich, S., "Vortex Stability and Breakdown: Survey and Extension," AIAA Journal, Vol. 22, No. 9, Sept. 1984, pp. 1192–1206.
5. Grabowski, W. J. and Berger, S. A., "Solutions of the Navier-Stokes Equations for Vortex Breakdown," Journal of Fluid Mechanics, Vol. 75, Part 3, 1976, pp. 525–544.
6. Hafez, M., Kuruvila, G. and Salas, M.D., "Numerical Study of Vortex Breakdown," Journal of Applied Numerical Mathematics, No. 2, 1987, pp. 292–302.
7. Salas, M. D. and Kuruvila, G., "Vortex Breakdown Simulation: A Circumspect Study of The Steady, Laminar, Axisymmetric Model," Computers and Fluids, Vol. 17, No. 1, 1989, pp. 247–262.
8. Wu, J. C. and Hwang, S., "Computational Study of Vortex Breakdown in Circular Tube," AIAA 91–1820, June 1991.
9. Menne, S. and Liul, C. Hl., "Numerical Simulation of a Three-Dimensional Vortex Breakdown," Z. Flugwiss. Weltraumforsch 14, 1990, pp. 301–308.
10. Spall, R. E., Gatski, T. B. and Ash, R. L., "The Structure and Dynamics of Bubble-Type Vortex Breakdown," Proc. R. Soc., London, A429, 1990, pp. 613–637.
11. Breuer, M. and Hänel, D., "Solution of The 3-D Incompressible Navier-Stokes Equations for the Simulation of Vortex Breakdown," Eight GAMM Conference, Delft, Netherlands, September 27–29, 1989.
12. Krause, E., "Vortex Breakdown: Physical Issues and Computational Simulation," Third International Congress of Fluid Mechanics, Cairo, Egypt, January 1990, Vol. 1, pp. 335–344.
13. Delery, J., Horowitz, E., Leuchter, O. and Solignac, J. L., "Fundamental Studies of Vortex Flows," La Recherche Aerospatiale, No. 1984–2, 1984, pp. 1–24.
14. Metwally, O., Settles, G. and Horstman, C., "An Experimental Study of Shock Wave/Vortex Interaction," AIAA 89–0082, January 1989.
15. Cutler, A. D. and Levey, B. S., "Vortex Breakdown in a Supersonic Jet," AIAA 91–1815, June 1991.

16. Rhode, D. L., Lilley, D. B. and McLaughlin, D. K., "On The Prediction of Swirling Flowfields Found in Axisymmetric Combustor Geometries," Transactions of ASME, Vol. 104, September 1982, pp. 378–384.

17. Kandil, O. A., Kandil, H. A. and Liu, C. H., "Computation of Steady and Unsteady Compressible Quasi-Axisymmetric Vortex Flow and Breakdown," AIAA 91–0752, January 1991.

18. Kandil, O. A., Kandil, H. A. and Liu, C. H., "Supersonic Quasi-Axisymmetric Vortex Breakdown," AIAA 91–3311–CP, September 1991, pp. 851–863.

19. Kandil, O. A., Kandil, H. A. and Liu, C. H., "Critical Effects of Downstream Boundary Conditions on Vortex Breakdown," AIAA 92–2601 CP, June 22-24, 1992, pp. 12–25.

20. Kandil, O. A., Kandil, H. A. and Liu, C. H., "Three-Dimensional Supersonic Vortex Breakdown," AIAA 93–0526, January 11–14, 1993.

21. Kandil, H. A., "Navier-Stokes Simulation of Quasi-Axisymmetric and Three-Dimenisonal Supersonic Vortex-Breakdown," Ph.D. Dissertation, Dept. of Mechanical Engineering and Mechanics, Old Dominion University, Norfolk, VA, May 1993.

22. Boersen, S. J. and Elsenaar, A., "Tests on the AFWAL 65° Delta Wing at NLR: A Study of Vortex Flow Development Between Mach = 0.4 and 4," Proceedings of Symposium on International Vortex Flow Experiment on Euler Code Validation, Stockholm, Sweden, October 1-3, 1986, pp. 23-36.

23. Bannik, W. J. and Houtman, E. M., "Experiments on the Transonic Flow Over a Delta Wing at High Angles of Attack," Proceedings of Symposium on International Vortex Flow Experiment on Euler Code Validation, Stockholm, Sweden, October 1-3, 1986, pp. 37–46.

24. Hartmann, K., "Force and Pressure Measurements Including Surface Flow Visualization on a Cropped Delta Wing," Proceedings of Symposium on International Vortex Flow Experiment on Euler Code Validation, Stockholm, Sweden, October 1-3, 1986, pp. 63–87.

25. Bütefisch, K. A., Pallek, D. and Sauerland, K., -H., "International Vortex Flow Experiment-Results of Three Component LDA Measurements on a 65° Delta Wing," DFVLR IB 222–87 A 34, 1987.

26. Elsenaar, A., Hjelmberg, L., Bütefisch, K. and Bannink, W. J., "The International Vortex Flow Experiment," AGARD-CP-437, Lison, Portugal, May 1988, Vol. 1., pp. 9.1–9.23.

27. Hitzel, S. M., "Wing Vortex-Flows Up into Vortex-Breakdown-A Numerical Simulation," AIAA 88-2518-CP, 1988, pp. 73–83.

28. Bannink, W. J. and Houtman, E. M., "Experimental and Computational Study of the Vortical Flow Over a Delta wing at High Angles of Attack," IUTAM Symposium on Fluid Dynamics of High Angle of Attack, University of Japan, Tokyo, Japan, September 14–17, 1992.

29. Laine, S., Siikonen, T. and Kaurinkoski, P-, "Calculation of Transonic Viscous Flow Around a Delta Wing," ICAS 92–4.2.1, Beijing, PRC, September 22-25, 1992, pp. 286–295.

30. Erickson, G. E., "Wind Tunnel Investigation of The Interaction and Breakdown Characteristics of Slender-Wing Vortices at Subsonic, Transonic and Supersonic Speeds," NASA Tech. paper 3114, November 1991.

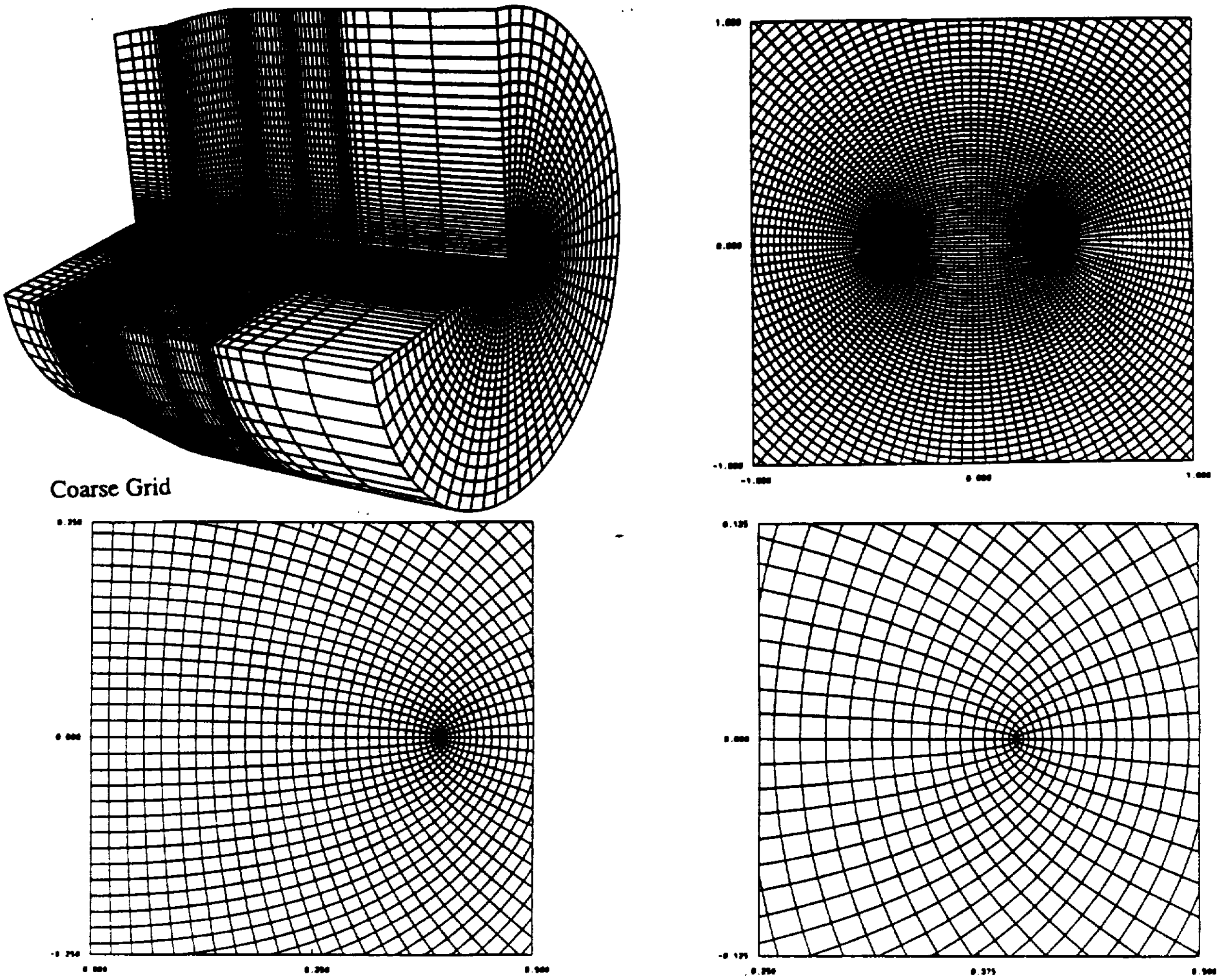
Coarse Grid
1.000
0.000
-1.000
-1.000
0.000
1.000
0.250
0.000
-0.250
0.000
0.250
0.500
0.125
0.000
-0.125
0.250
0.375
0.500

Fig. 1. Coarse grid; three-dimensional shape and cross-flow plane and its blow-up, 125×85×84

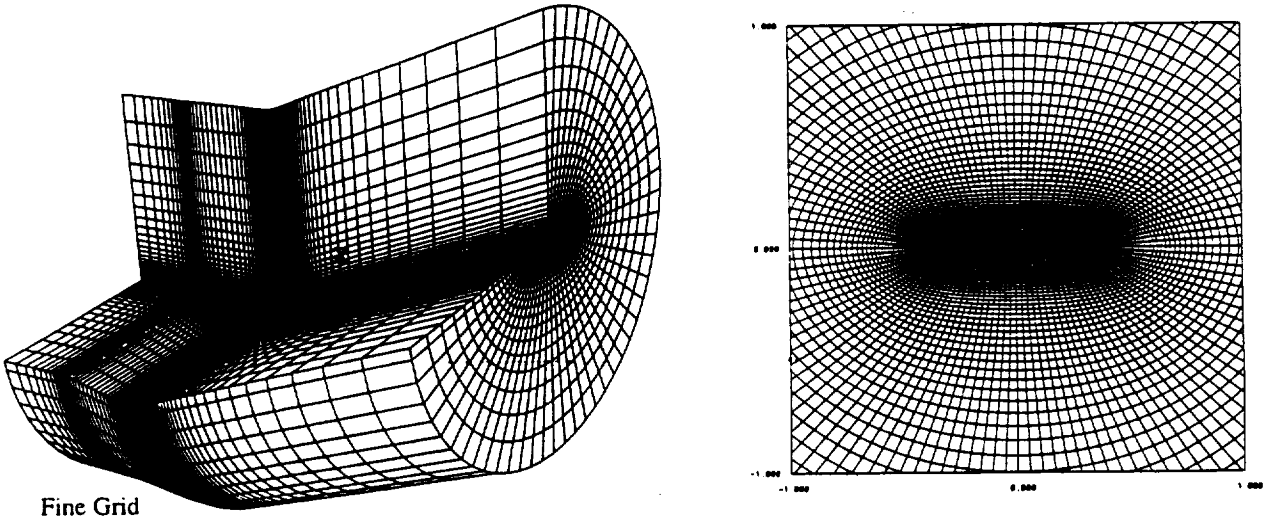
Fine Grid
1.000
0.000
-1.000
-1.000
0.000
1.000

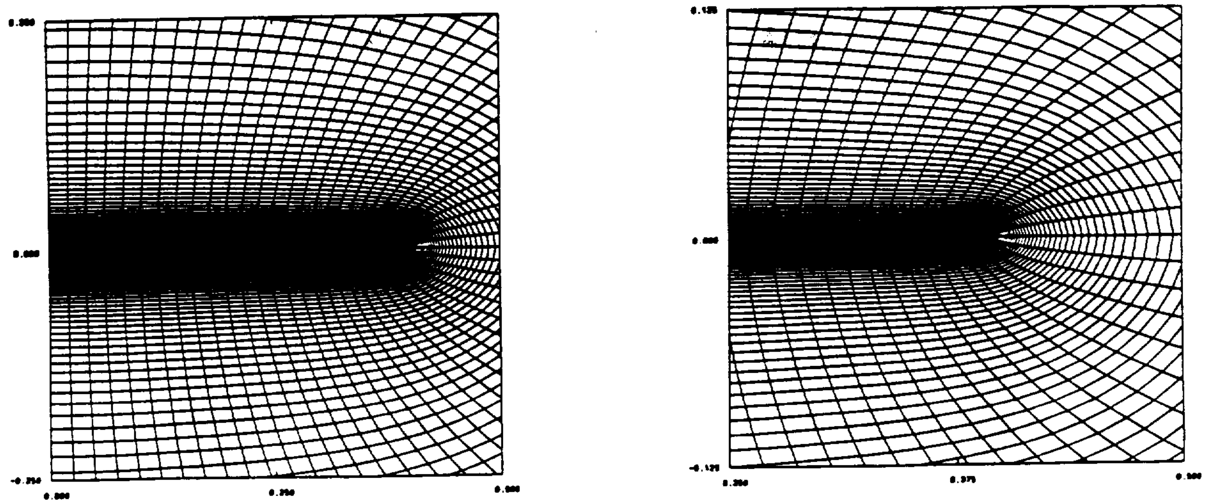
0.250
0.000
-0.250
0.000
0.250
0.500
0.125
0.000
-0.125
0.250
0.375
0.500

Fig. 2. Fine grid; three-dimensional shape and a cross-flow plane and its blow-up, 128×85×84

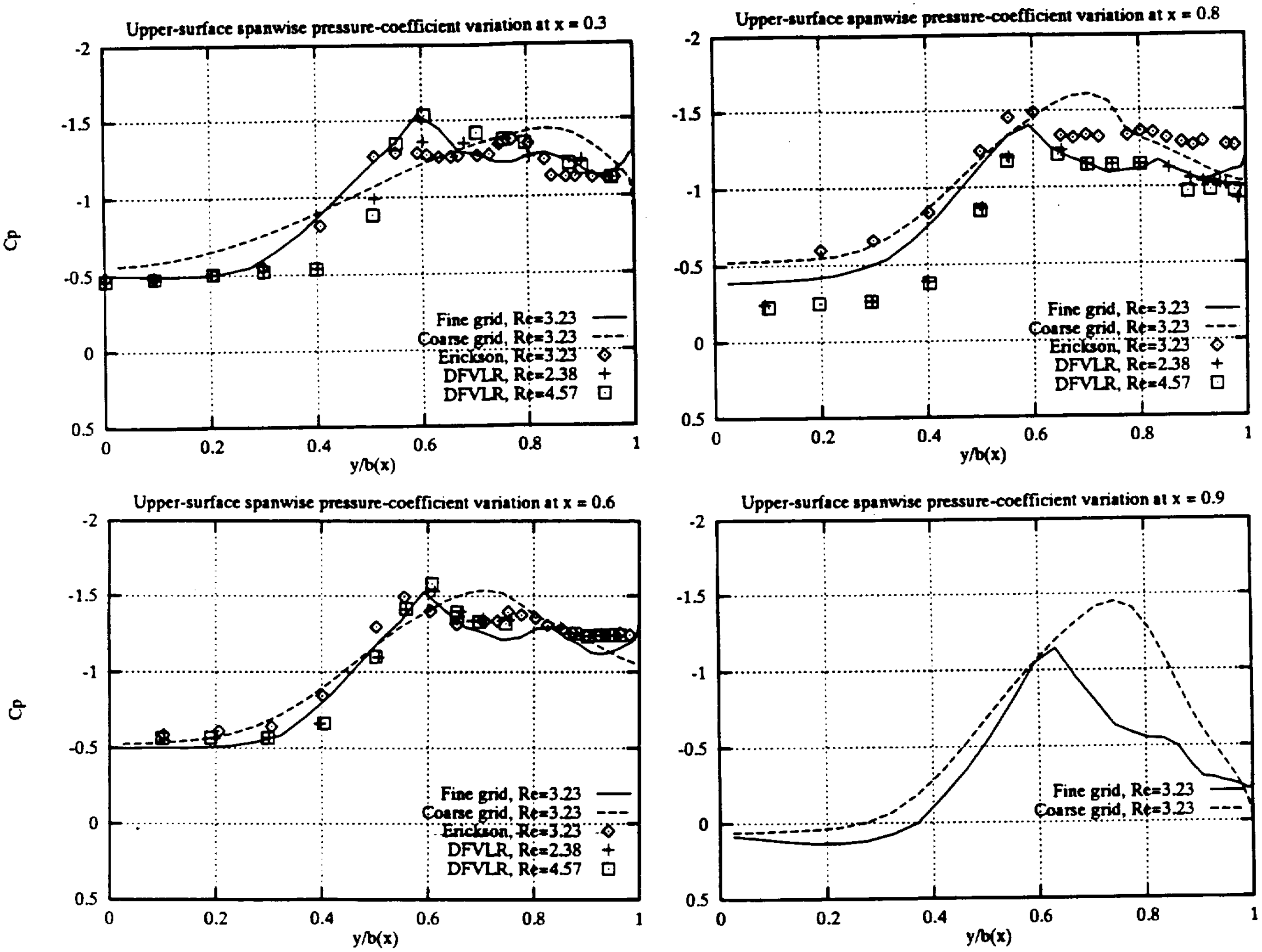

Fig. 3. Comparison of the computed and experimental spanwise, surface-pressure coefficient at different chord stations; $M_\infty = 0.85$, $\alpha = 20^\circ$, $t = 3.6$

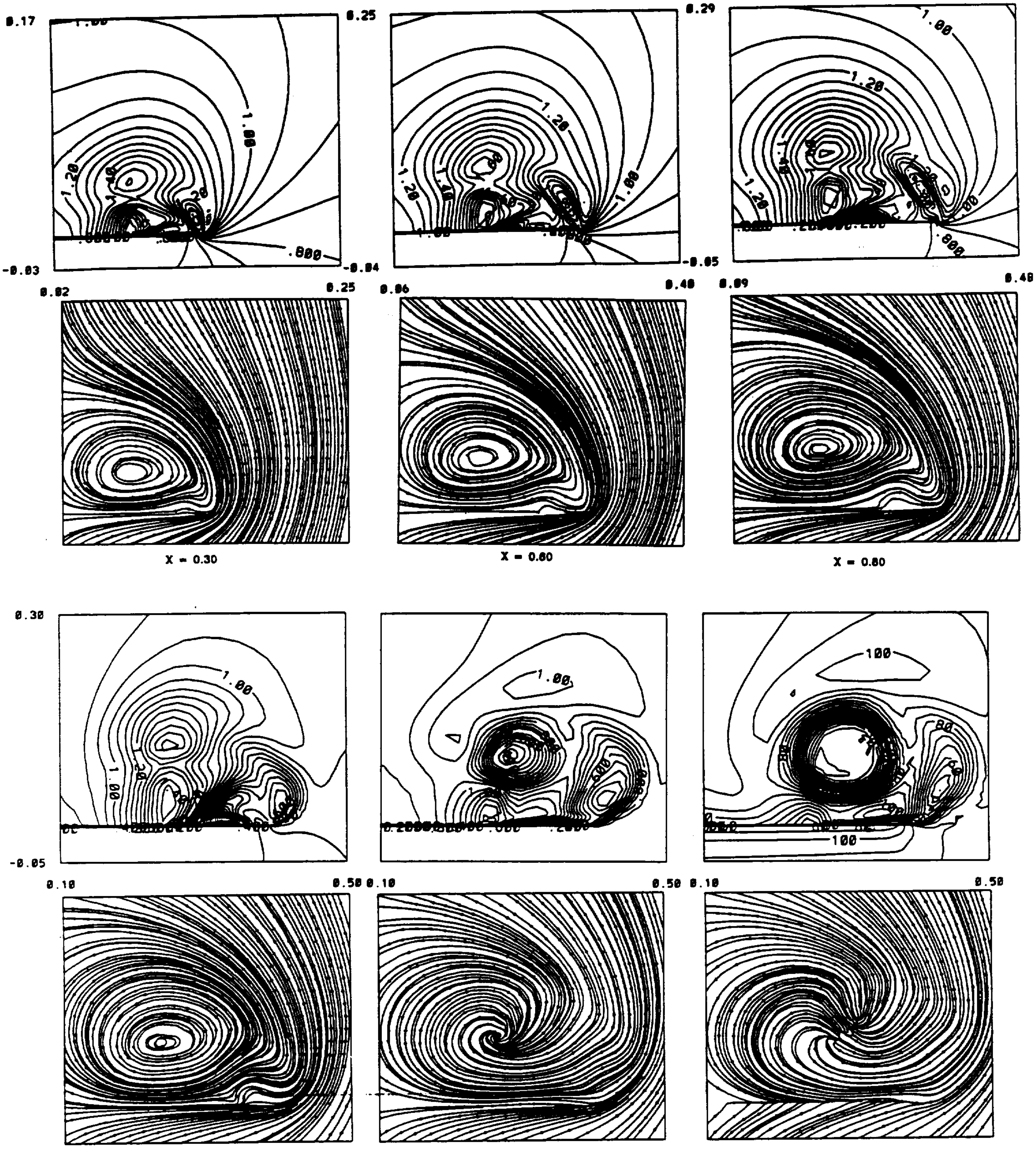

X = 0.30

X = 0.60

X = 0.80

X = 0.90

X = 0.97

X = 1.0

Fig. 4. Total-Mach contours and streamlines in cross-flow planes; $M_\infty = 0.85$, $\alpha = 20°$, $t = 3.6$

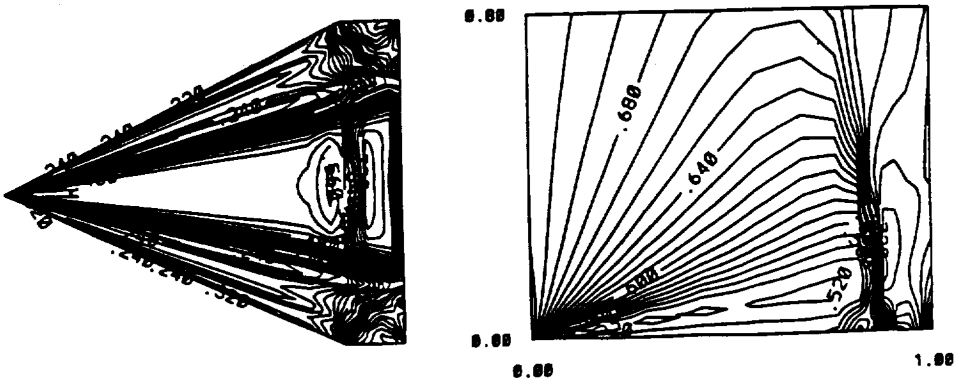

PRESSURE CONTOURS ON THE WING SURFACE

PRESS. CONTOURS ON THE PLANE OF SYMMETRY

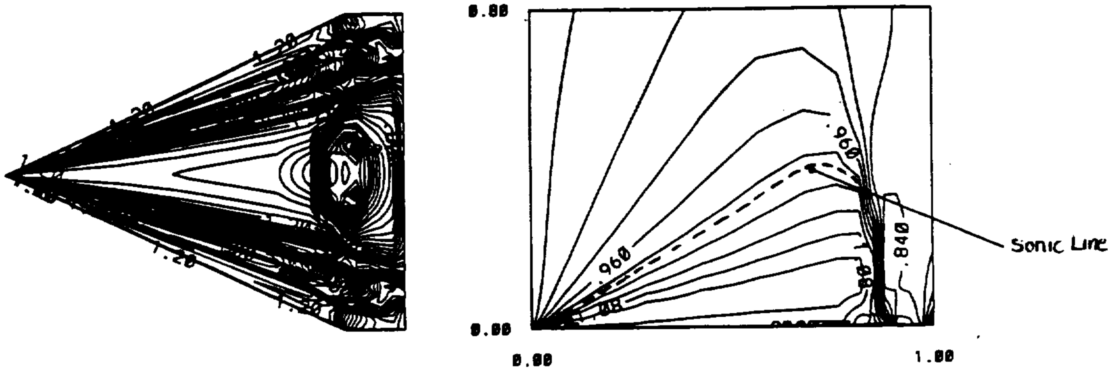

MACH CONTOURS ON A CONSTANT K PLANE

MACH CONTOURS ON THE PLANE OF SYMMETRY

Fig. 5. Static-pressure and Mach contours on the wing and the plane of symmetry; $M_\infty = 0.85$, $\alpha = 20°$, $t = 3.6$

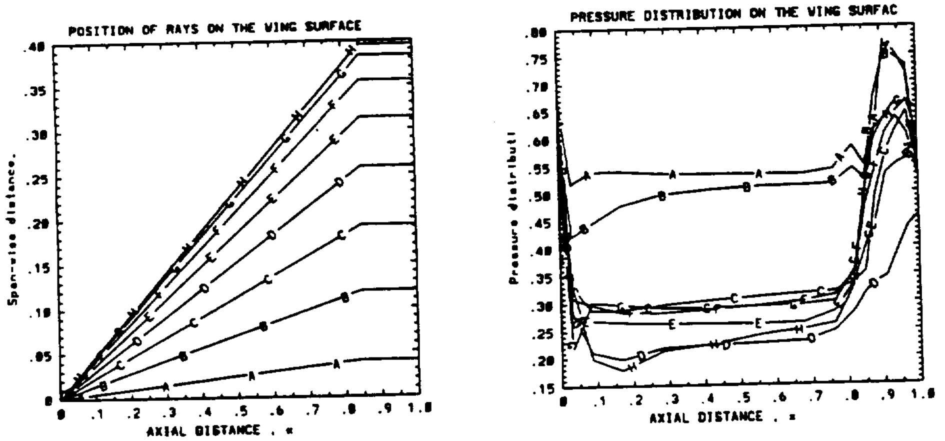

Fig. 6. Ray lines on the wing surface and the static-pressure variation along them; $M_\infty = 0.85$, $\alpha = 20°$, $t = 3.6$

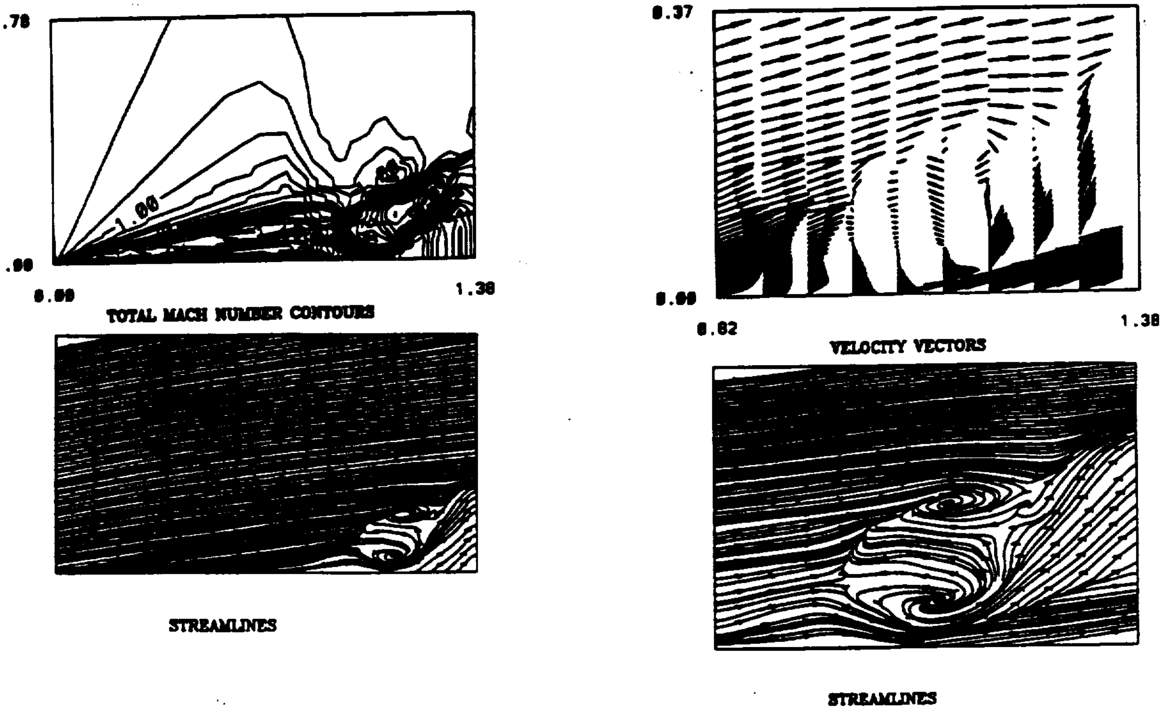

Fig. 7. Total-Mach contours, streamlines and velocity vectors on a ray plane passing through the vortex-breakdown two-bubble cell; $M_\infty = 0.85$, $\alpha = 20^\circ$, $t = 3.6$

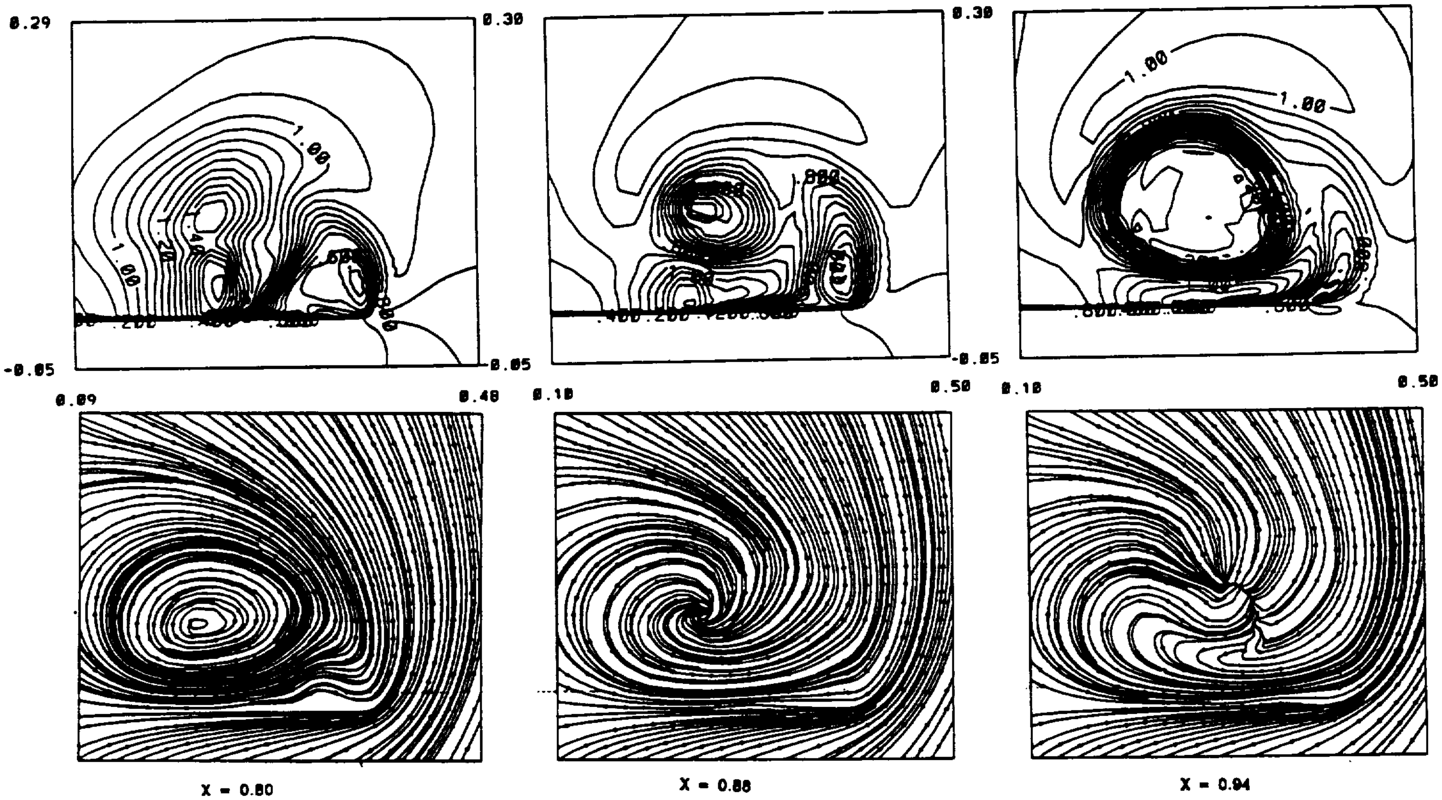

Fig. 8. Total-Mach contours and streamlines in cross-flow plane; $M_\infty = 0.85$, $\alpha = 20^\circ$, $t = 5.52$

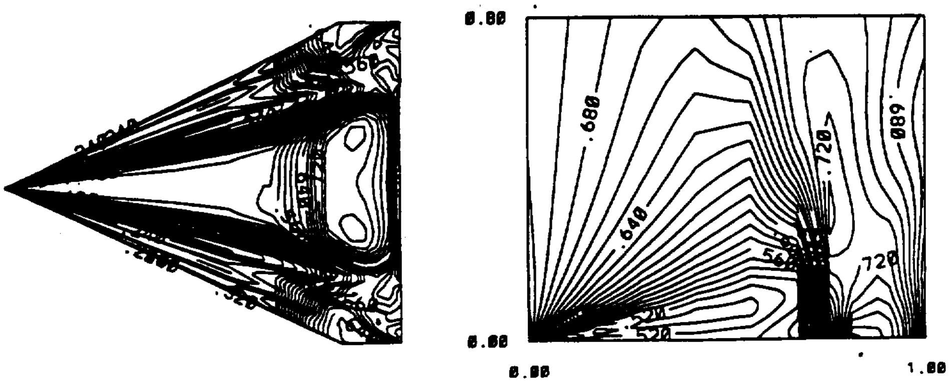

PRESSURE CONTOURS ON THE WING SURFACE

PRESS. CONTOURS ON THE PLANE OF SYMMETRY

Fig. 9. Static-pressure contours on the wing and the plane of symmetry; $M_\infty = 0.85$, $\alpha = 20^\circ$, $t = 5.52$

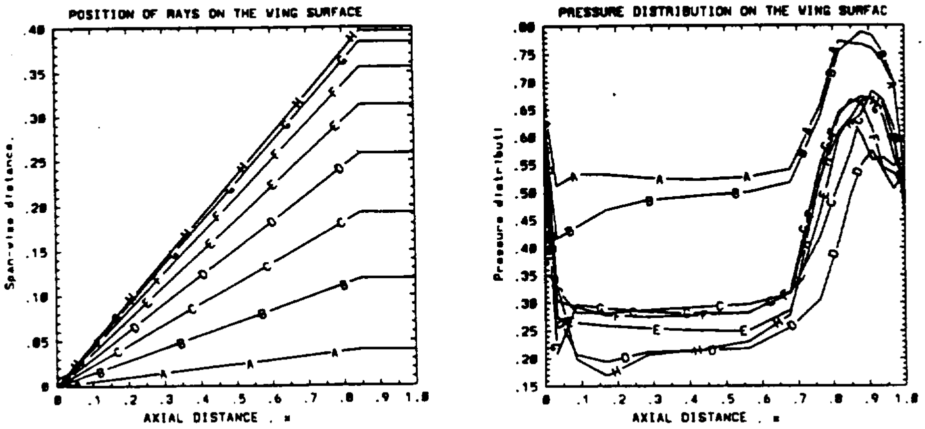

Fig. 10. Ray lines on the wing surface and the static-pressure variation along them; $M_\infty = 0.85$, $\alpha = 20^\circ$, $t = 5.52$

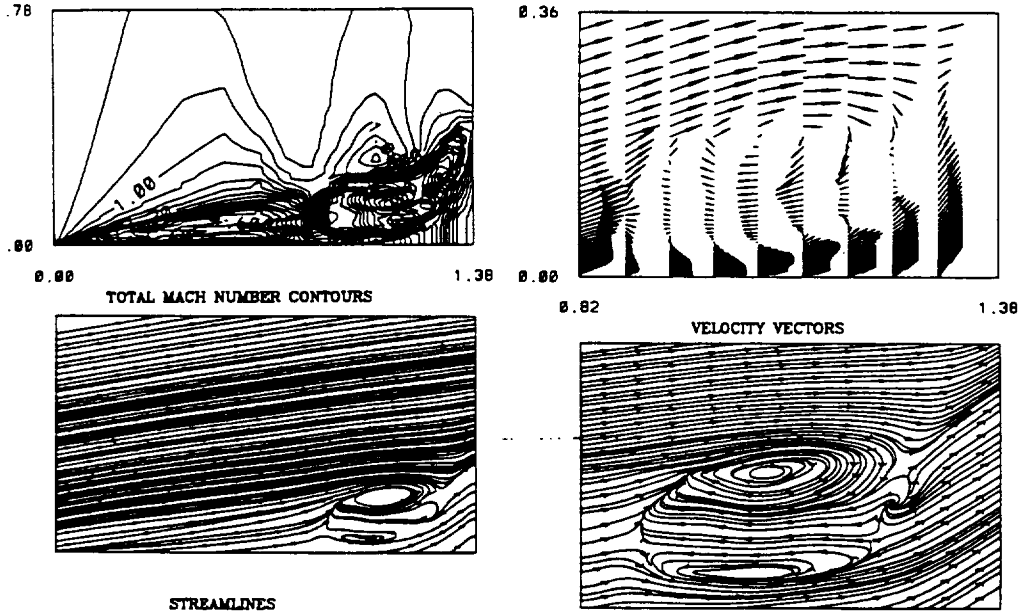

TOTAL MACH NUMBER CONTOURS

VELOCITY VECTORS

STREAMLINES

STREAMLINES

Fig. 11. Total-Mach contours, streamlines and velocity vectors on a ray plane passing through the vortex-breakdown bubbles; $M_\infty = 0.85$, $\alpha = 20^\circ$, $t = 5.52$

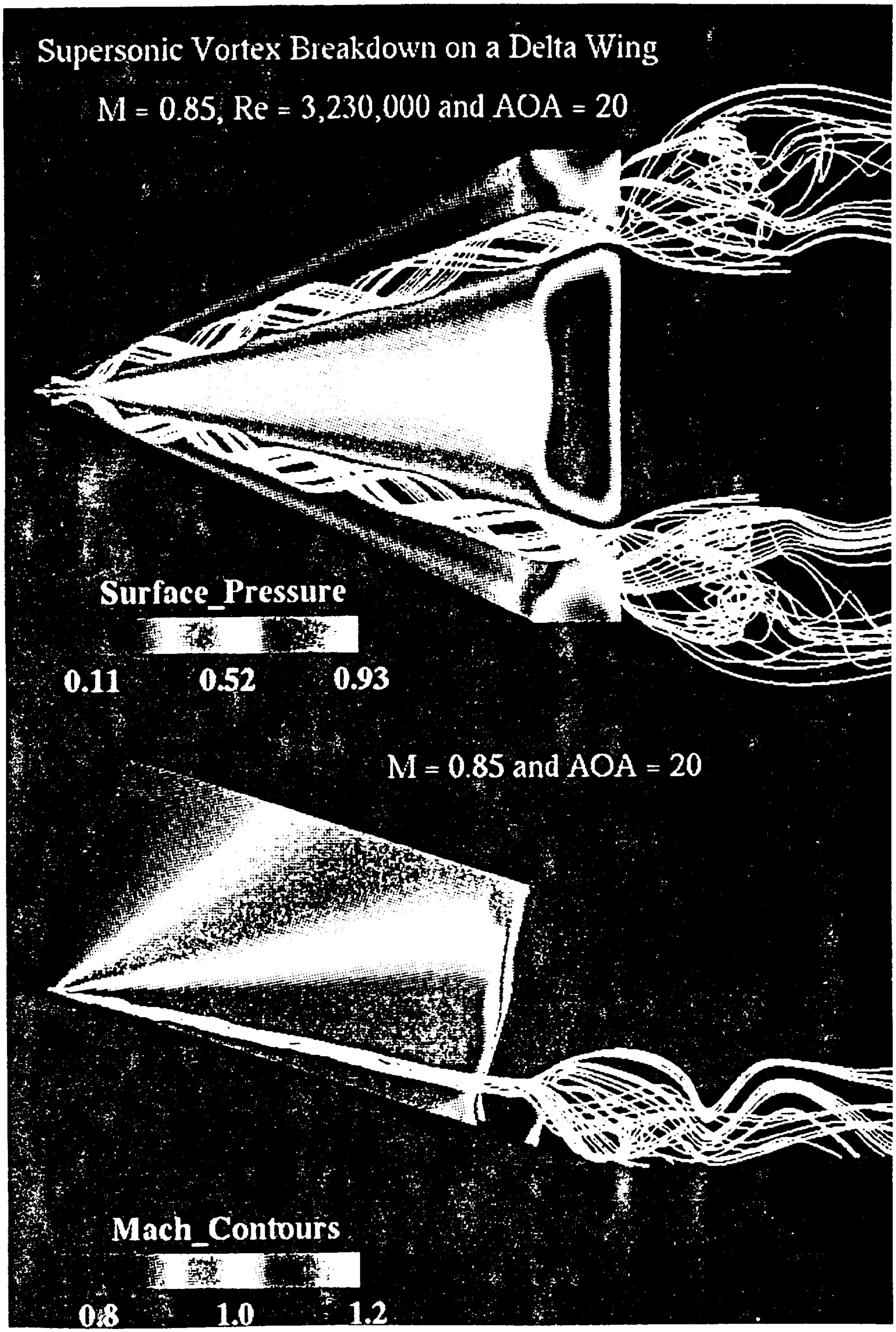
Supersonic Vortex Breakdown on a Delta Wing
M = 0.85, Re = 3,230,000 and AOA = 20
Surface_Pressure
0.11
0.52
0.93
M = 0.85 and AOA = 20
Mach_Contours
0.8
1.0
1.2

Fig. 12 Surface-pressure and Mach contours and particle trance on wing and symmetry planes; $M_\infty$ = 0.85, $\alpha$ = 20°, t = 3.6

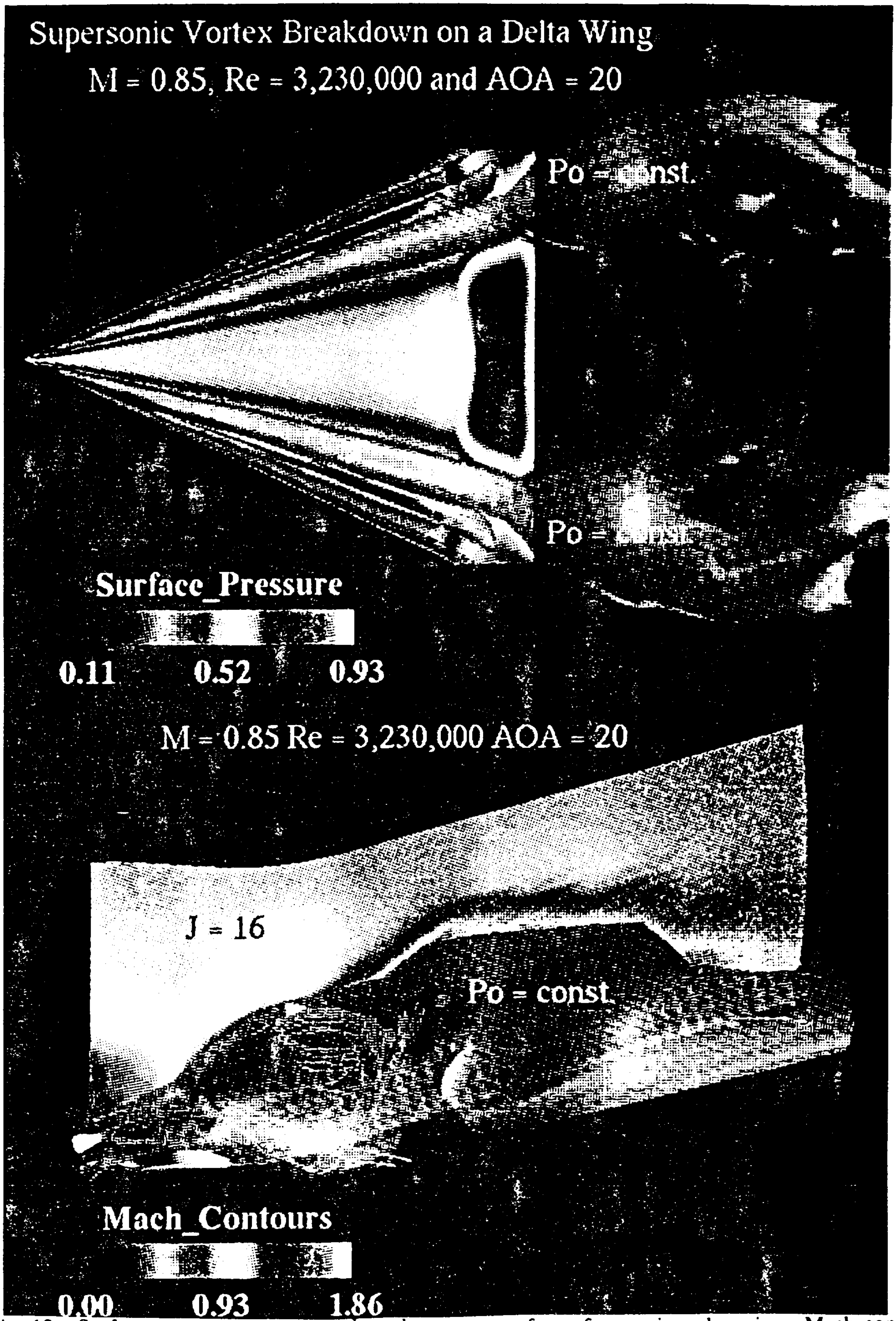

Fig. 13. Surface-pressure contours and total-pressure surfaces for a wing plan view; Mach contours and total-pressure surface on a ray plane passing through the vortex-breakdown bubble; $M_\infty = 0.85$, $\alpha = 20°$, $t = 3.6$

[illegible]

[illegible] 7

16P

# AIAA 93-0526

# THREE-DIMENSIONAL SUPERSONIC VORTEX BREAKDOWN

Osama A. Kandil and Hamdy A. Kandil
Old Dominion University, Norfolk, VA 23529

C. H. Liu
NASA Langley Research Center, Hampton, VA 23665

**31st Aerospace Sciences**
**Meeting & Exhibit**
January 11-14, 1993 / Reno, NV

**For permission to copy or republish, contact the American Institute of Aeronautics and Astronautics**
**370 L'Enfant Promenade, S.W., Washington, D.C. 20024**

# THREE-DIMENSIONAL SUPERSONIC VORTEX BREAKDOWN

**Osama A. Kandil* and Hamdy A. Kandil****
**Old Dominion University, Norfolk, VA 23529**
**and**
**C. H. Liu*****
**NASA Langley Research Center, Hampton, VA 23665**

## ABSTRACT

Three-dimensional, supersonic vortex-breakdown problems in bound and unbound domains are solved. The solutions are obtained using the time-accurate integration of the unsteady, compressible, full Navier-Stokes (NS) equations. The computational scheme is an implicit, upwind, flux-difference splitting, finite-volume scheme. Two vortex-breakdown applications are considered in the present paper. The first is for a supersonic swirling jet which is issued from a nozzle into a supersonic uniform flow at a lower Mach number than that of the swirling jet. The second is for a supersonic swirling flow in a configured circular duct. In the first application, an extensive study of the effects of grid fineness, shape and grid-point distribution on the vortex breakdown is presented. Four grids are used in this study and they show a substantial dependence of the breakdown bubble and shock wave on the grid used. In the second application, the bubble-type and helix-type vortex breakdown have been captured.

## INTRODUCTION

Longitudinal vortex/transverse shock-wave interaction is a complex flow phenomenon which develops in several external and internal flow applications. For external flows, the transonic flow around a delta wing in the high-angle-of-attack range[1,2] and the transonic and supersonic flows around a strake-delta wing configuration in the moderate to high-angle-of-attack range[3] are some of the applications. Vortex-breakdown usually occurs behind the transverse shock wave over the delta wing resulting in a loss of lift. Such a breakdown is undesirable and flow-control methods need to be developed to eliminate the vortex breakdown. For internal flows, the supersonic inlet ingesting a vortex and the supersonic combustor where fuel is injected in a swirling jet to enhance fuel-air mixing are some of the applications. Vortex breakdown behind the transverse shock wave in these applications is desirable since it enhances mixing and stability of the flame[4-7], and hence its occurrence need to be controlled for optimum performance.

For such problems, computational schemes are needed to study, predict and control vortex-shock interaction including vortex breakdown. Unfortunately, the literature lacks this type of analysis with the exception of the preliminary work of Liu, Krause and Menne[8], Copening and Anderson[3], Delery, et al.[4] and Kandil and Kandil[9].

The first time-accurate NS solution for a quasi-axisymmetric supersonic vortex-breakdown was developed by Kandil, Kandil and Liu in Ref. 10. A supersonic quasi-axisymmetric vortex flow in a configured circular duct was considered. The time-accurate solution of the unsteady, compressible NS equations was obtained using an implicit, upwind, flux-difference splitting finite-volume scheme. A shock wave was generated near the duct inlet and unsteady vortex-breakdown was predicted behind the shock. The predicted flow was characterized by the evolution, convection and shedding of vortex-breakdown bubbles. The Euler equations were also used to solve the same problem. The Euler solution showed larger size and number of vortex-breakdown bubbles in comparison with those of the NS solutions. The time-accurate solution was carried out for 3,200 time steps which were equivalent to a dimensionless time of 16. Only one value of Reynolds number of 10,000 was considered in Ref. 10.

In a later paper by Kandil, Kandil and Liu[11], the study of this flow was extended using time-accurate computations of the NS equations with a fine grid in the shock-vortex interaction region and for long computational times. Several issues were addressed in that study. First, the effect of Reynolds number on the temporal evolution and persistence of vortex-breakdown bubbles behind the shock was shown. In that stage of computations, the conditions at the downstream exit were obtained by extrapolating the components of the flowfield vector from the interior cell centers. Although the flow was supersonic over a large portion of the duct exit, subsonic flow existed over a small portion of the exit around the duct centerline. Therefore, selected flow cases were computed using Riemann-invariant-type boundary conditions at subsonic points of the duct exit. The effect of swirl ratio at

---

*Professor and Eminent Scholar, Dept. of Mechanical Engineering and Mechanics, Associate Fellow AIAA.

**Graduate Research Assistant, Member AIAA.

***Group Leader, Computational Aerodynamics Branch, Associate Fellow AIAA.

Copyright © 1993 by Osama Kandil. Published by The American Institute of Aeronautics and Astronautics, Inc. with permission.

the duct inlet was also investigated. Recently, the critical effects of the downstream boundary conditions on the supersonic vortex-breakdown was extensively investigated by the same authors[12] for both internal and external flows.

In Refs. 10–12, the present authors assumed the flow quasi-axisymmetric and the NS equations were solved using the three-dimensional solver "FTNS3D" by forcing the components of the flowfield vector to be equal on two axial planes in close proximity of each other. Quasi-axisymmetric solutions are one-order of magnitude less in computational cost than the corresponding three-dimensional solutions, and they still provide substantial physical understanding of the supersonic vortex breakdown. At this substantially reduced computational cost, we were able to study the effects of Reynolds number, swirl ratio and downstream exit-boundary conditions using time-accurate stepping. However, the previous experimental studies for both incompressible[13–15] and supersonic vortex breakdown[16] showed that the flow is three dimensional.

Hence, we consider the three-dimensional solution of the NS equations to realistically simulate the vortex breakdown problem. The computational solution of two main vortex-breakdown problems are presented in this paper: the first is for vortex breakdown of a supersonic swirling jet issued from a nozzle into a supersonic uniform flow at a lower Mach number than that of the swirling jet, and the second is for vortex breakdown of a supersonic swirling flow in a configured circular duct. In the first problem, an extensive study of the effects of grid fineness, shape and grid-point distribution on the breakdown bubble is presented. Four grids have been used in the study, and they show a substantial dependence of the breakdown bubble and shock wave on the grid used. In the second problem, the time-accurate solution shows two modes of supersonic vortex breakdown; a bubble type and a spiral type.

## HIGHLIGHTS OF THE FORMULATION AND COMPUTATIONAL SCHEME

The conservative, unsteady, compressible, laminar full Navier-Stokes equations in terms of time-independent, body-conformed coordinates $\xi^1$, $\xi^2$ and $\xi^3$ are used to solve the problem. The equations are given in Ref. 11 and hence they are not shown here. Along with these equations, boundary conditions are specified at the computational-domain inlet, side wall and downstream exit. The boundary conditions are presented in the next section. The initial conditions will also be presented in the next section.

The computational scheme used to solve the unsteady, compressible full NS equations is an implicit, upwind, flux-difference splitting, finite-volume scheme. It employs the flux-difference splitting scheme of Roe which is based on the solution of the approximate one-dimensional Riemann problem in each of the three directions. In the Roe scheme, the inviscid flux difference at the interface of a computational cell is split into left and right flux differences. The splitting is accomplished according to the signs of the eigenvalues of the Roe averaged-Jacobian matrix of the inviscid flux at the cell interface. The smooth limiter is used to eliminate oscillations in the shock region. The viscous and heat-flux terms are linearized and the cross-derivative terms of the viscous Jacobians are dropped in the implicit operator. These terms are differenced using second-order spatially accurate central differencing. The resulting difference equation is approximately factored and is solved in three sweeps in the $\xi^1$, $\xi^2$ and $\xi^3$ directions. The scheme is coded in the computer program which is called "FTNS3D".

## COMPUTATIONAL RESULTS AND DISCUSSION

### I. Three-Dimensional Vortex Breakdown of a Supersonic Swirling Jet

A supersonic swirling jet at a Mach number of $M_j$ = 3.0 is issued from a nozzle into a supersonic uniform flow at a Mach number of $M_\infty = 2.0$. The freestream Reynolds number, $R_e$, is 296,000. The nozzle-exit radius is the characteristic length and the length of the computational domain is 7.0 dimensionless units. The purpose of the present computational case is to simulate the flow of the experimental study of Ref. 16. It was reported in Ref. 16 by Metwally, et al. that it was difficult to detect any vortex-breakdown bubble behind the formed shock in the swirling jet flow and that the shock was oscillating around a mean position. For the present computational study, it is decided to use four types of structured grids to solve the unsteady, compressible NS equations accurately in time. The cross-section of the computational domain is taken as a square section for three types of grid which are called Grid type 1, 2 and 3. For the fourth grid, Grid type 4, a circular section is used. For Grid types 1, 2 and 3, the length of one-half the square-section side is 3.5 units and for Grid type 4, the radius length of the circular section is 3.5 units. A time step of 0.02 is used for all the four types of grids.

**I.1 Boundary and Initial Conditions:** The inflow boundary conditions are adapted from the limited experimental data of Ref. 16. Unfortunately, the experimental data available in Ref. 16 are given along one diameter only of the circular section. The profiles of the experimental data are not symmetric with respect to the diameter center point. To produce three-dimensional profiles from the experimental data, two methods are used. In the first method, the asymmetry of the experimental profiles is maintained by assuming the profiles on the right-hand side of the initial cross-section to be the same as those of the upper half of the experimental data and the profiles on the left-hand side of the initial cross-section to be the same as those of the lower half of the experimental data. In the second method, the initial cross-section profiles are assumed to be quasi-axisymmetric and are set equal to the profiles of the upper half of the experimental data. The average swirl ratio of the asymmetric profiles is 0.2 and the swirl ratio of the quasi-axisymmetric profiles is 0.22. The experimental data are used for $r < 1$, and for $1 < r \leq 3.5$ uniform wind-tunnel conditions corresponding to $M_\infty = 2.0$ are used. Figures 1 and 2 show the generated asymmetric and quasi-axisymmetric distributions of the axial velocity, $u$, tangential velocity $v$, density, $\rho$, and pressure, $p$.

The boundary conditions on the outer boundaries of the computational domain are assumed to be uniform conditions corresponding to $M_\infty = 2.0$.

The outflow boundary conditions at the exit of the computational domain are obtained by extrapolating all the flowfield components from the interior cell centers at the exit. This is justified since the experimental data of Ref. 16 show that the flow becomes supersonic a few radii downstream of the shock/vortex interaction region.

The initial conditions in the entire domain correspond to freestream conditions at $M_\infty = 2.0$. Hence, the present flow case simulates a sudden discharge of a swirling supersonic jet from a nozzle into a uniform supersonic flow.

**I.2 Grid Type 1:** A rectangular grid of 210×51×51 points in the axial (x direction) and cross-flow directions (y and z directions), respectively is considered. The grid points are clustered in the axial direction near the inflow boundary and near the vortex-core axis. The minimum grid size is 0.057 in the y and z directions and 0.0147 in the x direction. Figure 3 shows a side view and a cross-flow plane of the grid.

In Fig. 4, snapshots of the streamlines on a horizontal plane passing through the computational domain axis and the total Mach contours on the same plane are given at selected dimensionless times. At $t = 2.0$, the Mach contours show the existence of a strong shock wave at the centerline. The shock is formed due to the mismatch between the static pressures of the supersonic swirling jet and the supersonic uniform surrounding flow. Behind the shock wave, the streamlines indicate the existence of a reversed flow region. At $t = 3.0$, the recirculating bubble-flow grows in size and moves upstream. The formation of a two-bubble cell is clear. The Mach contours show that the shock also moves upstream ahead of the two-bubble cell. At $t = 4.0$ and $5.0$, the shock wave and the two-bubble cell still move upstream while the bubbles are growing in size. The bubbles reach their maximum size at $t = 5.0$. The snapshots of the solution for $t \geq 10.0$ show that the bubble-shock system is quasi-steady and oscillating around a mean axial location. The maximum change in the bubble size is less than 10%. The axial velocity recovers its supersonic values at the exit boundary, and hence the use of extrapolation boundary conditions is justified.

**I.3 Grid Type 2:** This grid consists of 145×61×61 points in the axial and cross-flow directions, respectively. The grid points are redistributed to obtain better solution of the vortex core and the vortex-shock interaction region. The minimum grid size is 0.024 in the y and z directions and 0.014 in the axial direction. Figure 5 shows a side view and a cross-flow plane of the grid.

In Fig. 6, snapshots of the streamlines and total Mach contours on a horizontal plane passing through the computational domain axis are given at selected dimensionless times. At $t = 2.0$, a two-bubble cell is formed behind a sharply oblique conical shock. The bubbles sizes are larger than those of Grid type 1 at the same time level. At $t = 3.0$, the two-bubble cell grows in time and moves upstream along with the shock wave. Again, the bubbles are larger in size and closer to the inflow boundary than those of Grid type 1. Moreover, it is interesting to notice that the bubbles are longer in the axial direction than their length in the lateral direction in comparison with those of Grid type 1. It should be noted here that the number of grid points around the computational domain axis for the present grid is larger than those of Grid type 1 and the number of grid points in the axial direction is less than those of Grid type 1. At $t = 4.0$, the two-bubble cell moves downstream, another small bubble appears and the shock splits into two shocks; a weak shock which is followed by a strong shock surrounding the bubbles. At $t = 5.0$, the shock shape changes to become more oblique and the two-bubble cell grows slightly. As the solution is advanced in time, it is observed that continuous changes in the bubbles size, shape and location occur with larger amplitudes than those of Grid type 1. For $t \geq 10.0$, the bubbles show highly unsteady flow with an oscillating shock wave.

**I.4 Grid Type 3:** In this grid, the number of grid points is kept the same as that of Grid type 2. The grid points are redistributed in the axial and cross-flow directions. In the axial directions, 90 grid points are used in the range of $x = 0$ to $2.0$, in comparison with 71 grid points in Grid type 2. The minimum cell size in the axial direction is 0.0084. In the cross-flow plane, the grid points are redistributed such that the grid aspect ratio does not exceed 4.0. Figure 7 shows the grid and Fig. 8 shows the results.

The results show that at $t = 2.0$, a small bubble is captured off the computational domain axis. Later on, at $t = 4.0$, the small bubble disappears. Another bubble is captured at $t = 6.0$ and it also disappears later on. For $t > 8.0$, no more bubbles are captured. A strong, almost-normal shock is captured around the axis. It is located a little more downstream from the inflow section in comparison with that of Grid type 2.

Next, it is decided to use the quasi-axisymmetric initial profiles (Fig. 2) which have higher swirl ratio than those of the asymmetric initial profiles (Fig. 1). The results are shown in Fig. 9. The results show the formation of a small two-bubble cell. The bubbles shape changes slowly with time and the shock oscillates with very small amplitude around a mean position which is a little more downstream than that of the previous case and the case of Grid type 2.

**I.5 Grid Type 4:** A circular grid consisting of 145×61×49 points in the axial, radial and circular directions, respectively, is used. The grid points are clustered around the axis for a good resolution of the vortex core and around r = 1 for good resolution of the shear layer between the swirling jet and the uniform freestream flow. In the axial direction, the grid points are distributed as those of Grid type 3. The circular grid has the advantage of offering better resolution near the axis, where it is needed. Moreover, with the circular grids, the number of grid points along a diameter in the cross-flow plane is doubled without increasing the total number of grid points, in comparison with the previous grids of square-section cross-flow planes. Figure 10 shows the circular grid.

As in the case of Grid type 3, two sets of initial profiles; namely the quasi-axisymmetric and asymmetric profiles, are used with this grid. As with Grid type 3 and for the asymmetric initial profiles, a small bubble is formed behind the shock and disappears after a few time steps.

Figure 11 shows snapshots of the streamlines and Mach number contours for the quasi-axisymmetric initial profiles. The results show the formation of a multi-bubble vortex breakdown behind the central strong part of the shock system. A two-bubble cell is then established and persists for the rest of the computational time. The relative size of the two bubbles is continuously changing and the global picture is looked at as a quasi-steady one.

This study exclusively shows why it was very difficult to see any vortex-breakdown bubbles as was reported in Ref. 16. It is understood now in view of the results of the four grids that the size of the bubbles are either very small to be seen for quasi-axisymmetric initial profiles or they are transient bubbles for asymmetric initial profiles.

## II. Three-Dimensional Supersonic Vortex Breakdown in a Configured Duct

The computational domain consists of a configured circular duct with a total length of 2.9 dimensionless units, where the duct radius is used as a characteristic length. The duct consists of a constant diameter cylindrical portion of radius one followed by a divergent portion which is intended to stabilize the formed shock wave, a constant cylindrical part and finally a convergent-divergent nozzle which is intended to accelerate the exhaust flow to supersonic speeds. The grid consists of 200×51×49 grid points in the axial, radial and circumferential directions, respectively. The grid points are clustered near the inlet section in the axial direction for a good resolution of the shock and the shock/vortex interaction region, and in the cross-flow plane around the duct axis for a good resolution of the vortex core. The gird points are also clustered near the duct walls for a good resolution of the boundary layer. The minimum cell size is 0.002. Figure 12 shows the computational grid. The freestream conditions correspond to $M_\infty = 1.75$ and Reynolds number of $10^5$.

**II.1 Boundary and Initial Conditions:** The initial profile for the tangential velocity is given by

$$\frac{v}{U_\infty} = \frac{k_\epsilon}{r}\left[1 - \exp\left(-\frac{r^2}{r_m^2}\right)\right] \qquad (1)$$

where $U_\infty = 1.74$, $r_m = 0.2$ and $k_\epsilon = 0.1$. The maximum $\frac{v}{U_\infty}$, swirl ratio $\beta$, is at $r = 0.224$ and its value is kept at 0.32. The radial velocity, $w$, at the initial station is set equal to zero and the radial momentum equation is integrated to obtain the initial pressure profile. Finally, the density $\rho$ is obtained from the definition of the speed of sound for the inlet flow. With these compatible set of profiles, the computations are carried out accurately in time with $\Delta t = 0.0025$ for two computational applications. The duct-wall boundary conditions follow the typical Navier-Stokes solid-boundary conditions for the first case. For the second case, inviscid duct-wall boundary conditions are used to reduce the effect of the boundary-layer separation on the vortex breakdown process. The downstream exit-boundary conditions are obtained by extrapolating the flowfield components from the interior cell centers at the exit.

The initial conditions correspond to stagnation conditions throughout the interior computational domain.

**II.2 Viscous Duct-Wall Boundary Conditions:** Figure 13 shows snapshots of the solution at selected time levels. At t = 2.0, a small recirculating region is formed behind the strong normal part of the shock wave. Two stagnation points are recognized along the duct axis. The total Mach number contours show the position of the shock front near the inflow section and the position of the recirculation zone behind the shock wave. As the computations is advanced in time, the bubble size grows in the axial and radial directions and the shock-bubble system moves downstream. At t = 3.5, it is noticed that the bubble size grows and the shock wave is deformed accordingly. The solution is quasi-axisymmetric as shown by the streamlines and Mach number contours. Starting at t = 4.0, the bubble size grows in the lateral direction, moves upstream towards the inflow boundary pushing the shock wave upstream. Small flow asymmetry is also noticed. For t ≥ 5.5, another phase of the solution history develops, where a reversed normal shock is formed inside the vortex-breakdown bubble (see Mach contours at t = 6.0). The normal shock wave turns the reversed flow to subsonic. As the computations advance in time, the bubble system starts to move downstream towards the duct exit with a new recirculating region formed behind the shock wave. The flow becomes quite asymmetric.

At t = 11.5, as the computations advance in time, some of the features noticed experimentally for incompressible vortex flows in pipes could be recognized; e.g., the asymmetric vortex breakdown seen at t = 11.5. The streamlines clearly show the spiral-type of vortex breakdown and the asymmetric shedding of the vortex breakdown bubbles. It should be noted here that such phenomenon was not captured using the quasi-axisymmetric assumption in Ref. 11 by the present authors. The shedding of the vortex-breakdown bubbles continues as new bubble systems were formed behind the shock wave. At t = 16.5, the shedding of two asymmetric bubbles can be seen and a two-bubble system is formed upstream along with a very small recirculating region just downstream of the central part of the shock wave. At t = 19, it is observed that two bubbles merge together while they are convected and shed.

An important parameter affecting the flow in the duct is the interaction of the shock with the boundary-layer flow on the duct wall. This causes the separation of the wall boundary layer, as can be seen at t = 31, 42 and 43. The Mach number contours show the separation of the boundary as a result of the interaction with the shock wave, and the streamlines show the reduction in the vortex-breakdown-bubble size as a result of the boundary-layer thickening. The shedding of the inclined vortex rings shown at t = 33 is similar to the spiral type of vortex breakdown, where the upper part of the vortex rings rotates in the clockwise direction and the lower part rotates in the opposite direction. A new vortex ring is formed behind the shock while the spiral-like system is moving downstream.

As the solution is advanced in time, the size of the breakdown region is reduced in the radial direction as a result of the boundary-layer thickening. An interesting breakdown mode is shown at t = 38.5 where a bubble-type vortex breakdown followed by a spiral-type is formed downstream of the shock wave. This phenomenon was observed in the experimental studies of Sarpkaya[13] and has never been captured computationally.

The reduction of the breakdown-region size continues with the advance in the time as can be seen at t = 41, 42 and 44. At t = 46, no recirculation zone is observed and the vortex-breakdown system is dissipated totally. It is also observed that the shock-wave system moves continuously in the downstream direction as of t > 31.

**II.3 Inviscid Duct-Wall Boundary Conditions:** The effect of the shock/boundary-layer interaction at the duct wall is further investigated by treating the duct wall as an inviscid wall. At t = 43.0, inviscid-wall boundary conditions are applied at the duct wall with all the other boundary conditions remaining the same. Samples of the results are shown in Fig. 14. At t = 43.5, the vortex-breakdown bubbles are recovered and the shock wave becomes normal to the duct wall. The shedding of the vortex rings continues as the solution is advanced in time as can be seen at t = 45.5, where the vortex rings are recognized. It is also noticed that the vortex-breakdown bubble size starts to increase in the radial direction. Further increase in the breakdown-region size is noticed at t = 47. It is also noticed that the position of the shock wave with respect to the duct inlet is fixed while the shape of the central part is continuously changing according to the shape of the bubbles behind the shock. The shedding of the vortex-breakdown bubbles continues in an asymmetric form as can be seen at t = 63, 69 and 72.5. It is interesting to notice that the vortex-breakdown system survives and is not dissipated as in the case of viscous duct wall. The computations is advanced until t = 75 without any sign of dissipation of the vortex-breakdown-bubbles. It is concluded that the disturbances caused by the wall boundary-layer separation are the reason behind the disappearance of the vortex-breakdown system in the case of viscous duct wall. This might be caused by the pressure gradients resulting from the change in the vortex-core outer boundaries.

Sarpkaya[13] noticed that the boundary-layer separation and reversed flow occurred on the tube wall in the case of a swirling incompressible flow in a divergent tube. He suggested that the bubble pressure gradient caused by the tube divergence and that caused by the vortex breakdown are the reasons behind the separation. He concluded that the viscous effects on vortex breakdown in tubes are very significant and that, because of the flow separation, a better simulation of the vortex breakdown is not likely to emerge from solving numerically the full Navier-Stokes equations even if the problems of numerical instability were to be solved. In the case of supersonic vortex breakdown, the problem is much more involved because of the shock/boundary layer interaction and the assumption of inviscid walls seems to isolate the wall viscous effects.

## CONCLUDING REMARKS

Three-dimensional, supersonic vortex-breakdown flows in bound and unbound domains are simulated computationally using the time-accurate solution of the unsteady, compressible, laminar, full Navier-Stokes equations. Two main vortex-breakdown applications are considered in this paper. The first application is for a supersonic swirling jet issued in a supersonic uniform flow at a lower Mach number. This flow case was considered earlier by Metwally and his co-workers in Ref. 16, where it was reported that no vortex breakdown bubble was seen behind the shock-wave system. A systematic computational investigation was carried out using four types of grids which ranged from coarse- to find-grid distributions and from rectangular to circular grid lines in the cross-flow planes. It has been shown that the coarse grid produces large vortex bubbles and the fine girds produce either transient small vortex bubbles or quasi-steady small vortex bubbles. Using the fine-grid results as the ones closely representing the experimental flow case, it is understood why Metwally, et al.[16] were not able to see any vortex-breakdown bubble. The bubbles were either small or small and transient. Moreover, this study shows why previous investigators[17,18] of incompressible vortex-breakdown flows were able to produce numerical results using coarse grids (coarser than the coarse grid used in the present paper) at low Reynolds numbers which were comparable to experimental results at high Reynolds numbers. It is now understood that coarse grids have made it possible to simulate experimental results at high Reynolds number.

The second application is for a supersonic swirling flow in a configured circular duct. Here, the duct-wall boundary conditions are used once for a viscous wall and another for an inviscid wall. With the viscous-wall boundary conditions, it has been observed that the vortex breakdown is transient and it has been dissipated by the effect of separated flow from the duct-wall boundary layer. However, during the transient formation of vortex-breakdown flows, both the bubble-type and spiral-type vortex breakdown are captured. Spiral-type vortex breakdown was not captured in Ref. 11 by the present authors due to the quasi-axisymmetric assumption used. With the inviscid duct-wall boundary conditions, the vortex breakdown is persistent and does not dissipate. The three-dimensional relieving effect on the vortex breakdown modes is apparent from the present results when they are compared with those of Ref. 11, where the quasi-axisymmetric assumption has been used.

## ACKNOWLEDGEMENT

For the first two authors, this research work has been supported by the NASA Langley Research Center under Grant No. NAG-1-994. The authors would like to acknowledge the computational resources which were provided by the NAS facilities at the NASA Ames Research Center.

## REFERENCES

1. Elsenaar, A., Hjelmberg, L., Bütefisch, K. and Bannink, W. J., "The International Vortex Flow Experiment," AGARD-CP-437, Lisbon, Portugal, May 1988, Vol. 1, pp. 9.1–9.23.
2. Erickson, G. E., "Wind Tunnel Investigation of the Interaction and Breakdown Characteristics of Slender-Wing Vortices at Subsonic, Transonic and Supersonic Speeds," NASA Tech. Paper 3114, November 1991.
3. Copening, G. and Anderson, J., "Numerical Solutions to Three-Dimensional Shock/Vortex Interaction at Hypersonic Speeds," AIAA 89–0674, January 1989.
4. Delery, J., Horowitz, E., Leuchter, O. and Solignac, J. L., "Fundamental Studies of Vortex Flows," La Recherche Aerospatiale, No. 1984–2, 1984, pp. 1–24.
5. Cutler, A. D. and Levey, B. S., "Vortex Breakdown in a Supersonic Jet," AIAA 91–1815, June 1991.
6. Rhode, D. L., Lilley, D. G. and McLaughlin, D. K., "On the Prediction of Swirling Flowfields Found in Axisymmetric Combustor Geometries," Transactions of ASME, Vol. 104, September 1982, pp. 378–384.
7. Altegeld, H., Jones, W. P. and Wilhelmi, J., "Velocity Measurements in a Confined Swirl Driven Recirculating Flow," Experiments in Fluids, Springer Verlag, Vol. 1, 1983, pp. 73–78.
8. Liu, C. H., Krause, E. and Menne, S., "Admissible Upstream Conditions for Slender Compressible Vortices," AIAA 86–1093, July 1986.
9. Kandil, O. A. and Kandil, H. A., "Computation of Compressible Quasi-Axisymmetric Slender Vortex Flow and Breakdown," IMACS 1st International Conference on Computational Physics, University of Colorado, Boulder, June 1990, pp. 46–51. Also in Computer Physics Communications, Vol. 65, North-Holland, March 1991, pp. 164–172.
10. Kandil, O. A., Kandil, H. A. and Liu, C. H., "Computation of Steady and Unsteady Compressible Quasi-Axisymmetric Vortex Flow and Breakdown," AIAA 91–0752, January 1991.
11. Kandil, O. A., Kandil, H. A. and Liu, C. H., "Supersonic Quasi-Axisymmetric Vortex Breakdown," AIAA 91–3311–CP, September 1991, pp. 851–863.
12. Kandil, O. A., Kandil, H. A. and Liu, C. H, "Critical Effects of Downstream Boundary Conditions on Vortex Breakdown," AIAA 92–2601–CP, June 1992, pp. 12–26.
13. Sarpkaya, T., "Effect of the Adverse Pressure Gradient on Vortex Breakdown," AIAA Journal, Vol. 12, No. 5, May 1974, pp. 602–607.
14. Escudier, M. P. and Zender, N., "Vortex Flow Regimes," Journal of Fluid Mechanics, Vol. 115, 1982, pp. 105–122.
15. Leibovich, S., "Vortex Stability and Breakdown: Survey and Extension," AIAA Journal, Vol. 22, No. 9, September 1984, pp. 1192–1206.
16. Metwally, O., Settles, G. and Horstman, C., "An Experimental Study of Shock Wave/Vortex Interaction," AIAA 89–0082, January 1989.
17. Spall, R. E., Gatski, T. B. and Ash, R. L., "The Structure and Dynamics of Bubble-Type Vortex Breakdown," Proc. R. Soc., London, A429, 1990, pp. 613–637.
18. Breuer, M. and Hänel, D., "Solution of the 3-D Incompressible Navier-Stokes Equations for the Simulation of Vortex Breakdown," Eight GAMM Conference, Delft, Netherlands, September 27–29, 1989.

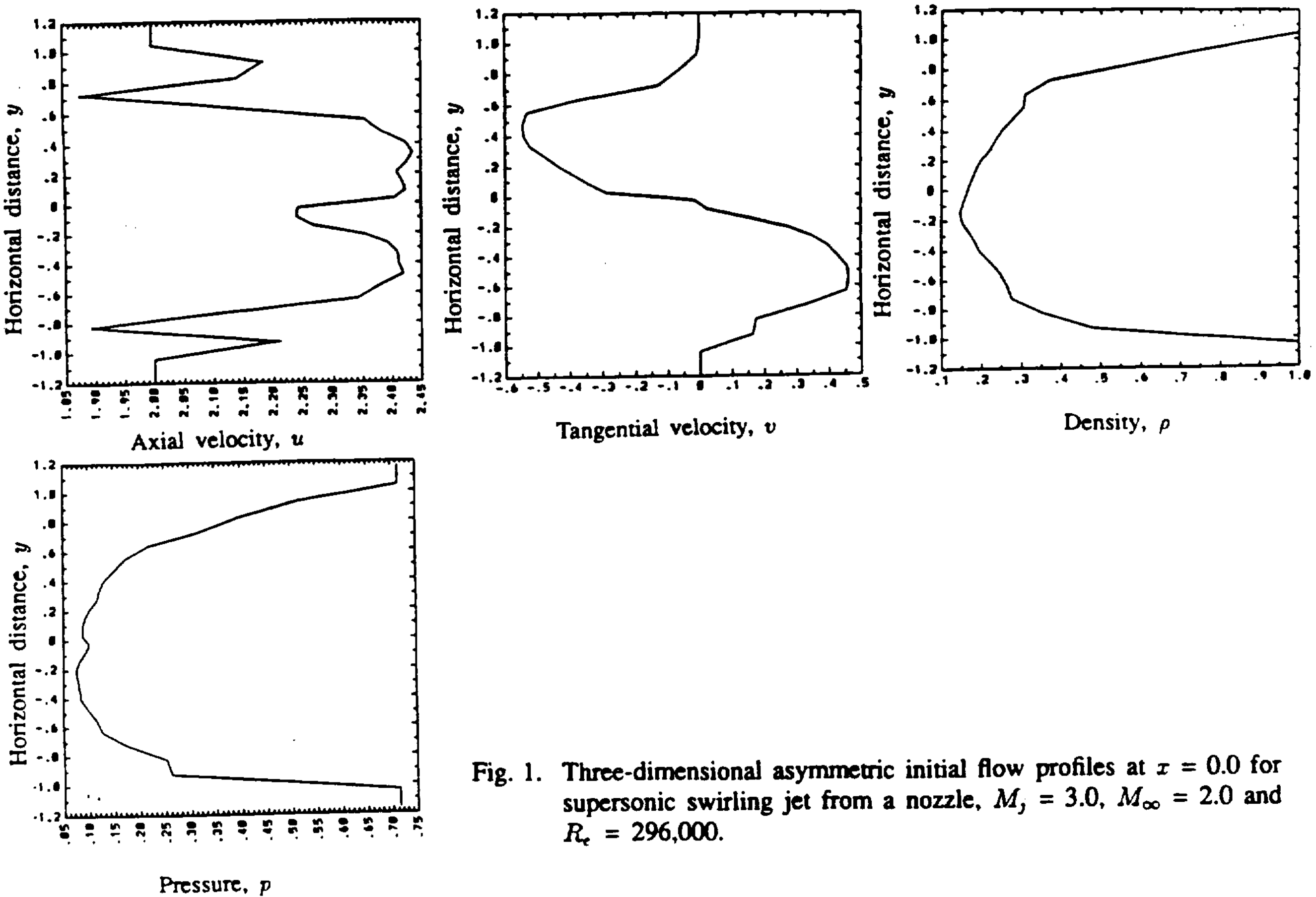

Fig. 1. Three-dimensional asymmetric initial flow profiles at $x = 0.0$ for supersonic swirling jet from a nozzle, $M_j = 3.0$, $M_\infty = 2.0$ and $R_e = 296{,}000$.

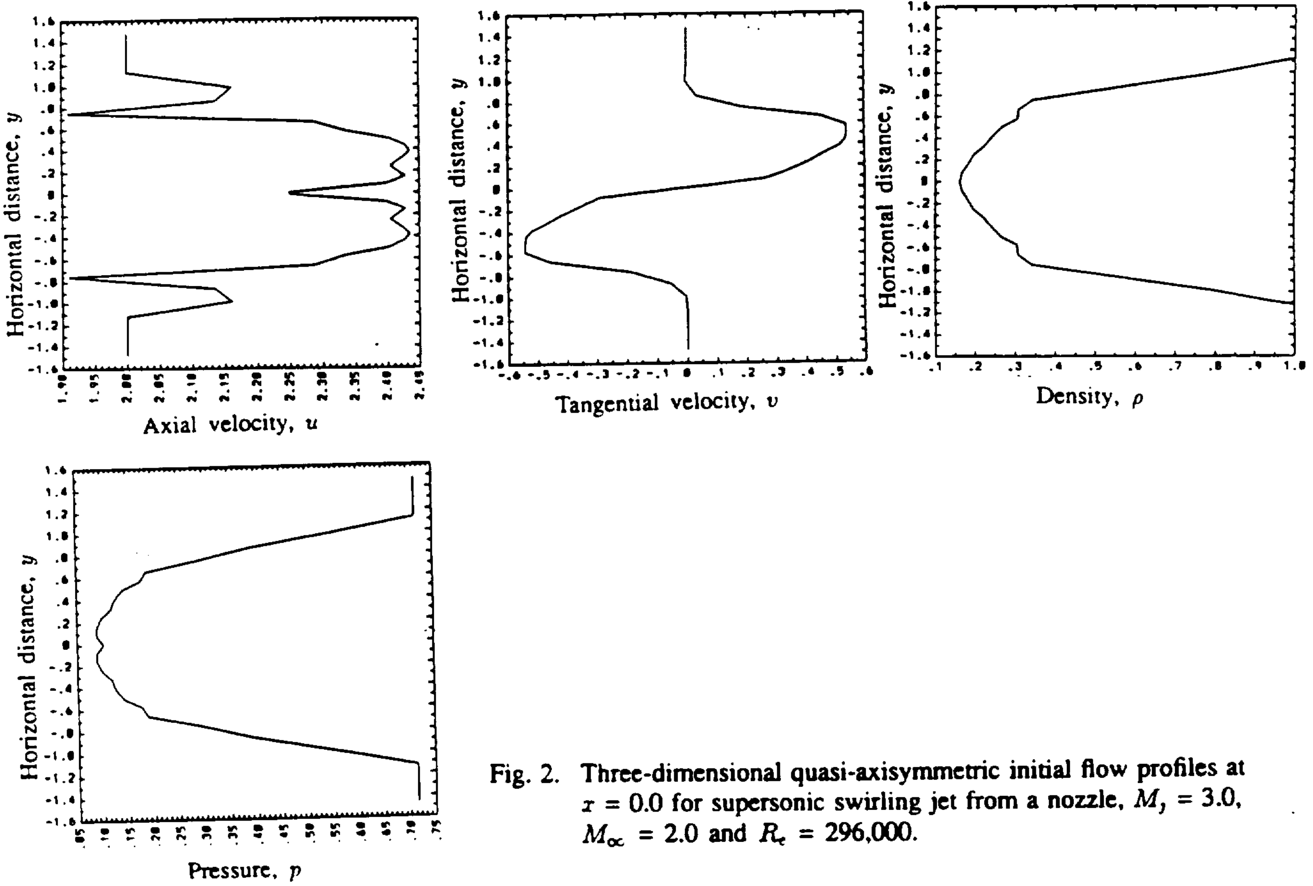

Fig. 2. Three-dimensional quasi-axisymmetric initial flow profiles at $x = 0.0$ for supersonic swirling jet from a nozzle, $M_j = 3.0$, $M_\infty = 2.0$ and $R_e = 296{,}000$.

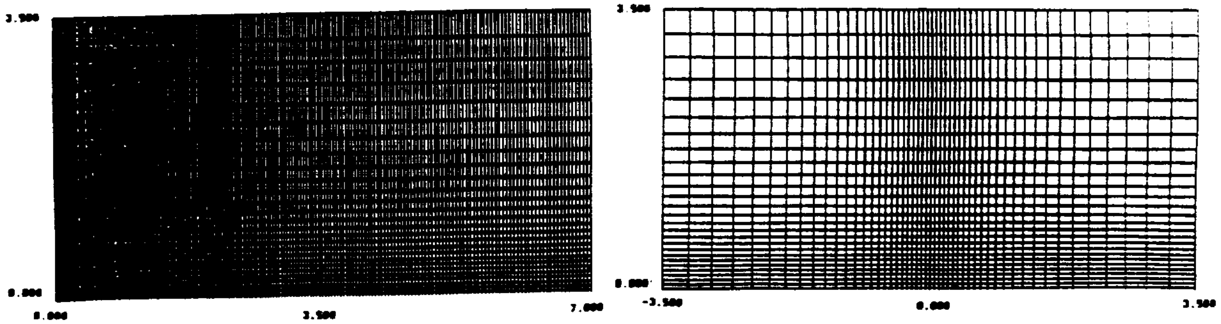
3.500
0.000
0.000
3.500
7.000
3.500
0.000
-3.500
0.000
3.500

Fig. 3. Grid type 1 (rectangular coarse grid in the cross-flow plane), 210×51×51 grid points in the axial and cross-flow plane, respectively.

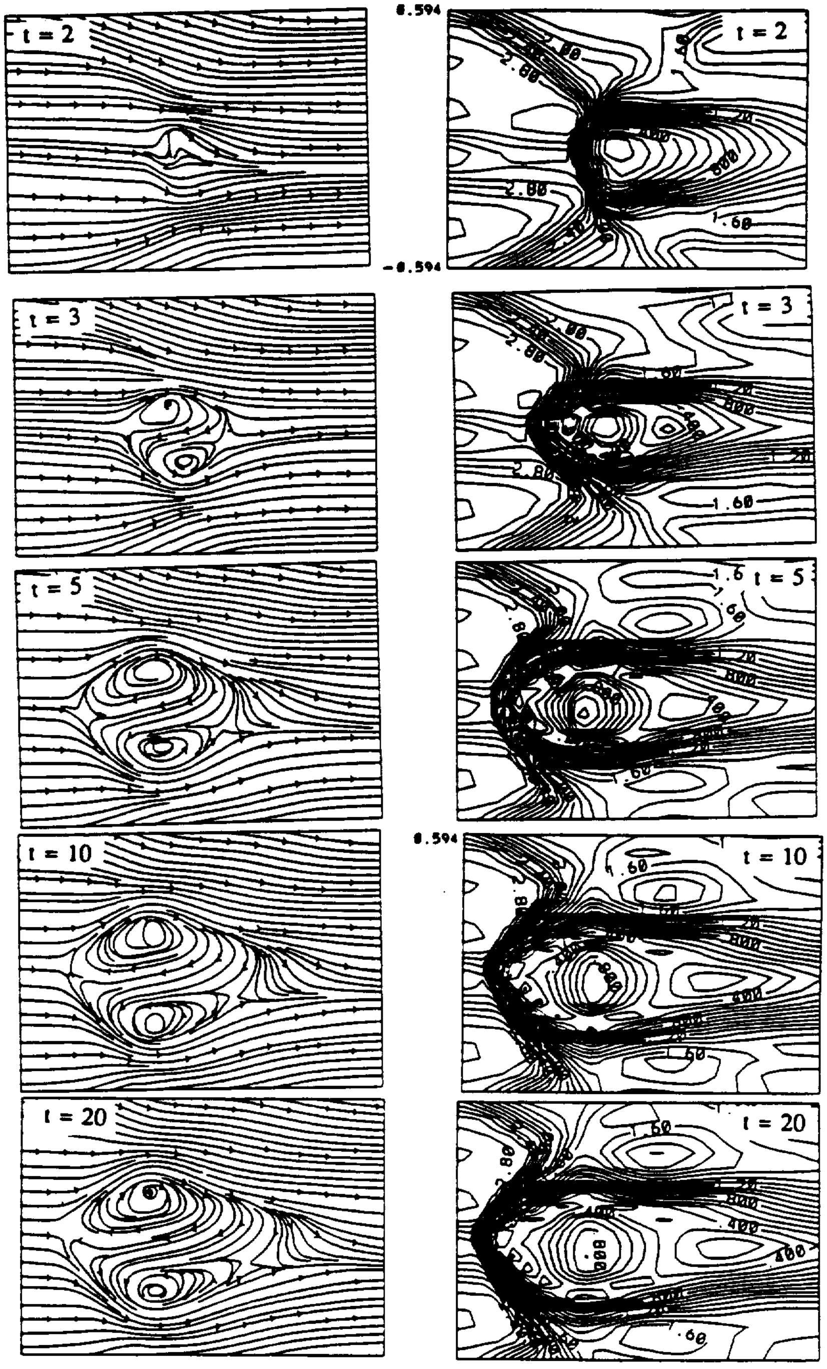

Fig. 4. Streamlines and Mach contours in a horizontal plane for a supersonic swirling jet using Grid type 1, $M_j$ = 3.0, $M_\infty$ = 2.0 and $R_e$ = 296,000.

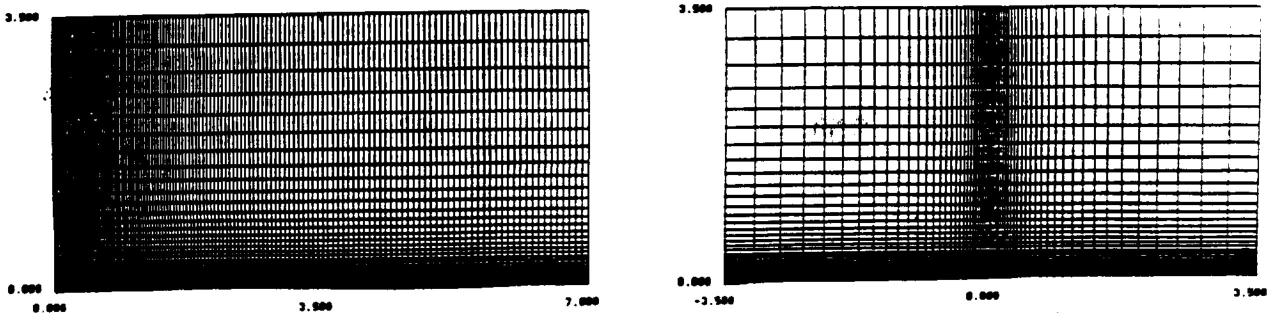
3.500
0.000
0.000
3.500
7.000
3.500
0.000
-3.500
0.000
3.500

Fig. 5. Grid type 2 (rectangular fine gird in the cross-flow plane), 145×61×61 grid points in the axial and cross-flow plane, respectively.

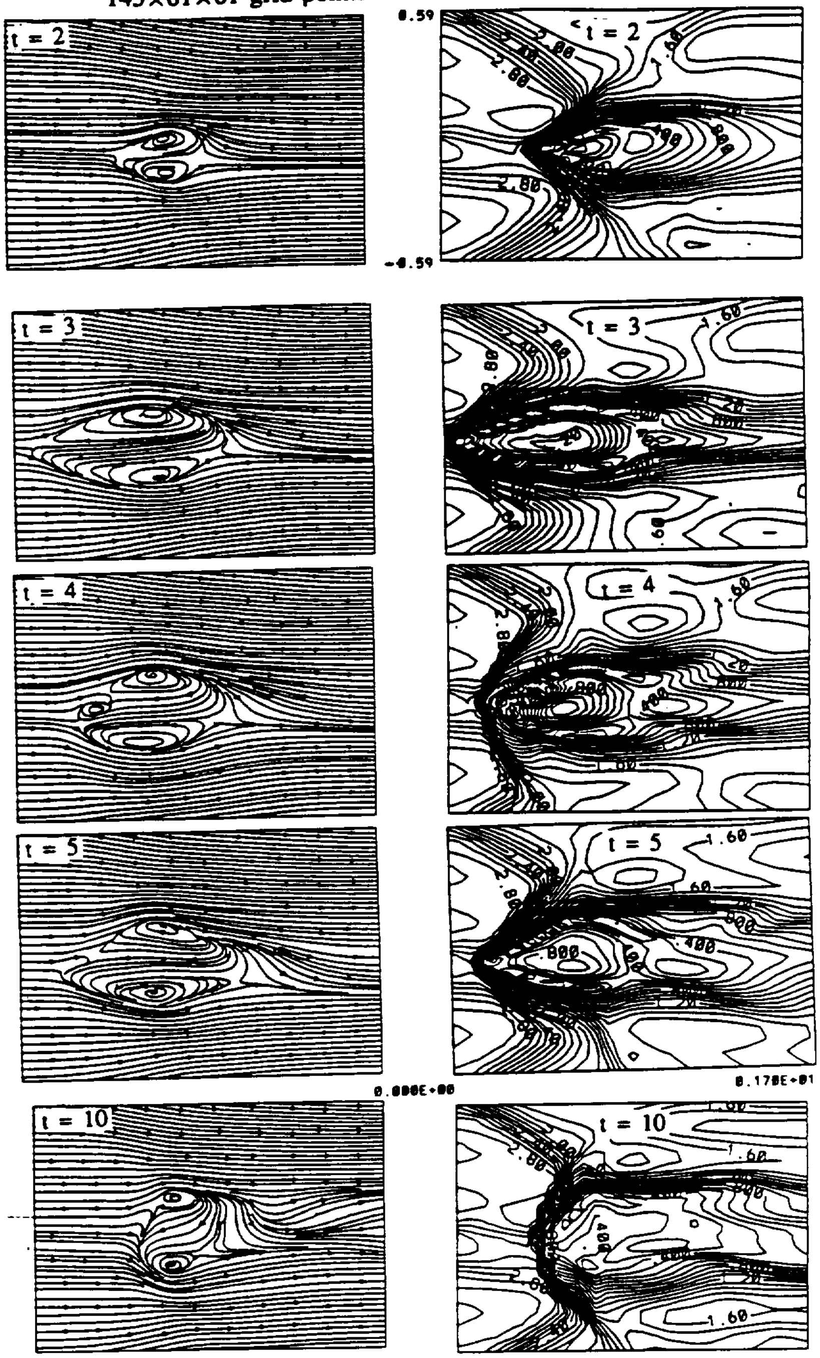

Fig. 6. Streamlines and Mach contours in a horizontal plane for a supersonic swirling jet using Grid type 2, $M_j$ = 3.0, $M_\infty$ = 2.0 and $R_e$ = 296.000.

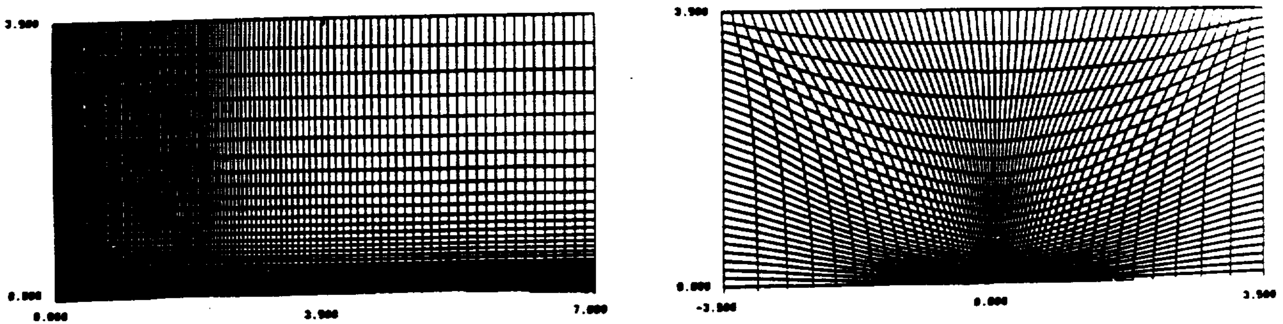
3.500
0.000
0.000
3.500
7.000
3.500
0.000
-3.500
0.000
3.500

Fig. 7. Grid type 3 (rectangular fine grid), 145×61×61 grid points in the axial and cross-flow plane, respectively.

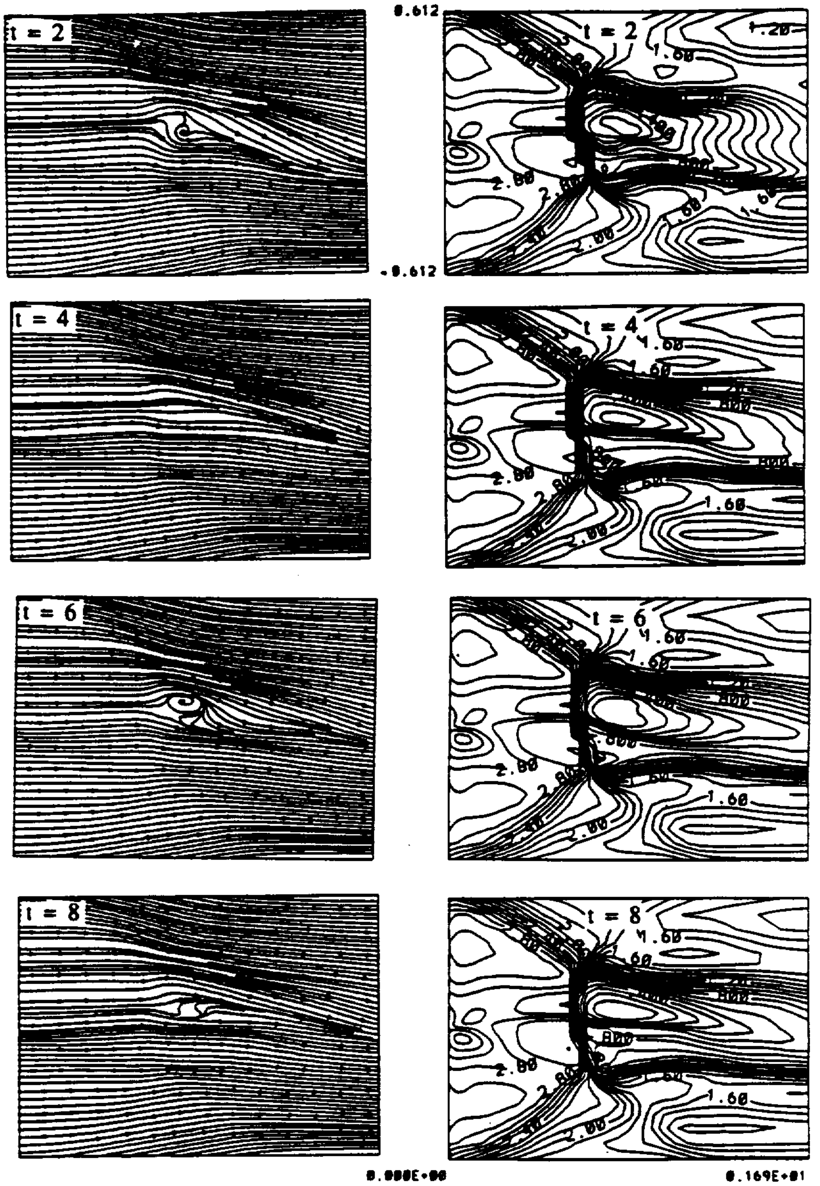

Fig. 8. Streamlines and Mach contours in a horizontal plane for a supersonic swirling jet using Grid type 3 with asymmetric initial flow profiles, $M_j$ = 3.0, $M_\infty$ = 2.0 and $R_e$ = 296,000.

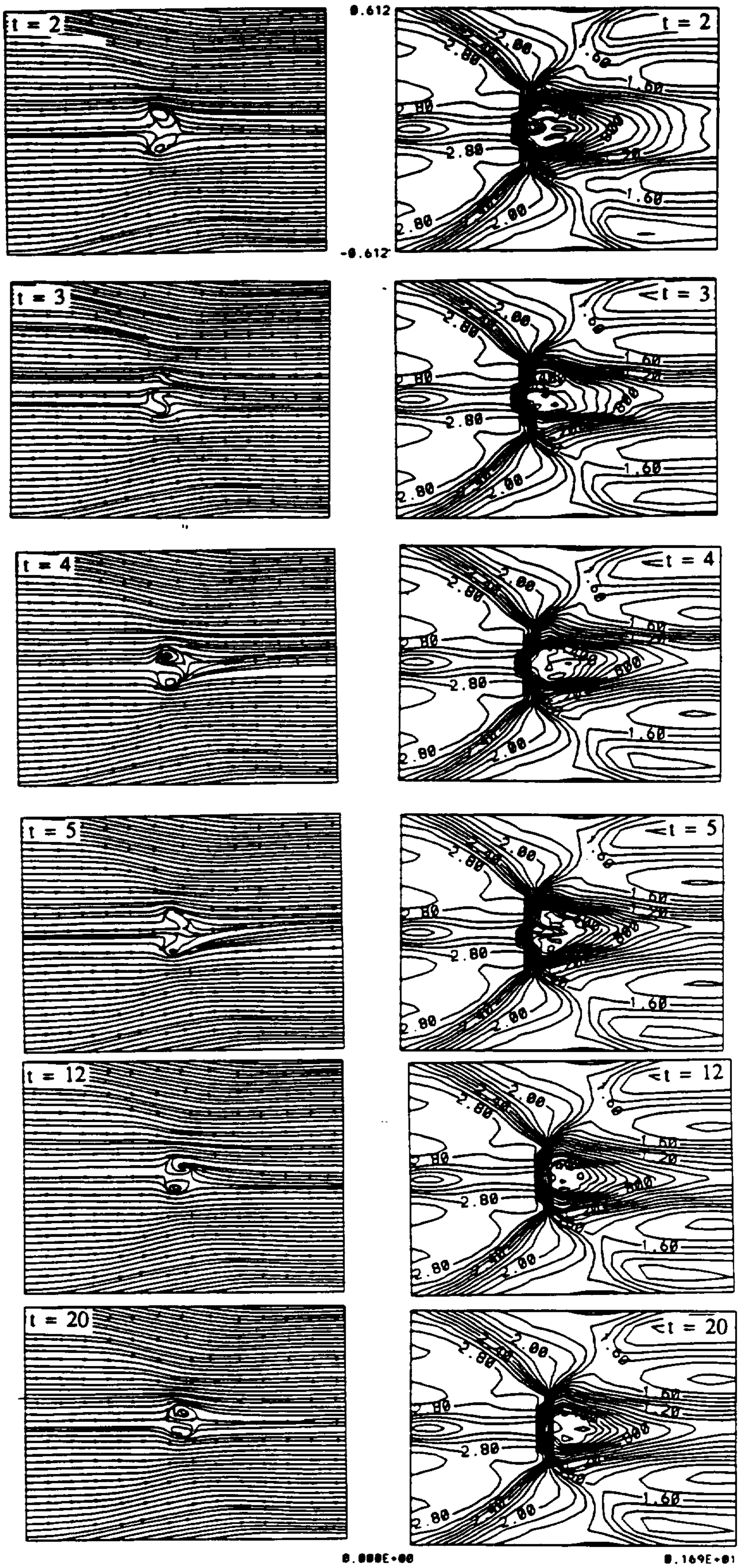

Fig. 9. Streamlines and Mach contours in a horizontal plane for a supersonic swirling jet using Grid type 3 with quasi-symmetric initial flow profiles, $M_j$ = 3.0, $M_\infty$ = 2.0 and $R_e$ = 296,000.

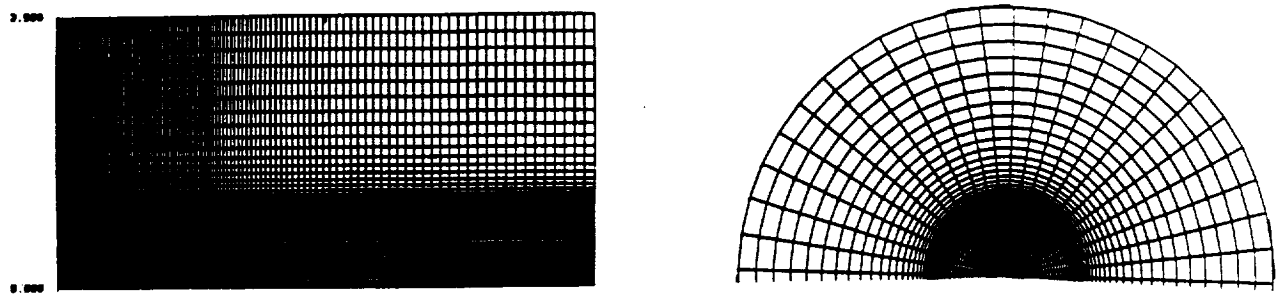

Fig. 10. Grid type 4 (circular fine grid), 145×61×61 grid points in the axial and cross-flow plane, respectively.

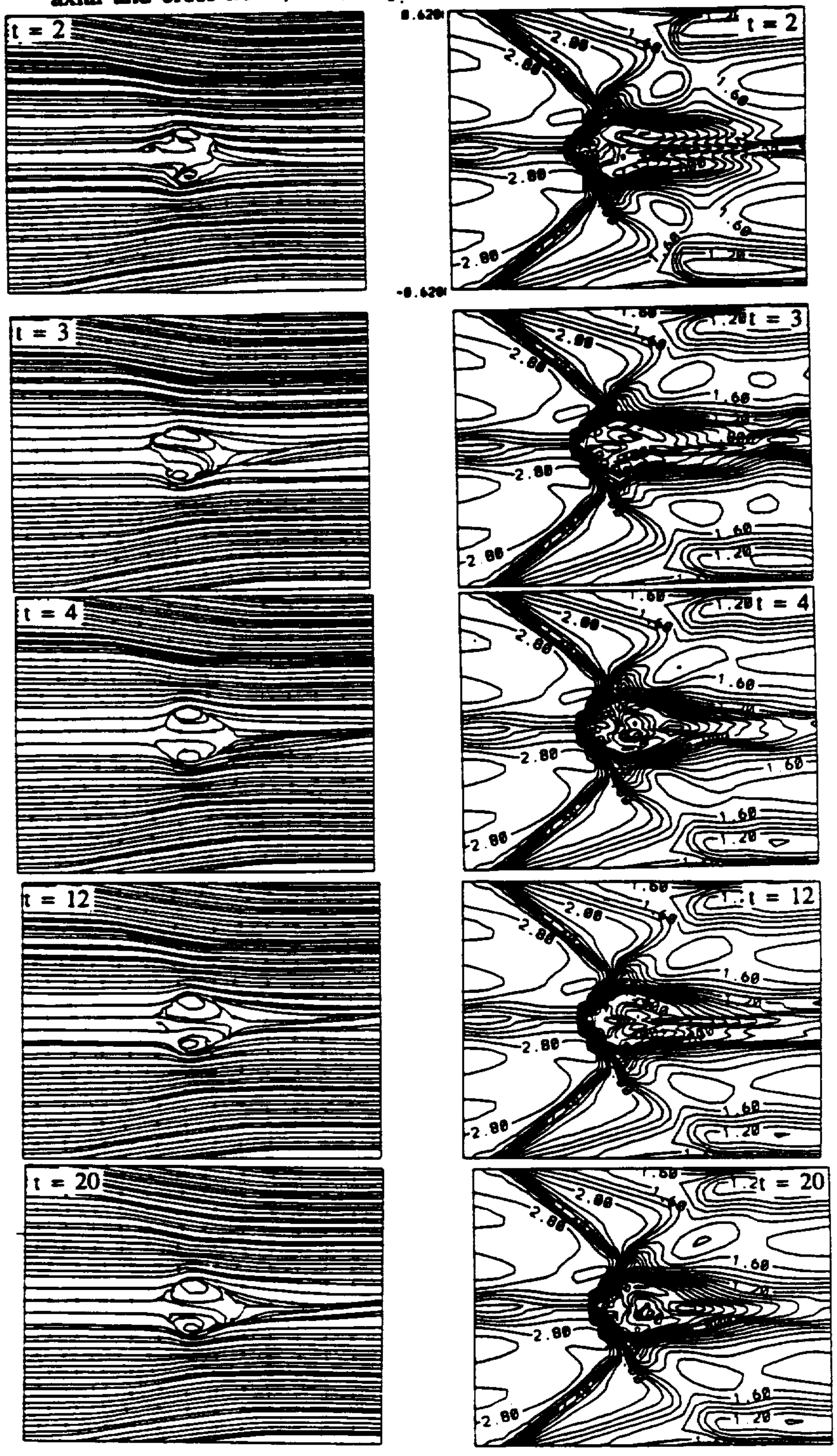

Fig. 11. Streamlines and Mach contours in a horizontal plane for a supersonic swirling jet using Grid type 4, $M_j$ = 3.0, $M_\infty$ = 2.0 and $R_e$ = 296,000.

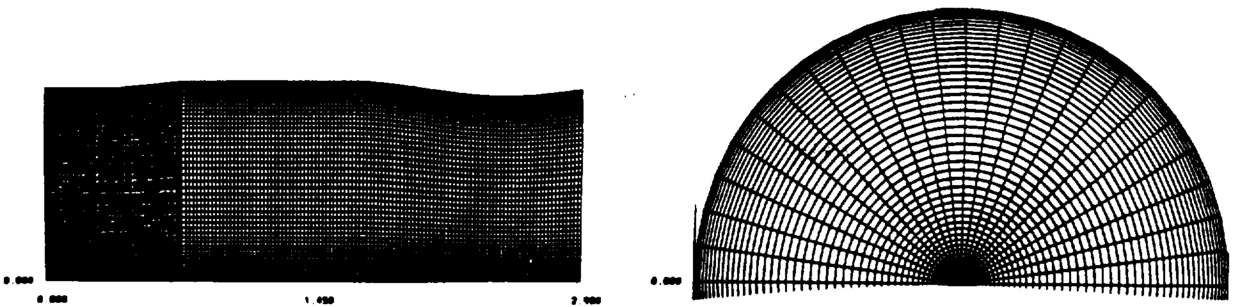
0.000
0.000
1.400
2.800
0.000

Fig. 12. Configured-circular-duct computational domain and grid, 200×51×49 grid points in the axial, radial and circular directions, respectively.

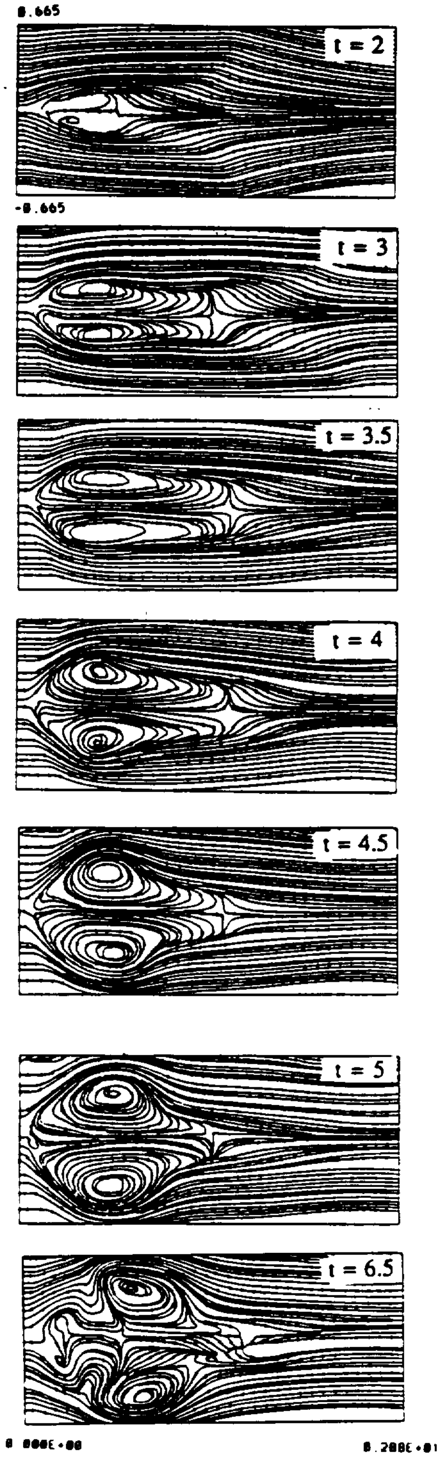

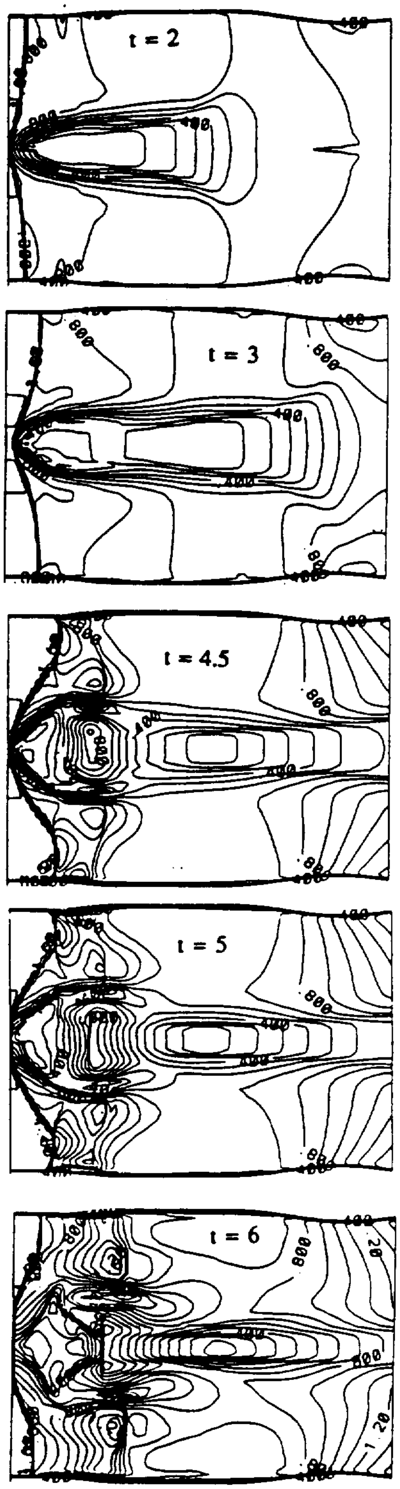

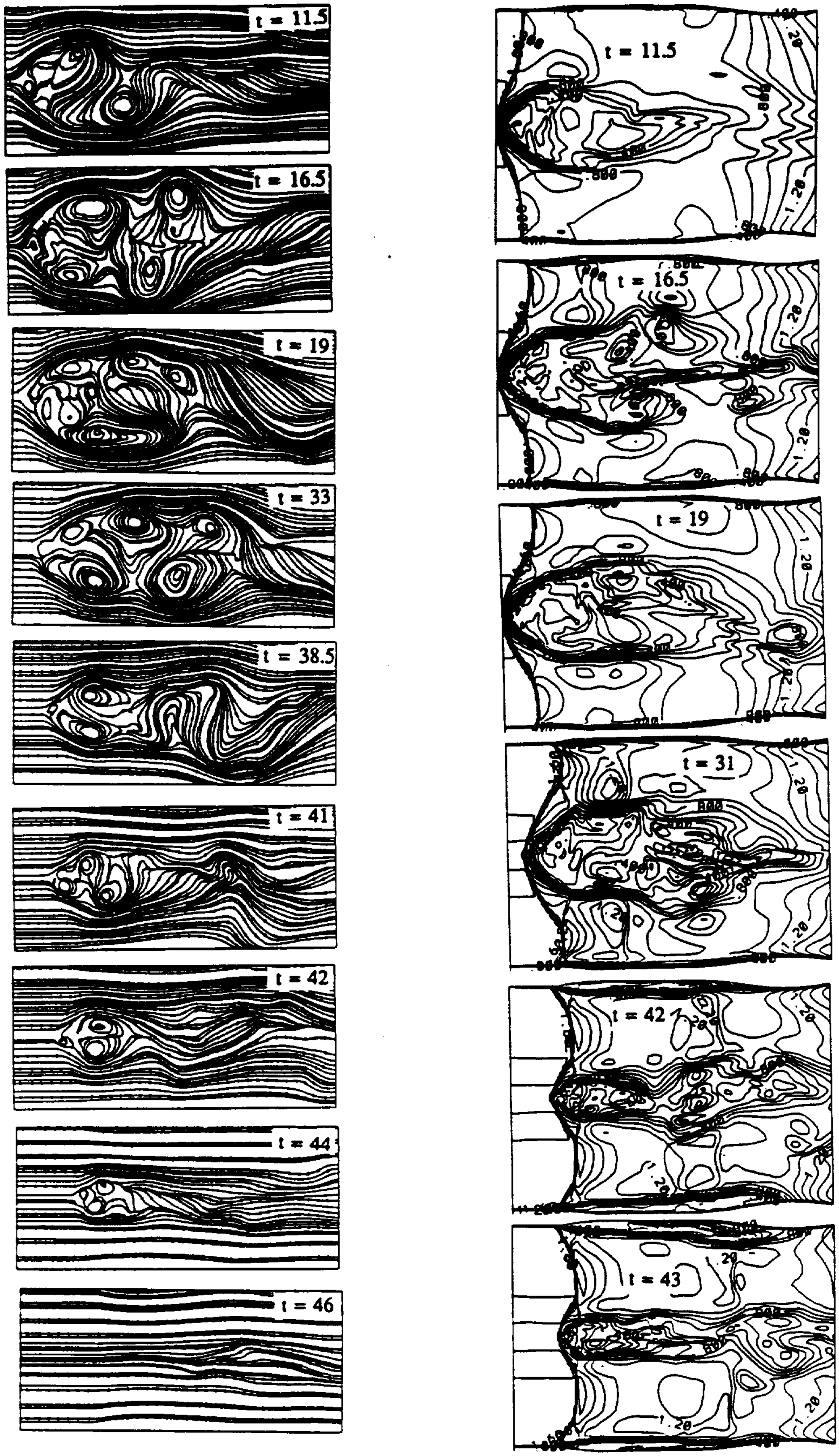

Fig. 13. Streamlines and Mach contours in a horizontal plane for a supersonic swirling flow in a circular duct, $M_\infty$ = 1.75, $\beta$ = 0.32 and $R_e$ = 100,000, viscous wall.

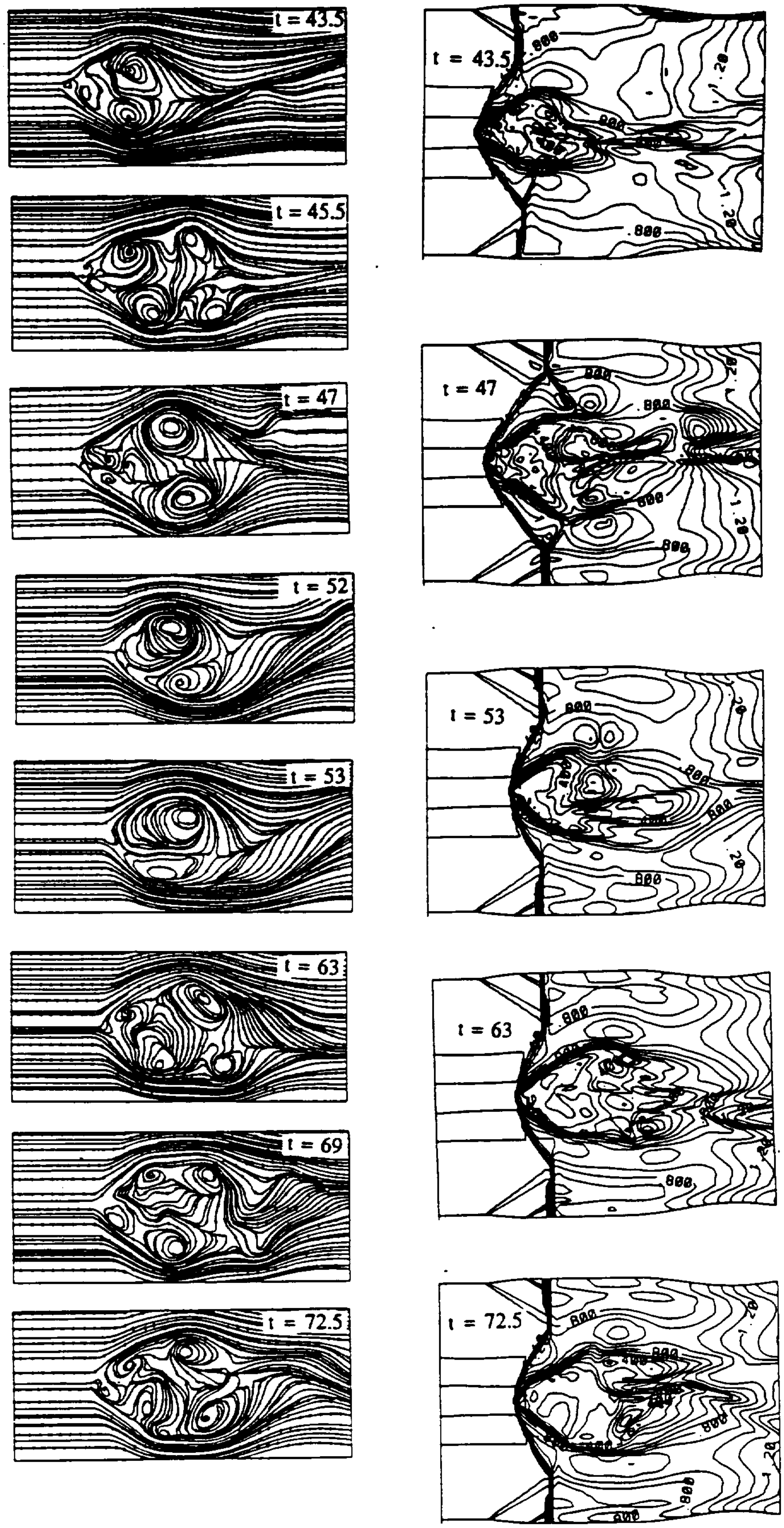

Fig. 14. Streamlines and Mach contours in a horizontal plane for a supersonic swirling flow in a circular duct, $M_\infty = 1.75$, $\beta = 0.32$ and $R_e = 100{,}000$, inviscid wall.

*Computers Fluids* Vol. 22, No. 4/5, pp. 607–622, 1993
Printed in Great Britain

0045-7930/93 $6.00 + 0.00
Pergamon Press Ltd

N94-14237

56P

# NUMERICAL SIMULATION AND PHYSICAL ASPECTS OF SUPERSONIC VORTEX BREAKDOWN

C. H. LIU,[1] O. A. KANDIL[2] and H. A. KANDIL[2]

[1]Computational Aerodynamics Branch, NASA Langley Research Center, MS 128, Hampton, VA 23681-0001, U.S.A.

[2]Department of Mechanical Engineering and Mechanics, Old Dominion University, Norfolk, VA 23529-0247, U.S.A.

*(Received 11 February 1993)*

**Abstract**—Existing numerical simulations and physical aspects of subsonic and supersonic vortex-breakdown modes are reviewed. The solution to the problem of supersonic vortex breakdown is emphasized in this paper and carried out with the full Navier–Stokes equations for compressible flows. Numerical simulations of vortex-breakdown modes are presented in bounded and unbounded domains. The effects of different types of downstream-exit boundary conditions are studied and discussed.

## INTRODUCTION

At sufficiently high angles of attack, vortex breakdown has been observed along the primary leading-edge vortex cores of a delta wing. Two distinct forms of vortex breakdown have been documented experimentally [1]. The first form is the bubble type, and the second is the spiral type. The bubble type shows a sudden, nearly axisymmetric swelling of the vortex core into a bubble; the spiral type shows an asymmetric spiral vortex filament, which is followed by a rapidly spreading turbulent flow. Both types of breakdown are characterized by an axial stagnation point and a limited region of reversed axial flow. Much of our knowledge of vortex breakdown has been obtained from experimental studies of incompressible flows in pipes, where both types of breakdown (and other types as well) are generated and documented [2–4].

The major effort in the numerical studies of vortex-breakdown flows has been focused on incompressible, quasi-axisymmetric isolated vortices. Grabowski and Berger [5] were the first to use the incompressible, quasi-axisymmetric Navier–Stokes (NS) equations to study isolated vortex flow in an unbounded region. Hafez *et al.* [6] solved the incompressible, steady, quasi-axisymmetric Euler and NS equations with the stream function–vorticity formulation for isolated vortex flows. They predicted vortex-breakdown flows similar to those of Garbowski and Berger [5]. Salas and Kuruvila [7] solved the unsteady, quasi-axisymmetric NS equations in a straight circular pipe and obtained steady, multiple-bubble vortex breakdown for the Reynolds number, Re (based on the pipe diameter), range 100–1800. Menne [8] has also used the stream function–vorticity formulation for studying unsteady, incompressible quasi-axisymmetric isolated vortex flows. Wu and Hwang [9] used the stream function–vorticity formulation to study quasi-axisymmetric vortex breakdown in a pipe. Their study focused on the effects of inflow conditions, wall boundary conditions and Re on breakdown structure. They showed that the evolution of breakdown can be steady, periodic or unsteady, dependent on the inflow velocity profiles and Re. Menne and Liu [10] integrated the laminar, incompressible NS equations for breakdown of a vortex in a slightly diverging pipe. They showed breakdown flow cases that are based on the purely quasi-axisymmetric and nonaxisymmetric analyses. The results were in good agreement with the experimental results of Leibovich [4]. Spall *et al.* [11] used the vorticity–velocity formulation of the incompressible NS equations to study three-dimensional vortex breakdown. Breuer and Hänel [12] solved the unsteady incompressible NS equations with a dual time-stepping, upwind scheme to study the temporal evolution of the three-dimensional vortex breakdown. In Refs [11, 12], both types of breakdown (the bubble and the spiral type) were predicted. Reviews of the physical and computational aspects of the incompressible vortex breakdown have been presented by Krause [13, 14]. One of the most important aspects of vortex breakdown, which Krause discusses in Ref. [14], is the effect of side-wall

PRECEDING PAGE BLANK NOT FILMED

boundary conditions on the upstream or downstream motion of the breakdown point. Also, he discusses different outflow boundary conditions.

Longitudinal vortex and transverse shock-wave interactions are typical phenomena that appear in transonic and supersonic flows over strake-wing configurations at moderate to high angles of attack, at a supersonic inlet as a vortex is injested and inside a supersonic combustor where fuel is injected in a swirling jet to enhance fuel–air mixing [15–17]. For the strake-wing configuration, vortex breakdown is undesirable because the stall phenomenon results; hence, its occurrence must be delayed. On the other hand, vortex breakdown for the other two applications is desirable because it enhances the mixing of air and fuel and stability of the flame [18, 19]; hence, its occurrence must be controlled for optimum performance. Unfortunately, the literature lacks this type of analysis, with the exception of the preliminary work of Liu *et al.* [29], Copening and Anderson [21], Delery *et al.* [15], Kandil and Kandil [22] and Meadows *et al.* [23].

The first time-accurate, NS solution for a supersonic vortex breakdown was developed by Kandil *et al.* [24]. A supersonic quasi-axisymmetric vortex flow in a configured circular duct was considered. The time-accurate solution to the unsteady, compressible NS equations was obtained with an implicit, upwind, flux-difference splitting, finite-volume scheme. A shock wave was generated near the duct inlet and unsteady vortex breakdown was predicted behind the shock. The predicted flow was characterized by the evolution, convection and shedding of vortex-breakdown bubbles. The Euler equations were also used to solve the same problem. The Euler solution predicted increases in both the size and number of vortex-breakdown bubbles, in comparison with the NS solutions. The time-accurate solution was carried out for 3200 times steps, which was equivalent to a dimensionless time of 16. A single Re value (10,000 based on the inlet radius) was considered in that study [24].

In a later paper [25], the study of this flow was extended with time-accurate computations of the NS equations with a fine grid in the shock–vortex interaction region and for longer computational times. Several issues were addressed in that study. First, the effect of Re on the temporal evolution and persistence of vortex-breakdown bubbles behind the shock was shown. In that stage of the computations, the conditions at the downstream exit were obtained by extrapolating the components of the flow-field vector from the interior cell centers. Although the flow was supersonic over a large portion of the duct exit, subsonic flow existed over a small portion of the exit around the duct centerline (CL). Therefore, selected flow cases were computed with Riemann-invariant boundary conditions at the subsonic points of the duct exit. The effect of swirl ratio at the duct inlet was also investigated.

Recently, the critical effects of the downstream boundary conditions on the supersonic vortex breakdown have been investigated extensively by the same authors [26] for both internal and external flows.

In the present paper, the numerical simulation of supersonic vortex-breakdown flows for bounded and unbounded domains are reviewed. The effects of Re, swirl ratio and downstream-exit boundary conditions are considered and discussed along with certain physical and numerical issues.

## OVERVIEW OF THE FORMULATION AND COMPUTATIONAL SCHEME

The conservative, unsteady, compressible, full NS equations, in terms of the time-independent, body-conformed coordinates $\xi^1$, $\xi^2$ and $\xi^3$ have been used to solve the problem. The equations are given in Ref. [25] and are not shown here. With these equations, boundary conditions are specified at the computational domain inlet, side wall and downstream exit. The downstream-exit boundary conditions are presented and discussed in the next section. The initial conditions will also be presented in the next section.

The computational scheme used to solve the unsteady, compressible, full NS equations is an implicit, upwind, flux-difference splitting, finite-volume scheme. This scheme employs the flux-difference splitting scheme of Roe, which is based on the solution to the approximate one-dimensional Riemann problem in each of the three directions. In the Roe scheme, the inviscid flux difference at the interface of a computational cell is split into left and right flux differences. The splitting is accomplished in accordance with the signs of the eigenvalues of the Roe averaged-Jacobian matrix of the inviscid flux at the cell interface. The smooth limiter is used to eliminate oscillations in the shock region. The viscous and heat-flux terms are linearized and the cross-derivative terms of the viscous Jacobians are dropped in the implicit operator. These terms are differenced with second-order, spatially-accurate central differencing. The resulting difference equation is approximately factored and is solved in three sweeps in the $\xi^1$, $\xi^2$ and $\xi^3$ directions. The scheme is coded in the computer program "FTNS3D".

The quasi-axisymmetric solutions are obtained with the three-dimensional code by forcing the flow-field vectors to be equal on two axial planes, which are in close proximity to each other. Quasi-axisymmetric solutions require 1 order of magnitude less in computational time than the three-dimensional solutions. They still provide substantial physical understanding of the supersonic vortex breakdown and the dominant parameters that affect it.

## COMPUTATIONAL RESULTS AND DISCUSSION

### *Vortex Breakdown in a Configured Circular Duct*

Figure 1 shows a configured circular duct with a short, straight cylindrical part at the inlet which is followed by a short divergent cylindrical part until the axial length of 0.74 dimensionless unit, where the duct inlet radius is the characteristic length. The divergence angle is 6°. The duct radius is then kept constant and a convergent–divergent nozzle with a throat radius of 0.95 is attached. The duct exit radius is 0.98 and its total length is 2.9. The divergent part of the duct ensures that the formed shock stays in the inlet region. The overall configuration of the duct ensures that the supersonic inflow becomes supersonic at the exit. As the computations will show, a small portion of the duct exit flow near its CL becomes subsonic at certain times for the specified inflow conditions. This configured duct has also been used by Delery *et al.* [15] for the Euler equation computations of supersonic vortex breakdown to computationally model their experimental setup.

The NS solver uses a grid of 221 × 51 grid points on two axial planes, where 221 points are in the axial direction and 51 points are in the radial direction. In the inlet region up to the 0.74 axial station, 100 grid points are used; the other 121 points are used in the remaining part of the duct. The grid is also clustered at the CL and the wall. The minimum radial grid size at the CL is 0.002. The two axial planes are spaced circumferentially at a prescribed angle so that the aspect ratio of the minimum grid size will be $<2$. The present grid size and distribution resulted from initial studies of their effect on the accuracy of the solution. The upstream Mach number is supersonic and is kept at 1.75. The initial profile for the tangential velocity is given by

$$\frac{v}{U_\infty} = \frac{k_e}{r}\left[1 - \exp\left(-\frac{r^2}{r_m^2}\right)\right], \tag{1}$$

where $U_\infty = 1.74$, $r_m = 0.2$ and $k_e = 0.1$. The maximum $v/U_\infty$ (swirl ratio $\beta$) is at $r = 0.224$. The radial velocity $w$ at the initial station is equal to zero, and the radial momentum equation is integrated to obtain the initial pressure profile. Finally, the density $\rho$ is obtained from the definition of the speed of sound for the inlet flow. With this compatible set of profiles, the computations are carried out accurately in time with $\Delta t = 0.0025$. The wall boundary conditions follow the typical

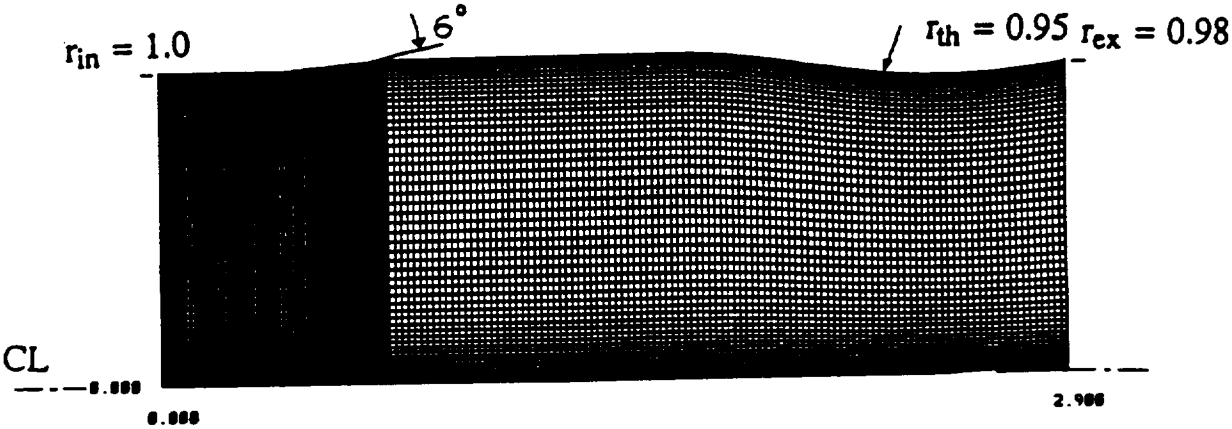

Fig. 1. Grid of the configured duct (221 × 51).

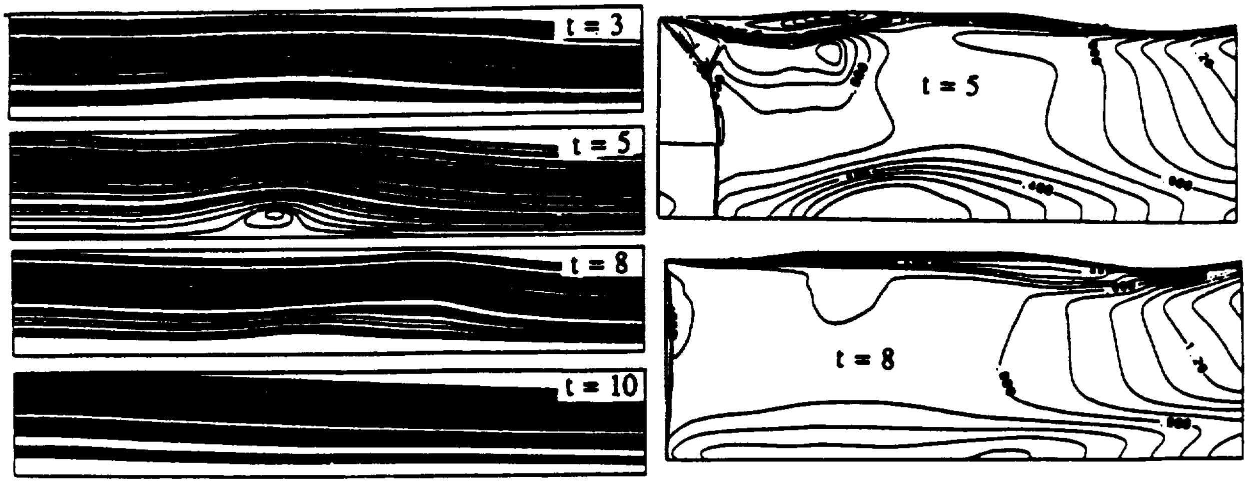

Fig. 2. Streamlines and Mach contours for swirling flow with transient single-bubble breakdown; with $M_\infty = 1.75$, $\beta = 0.32$ and Re = 4,000.

NS solid boundary conditions. These computations have been carried out on the CRAY 2 at NASA Langley Research Center. The CPU time is 28 $\mu$s per grid point per iteration for the NS calculations.

Next, we present the results of the computational study on the effects of Re, exit boundary conditions and swirl ratio.

*Effect of Re*

The effect of Re on the vortex-breakdown modes is studied by varying Re between 2000 and 100,000. The Re is based on the radius of the duct inlet. The swirl ratio is kept fixed at 0.32 and the downstream-exit conditions are obtained by extrapolating all of the flow variables from the cell centers at the exit.

For Re = 2000, a shock is captured at the duct inlet, but no vortex breakdown is detected. The flow at the exit boundary is supersonic.

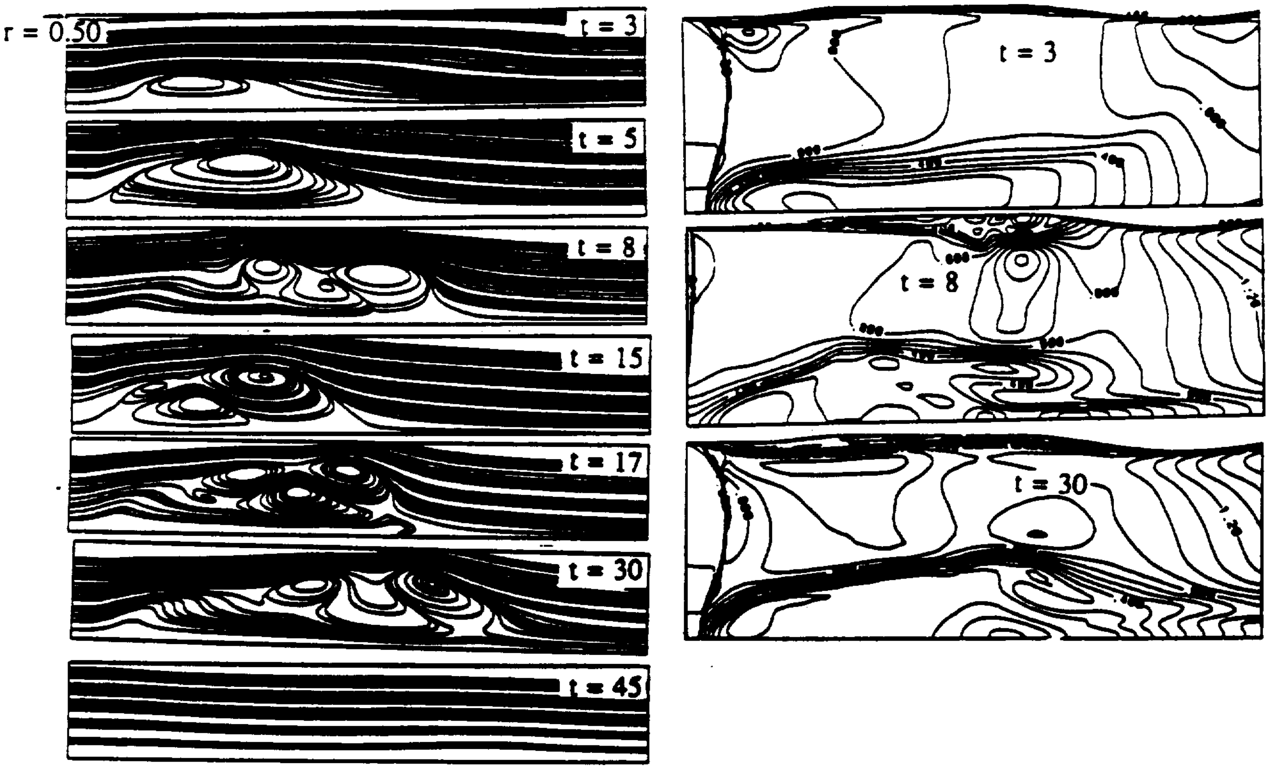

Fig. 3. Streamlines for swirling flow with transient multibubble breakdown; with $M_\infty = 1.75$, $\beta = 0.32$ and Re = 20,000.

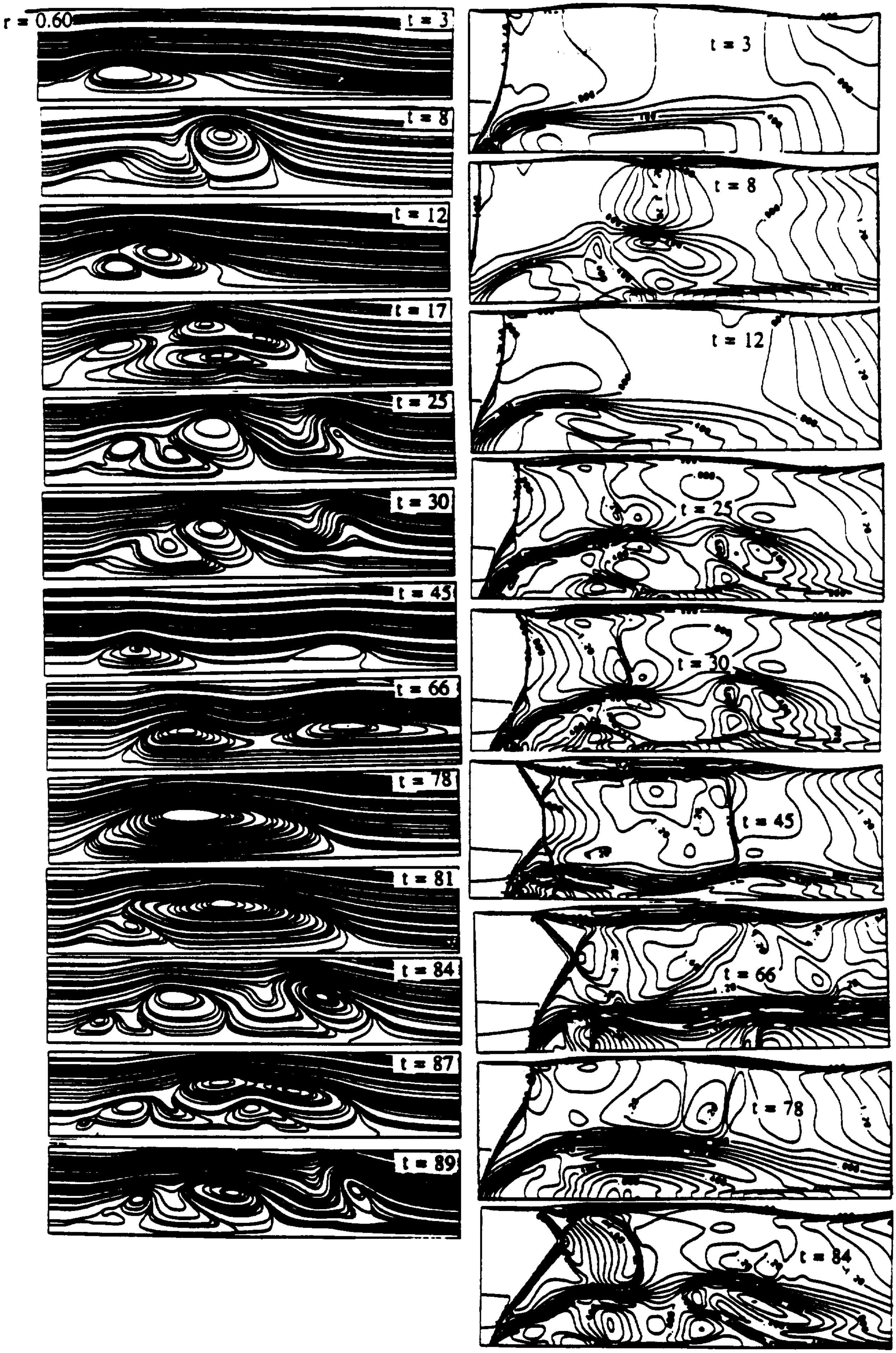

Fig. 4. Streamlines for swirling flow with periodic multifrequency, multibubble breakdown; with $M_\infty = 1.75$, $\beta = 0.32$ and Re = 100,000.

For Re = 4000, Fig. 2 shows snapshots of the streamlines and Mach contours of the solution. For this Re, a single breakdown bubble is seen at $t = 5$ and is convected downstream as time passes. This breakdown bubble is formed during the downstream motion of the inlet shock, which reaches its maximum downstream displacement at $t = 5$. Later on, the shock moves upstream (as is seen at $t = 8$) and the breakdown bubble is convected in the downstream direction. Thereafter, the shock stays stationary at the inlet and no vortex-breakdown bubbles are formed behind the shock. This swirling flow case shows a transient single-bubble breakdown flow.

For Re = 20,000, Fig. 3 shows snapshots of the streamlines and Mach contours of the solution. These snapshots show a vortex-breakdown mechanism of evolution, convection, merging and shedding of bubbles, and the inlet shock first moves downstream, then upstream and finally downstream. Thereafter, the inlet shock becomes stationary, and no bubbles are formed behind the shock. This swirling flow case shows a transient multibubble breakdown flow.

For Re = 100,000, Fig. 4 shows snapshots of the streamlines and Mach contours of the solution. The streamline snapshots show multibubble vortex-breakdown evolution, convection, merging and shedding. The time-accurate integration was carried out up to $t = 200$, and the solution showed periodic multifrequency cycles of vortex-breakdown bubbles. An example of the merging of vortex-breakdown bubbles of the same sign of vorticity is shown at $t = 17$. An example of the

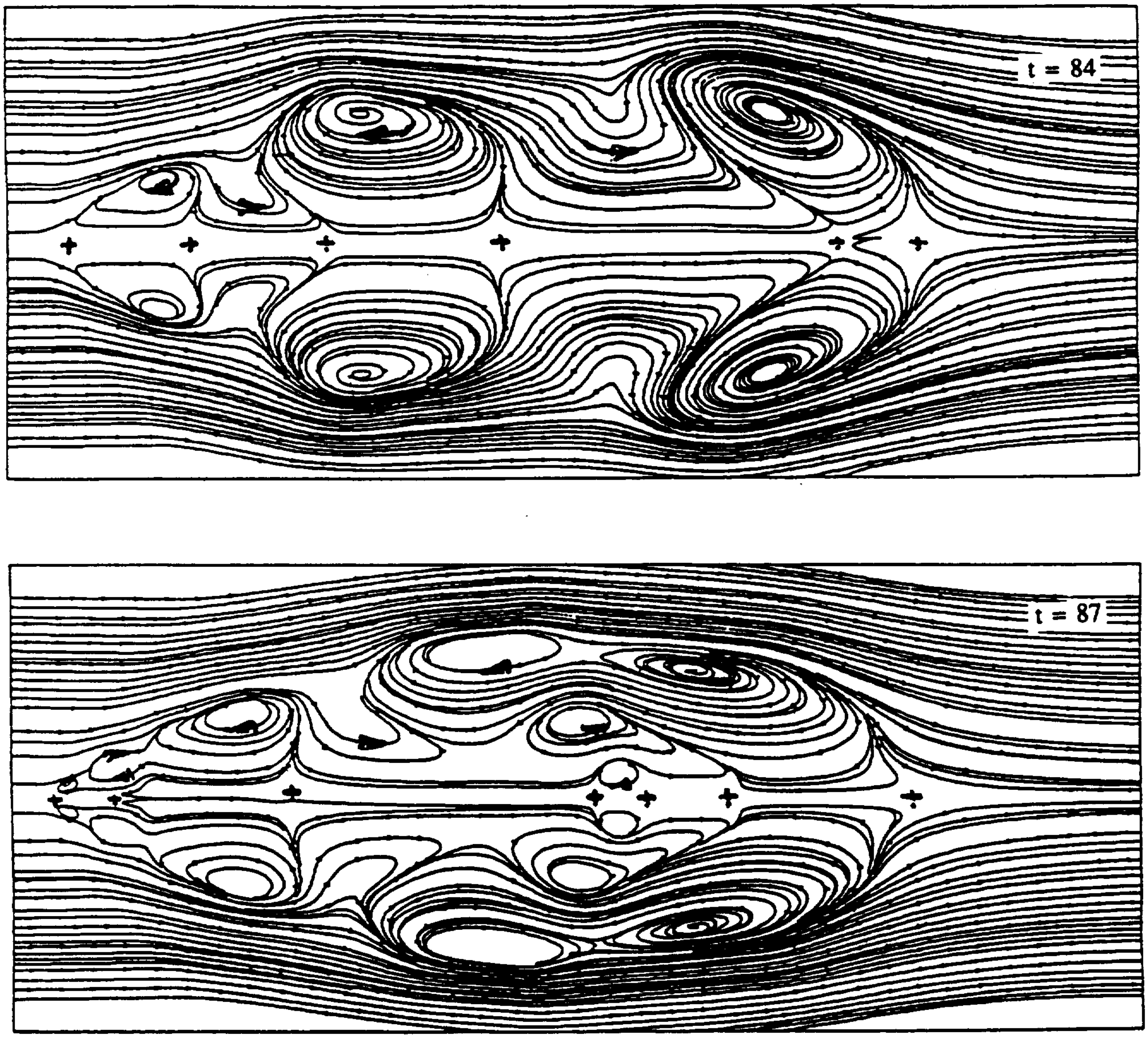

Fig. 5. Enlargement of streamlines of periodic multifrequency, multibubble breakdown; with $t = 84$ and 87.

convection and shedding of vortex-breakdown bubbles is shown at $t = 25$. In a comparison of the streamline solutions at $t = 25$ and 89, the solutions are almost identical. This result conclusively shows that the breakdown process is periodic. The Mach contours show the dynamics of inlet shock motion. In the time range $3 \leqslant t \leqslant 8$, the inlet shock moves upstream toward the inlet, and its central

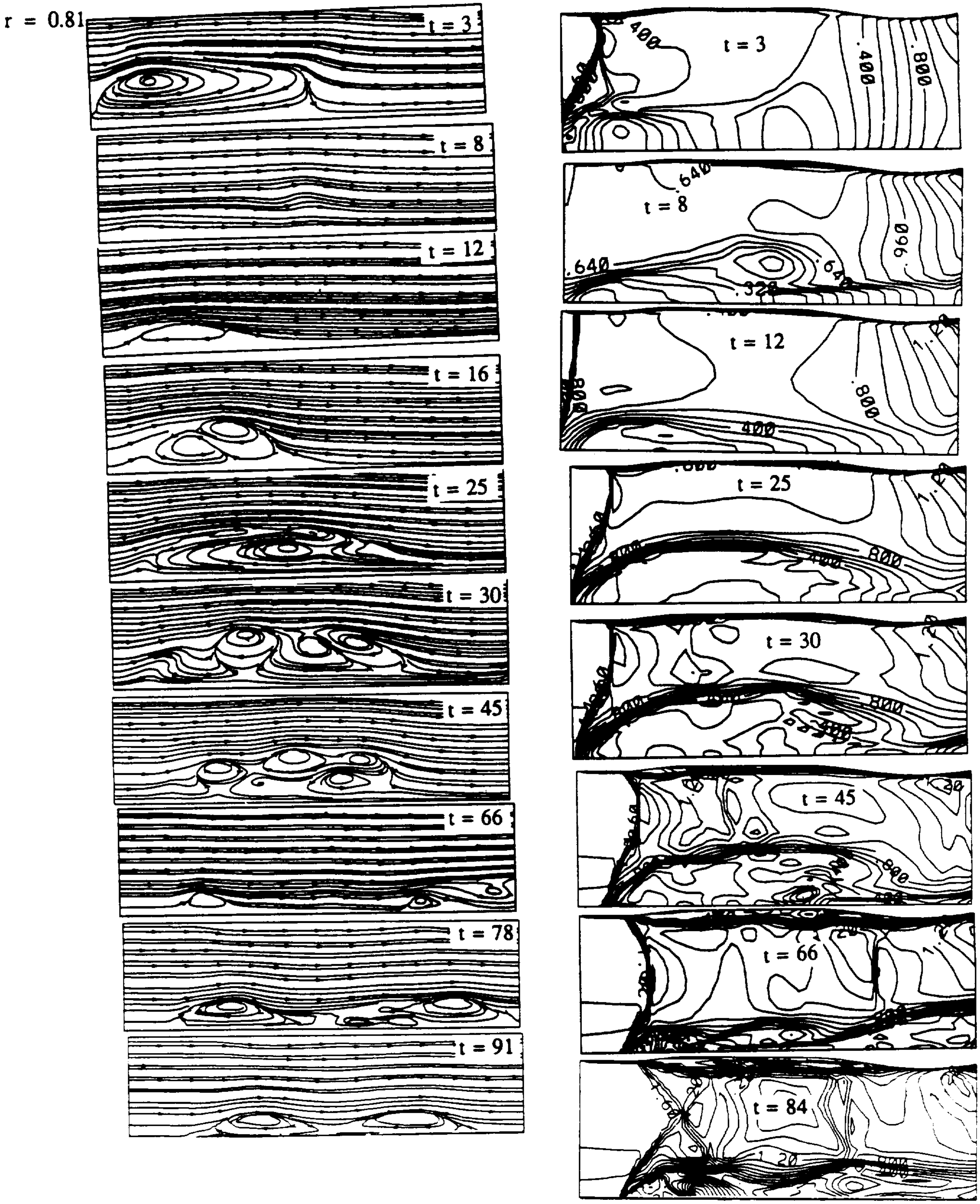

Fig. 6. Streamlines and Mach contours for swirling flow with periodic multibubble, multifrequency vortex breakdown; with $p_b = 2p_\infty$, Riemann-invariant boundary conditions, $M_\infty = 1.75$, $\beta = 0.32$ and $Re = 100{,}000$.

portion moves outside the inlet section at $t = 8$. In the time range $8 \leqslant t \leqslant 25$, the inlet shock moves downstream with corresponding evolution, convection, merging and shedding of breakdown bubbles. In the time range $25 \leqslant t \leqslant 45$, the inlet shock maintains its motion in the downstream direction at a slower rate than before, while another shock, which is downstream of the inlet shock, appears and also moves in the downstream direction. The evolution, convection and shedding

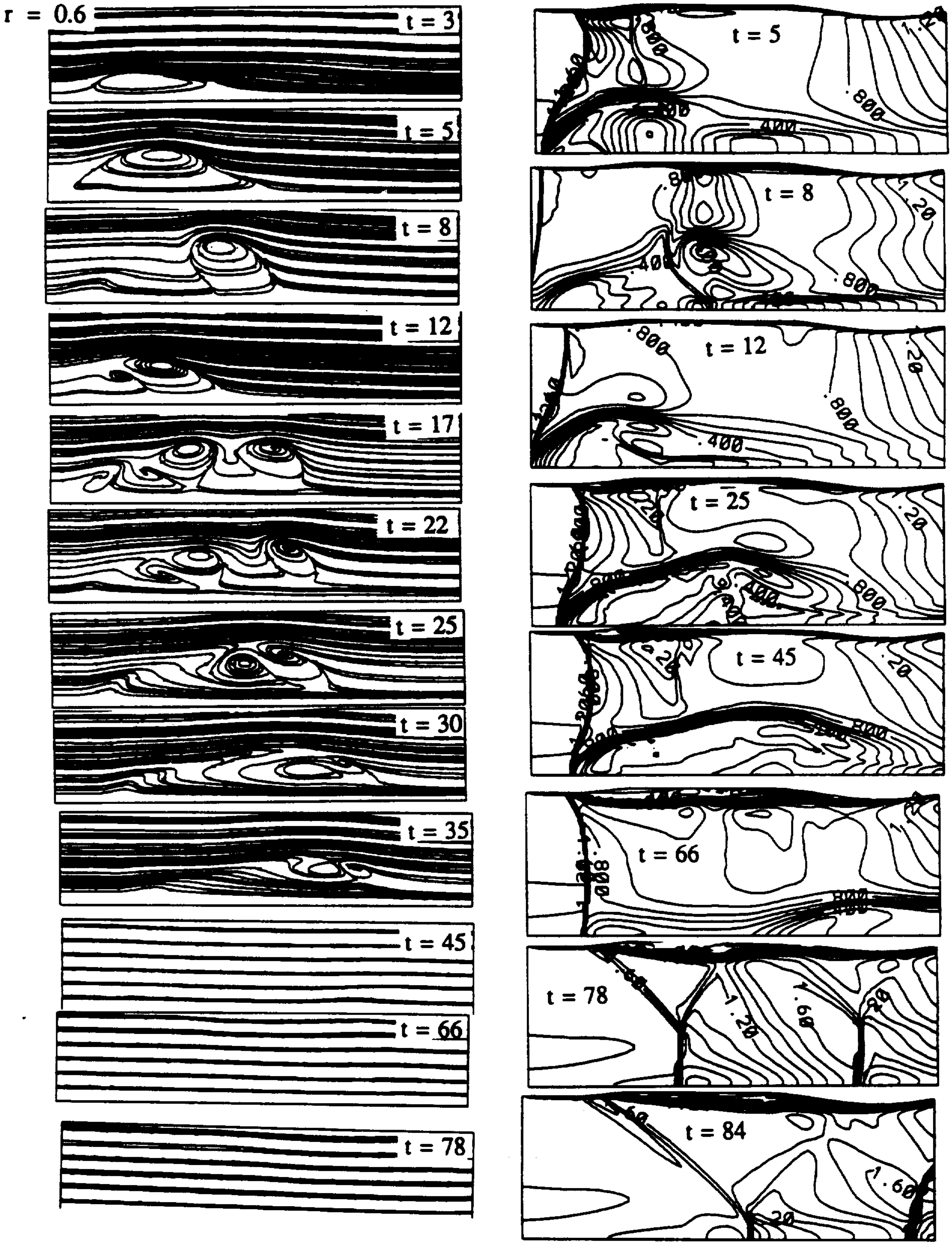

Fig. 7. Streamlines and Mach contours for swirling flow with transient multibubble vortex breakdown; with $\partial p/\partial x = c$, Riemann invariant boundary conditions, $M_\infty = 1.75$, $\beta = 0.32$ and Re = 100,000.

slowly continue until $t = 66$. In the time range $66 \leqslant t \leqslant 78$, the downstream shock disappears, and a large vortex-breakdown bubble appears and moves upstream. This motion of the bubble is accompanied by upstream motion of the inlet shock ($t = 78$). Later, the inlet shock again moves in the downstream direction, and the process is repeated. An animated movie has been produced to show the breakdown modes until a total dimensionless time of $t = 200$.

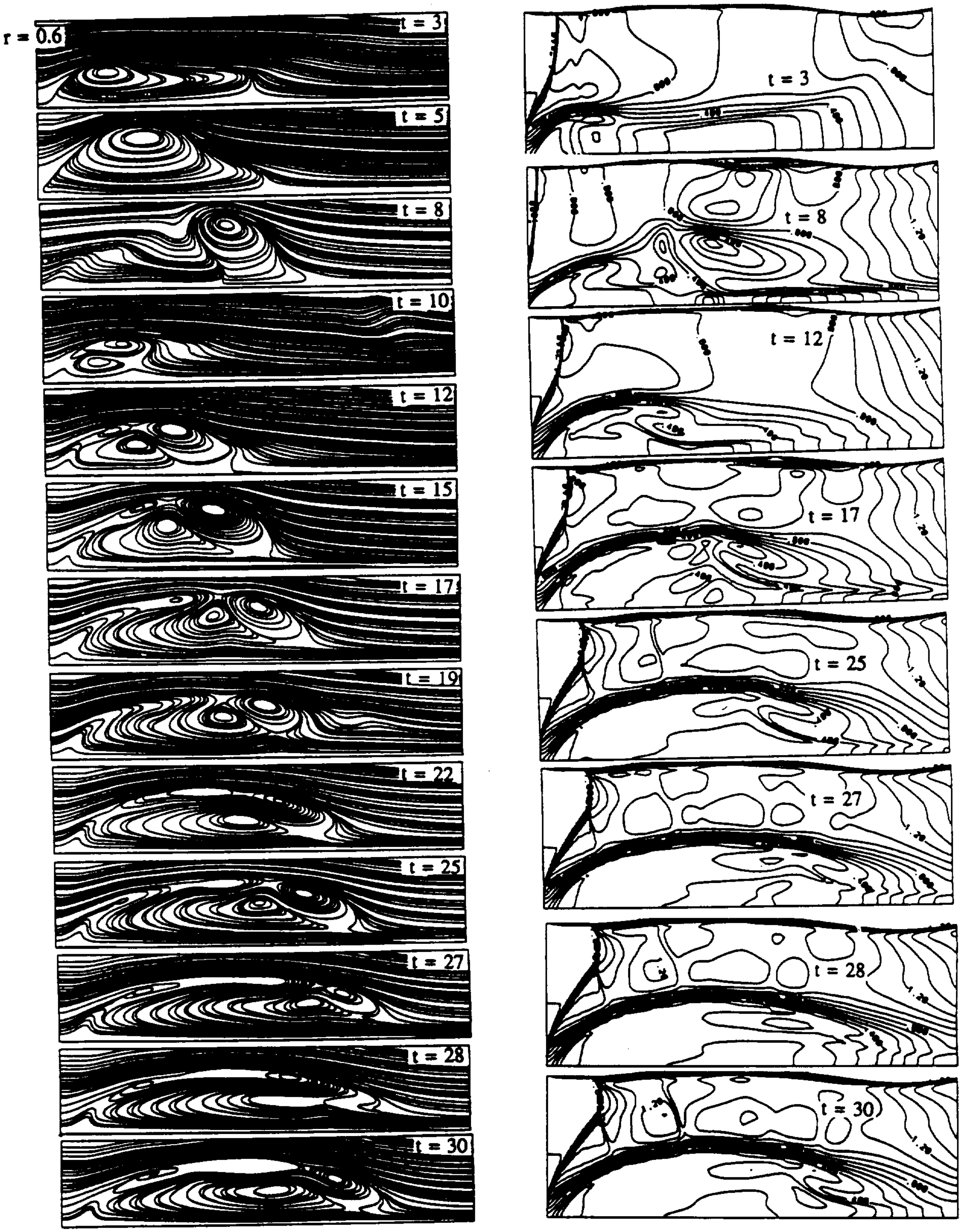

Fig. 8. Streamlines and Mach contours for swirling flow with quasi-steady breakdown; with $M_\infty = 1.75$, $\beta = 0.32$ and Re = 100,000.

Figure 5 shows an enlargement of two snapshots of the streamline solutions at $t = 84$ and 87. At $t = 84$, five vortex-breakdown bubbles spatially alternate in their sign of vortex strength. Six stagnation points exist at the axis. At $t = 87$, seven vortex-breakdown bubbles and seven stagnation points can be seen. The figure shows the merging of two bubbles of same sign of vorticity. This swirling flow case shows a periodic multifrequency, multibubble breakdown flow.

### *Effect of the type of boundary conditions at the exit*

In the present study, the downstream-exit boundary conditions at the subsonic points are replaced by using the Riemann-invariant boundary conditions. The Riemann-invariant boundary conditions at the subsonic points are applied with three different values of pressure, called the back pressure $p_b$: for the first value, $p_b = p_\infty$; for the second value, $p_b = 2p_\infty$; and for the third value, $p_b$ is obtained from $\partial p_b/\partial x = \text{const}$. The other four flow variables are extrapolated from the interior cell centers at the duct exit. The Re and $\beta$ are fixed at 100,000 and 0.32, respectively.

For $p_b = p_\infty$ up to $t = 35$, the solution is the same as that where the exit boundary conditions are extrapolated from the cell centers. (See Fig. 4.) Thereafter, for $t > 35$, the inlet shock continuously moves in the downstream direction and the vortex-breakdown bubbles move ahead of the shock. The shock and vortex bubbles are shed and disappear from the duct at advanced levels of time. The breakdown mode is termed as a transient multibubble vortex breakdown. The shock/vortex-breakdown/bubble system disappears because the back pressure is too low to support the inlet shock sufficiently to keep it in the inlet region. Moreover, the Riemann-invariant boundary conditions at subsonic points allow the downstream effects to propagate upstream as time increases.

For $p_b = 2p_\infty$, Fig. 6 shows snapshots of the streamlines and Mach contours of the solution. A comparison of the present solution with the solution in Fig. 4 shows that the two solutions are similar, except that the present solution lags that of Fig. 4 in time. The reason for this lag is that the back pressure $p_b$ of the present case is larger than that shown in Fig. 4. Moreover, the Riemann-invariant conditions at subsonic points allow the downstream effects to propagate upstream as time increases. The large back pressure, which is felt upstream, supports the inlet shock and keeps it in the inlet region.

For $\partial p_b/\partial x = \text{const}$, Fig. 7 shows snapshots of the streamlines and Mach contours of the solution. A comparison of the present solution with the solution in Fig. 4 shows that the two solutions are similar until $t = 22$. Thereafter, for $t > 22$, the inlet shock continuously moves in the downstream direction with the vortex-breakdown bubbles moving ahead of the shock. Again, as in the case of $p_b = p_\infty$, the shock and vortex bubbles are shed and disappear from the duct at advanced levels of time. The breakdown is a transient multibubble vortex breakdown. The shock/vortex-breakdown/bubble system disappears because the back pressure obtained from the $\partial p_b/\partial x = \text{const}$ condition is too low to support the inlet shock and keep it in the inlet region. Moreover, the Riemann-invariant conditions at subsonic points allow the downstream effects to propagate upstream as time increases.

### *Effect of the swirl ratio $\beta$*

In this section, the effect of the swirl ratio on the vortex-breakdown modes is studied. The downstream-exit boundary conditions are obtained by extrapolating the flow-field variables from the interior cell centers at the boundary. The Re for all the cases considered is 100,000; $\beta$ is varied between 0.2 and 0.38.

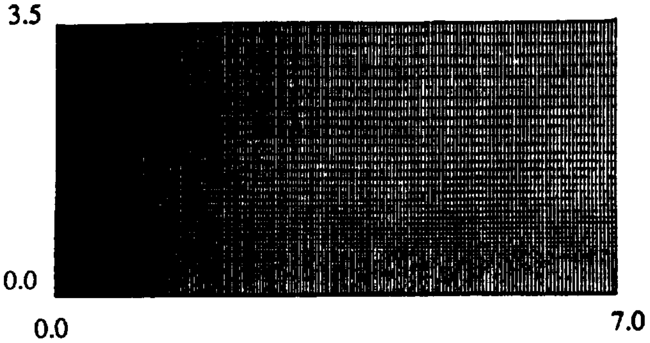

Fig. 9. Grid of nozzle flow (221 × 51).

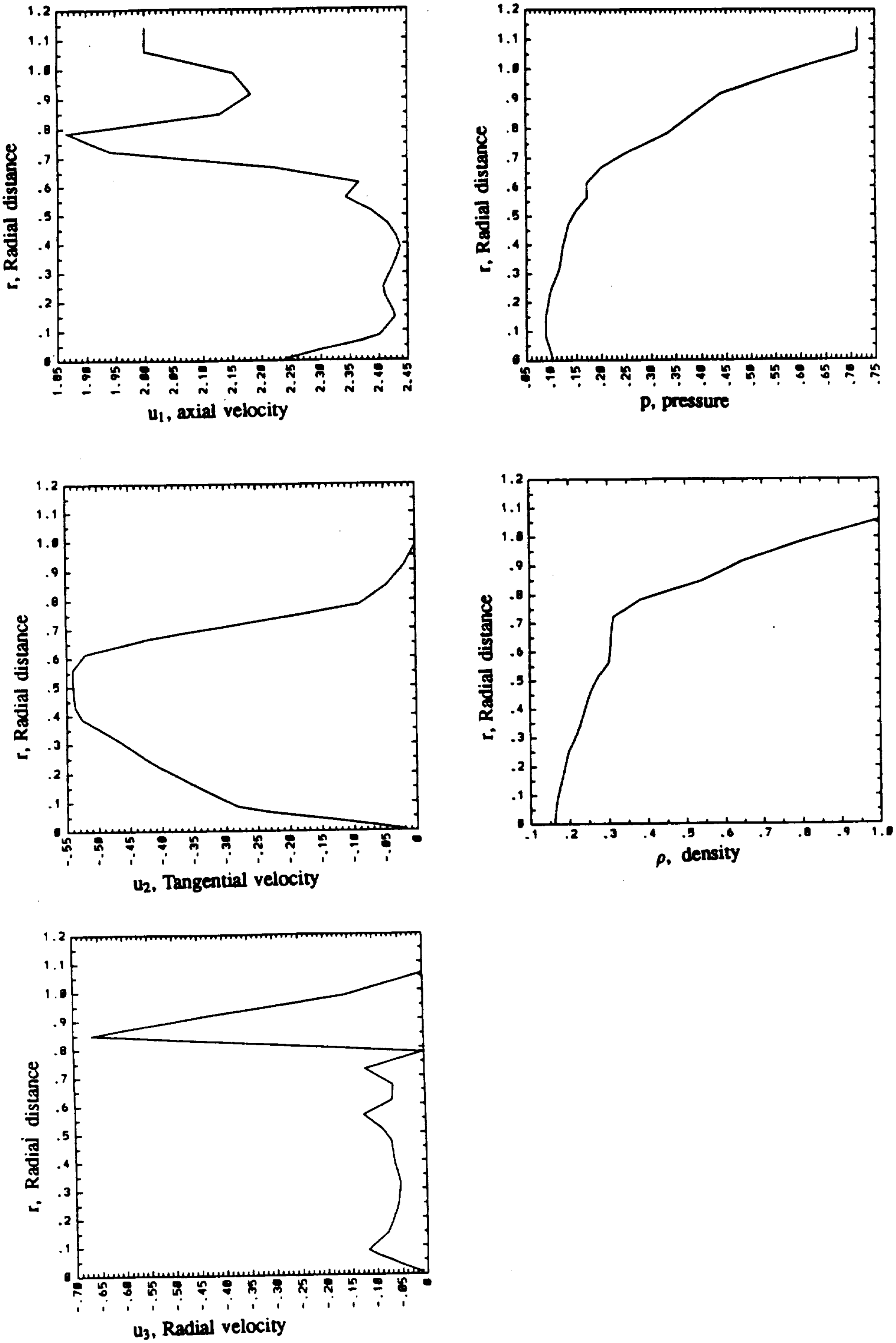

Fig. 10. Quasi-axisymmetric flow profiles at $x = 0$ for a supersonic swirling jet from the nozzle; with $M_j = 3.0$, $M_\infty = 2.0$ and Re = 296,000.

For the $\beta$ range 0.2–0.27, a shock is captured at the duct inlet and moves slowly in the downstream direction in the subsequent time steps until it stops just before the end of the straight inlet portion of the duct. Thereafter, it becomes stationary. No vortex breakdown is detected, and the flow at the exit boundary remains supersonic. This result shows that as $\beta$ is decreased by 15.6% from its original value of 0.32 (Fig. 4), vortex breakdown does not develop.

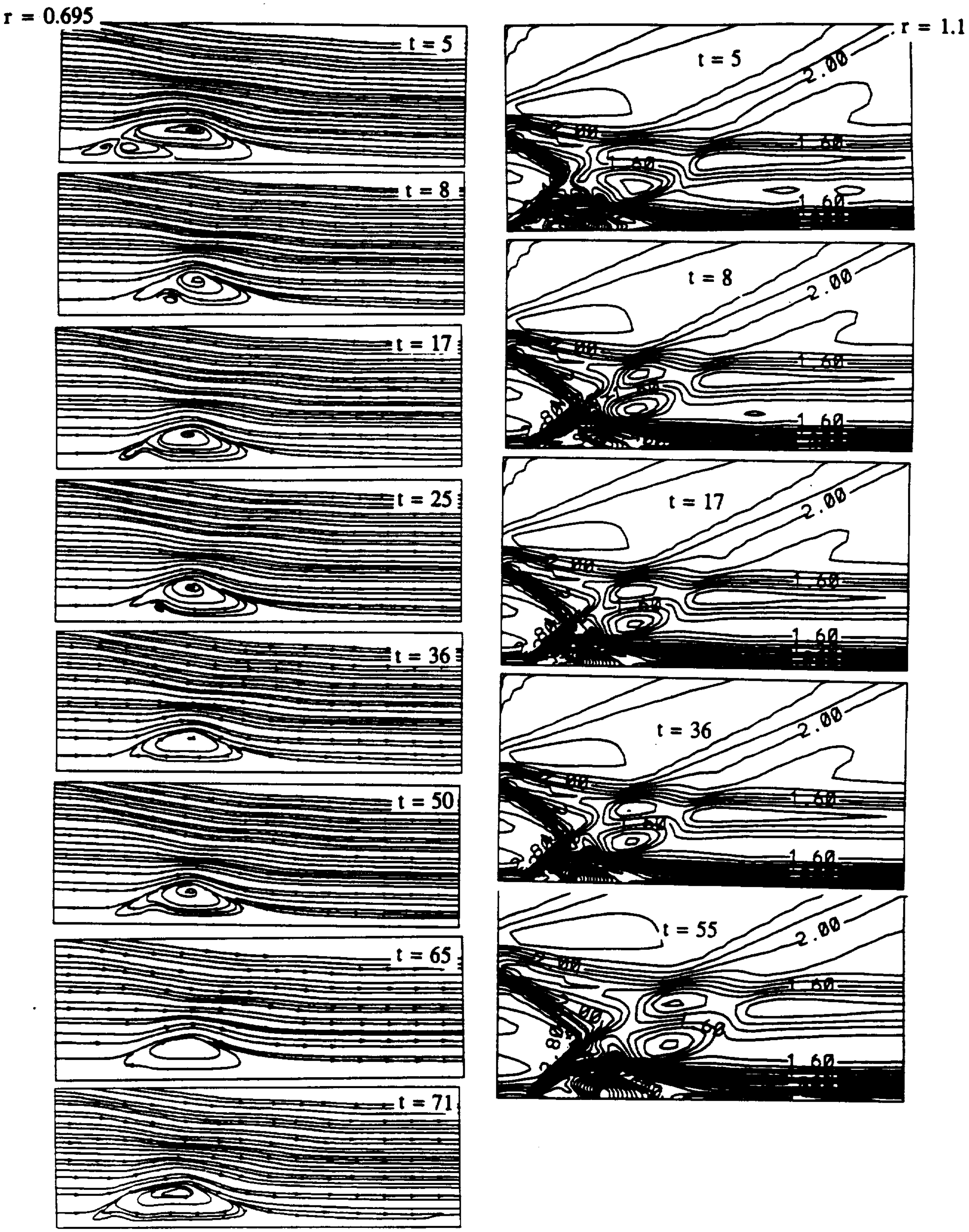

Fig. 11 *continued opposite.*

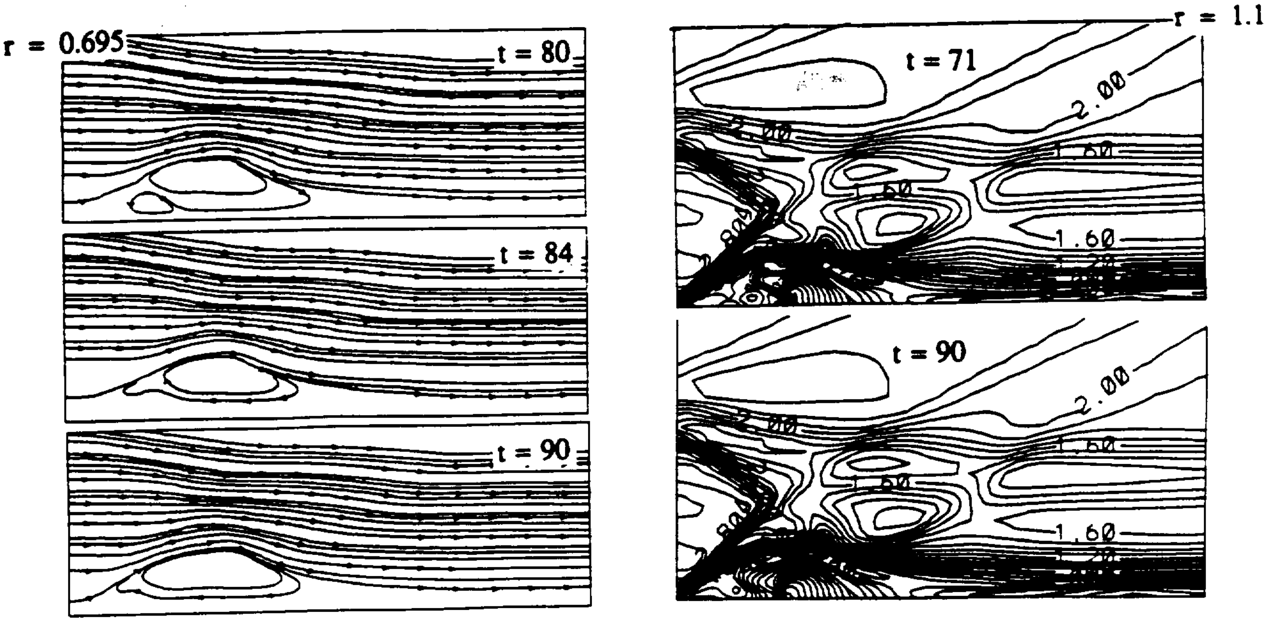

Fig. 11. Streamlines and Mach contours for a supersonic swirling jet from the nozzle; with low-frequency, almost single-bubble vortex breakdown and extrapolation from interior boundary conditions.

For the $\beta$ range 0.28–0.3, a transient single-bubble vortex breakdown is captured that is similar to the case in Fig. 2, where $Re = 4000$ and $\beta = 0.32$. This result shows the dominant effect of the swirl ratio on the vortex-breakdown development. With a decrease in $\beta$ of 6.3% from its original value of 0.32, the vortex-breakdown mode changes from a periodic, multifrequency multibubble breakdown to a transient, single-bubble vortex breakdown.

For $\beta = 0.38$, Fig. 8 shows snapshots of the streamlines and Mach contours of the solution. The vortex-breakdown bubbles are larger than those shown in Fig. 4. In the initial time range up to $t = 17$, the process of evolution, convection, merging and shedding of vortex breakdown bubbles continues, and the inlet shock moves first downstream, then upstream and finally downstream. For $t > 17$, a large vortex-breakdown bubble is formed behind the inlet shock, which oscillates with very small amplitude around a mean position. The process of evolution, convection, merging and shedding of additional small vortex-breakdown bubbles continues, and the large vortex-breakdown bubble oscillates with a very small amplitude around a mean position. This vortex-breakdown case introduces a new mechanism that is different from those encountered earlier.

### *Vortex Breakdown of a Supersonic Flow from a Nozzle*

In this case, a supersonic swirling jet at $M_j = 3$, which is issued from a nozzle into a supersonic uniform flow of $M_\infty = 2$, is considered. A grid of $221 \times 51 \times 2$ in the axial, radial and tangential directions, respectively, is used. The computational domain in an axial plane has the dimensions $7 \times 3.5$ in the axial and radial directions, respectively, where the nozzle exit radius $r = 1$. The free-stream $Re = 296{,}000$. Figure 9 shows the computational domain and a typical grid for this external flow case. The grid is clustered at the nozzle exit and at the CL.

Figure 10 shows the inflow profiles of the axial velocity, swirl velocity, radial velocity, pressure and density, which are taken from the experimental data of Ref. [16]. The initial profiles are used as quasi-axisymmetric profiles for the present computations. On the cylindrical boundary (side wall) of the flow at $r = 3.5$, free-stream conditions are imposed that correspond to $M_\infty = 2$. The initial conditions in the computational domain are those that correspond to the free-stream conditions at $M_\infty = 2$. The problem is solved with two types of exit boundary conditions at $x = 7$. First an extrapolation of all five variables from the interior cell center is used; then the Riemann-invariant boundary conditions are used.

#### *Extrapolation from interior cell centers*

Figure 11 shows snapshots of streamlines and Mach contours of the solution. The streamlines show multibubble breakdown at the early levels. These bubbles develop because of the shock system

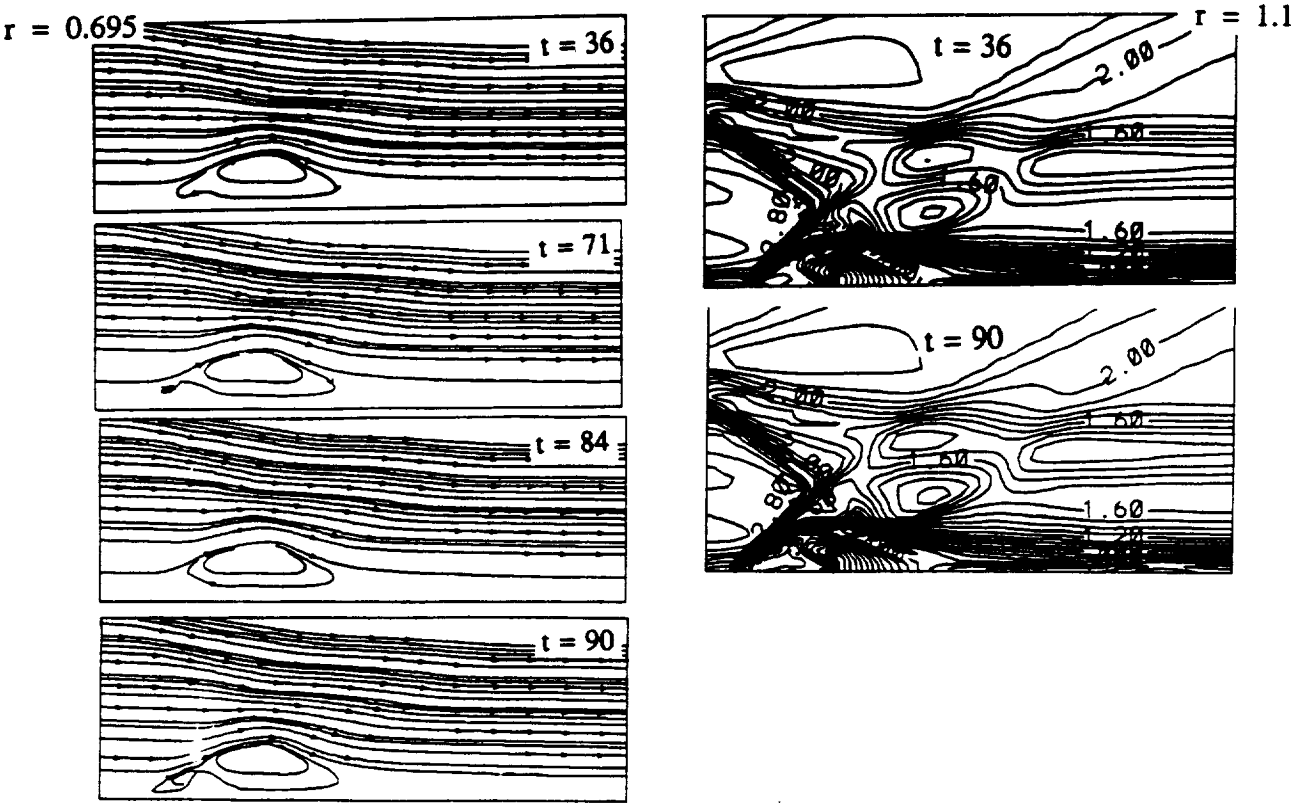

Fig. 12. Streamlines and Mach contours for a supersonic swirling jet from the nozzle with low-frequency, almost single-bubble vortex breakdown and Riemann-invariant boundary conditions.

that is formed at the nozzle exit in the vicinity of the CL. A strong portion of the shock exists at the CL, which splits into two oblique shocks; one is a weak shock and the other is a strong shock. Vortex-breakdown bubbles develop behind the strong shock. Thereafter, for $t > 5$, the shock system and the vortex-breakdown bubbles move slowly in the downstream direction. At $t > 55$, both the shock system and the vortex-breakdown bubble move upstream. The slow motion of the shock system and the vortex-breakdown bubble continues back and forth between these two locations. No vortex shedding has been captured during the computations for this case. Most of the exit points are continuously supersonic; hence, no upstream effects exist except within a very thin layer around the CL.

### *Riemann-invariant boundary conditions*

Next, the boundary conditions at the exit are replaced by the Riemann-invariant boundary conditions with $p_b = p_\infty$ at the subsonic points. Figure 12 shows snapshots of the streamlines and Mach contours of the solution. A comparison of the present solution with the previous case shown in Fig. 11 shows that the present boundary condition has only a slight effect on the solution. This result is not unusual because the subsonic region at the exit is very small and, moreover, the exit boundary is far from the nozzle exit.

Figure 13 shows an enlargement of the Mach contours at $t = 55$ for the flow case shown in Fig. 11. The shock system near the nozzle exit is clearly seen.

## CONCLUDING REMARKS

The numerical simulation and the study of supersonic vortex-breakdown phenomena have been examined for internal and external supersonic swirling flows. A time-accurate solution of the unsteady, compressible, full NS equations is used to produce the solutions. The equations are solved for laminar flows with an implicit, upwind, flux-difference splitting, finite-volume scheme. The solutions are obtained for quasi-axisymmetric flows with a three-dimensional code, FTNS3D, by forcing the flow-field vector to be equal on two axial planes in close proximity to each other. Quasi-axisymmetric flow solutions require 1 order of magnitude less in computational time than

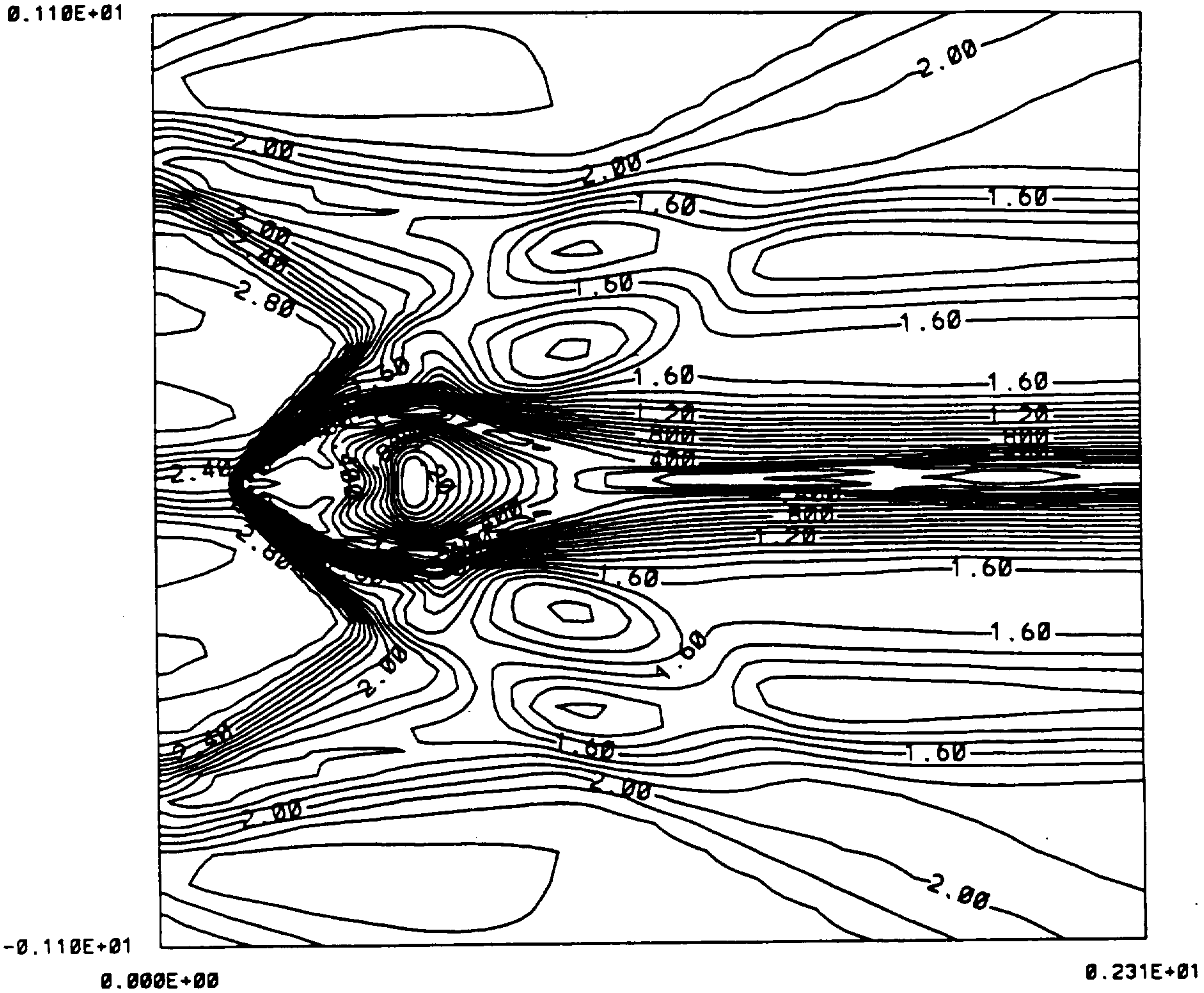

Fig. 13. Enlargement of Mach contours at $t = 55$ for a supersonic swirling jet from the nozzle.

the three-dimensional flow solutions and still provide substantial physical understanding of the supersonic vortex breakdown and the dominant parameters that affect it.

In the present study, two supersonic swirling flow cases are considered: the first case is a supersonic swirling flow in a configured duct; the second case is a supersonic swirling jet flow that is issued from a nozzle into another supersonic uniform flow of lower Mach number than the nozzle flow. For the configured duct, the effects of Re, the type of downstream-exit boundary conditions and the swirl ratio $\beta$ are studied. As Re is varied from 4000 to 100,000, different modes of vortex breakdown are obtained: a transient single-bubble breakdown; a transient multibubble breakdown; and a periodic multifrequency, multibubble breakdown. These solutions have been obtained with extrapolated flow conditions from the interior cell centers at the exit. For the flow case with Re = 100,000, the downstream-exit boundary conditions have been replaced with the Riemann-invariant boundary conditions with $p_b = p_\infty$, $p_b = 2p_\infty$ and $\partial p_b/\partial x$ = const. The solutions have shown substantially different vortex-breakdown modes which are dependent upon the type of exit boundary conditions. The reason for this result is the upstream effect of the type of exit boundary condition at the exit subsonic points. Again, for the flow case with Re = 100,000, $\beta$ has been varied from 0.2 to 0.38. No vortex breakdown develops in the $\beta$ range 0.2–0.27. In the $\beta$ range 0.28–0.3, a transient single-bubble breakdown develops. At $\beta = 0.38$, a quasi-steady, large vortex-breakdown bubble develops with small bubbles that experience convection, merging and shedding around the large bubble.

For nozzle jet flow, the type of downstream-exit-boundary condition has very little effect on the vortex-breakdown mode. This result occurs for two reasons: first, most of the exit portion of the flow is supersonic, and only a very thin subsonic portion exists around the CL; second, the downstream exit is located at a large distance from the nozzle exit—therefore, the upstream propagation of the type of exit boundary condition at the subsonic points is very small.

*Acknowledgements*—For the second and third authors, this research work is supported by NASA Langley Research Center under Grant No. NAG-1-994. The authors would like to acknowledge the computational resources provided by NASA Langley Research Center and the NAS facilities at the Ames Research Center.

## REFERENCES

1. N. C. Lambourne and D. W. Bryer, Bursting of leading-edge vortices: some observations and discussion of the phenomenon. R&M 3282, Aeronautical Research Council (1961).
2. T. Sarpkaya, Effect of the adverse pressure gradient on vortex breakdown. *AIAA Jl* **12,** 602 (1974).
3. M. P. Escudier and N. Zender, Vortex flow regimes. *J. Fluid Mech.* **115,** 105 (1982).
4. S. Leibovich, Vortex stability and breakdown: survey and extension. *AIAA Jl* **22,** 1192 (1984).
5. W. J. Grabowski and S. A. Berger, Solutions of the Navier–Stokes equations for vortex breakdown. *J. Fluid Mech.* **75,** 525 (1976).
6. M. Hafez, G. Kuruvila and M. D. Salas, Numerical study of vortex breakdown. *J. Appl. Numer. Math.* **2,** 291 (1987).
7. M. D. Salas and G. Kuruvila, Vortex breakdown simulation: a circumspect study of the steady, laminar, axisymmetric model. *Computers Fluids* **17,** 247 (1989).
8. S. Menne, Vortex breakdown in an axisymmetric flow. AIAA Paper 88-0506 (1988).
9. J. C. Wu and S. Hwang, Computational study of vortex breakdown in a circular tube. AIAA Paper 91-1820 (1991).
10. S. Menne and C. H. Liu, Numerical simulation of a three-dimensional vortex breakdown. *Z. Flugwiss Weltraumforsch.* **14,** 301 (1990).
11. R. E. Spall, T. B. Gatski and R. L. Ash, The structure and dynamics of bubble-type vortex breakdown. *Proc. R. Soc. Lond.* **A429,** 613 (1990).
12. M. Breuer and D. Hänel, Solution of the 3-D incompressible Navier–Stokes equations for the simulation of vortex breakdown. Presented at the *8th GAMM Conf.*, Delft, The Netherlands (1989).
13. E. Krause, Vortex breakdown: physical issues and computational simulation. In *Proc. 3rd Int. Congr. of Fluid Mechanics*, Cairo, Egypt, Vol. 1, pp. 335–344 (1990).
14. E. Krause, The solution of the problem of vortex breakdown. Presented at the *Int. Conf. on Numerical Methods for Fluid Dynamics*, Oxford, U.K. (1990).
15. J. Delery, E. Horowitz, O. Leuchter and J. L. Solignac, Fundamental studies of vortex flows. *Rech. Aéospat.* **1984**(2), 1 (1984).
16. O. Metwally, G. Settles and C. Horstman, An experimental study of shock wave/vortex interaction. AIAA Paper 89-0082 (1989).
17. A. D. Cutler and B. S. Levey, Vortex breakdown in a supersonic jet. AIAA Paper 91-1815 (1991).
18. D. L. Rhodes, D. G. Lilley and D. K. McLaughlin, On the prediction of swirling flowfields found in axisymmetric combustor geometries. *Trans. ASME* **104,** 378 (1982).
19. H. Altegeld, W. P. Jones and J. Wilhelmi, Velocity measurements in a confined swirl driven recirculating flow. In *Experiments in Fluids*, Vol. 1, pp. 73–78. Springer-Verlag, New York (1983).
20. C. H. Liu, E. Krause and S. Menne, Admissible upstream conditions for slender compressible vortices. AIAA Paper 86-1093 (1986).
21. G. Copening and J. Anderson, Numerical solutions to three-dimensional shock/vortex interaction at hypersonic speeds. AIAA Paper 89-0674 (1989).
22. O. A. Kandil and H. A. Kandil, Computation of compressible quasi-axisymmetric slender vortex flow and breakdown. In *Computer Physics Communications*, Vol. 65, pp. 164–172. North-Holland, Amsterdam (1991).
23. K. Meadows, A. Kumar and M. Hussaini, A computational study on the interaction between a vortex and a shock wave. AIAA Paper 89-1043 (1989).
24. O. A. Kandil, H. A. Kandil and C. H. Liu, Computation of steady and unsteady compressible quasi-axisymmetric vortex flow and breakdown. AIAA Paper 91-0752 (1991).
25. O. A. Kandil, H. A. Kandil and C. H. Liu, Supersonic quasi-axisymmetric vortex breakdown. AIAA Paper 91-3311-CP, pp. 851–863 (1991).
26. O. A. Kandil, H. A. Kandil and C. H. Liu, Critical effects of downstream boundary conditions on vortex breakdown. AIAA Paper 92-2601-CP, pp. 12–26 (1992).

Fluid Dynamics Research 10 (1992) 409–450
North-Holland

FLUID DYNAMICS
RESEARCH

# Prediction of asymmetric vortical flows around slender bodies using Navier–Stokes equations

C.H. Liu [a], Tin-Chee Wong [b] and Osama A. Kandil [b]

[a] *Computational Aerodynamics Branch, NASA Langley Research Center, Hampton, VA 23681, USA*
[b] *Department of Mechanical Engineering and Mechanics, Old Dominion University, Norfolk, VA 23529, USA*

Received 2 December 1991

**Abstract.** Steady and unsteady asymmetric vortical flows around slender bodies at high angles of attack are solved using the unsteady, compressible, this-layer Navier–Stokes equations. An implicit, upwind-biased, flux-difference splitting, finite-volume scheme is used for the numerical computations. For supersonic flows past point cones, the locally conical flow assumption has been used for efficient computational studies of this phenomenon. Asymmetric flows past a 5° semiapex-angle circular cone at different angles of attack, free-stream Mach numbers, and Reynolds numbers has been studied in responses to different sources of disturbances. The effects of grid fineness and computational domain size have also been investigated. Next, the responses of three-dimensional supersonic asymmetric flow around a 5° circular cone at different angles of attack and Reynolds numbers to short-duration sideslip disturbances are presented. The results show that flow asymmetry becomes stronger as the Reynolds number and angles of attack are increased. The asymmetric solutions show spatial vortex shedding which is qualitatively similar to the temporal vortex shedding of the unsteady locally conical flow. A cylindrical afterbody is also added to the same cone to study the effect of a cylindrical part on the flow asymmetry. One of the cases of flow over a cone–cylinder configuration is validated fairly well by experimental data.

## 1. Introduction

Most flight vehicles are designed for attached flow at low angle-of-attack cruise conditions. However, for fighter aircraft or missiles under maneuvering conditions, the high angle-of-attack flight regime is of vital importance. At high angle of attack, slender bodies and highly swept wings, common to both fighter aircraft and missiles, led to extensive regions of vortical flow on the leeside of the body because of three-dimensional boundary-layer separation. If the vortices are both symmetric and stable, their influences can be exploited favorably to provide high lift and maneuverability for the vehicle. The region of favorable influence is terminated by the onset of asymmetric vortices and the occurrence of vortex breakdown. Such phenomena produce large side forces and moments, which may be larger than those attainable by the vehicle control system, thus jeopardizing flight safety.

In the next section, the physical characteristics of vortical flows about various slender bodies are described. This is followed by a survey of the experimental and computational research work on asymmetric vortex flows.

*Correspondence to:* C.H. Liu, Computational Aerodynamics Branch, NASA Langley Research Center, Hampton, VA 23681, USA.

0169-5983/92/$11.50 © 1992 – The Japan Society of Fluid Mechanics / Elsevier Science Publishers B.V.
All rights reserved

PRECEDING PAGE BLANK NOT FILMED

### *1.1. Physics and experimental work*

Keener and Chapman (1977) categorized vortical flow regimes into four distinct flow patterns for slender bodies at various angles of attack (with zero sideslip). These patterns also reflect the diminishing influence of the axial flow component (fig. 1). The first pattern develops in the very low angle-of-attack range, where the flow is attached and vortex free, and the axial flow is dominant. At moderate to high angles of attack, the crossflow influence becomes of the same order of magnitude as that of the axial flow, and large scale vortices are formed on the leeward side of bodies because of three-dimensional boundary-layer separation. In this angle-of-attack range, the vortices are both stable and symmetric, and the large increments in normal force due to the low pressure induced on the leeward surface by the vortices can be exploited to aerodynamic advantage. A majority of the research work in vortical flows has been focused on understanding this symmetric flow pattern. At even higher angles of attack, the crossflow effects start to dominate and the vortices may lose their stability or even symmetry, which may lead to asymmetric vortices about a symmetric body or breakdown of the vortices. Either phenomenon may occur in a quasi-steady or unsteady fashion. Both the asymmetric disposition of the vortices and vortex breakdown give rise to sudden and potentially catastrophic changes in side-force and moment characteristics. Hence, prediction and understanding of the onset of vortex asymmetry and vortex breakdown are essential. The fourth flow pattern develops at extremely high angles of attack (up to 90°), where the crossflow influence dominates completely, and the leeside flow is characterized by an unsteady diffuse wake, with the possibility of having either random or periodic vortex shedding depending upon the Reynolds number, Mach number, and geometric details. The asymmetric time-dependent vortex shedding is similar to the von Kármán vortex sheet in two-dimensional flows around cylinders.

Historically, highly swept, round and sharp leading-edge wings and pointed slender bodies are common generic models for the principal components of real fighter aircraft and missiles. The study of vortical flows around these isolated aerodynamic components plays an important role in the understanding of vortex flows under various conditions including unsteady vortex-dominated flows, vortex/shock interaction, asymmetric vortex flow, and vortex breakdown. For the design of modern fighter aircraft and missiles, the prediction of the onset of vortical flow asymmetry is essential. For isolated pointed forebodies, the onset of asymmetry occurs when the relative incidence (ratio of angle of attack to semiapex angle of the forebody)

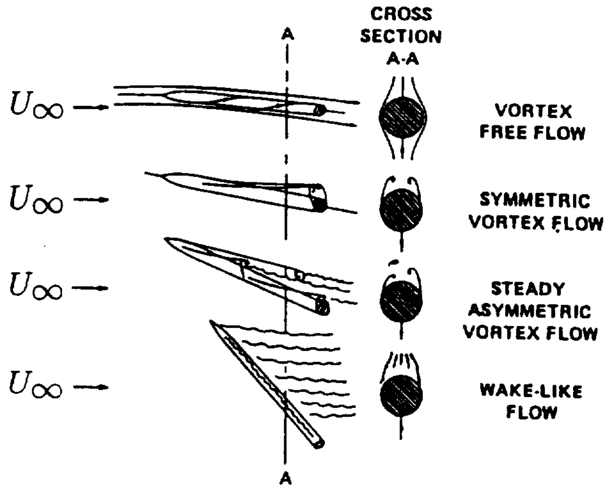

Fig. 1. Effect of angle of attack on leeside flow field.

exceeds a certain value, e.g., for a pointed circular cone, the relative incidence must be higher than two, which has been documented by Peake and Tobak (1982). This flow pattern develops about symmetric slender bodies at zero-degree sideslip in response to small perturbations in body geometry at the nose or in the flight conditions such as transient sideslip and acoustic disturbances. The sudden changes in side force and moment characteristics resulting from the asymmetry, in many instances, are sufficiently large to trigger an aircraft or missile to spin. At relative incidences near the onset of the asymmetry, the flow is nominally steady. At sufficiently high relative incidences, the flow becomes unsteady and asymmetric, with vortex shedding either randomly or periodically.

The literature and recent research work, both computational and experimental, show extensive work in the area of study of symmetric vortex flows. Surprisingly, very limited research work exists in the area of steady and unsteady asymmetric flows. Recently, a small number of computational research studies by several investigators have focused on predicting and analyzing the onset of flow asymmetry over slender bodies. This asymmetric vortex formation is still an outstanding problem whose physics are poorly understood. While experimental studies have produced flow visualization of steady and unsteady asymmetric flows on slender bodies, the mechanisms which lead to flow asymmetry are not well understood.

Currently, two mechanisms exist in the literature for explaining the evolution of asymmetry (for example, Peak and Tobak, 1982; Skow and Peake, 1982; Lamont, 1982; Yanta and Wardlaw, 1982). The first of two these hypotheses appears to operate in both the laminar and fully turbulent separation regimes. It suggests that the asymmetry occurs because of the instability of the velocity profiles in the vicinity of the saddle point that exists in the crossflow planes above the projections of the body vortices. The second hypothesis relates the asymmetry to the occurrence of asymmetric boundary-layer transition, leading to an effectively asymmetric mean flow about a given body. The onset of asymmetry over slender bodies is accompanied by a rapid, local asymmetric movement of the secondary separation line and then the primary separation lines circumferentially, precipitated by an asymmetric transition region. Although the second mechanism is operable only within the transition zone, the former mechanism plays a role in both laminar and fully turbulent flows. For pointed slender bodies, the first mechanism produces higher side forces than those produced by the second mechanism. Indeed, the implications from the experimental work of Lamont (1980, 1982) with tangent-ogive cylinders is that the vortex wake is less structured in the transition domain, leading to reduced side and normal forces. In the laminar or fully turbulent regions, the vortex structure is well organized, giving rise to larger forces.

The asymmetric vortex wake usually develops from asymmetric separation line positions on the body, but the latter does not appear to be a necessary condition for the former to occur. Asymmetric flow has been documented for sharp-edge delta wings where the primary separation is fixed at the leading edge (for example, Shanks, 1963; Keener and Chapman, 1977; Ayoub, 1987; Rediniotis and Telionis, 1989). Generally, even though the separation lines are fixed at the sharp leading edges, asymmetry occurs at higher relative incidences than those obtained with smooth pointed forebodies or forebody–cylinder configurations. The occurrence of asymmetry is attributed to the hydrodynamic instability in the vortex flowfield resulting from the crowding together of the vortices as the wing semi-nose angle is decreased.

The obvious challenges to computational fluid dynamicists is to simulate the asymmetric vortex flows through the existing two hypothesized mechanisms, which has been discussed earlier. The second challenge is to investigate the determinable parameters for the onset of vortical flow asymmetry. These challenges represent the motivation behind the present paper.

### *1.2. Computational work*

Recently, several attempts have been carried out to computationally simulate steady and unsteady asymmetric vortical flows around slender bodies of revolution. Graham and Hankey (1982) presented the first attempt to compute asymmetric vortical flow over a cone-cylinder body, which had been tested experimentally by Thomson and Morrison (1971). They used the MacCormack explicit finite-difference scheme to solve the unsteady full Navier–Stokes equations for a laminar flow on a relatively coarse grid. The computed asymmetric vortical flow was found to be numerically induced by the MacCormack algorithm by its noncentered spatial differencing. It was believed that a very small perturbation was induced by the finite-difference algorithm truncation error, which triggered an instability at the saddle point above the body. Hence, the instability was induced by numerical bias which was physically amplified to produce the asymmetry. By switching the algorithm's sweep direction, the asymmetry pattern was reversed. Discrepancies between numerical and wind-tunnel results were attributed to insufficient grid resolution, since small disturbances would not be amplified on the coarse grid.

In an attempt to simulate asymmetric vortex flow around an ogive-cylinder body at very high angles of attack and at subsonic speeds, Degani and Schiff (1989) obtained asymmetric flow solutions to the thin-layer Navier–Stokes equations by introducing a forced asymmetric disturbance near the body nose in the form of a small surface jet. When the jet was turned off, the flow asymmetry was dissipated and the flow recovered its symmetry. In a later paper by Schiff, Degani and Gavali (1989), the unsteady, thin-layer Navier–Stokes equations were used to compute the same problem. Vortex unsteadiness developed with increasing angles of attack. The behavior of the fluctuations with incidence paralleled the trends observed in experiments by Degani and Zilliac (1988). Degani (1990) used the same computational scheme to predict the flow around the same ogive-cylinder body for angles of attack $\alpha = 20°$ to 80°. His numerical experiments were focused on investigating the origin of the vortex asymmetry. Based on his results, the flow field around slender bodies was divided into three main groups, depending on the angle-of-attack range. In the range $0° < \alpha < 30°$, the results show that the flow was symmetric and introduction of small disturbances near the nose had only a small effect on the flow asymmetry. In the second range, $30° < \alpha < 60°$, the flow became steady asymmetric upon introduction of a spaced-fixed forced disturbance near the nose. However, when the disturbance was removed, the flow recovered its symmetric shape. The origin of asymmetry was attributed to a convective-type instability mechanism. In the very high range, $60° < \alpha < 80°$, the flow became unsteady with vortex shedding upon introduction of a small transient disturbance with short duration. The origin of flow unsteadiness and vortex shedding was attributed to an absolute-type instability mechanism. Although this investigation revealed good tentative conclusions, there are several remaining questions to be addressed. These questions are related to the dissipative effects of the scheme, particularly in the crossflow planes, and to the grid fineness and its resolution of the disturbance growth.

Steady solutions of the incompressible, full Navier–Stokes equations for vortical flow over a sideslipping delta wing have first been presented by Hsu and Liu (1990). Results were compared with measured data for force and moment coefficients as well as vortex-core positions. However, the vortical strength was underpredicted, because of either a lack of grid resolution in the vortical region or an inadequate turbulence model for this massively separated flow. Strong flow asymmetry was obtained due to the 12° sideslip angle.

Asymmetric vortical flow simulation due to various types of short-duration disturbances was attempted by several investigators. Siclari and Marconi (1989) also used the unsteady, full Navier–Stokes equations with a multi-grid, central-difference, finite-volume scheme to solve for steady, asymmetric, locally-conical flows around a 5° semiapex-angle cone over a wide range of angles of attack. At very high incidences, a steady asymmetric solution was captured. Later, the same scheme was applied to solve for steady, asymmetric, locally conical flows around cones with elliptic, diamond, and biparabolic sections (Siclari, 1990).

The present authors (Liu et al., 1990; Kandil et al., 1990a–c) investigated the prediction and control of asymmetric supersonic vortex flows around circular and noncircular cones over wide ranges of angles of attack, Mach numbers, and Reynolds numbers with locally conical flow assumptions. Unsteady asymmetric vortex flows with periodic vortex shedding were captured using several different schemes. Later, Kandil et al. (1991a) compared the asymmetric flow solutions using thin-layer Navier–Stokes and full Navier–Stokes equations. The three-dimensional asymmetric flow solutions around circular cones and cone-cylinder configurations were also studied by the Kandil et al. (1991b). A comprehensive review of the research work done by the present authors is presented in the next section.

### *1.3. Present work*

In this work, the unsteady, compressible, thin-layer Navier–Stokes equations are used to study supersonic, asymmetric, vortical flows. The onset of flow asymmetry occurs when the relative incidence of pointed forebodies exceeds certain critical values. At these critical values of relative incidence, flow asymmetry develops due to natural and/or forced disturbances. In actual flows, the origin of natural disturbances may be a transient sideslip, an acoustic disturbance, or similar disturbances of short duration. The origin of forced disturbances may be geometric imperfections in the nose region or similar disturbances of a permanent nature. The present work is focused on the evolution of flow asymmetry due to assumed natural-type disturbances. Two types of flow disturbances are studied: a random round-off error disturbance and a controlled transient sideslip disturbance with short duration. In addition to relative incidence as one of the determinable parameters for the onset of flow asymmetry, the effects of free-stream Mach number, Reynolds number, and cylindrical afterbody are studied and have been determined to be important parameters.

Because of the expensive computational resources required for solving three dimensional problems, the first part of the computational studies have been applied to supersonic, locally conical flows around point cones. Therefore, the mechanism for the onset of steady and unsteady flow asymmetry can be studied efficiently and delineated by solving the locally conical problems before the three-dimensional problems are examined. In the second part, three-dimensional asymmetric supersonic flows over a cone and cone-cylinder configurations are investigated, based on the study of the locally conical flow solutions.

## 2. Formulation

In high Reynolds number viscous flows the effects of viscosity are mostly concentrated in narrow regions adjacent to solid bodies and in narrow regions of freeshear layers. Owing to computer memory limitations, only a limited number of grid points is available for clustering mesh points in these regions. As a result, fine-grid spacing is used in directions which are nearly normal to these regions, and coarse-grid spacing must be used tangent to these regions. In boundary-layer theory, perturbation analysis shows that streamwise components of the viscous terms can be neglected relative to those in the normal direction. Similar arguments can be applied to the Navier–Stokes equations as a justification for the thin-layer approximation. The thin-layer approximation is not the same as the boundary-layer approximation, since an approximate form of the normal momentum equation is retained and pressure variation across the boundary-layer thickness is taken into consideration. The thin-layer approximation breaks down for low Reynolds numbers and a regions where viscous effects become significant in all directions. Of course, the full Navier–Stokes equations can be incorporated if sufficient resolution is provided by the limited grid and if the physical situation warrants it. Therefore, in the present work, thin-layer Navier–Stokes equations are chosen to formulate two- and three-dimensional flow problems.

### *2.1. Thin-layer Navier–Stokes equations*

In many computational applications, the body surface is a boundary of the computational domain, and hence the use of body conformal coordinates makes the surface boundary condition easy to apply. The transformation of the governing equations from the physical Cartesian coordinate system $(x_1, x_2, x_3)$, to time-independent curvilinear coordinates, $(\xi^1, \xi^2, \xi^3)$, is given by

$$\xi^m = \xi^m(x_1, x_2, x_3). \tag{1}$$

Using the above transformation, the thin-layer Navier–Stokes equations are

$$\partial\hat{\boldsymbol{q}}/\partial t + \partial\hat{\boldsymbol{E}}_m/\partial\xi^m - \partial(\hat{\boldsymbol{E}}_{\mathrm{v}})_3/\partial\xi^3 = 0, \quad m = 1, 2, 3, \tag{2}$$

where the flowfield vector, $\hat{\boldsymbol{q}}$, is given by

$$\hat{\boldsymbol{q}} = J^{-1}\boldsymbol{q} = J^{-1}\begin{pmatrix} \rho \\ \rho u_1 \\ \rho u_2 \\ \rho u_3 \\ e_{\mathrm{t}} \end{pmatrix}, \tag{3}$$

the inviscid fluxes, $\hat{\boldsymbol{E}}_m$, are given by

$$\hat{\boldsymbol{E}}_m = J^{-1}\begin{pmatrix} \rho U_m \\ \rho u_1 U_m + \xi^m_{x_1} p \\ \rho u_2 U_m + \xi^m_{x_2} p \\ \rho u_2 U_m + \xi^m_{x_3} p \\ U_m(e_{\mathrm{t}} + p) \end{pmatrix}, \tag{4}$$

and the viscous and heat-conduction flux in $\xi^3$ direction, $(\hat{\boldsymbol{E}}_{\mathrm{v}})_3$, is given by

$$(\hat{\boldsymbol{E}}_{\mathrm{v}})_3 = J^{-1}\begin{pmatrix} 0 \\ \xi^3_{x_j}\tau_{j1} \\ \xi^3_{x_j}\tau_{j2} \\ \xi^3_{x_j}\tau_{j3} \\ \xi^3_{x_j} b_j \end{pmatrix}, \quad j = 1, 2, 3. \tag{5}$$

The contravariant velocity component in the $\xi^m$ direction is

$$U_m = \xi^m_{x_j} u_j, \tag{6}$$

and any element corresponding to the three momentum equations in eq. (5) is given by

$$\xi^3_{x_j}\tau_{jl} \equiv \frac{\mu M_\infty}{\mathrm{Re}}\left(\tfrac{1}{3}\xi^3_{x_l}\xi^3_{x_j}\frac{\partial u_j}{\partial\xi^3} + \xi^3_{x_j}\xi^3_{x_j}\frac{\partial u_l}{\partial\xi^3}\right), \quad l = 1, 2, 3, \tag{7}$$

where $\xi^3_{x_j} \equiv \partial\xi^3/\partial x_j$. The last element in eq. (5) is

$$\xi^3_{x_j} b_j = \frac{\mu M_\infty}{\mathrm{Re}}\left[\tfrac{1}{3}\xi^3_{x_j}\frac{\partial u_j}{\partial\xi^3}U_3 + \xi^3_{x_j}\xi^3_{x_j}\left(u_k\frac{\partial u_k}{\partial\xi^3} + \frac{1}{(\gamma-1)\mathrm{Pr}}\frac{\partial a^2}{\partial\xi^3}\right)\right]. \tag{8}$$

In eq. (5), the $\tau$s represent the Cartesian components of the shear-stress tensor for a Newtonian fluid, assuming Stokes hypothesis and the $b$s are the shear-dissipation power and conduction heat transfer. The inverse of the Jacobian matrix of transformation is

$$J^{-1} = \frac{\partial(x_1, x_2, x_3)}{\partial(\xi^1, \xi^2, \xi^3)} = \begin{vmatrix} x_{1\xi^1} & x_{1\xi^2} & x_{1\xi^3} \\ x_{2\xi^1} & x_{2\xi^2} & x_{2\xi^2} \\ x_{3\xi^1} & x_{3\xi^2} & x_{3\xi^3} \end{vmatrix}, \tag{9}$$

and the metric terms are

$$\frac{\partial\xi^n}{\partial x_m} = \tfrac{1}{2}J^{-1}e_{ijn}e_{lkm}\frac{\partial x_l}{\partial\xi^i}\frac{\partial x_k}{\partial\xi^j}, \tag{10}$$

where $e_{ijn}$ and $e_{ikm}$ are the permutation symbols.

For convenience, all the tensors are expressed in indicial notation. The flow variables are introduced in non-dimensional form, and each is referenced to its appropriate free-stream value. The non-dimensional density, $\rho$, Cartesian velocity components $u_1$, $u_2$, $u_3$, total energy $e_t$, viscosity $\mu$, and speed of sound $a$, are defined as the ratio of the corresponding physical quantities to those in the free stream, namely $\rho_\infty$, $a_\infty$, $\rho_\infty a^2_\infty$, $\mu_\infty$, and $a_\infty$, respectively. The pressure, $p$, is non-dimensionalized by $\rho_\infty a^2_\infty$, and is related to the total energy for an ideal gas by the equation

$$p = (\gamma - 1)\left(e_t - \tfrac{1}{2}\rho u_j u_j\right), \tag{11}$$

where $\gamma$ is the ratio of specific heats, and its value is taken to be 1.4 in the present research work. The coordinates $x_1$, $x_2$, $x_3$, and time, $t$, are non-dimensionalized by a characteristic length, $L$, and a characteristic time, $L/a_\infty$, respectively. The viscosity, $\mu$, is evaluated by using Sutherland's law

$$\mu = T^{3/2}[(1 + C)/(T + C)], \tag{12}$$

where $T$ is the temperature and $C$ is the Sutherland constant, which is 110.4 K. The Prandtl number, Pr, is chosen to be 0.72. The Reynolds number is defined as $\mathrm{Re} = \rho_\infty U_\infty L/\mu_\infty$, and the characteristic length, $L$ is chosen as the length of the body.

The values of all the free-stream flow quantities which are used as the initial conditions for all applications are given as follows:

$$\begin{gathered} \rho_\infty = 1, \quad u_{1\infty} = M_\infty \cos\alpha\cos\beta, \quad u_{2\infty} = -M_\infty \sin\beta, \\ u_{3\infty} = M_\infty \sin\alpha\cos\beta, \quad e_{t\infty} = 1/\gamma(\gamma-1) + \tfrac{1}{2}M^2_\infty, \quad p_\infty = 1/\gamma, \\ a_\infty = T_\infty = 1, \quad U_\infty = (u_{j\infty}u_{j\infty})^{1/2}, \quad M_\infty = U_\infty/a_\infty, \end{gathered} \tag{13}$$

where $M_\infty$ is the free-stream Mach number, $\alpha$ is the angle of attack, and $\beta$ is the sideslip angle.

### 2.2. Locally conical Navier–Stokes equations

For supersonic flows, the three-dimensional Navier–Stokes equations can be transformed into the simpler conical flow equations by using the conical coordinates, $X$, $Y$, and $Z$, with

$$X = x_1, \quad Y = x_2/x_1, \quad Z = x_3/x_1. \tag{14}$$

Physically, a conical flow has the property that all flow quantities are invariant along rays that emanate from the apex of the conical surface. Using eq. (14) to transform the full Navier–Stokes equations to $X$, $Y$, $Z$ coordinates and imposing the conical flow property, the resulting equations in abstract form are given by

$$X\frac{\partial \boldsymbol{q}}{\partial t}+\frac{\partial(\boldsymbol{F}-\boldsymbol{F}_{\mathrm{v}})}{\partial Y}+\frac{\partial(\boldsymbol{G}-\boldsymbol{G}_{\mathrm{v}})}{\partial Z}+2(\boldsymbol{E}_1-\boldsymbol{E}_{\mathrm{v}1})=0, \tag{15}$$

where the inviscid fluxes are

$$\boldsymbol{F}=\boldsymbol{E}_2-Y\boldsymbol{E}_1=\begin{pmatrix}\rho u_2\\ \rho u_1u_2\\ \rho u_2^2+p\\ \rho u_2u_3\\ u_2(e_t+p)\end{pmatrix}-Y\begin{pmatrix}\rho u_1\\ \rho u_1^2+p\\ \rho u_1u_2\\ \rho u_1u_3\\ u_1(e_t+P)\end{pmatrix}, \tag{16}$$

$$\boldsymbol{G}=\boldsymbol{E}_3-Z\boldsymbol{E}_1=\begin{pmatrix}\rho u_3\\ \rho u_1u_3\\ \rho u_2u_3\\ \rho u_3^2+p\\ u_3(e_t+p)\end{pmatrix}-Z\begin{pmatrix}\rho u_1\\ \rho u_1^2+p\\ \rho u_1u_2\\ \rho u_1u_3\\ u_1(e_t+p)\end{pmatrix}, \tag{17}$$

and the viscous fluxes are

$$\boldsymbol{F}_{\mathrm{v}}=\boldsymbol{E}_{\mathrm{v}2}-Y\boldsymbol{E}_{\mathrm{v}1}=\begin{pmatrix}0\\ \tau_{21}\\ \tau_{22}\\ \tau_{23}\\ b_2\end{pmatrix}-Y\begin{pmatrix}0\\ \tau_{11}\\ \tau_{12}\\ \tau_{13}\\ b_1\end{pmatrix}, \tag{18}$$

$$\boldsymbol{G}=\boldsymbol{E}_{\mathrm{v}3}-Z\boldsymbol{E}_{\mathrm{v}1}=\begin{pmatrix}0\\ \tau_{31}\\ \tau_{32}\\ \tau_{33}\\ b_3\end{pmatrix}-Z\begin{pmatrix}0\\ \tau_{11}\\ \tau_{12}\\ \tau_{13}\\ b_1\end{pmatrix}. \tag{19}$$

The shear stresses, dissipation power, and heat transfer terms are obtained by using chain-rule differentiation and enforcing the conical flow property, i.e. all derivatives in the $X$-direction are zero. For example, the principal stress, $\tau_{11}$, can be simplified as

$$\tau_{11}=-\frac{2\mu M_\infty}{\mathrm{Re}X}\left(2Y\frac{\partial u_1}{\partial Y}+2Z\frac{\partial u_2}{\partial Z}+\frac{\partial u_2}{\partial Y}+\frac{\partial u_3}{\partial Z}\right). \tag{20}$$

The resulting equations (15) have spatial variation in the $Y$- and $Z$-directions only. Thus, these equations are two-dimensional equations with source terms. Hence, they are more economical to solve than the three-dimensional equations. It is also noticed that the time-derivative term in eq. (15) is multiplied by $X$ and an axial length-scale dependence exists in the viscous terms (20). Hence, eq. (15) is not self-similar in $X$-direction, and thus it does not represent a globally conical flow. Only the steady inviscid flow equation represents a globally conical flow. However, for unsteady viscous flow over a conical body, if $X$ is fixed at a certain location, the flow may be thought of as "locally conical", with the Reynolds number determining the location of the conical plane in which eq. (15) is solved. The best that can be done to make use of this equation is to select a constant value for $X$, and solve the resulting equation for what we call "locally conical flow".

## 3. Computational scheme

The computational scheme used to solve the governing equations is an implicit, upwind-biased flux-difference splitting, finite-volume scheme. The discretized equation is integrated numerically in time using the Euler implicit time-differencing method. The linearized, backward-time approximation for the flowfield vector is written in the delta form as

$$\left[\frac{I}{J\,\Delta t} - \left(\frac{\partial R}{\partial \hat{\boldsymbol{q}}}\right)^{n}\right] \Delta \hat{\boldsymbol{q}}^{n} = R(\hat{\boldsymbol{q}}^{n}), \tag{21}$$

where

$$\Delta \hat{\boldsymbol{q}}^{n} = \hat{\boldsymbol{q}}^{n+1} - \hat{\boldsymbol{q}}^{n},$$

$$R(\hat{\boldsymbol{q}}^{n}) = -\left[\delta_{\xi^{j}}\left(\hat{\boldsymbol{E}}_{j}\right)^{n} - \delta_{\xi^{3}}\left(\hat{\boldsymbol{E}}_{\mathrm{v}}\right)_{3}^{n}\right]. \tag{22}$$

In eq. (22), $\delta_{\xi^{j}}$ is the spatial difference operator. The convective and pressure terms are discretized using the flux-difference splitting scheme of Roe and differenced using the MUSCL (Monotone Upstream-centered Scheme for Conservation Laws) of van Leer. The flux-difference splitting of Roe is based on the approximate Riemann problem. The Riemann problem is used as a mechanism to divide the flux difference between the neighboring states, such as the interface of two computational cells, into component parts associated with each wave field. As each eigenvalue is also associated with its own wave field, so the splitting can be done based on the eigenvalues. The smooth flux limiters are used to eliminate oscillations in the shock region, and the viscous and heat-flux terms are centrally differenced. The resulting difference equations are solved using a spatially split approximate factorization along the $\xi^1$, $\xi^2$, $\xi^3$ directions, respectively. The scheme is first-order accurate in time and third order accurate in space. Details of the above described scheme are given by Wong (1991).

Since the applications in this paper cover some locally conical flow problems, locally conical flow solutions can be obtained by solving the problem in three conical planes using a three-dimensional solver. This is achieved by setting the conserved components of the flowfield vector, $\hat{\boldsymbol{q}}$, to be equal at two planes. All of the locally conical solutions in the present work are obtained in this way.

### 3.1. Initial and boundary conditions

All the numerical calculations of the steady-flow problems are obtained by using impulsively-started initial conditions, i.e. bodies are suddenly placed in the free stream at angles of attack specified by the problem. For unsteady-flow problems, solutions obtained from the pseudo time-stepping calculation corresponding to the same flow conditions are used as initial conditions in order to save the computational cost for the transient state.

The boundary conditions for the present work are implemented explicitly. On the solid boundary, the no-slip and no-penetration conditions are enforced, i.e. $u_1 = u_2 = u_3 = 0$, and the normal pressure gradient is assumed to be zero. The adiabatic condition is maintained on solid surface.

To obtain a locally conical flow or three-dimensional solution for supersonic free-stream Mach numbers, the computational domain is extended far enough to permit capture of the bow-shock formed outside of the body as part of the solution. Since the disturbance from the body will not propagate beyond the bow-shock in the crossflow plane, the conditions outside the conical shock are the same as the free-stream conditions. Therefore, the farfield boundary conditions are specified to be the free-stream conditions. Since the locally conical flow solutions are obtained by solving the problem in three conical planes using a three-dimensional solver, free-stream conditions are enforced on the farfield boundary of the first and third conical planes. For the three-dimensional flows, first-order extrapolation from the interior points at the outflow boundary is used. At the geometric plane of symmetry, periodic conditions are used since the problem is solved for the whole computational domain.

## 4. Results and discussion

### *4.1. Locally conical flows*

The mechanisms which lead to steady and unsteady asymmetric vortical flows past slender wings and bodies at high angles of attack at zero sideslip are not well understood. From experimental studies of these phenomena, several investigators proposed two mechanisms for explaining the origin of the flow asymmetry. These have already been described in the previous section. The first mechanism, asymmetric flow due to a saddle-point instability, is demonstrated in this section. Two types of flow disturbance, a random round-off error disturbance and a controlled transient sideslip disturbance with short duration, are used to demonstrate the mechanism which leads to flow asymmetry. In addition to the relative incidence as one of the determinable parameters for the onset of flow asymmetry, other influential parameters such as the Mach number are studied and presented in this section.

### *4.1.1. Steady asymmetric flows over a cone*

Supersonic flows over a 5° semiapex angle cone at a Reynolds number $\mathrm{Re} = 10^5$ have been computed. The grids used in all the numerical tests in this section are generated by using the modified Joukowski transformation with a geometric series for grid clustering near the cone surface. For all the cases, a grid of $161 \times 81$ points is used, where the first number is the number of points around the cone and the second number is the number of points normal to the cone surface. A $241 \times 121$ grid and a $161 \times 81$ grid with different mesh fineness ratios or different computational domain sizes have also been used to test the effect of grid fineness and domain size on the numerical solutions. A typical grid of $161 \times 81$ points is shown in fig. 2.

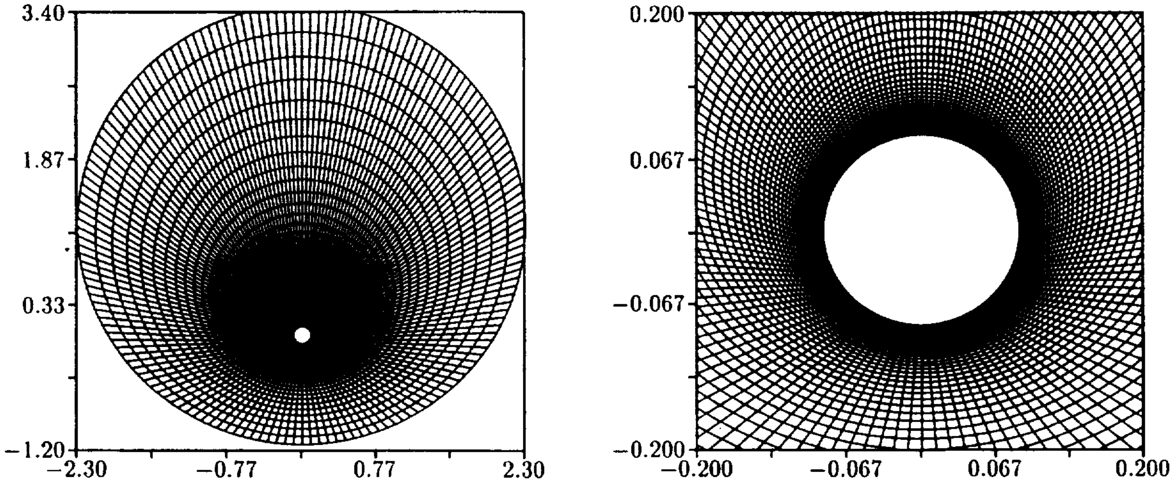

Fig. 2. A typical grid of 161×81 points for a circular cone.

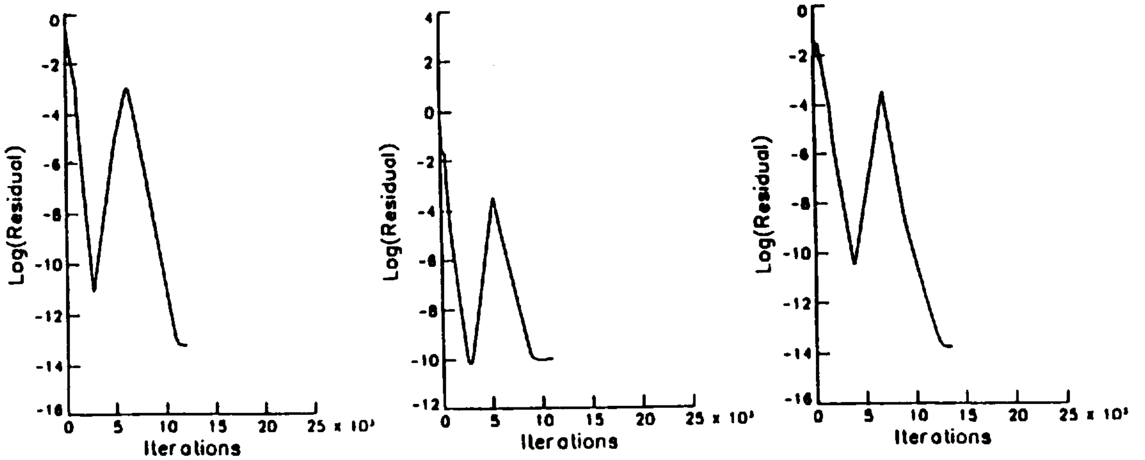

convergent history

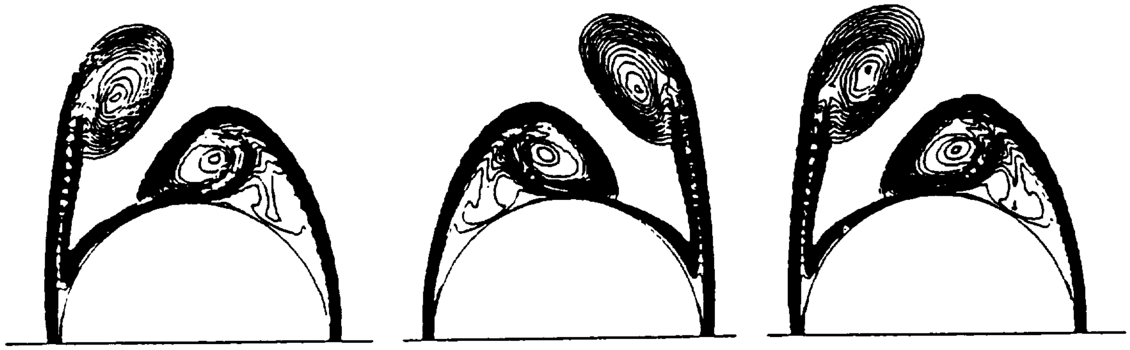

total-pressure-loss contours

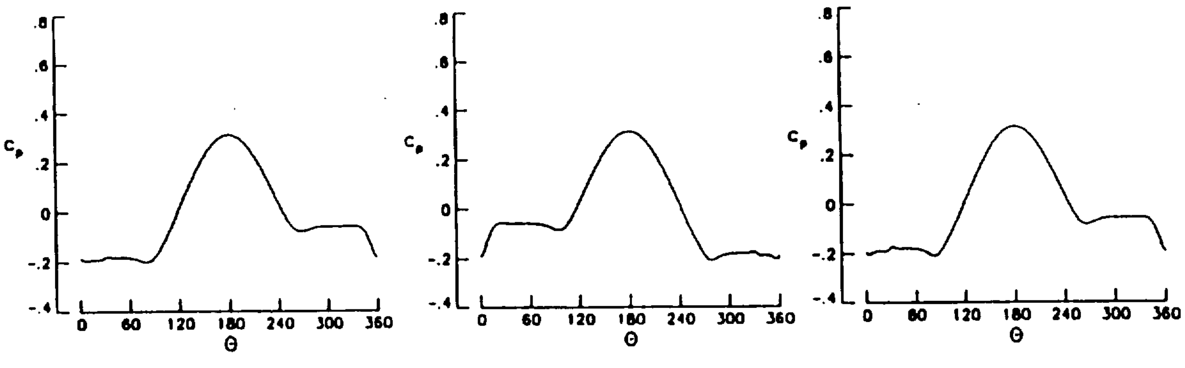

surface-pressure coefficient

(a) $\Delta\xi^3_{min} = 10^{-3}$ (b) $\Delta\xi^3_{min} = 10^{-4}$ (c) $\Delta\xi^3_{min} = 10^{-5}$

Fig. 3. Effect of minimum spacing $\Delta\xi^3_{\min}$ on the asymmetric solution ($\alpha = 20°$, $M_\infty = 1.8$, $\mathrm{Re} = 10^5$, $161 \times 81$ points, $R_l = 21r$).

To establish an optimum grid and to ensure that the asymmetric flow solution is unique, irrespective of the grid fineness and the computational domain size, numerical tests have been carried out with several different grids. The tests have computed the supersonic flow around a cone at $\alpha = 20°$, $M_\infty = 1.8$, and $\mathrm{Re} = 10^5$ (relative incidence is four for this case). A grid of $161 \times 81$ points in the circumferential and normal directions, respectively, has been used with different minimum grid spacing, $\Delta\xi^3$, at the solid boundary, while the maximum radius of the computational domain, $r_l$, is fixed at $21r$, where $r$ is the radius of the circular cone at the axial station of unity. Three cases, computed using $\Delta\xi^3 = 10^{-3}$, $10^{-4}$, and $10^{-5}$, are shown in fig. 3. In fig. 3, the logarithmic residual error versus the number of iterations, the surface pressure versus the azimuthal angle, $\Theta$, which is measured from the leeward plane of geometric symmetry, and the total-pressure-loss contours are shown. The residual error

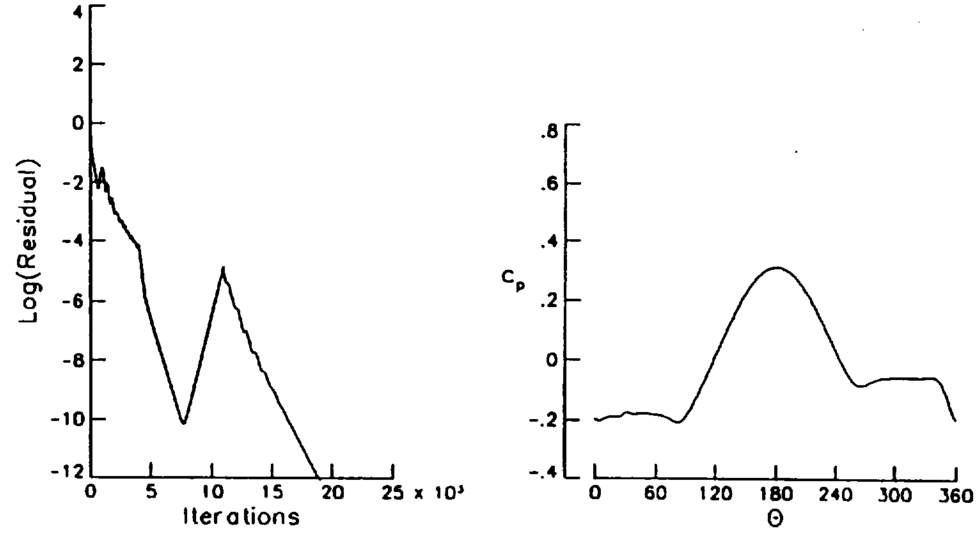

convergent history

surface-pressure coefficient

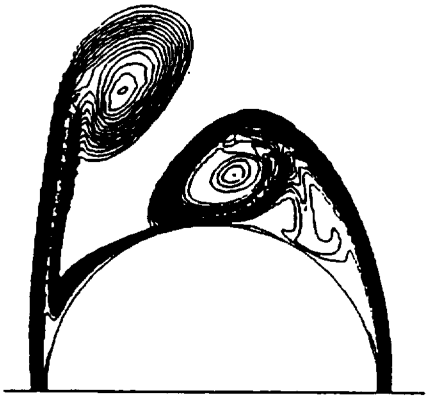

total-pressure-loss contours

Fig. 4. Effect of increased grid density on the asymmetric solution ($\alpha = 20°$, $M_\infty = 1.8$, $\mathrm{Re} = 10^5$, $241 \times 121$ points, $\Delta\xi^3_{\min} = 10^{-6}$, $R_l = 21r$).

figures show that the error reaches machine zero ($10^{-10}$ to $10^{-11}$) in about 2500 time steps in all cases and the solutions are symmetric at this point. Afterwards, with the machine round-off error is acting as a random disturbance to the flow field, the residual error grows, then drops down by at least another seven orders of magnitude, and finally stays constant thereafter (constant residual error for 2000 iterations is shown). The pressure coefficient and total-pressure-loss contours show that the flow becomes steady, asymmetric, and stable. The solution of the three cases are not necessarily the same because the source of disturbance is a random one, and it is possible that the solutions are mirror images of each other. Other types of disturbances will be discussed in the next section. Furthermore, a grid of 241 × 121 points with minimum spacing of $10^{-6}$ is used to test the effect of grid density on the asymmetric solution. Figure 4 shows the results of this case. The residual error figure shows that the error

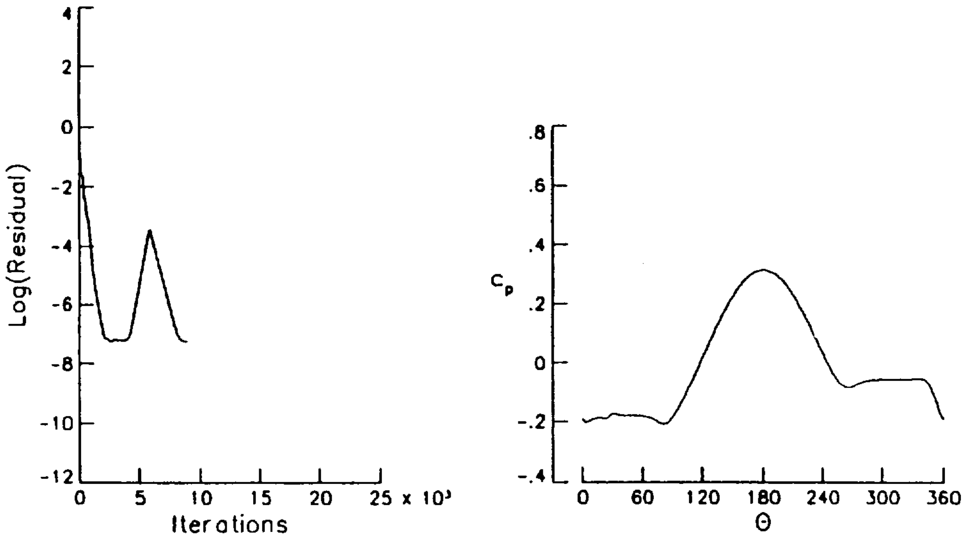

convergent history

surface-pressure coefficient

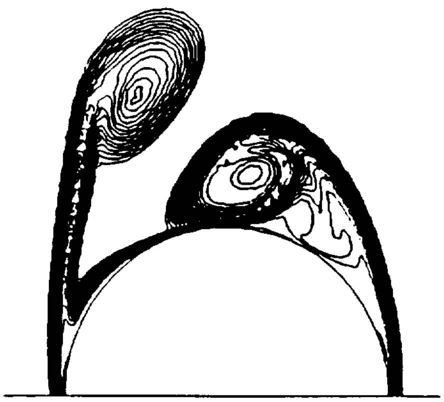

total-pressure-loss contours

Fig. 5. Effect of increased computational domain size on the asymmetric solution ($\alpha = 20°$, $M_\infty = 1.8$, Re = $10^5$, 161 × 81 points, $\Delta\xi^3_{\min} = 10^{-4}$, $R_l = 32r$).

drops ten orders of magnitude in 7500 time steps, then grows about five orders of magnitude after being triggered by the machine round-off error and then converges to the same asymmetric solution. Since the asymmetric solution is unique, irrespective of the size of minimum grid spacing and grid density, an optimum grid spacing of $10^{-4}$ is chosen in the present study.

Two grids of 161 × 81 points with the maximum computational domain radius increased from $21r$ to $32r$ are used to test the effect of the domain size on the solution. The optimum minimum spacing is used for the grid. The results of this case are shown in fig. 5. The residual history shows a similar trend in going through a symmetric unstable solution and then to an asymmetric stable solution. The pressure coefficient and total-pressure-loss contours figures

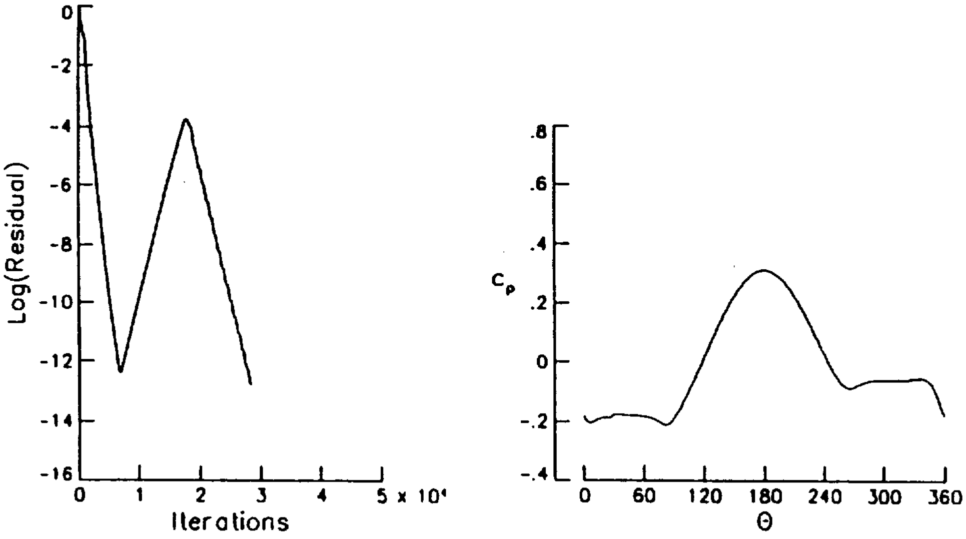

convergent history

surface-pressure coefficient

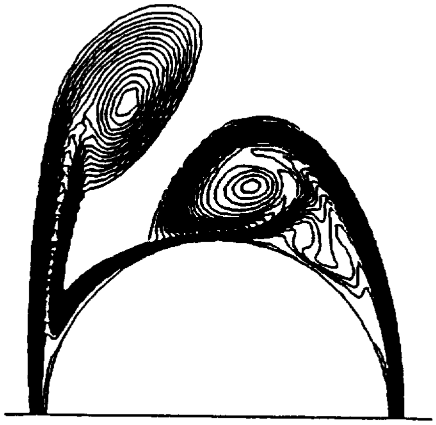

total-pressure-loss contours

Fig. 6. Effect of spatial disturbance on the asymmetric solution ($\alpha = 20°$, $M_\infty = 1.8$, Re = $10^5$, 161 × 81 points, $\Delta\xi^3_{\min} = 10^{-4}$, $R_l = 21r$).

are consistent with the results shown in fig. 3b. Thus, the optimum grid spacing of $\Delta\xi^3 = 10^{-4}$ and the maximum radius of $21r$ are chosen to be used for all the cases presented in this paper.

As mentioned in the previous section, the locally conical flow solution is obtained by forcing the equality of the flow-field vector at two cross sections, which are taken as $\xi^1 = 0.95$ and 1. A numerical test has been performed for the same flow conditions except that the solution is achieved by forcing the equality of the vector, $\hat{q}$, at $\xi^1 = 0.995$ and 1. The purpose of this task is to test the spatial disturbance on the asymmetric solution. Figure 6 shows the results of convergence history, pressure coefficient, and total-pressure-loss contours. The

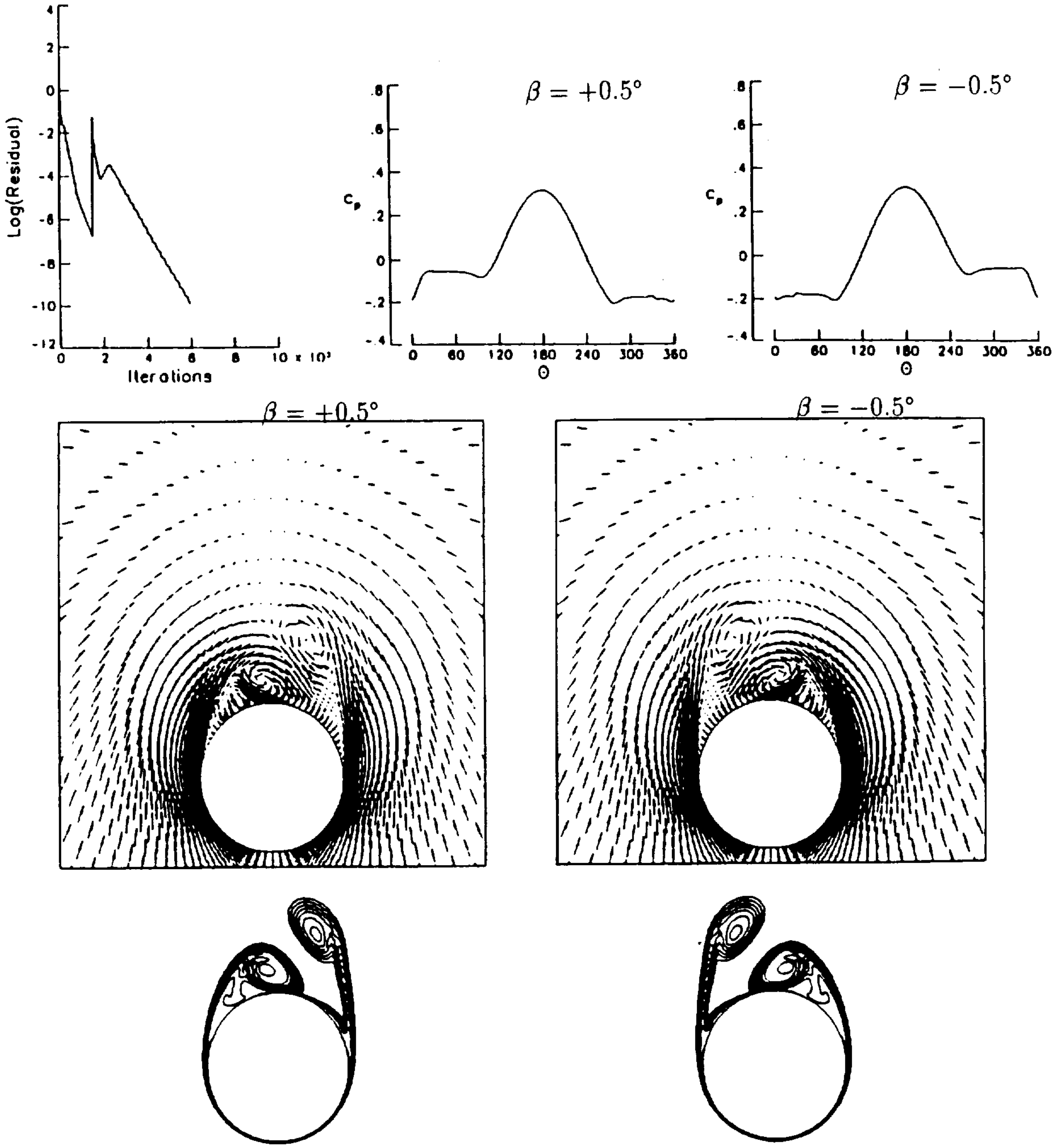

Fig. 7. Steady asymmetric flow solution for circular cone due to ±0.5° transient sideslip ($\beta$) ($\alpha = 20°$, $M_\infty = 1.8$, $Re = 10^5$).

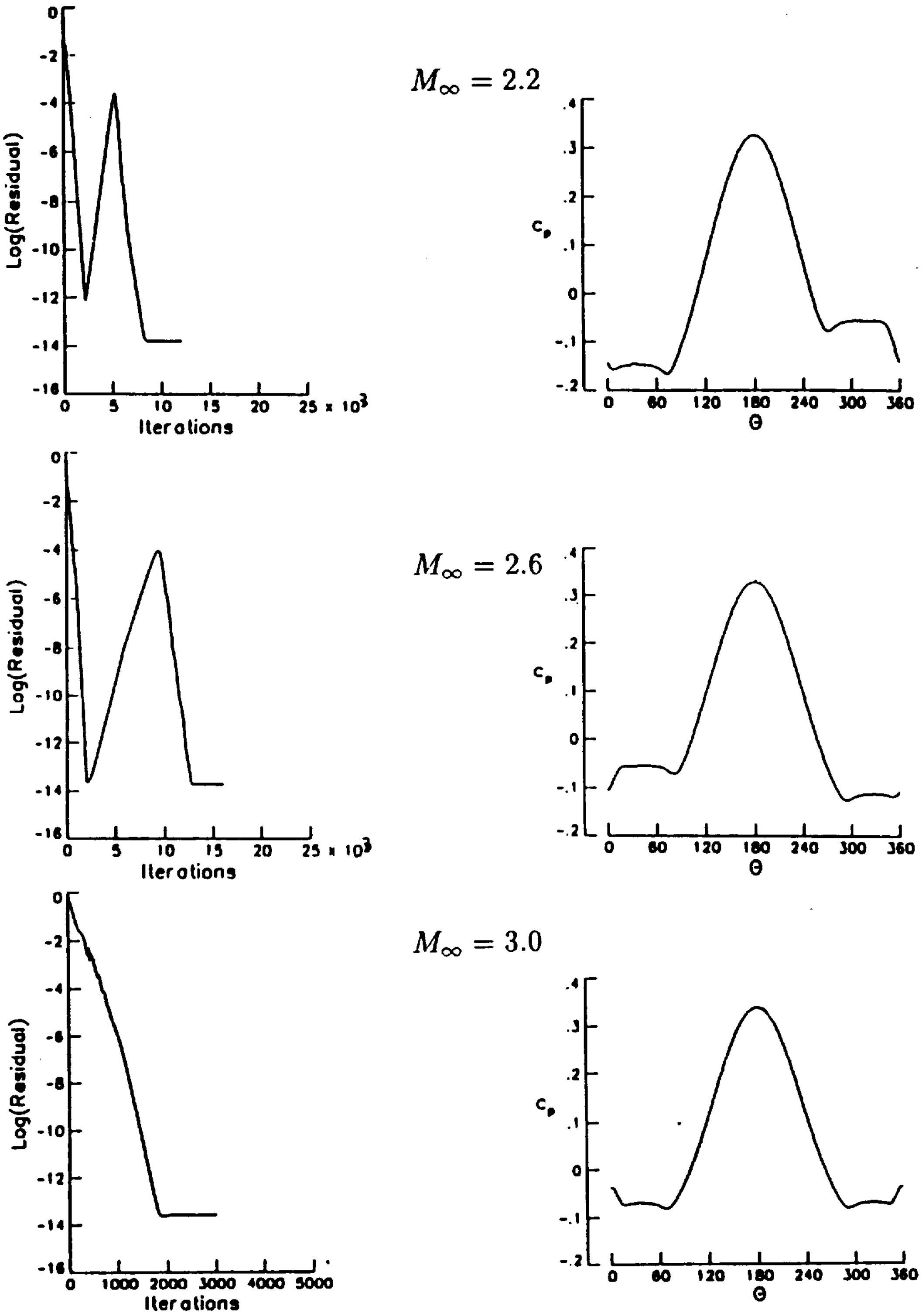

Fig. 8. Comparison of residual-error history and surface pressure for circular cone at different Mach numbers ($\alpha = 20°$, $Re = 10^5$).

residual error shows that the solution takes larger number of time steps for the asymmetry to be triggered by the machine round-off error. However, the surface pressure and the total-pressure-loss contours confirm the uniqueness of the asymmetric solution. Since $\Delta\xi^1 = 0.005$ is a small disturbance to the locally conical flow assumption, it is reasonable to have longer time steps to obtain the asymmetric solutions. To efficiently use of the limited computational resources, $\Delta\xi^1 = 0.05$ is used for all the locally conical flow problems in the present work.

Since the magnitude of residual errors shown in the above cases is so small, it is believed that the disturbance which triggered the flow asymmetry can be attributed to the machine

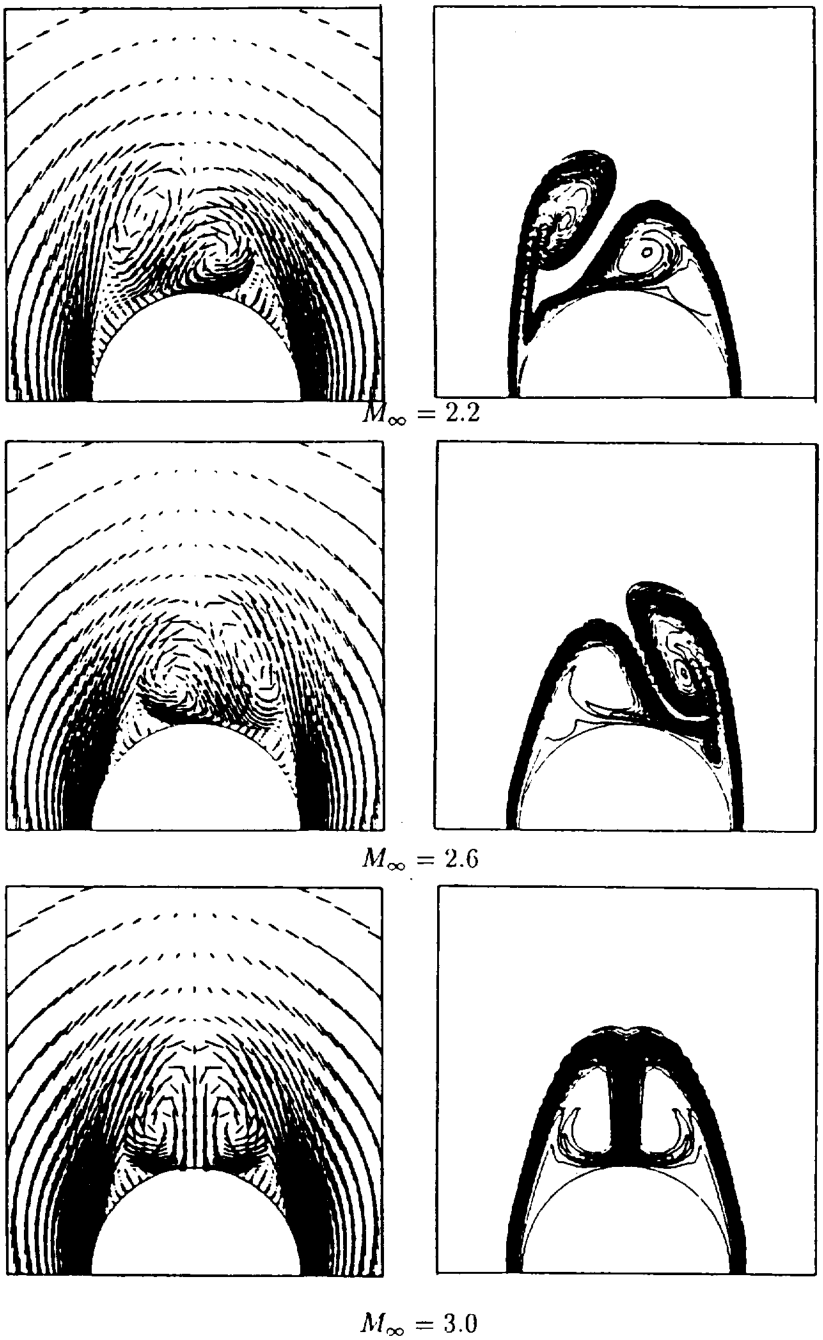

Fig. 9. Comparison of crossflow velocity vectors and total-pressure-loss contours for circular cone at different Mach numbers ($\alpha = 20°$, $\mathrm{Re} = 10^5$).

round-off error. This type of disturbance is random in nature. In the next section, the results of a controlled type of disturbance are presented.

### *4.1.2. Controlled transient sideslip disturbance*

In this section, steady asymmetric flow solutions due to a transient sideslip disturbance of short duration are presented. Results of the transient sideslip, $\beta = \pm 0.5°$, are shown in fig. 7. The residual error figures show a drop of seven orders of magnitude in the first 2000 time steps. At this step, a sideslip disturbance is imposed for six time steps, then it is removed. Irrespective of the magnitude or the direction of the sideslip disturbance, the residual error increases by six orders of magnitude, then drops down very rapidly and a stable asymmetric flow solution is obtained. The asymmetric solutions corresponding to the $\pm 0.5°$ sideslip disturbances are mirror images of each other, as can be seen from the surface-pressure distributions, crossflow velocity vectors, and total-pressure-loss contours. Moreover, the final stable asymmetric solutions of the $\pm 0.5°$ sideslip disturbances are the same or mirror images as those from random disturbances shown in figs. 3–5.

### *4.1.3. Steady asymmetric flow at different Mach numbers*

Using the same optimum grid and the same 5° semiapex angle cone at $\alpha = 20°$, three cases of locally conical flow solutions with free-stream Mach numbers ranging from 2.2 to 3.0 have been computed. The effect of the free-stream Mach number on the convergence history, surface pressure, crossflow velocity, and total-pressure-loss contours are shown in fig. 8 and 9. At $M_\infty = 2.2$, the residual error shows that the stable asymmetric flow is obtained within the same number of time steps as that of the $M_\infty = 1.8$ case. At $M_\infty = 2.6$, the residual error shows that the final asymmetric solution is obtained after a larger number of time steps. At $M_\infty = 3.0$, no asymmetric flow has been captured and the flow stayed symmetrically stable. The surface pressure figures show that the flow asymmetry gets weaker as the Mach number is increased. This conclusion is strongly supported by the crossflow velocity vectors and the total-pressure-loss contours, as shown in fig. 9. It is also noted that since the nature of disturbance is random, flow asymmetry changes sides as the Mach number increases, until it disappears. The significant feature of these numerical tests is that the asymmetric/symmetric

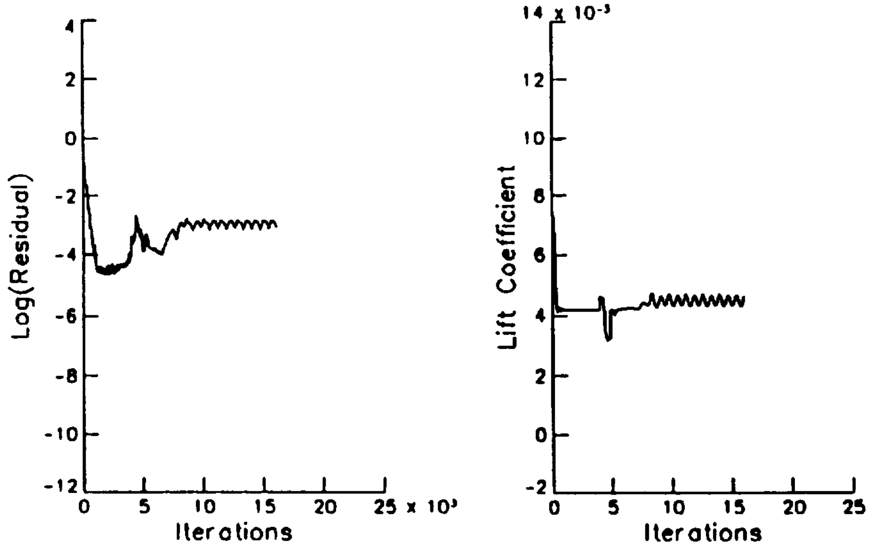

Fig. 10. Time histories of residual error and lift coefficient for unsteady asymmetric flow around circular cone ($\alpha = 30°$, $M_\infty = 1.8$, $\mathrm{Re} = 10^5$).

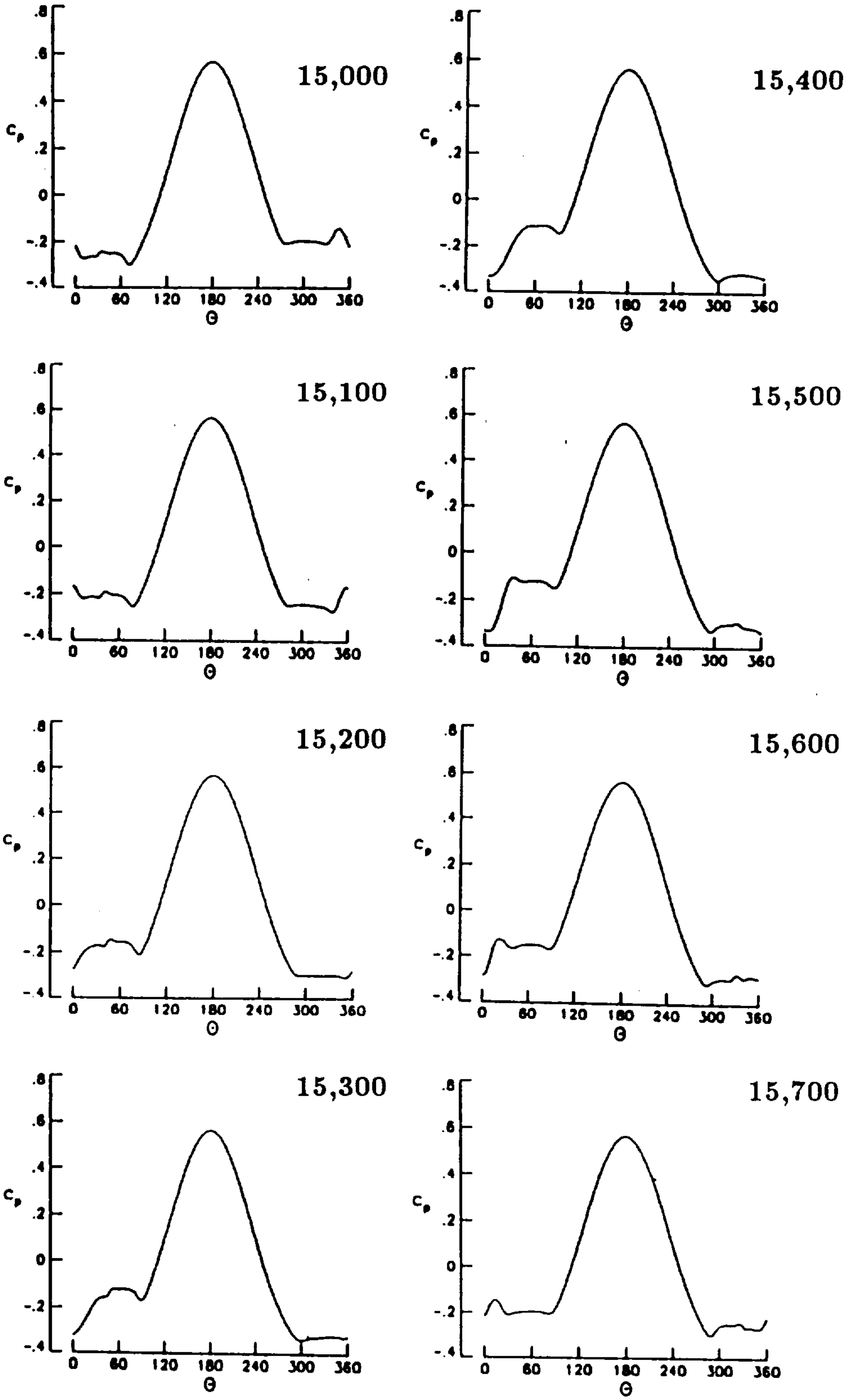

Fig. 11. Snapshots of surface-pressure coefficient for unsteady asymmetric flow around circular cone ($\alpha = 30°$, $M_\infty = 1.8$, Re $= 10^5$, $\Delta t = 10^{-3}$).

behavior of the solutions is continuous and the general trends with Mach number are in agreement with the experimental observations by Peake and Tobak (1982).

### *4.1.4. Unsteady asymmetric flows over a cone*

Keeping the Mach number at 1.8 and Reynolds number at $10^5$, the angle of attack is increased to 30° for the flow around the same circular cone (relative incidence is six for this case). The histories of the logarithmic residual error and the lift coefficient versus the number of iteration up to 15 900 time steps are shown in fig. 10. First, pseudo-time stepping has been used up to 8000 iterations and the solution has been monitored every 500 iterations. The solution is still symmetric at 3000 iterations. Thereafter, the flow asymmetry has been

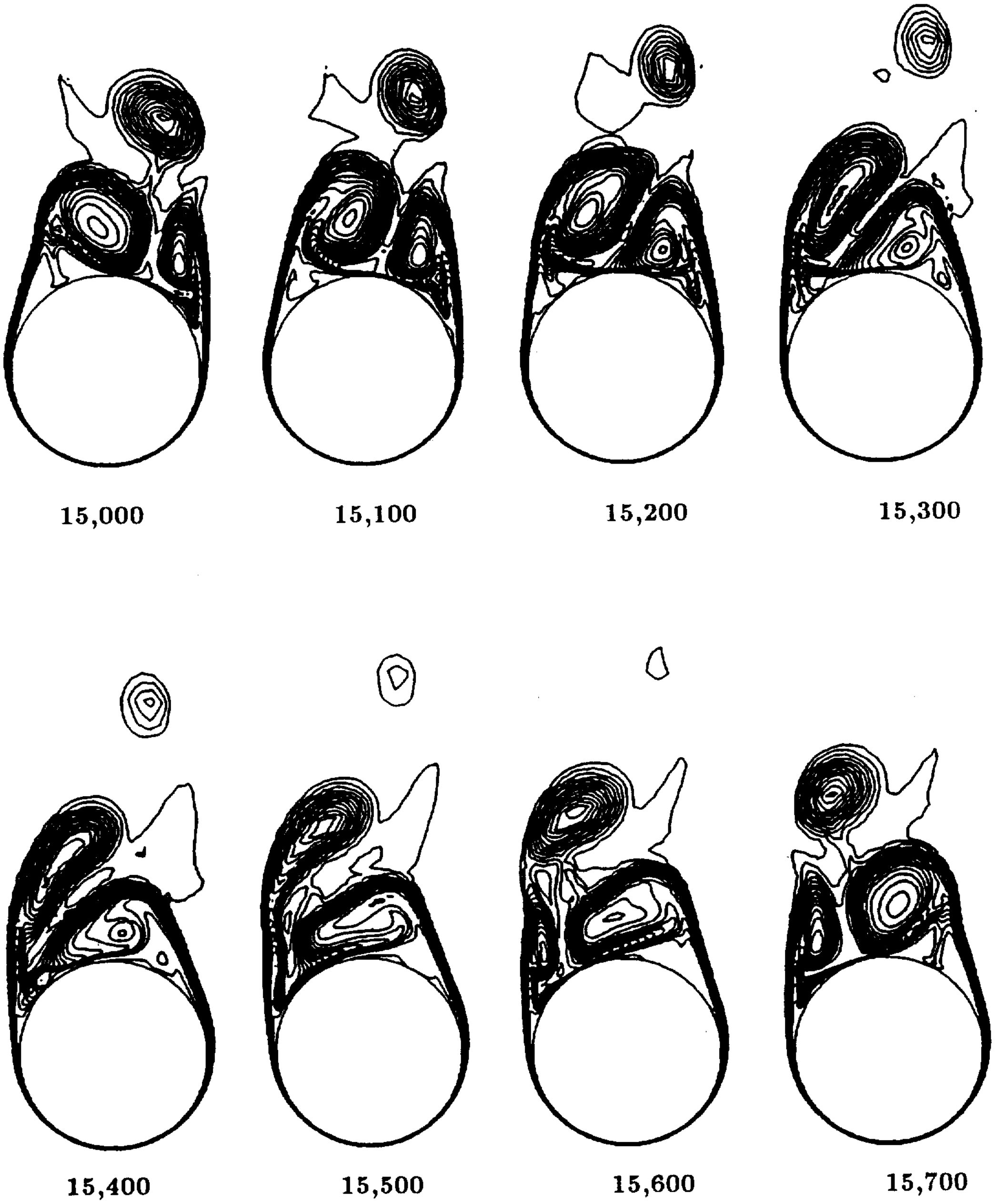
15,000 15,100 15,200 15,300

15,400 15,500 15,600 15,700

Fig. 12. Snapshots of total-pressure-loss contours for unsteady asymmetric flow around circular cone ($\alpha = 30°$, $M_\infty = 1.8$, $\mathrm{Re} = 10^5$, $\Delta t = 10^{-3}$).

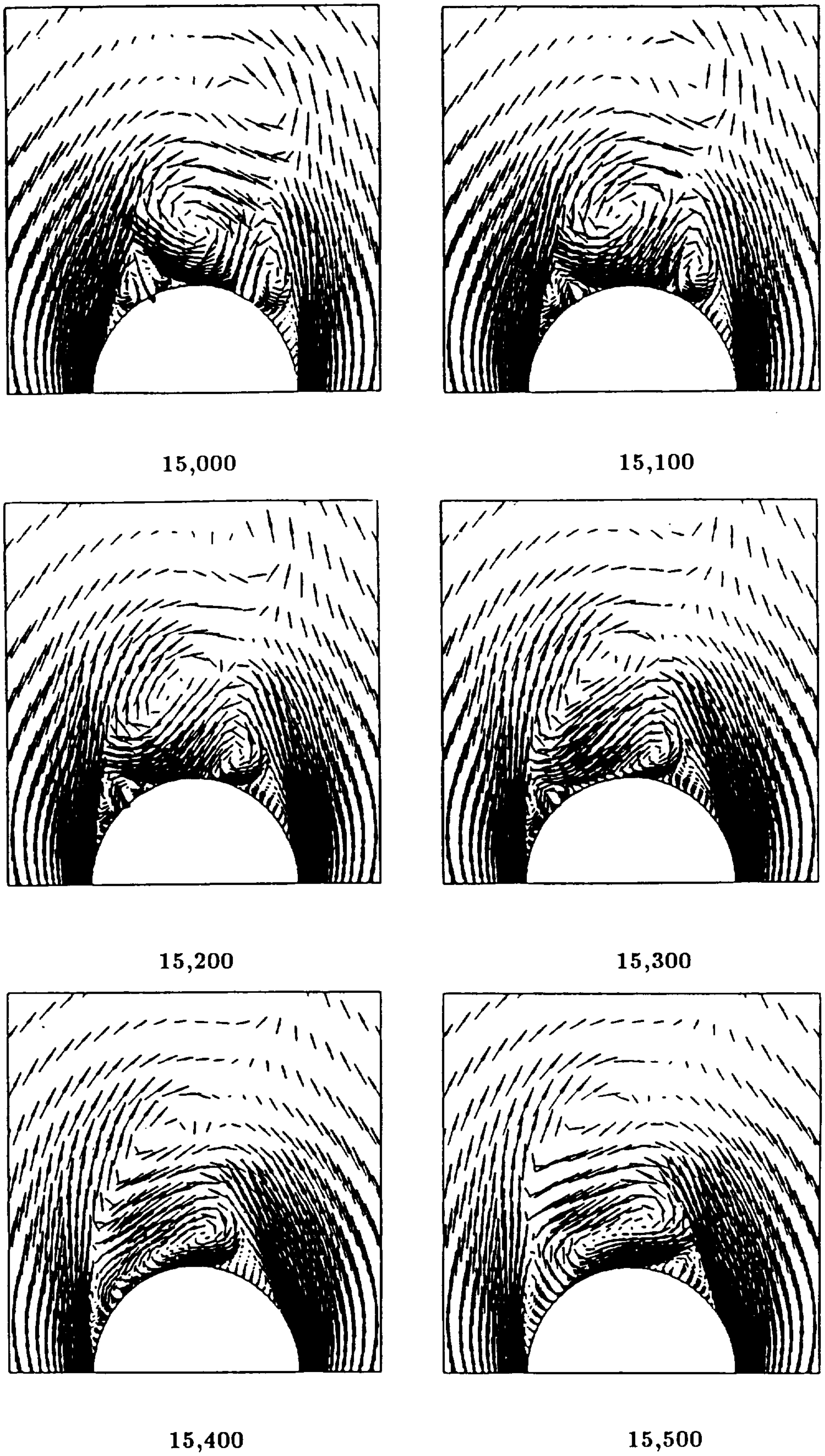

15,000

15,100

15,200

15,300

15,400

15,500

Fig. 13. Snapshots of crossflow velocity vectors for unsteady asymmetric flow around circular cone ($\alpha = 30°$, $M_\infty = 1.8$, $\mathrm{Re} = 10^5$, $\Delta t = 10^{-3}$).

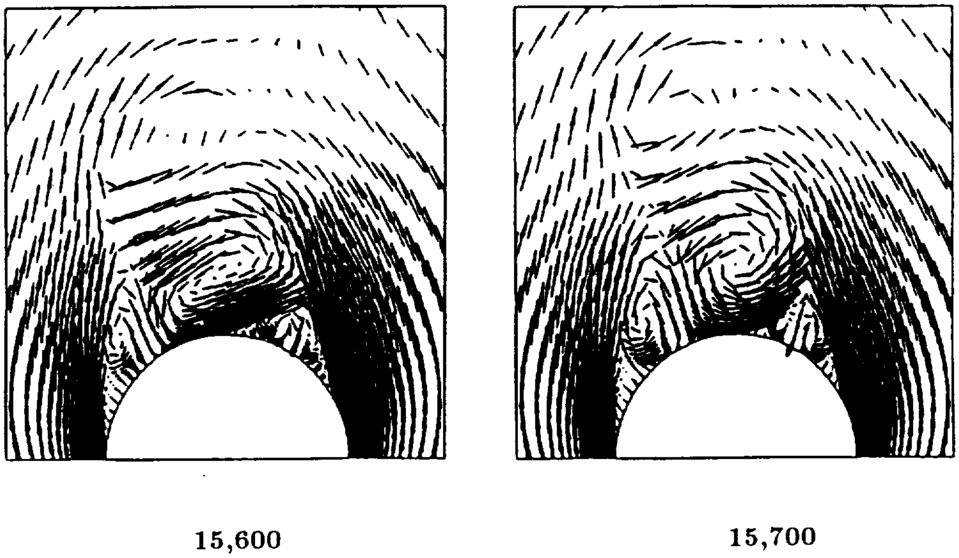

Fig. 13. (Continued).

obtained through the random disturbance of the scheme. The asymmetry changes randomly from the left side to the right side, which indicates a possibility of unsteady asymmetric vortex shedding. Therefore, the computations have been restarted from the 8000th time step using time-accurate stepping with a minimum global time step, $(\Delta t)_{\min} = 10^{-3}$. The residual-error and lift-coefficient histories show that, after switching to the time-accurate stepping, a short

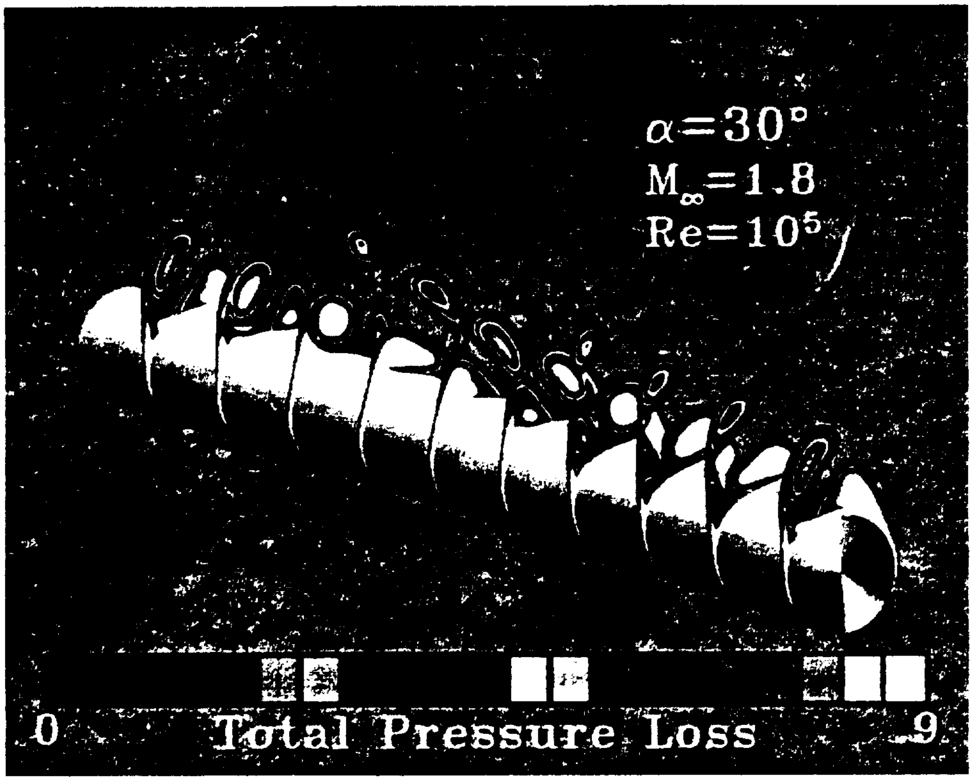

Fig. 14. Snapshots of total-pressure-loss contours for unsteady asymmetric flow around circular cone within one cycle (cylinder axis is a time axis; $\alpha = 30°$, $M_\infty = 1.8$, Re $= 10^5$, $\Delta t = 10^{-3}$).

transient response is followed by a periodic response. Figures 11, 12 and 13 show snapshots of the time history of the solution for the surface-pressure coefficient, total-pressure-loss contours, and crossflow velocity vectors. The solutions are shown every 100 time steps starting from the time step of 15 000 to 15 700. At a time step of 15 000, the asymmetric flow is seen with a vortex already shed from the right side. As time passes, the shed vortex is convected into the flow, and the primary vortex on the left side stretches, while the primary vortex on the right gets stronger, as seen from the surface-pressure curves in fig. 11. At a time step of 15 600, the primary vortex on the left side is about to be shed. At the time step of 15 700, the primary vortex on the left side is shed into the flow field. It is also noted that the solution at the time step of 15 700 is a mirror image to that of the 15 000 time step. Hence, the solution from the 15 000 to the 15 700 time steps represents the one half cycle of shedding. The periodicity of the shedding motion has been captured. The period of oscillation is $10^{-3} \times 1400 = 1.4$, which corresponds to a shedding frequency of 4.488 (Strouhal number). Figure 14 shows a snapshot of the total-pressure-loss contours over one period on a cylinder, with the axis of the cylinder representing the time axis. The present unsteady asymmetric flow solution has also been obtained exactly by using the flux-vector splitting scheme with the thin-layer Navier–Stokes equations and the flux-difference splitting scheme with the full Navier–Stokes equations on a finer grid (Kandil et al., 1991). Hence, the present solution is unique and independent of the computational scheme or the approximation level of the Navier–Stokes equations.

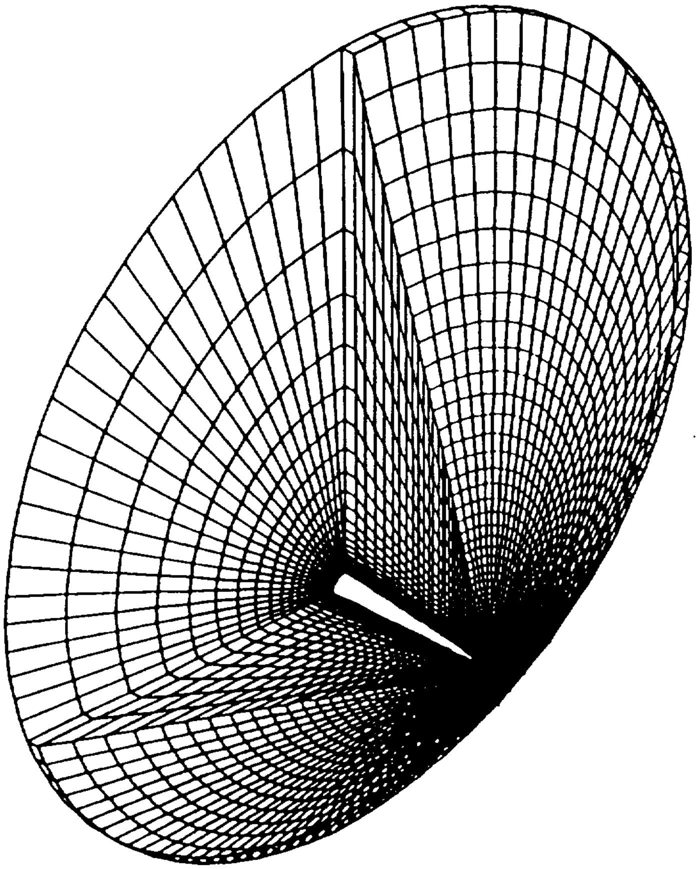

Fig. 15. A typical grid of 65 × 161 × 81 points for a 5° semiapex-angle cone.

### *4.2. Three-dimensional flows*

Steady and unsteady solutions using the locally conical flow assumptions for supersonic flows around a circular cone have been presented in the previous section. For such problems, these assumptions reduce the computational time and memory. However, the three-dimensional effects cannot be neglected in certain vortical regions, such as for flows with massive three-dimensional separation, vortex shedding, vortex breakdown, and others. In these regions, one has to rely on solutions of three-dimensional Navier–Stokes equations.

In this section, solutions of three-dimensional asymmetric flows around a 5° semiapex-angle circular cone and two cone-cylinder configurations are presented. Two issues concerning the flow asymmetry around a circular-section cone in response to a short duration transient sideslip disturbance are addressed. First, for the same cone section and for the same flow conditions and disturbance, does the three-dimensional flow solution produce the same solution as that of the locally conical solution presented in the previous section? Second, what are the effects of angle of attack, Reynolds number, and cylindrical afterbody on flow asymmetry? Finally, the results of the asymmetric flow solution are validated with those of the experimental data by Landrum (1977).

#### *4.2.1. Steady asymmetric flow over a cone*

An O–H grid of $65 \times 161 \times 81$ points in the streamwise ($\xi^1$), circumferential ($\xi^2$), and normal ($\xi^3$) directions, respectively, has been used. The grid is generated in the crossflow planes using a modified Joukowski transformation which is applied locally at the grid length stations, with algebraic stretching at the cone surface. The crossflow grid ($161 \times 81$) is of the same size as that used for the locally conical solutions. In order to retain the same resolution for each conical section, the outer boundary is a conical surface with the maximum radius of $3L$ at the cone base, where the $L$ is the length of the cone. The minimum spacing at the cone surface ranges from $10^{-5}$ at the cone base to $10^{-6}$ at the cone apex. In the circumferential direction, the grid is equally distributed for the whole computational domain. A typical grid is shown in fig. 15.

For the same flow conditions, $\alpha = 20°$, $M_\infty = 1.8$, and $\mathrm{Re} = 10^5$, at which the locally conical flow solution is asymmetric, a symmetric flow solution has been obtained using the three-dimensional calculation. The difference is explainable as a Reynolds number effect, since the locally conical solution is obtained at a fixed axial station, $\xi^1 = 1.0$. As mentioned in the formulation, a length scale in the viscous terms (Reynolds number) for steady viscous flow remains after the conical transformation. The resulting equations are not self-similar, and the location of the conical plane in the transformed equation determines the Reynolds number.

A slight asymmetric flow solution has been obtained for the three-dimensional cone flow after increasing the angle of attack to 40°, and the free-stream Reynolds number to $4 \times 10^6$, and reducing the free-stream March number to 1.4. The flow is assumed fully laminar in the numerical computation. During this computation, it has been observed that the computed flow remains symmetric about the geometric plane of symmetry at the leeside of the body. The symmetry of the solution is then disturbed by introducing a sideslip angle of 2° to the flow field for about 100 time steps and then it is removed. Thereafter, the pseudo-time stepping is continued until the residual error drops again four orders of magnitude and a stable asymmetric solution is obtained. The total-pressure-loss contours of this case are shown in fig. 16. Although the resulting flow is no longer symmetric, the asymmetry is relatively small. In this case, the vortices still lie close to the leeward-body surface, and the size of the shear layer and height of the primary vortices grow with increasing distance downstream. It is also seen that the solution is almost self-similar over a long distance of the cone length.

Next, the Reynolds number is increased to $5 \times 10^6$ and $6 \times 10^6$, keeping the other flow conditions the same as those of the previous flow case. Again, the source of the disturbance to

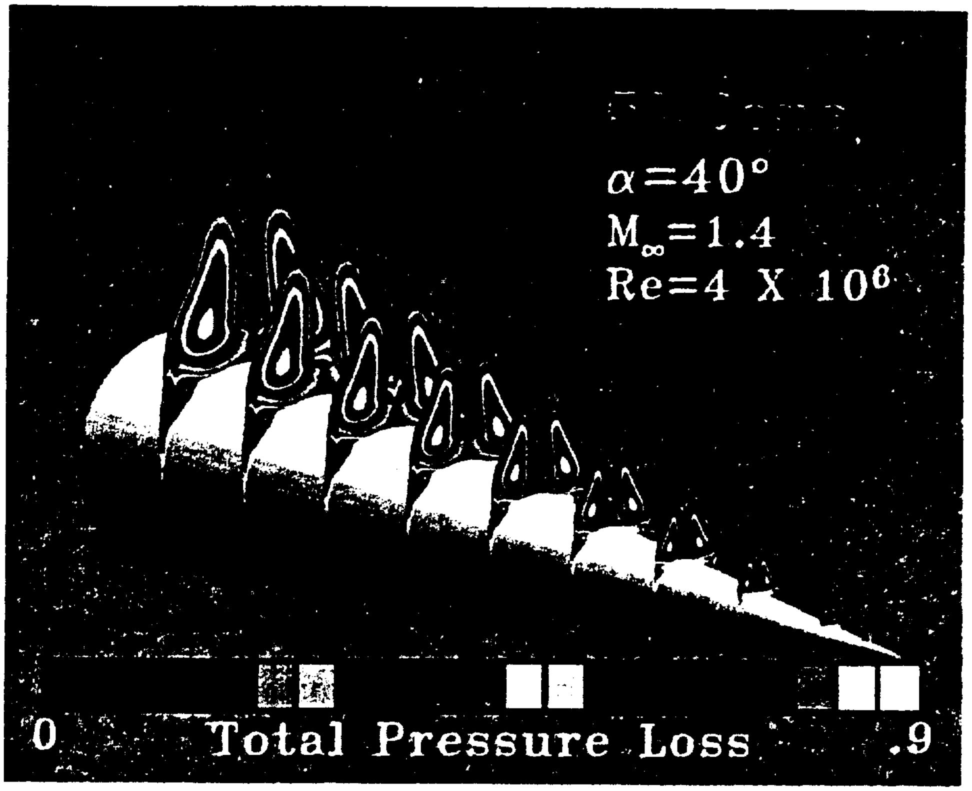

Fig. 16. Total-pressure-loss contours of flow around at 5° semiapex-angle cone ($\alpha = 40°$, $M_\infty = 1.4$, Re $= 4 \times 10^6$).

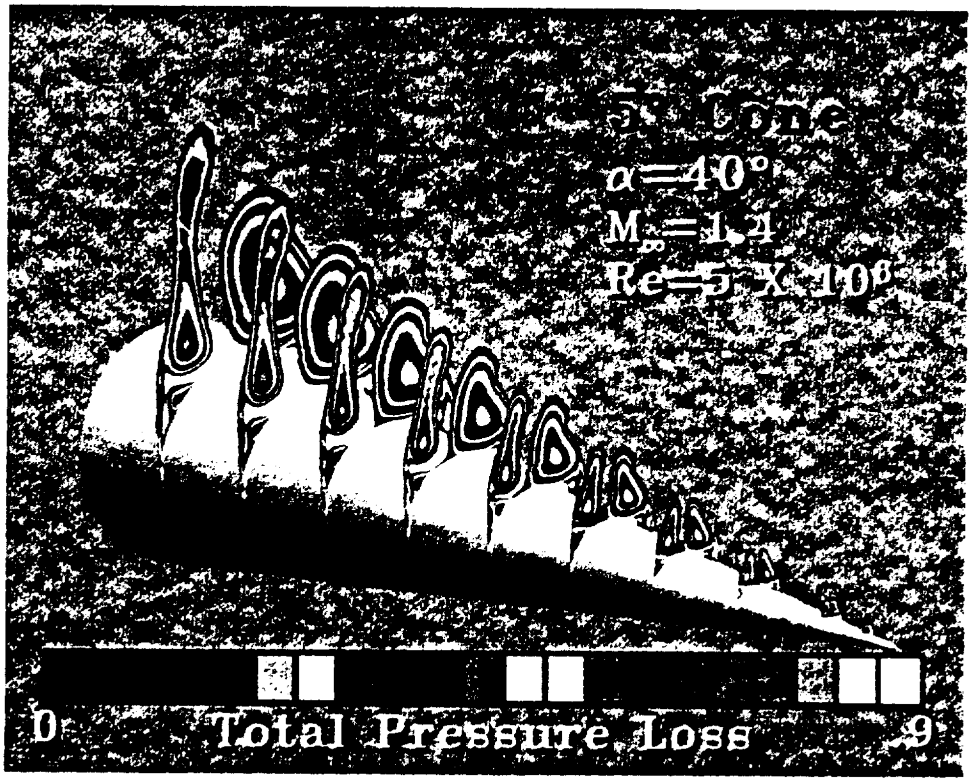

Fig. 17. Total-pressure-loss contours of flow around 5° semiapex-angle cone ($\alpha = 40°$, $M_\infty = 1.4$, Re $= 5 \times 10^6$).

break the symmetry of the solution is a 2° transient sideslip of short duration. The computation has been monitored every 300 time steps until there are no significant changes in the steady-state solutions. Figures 17 and 18 show the total-pressure-loss solutions for these cases. Figure 17 shows that the asymmetry of the vortical flow becomes strong and the self similarity of the flow asymmetry is substantially lost. However, it is seen that the primary vortices do not change sides as moving in the downstream direction. Figure 18, which corresponds to the free-stream Reynolds number of $6 \times 10^6$, shows flow asymmetry that changes sides as the solutions develop along the length of the cone and as vortices are shed into the flow field. Since the solution is steady, the vortex shedding is a spatial one. A close study of the solutions shown between the fourth crossflow plane and seventh crossflow plane reveals that the vortex shedding changes from the right side (looking downstream, fourth crossflow plane) to the left side (seventh crossflow plane). The solutions on these two planes are nearly scaled mirror images of each other. The present spatial flow asymmetry is qualitatively similar to the temporal flow asymmetry of the locally conical flow solution shown in fig. 14. It is seen that most of the asymmetric vortex flow characteristics and physics in the crossflow can be captured quantitatively by the locally conical flow solutions.

Figure 19 shows the total-pressure-loss solution for the same cone for $\mathrm{Re} = 8 \times 10^6$. The asymmetry of the vortex flow becomes much stronger, as compared with the previous cases of figs. 16–18. By comparing the solution of this case with that of the $\mathrm{Re} = 6 \times 10^6$, it is noticed that the flow asymmetry of the case with $\mathrm{Re} = 8 \times 10^6$ changes sides along a shorter axial distance (third and fifth crossflow planes). Moreover, the flow asymmetry of the case with higher Reynolds number changes sides one more time (fifth and ninth crossflow planes) and, thus, a complete wave length of flow asymmetry is formed between the third and ninth crossflow planes. A close study of the mechanism of spatial vortex shedding along the cone reveals that it is similar to the unsteady vortex shedding of the locally conical flow solution. At the third crossflow plane ($x_1/L = 0.2$), the asymmetric flow is seen with vortex already shed from the right side. Moving downstream, the shed vortex is convected into the flow, and the shear layer on the right side stretches, while the primary vortex on the left side gets stronger, as seen from the surface-pressure curves in fig. 20. At the fifth crossflow plane ($x_1/L = 0.4$), the primary vortex on the right side is about to be shed. At the ninth crossflow plane ($x_1/L = 0.9$), the primary vortex on the right side is almost shed in the flow field, while the lower part of shear layer on the same side has stretched and shrunk in thickness. It is also seen that at the ninth crossflow plane, the flow is approximately a mirror image of that at the third crossflow plane. The behavior of the flow asymmetry over one period in fig. 14 is qualitatively similar to that of the flow asymmetry over one wave length in fig. 19.

### *4.2.2. Unsteady asymmetric flow over a cone*

In this section, solutions of the unsteady supersonic asymmetric flow around the same circular cone at an angle of attack of 50° are presented. The free-stream Reynolds number and Mach number of this case are $8 \times 10^6$ and 1.4, respectively. The present flow case has been started from the solution obtained for $\alpha = 40°$, instead of initializing with free-stream conditions everywhere. In addition, this steady asymmetric initial condition can be considered as the source of disturbance to the flow field, so the use of transient sideslip disturbance is not necessary for this case.

In the computation of locally conical flow problems it has been shown that, once unsteady, asymmetric vortex shedding is initiated, the perturbation can be removed. The vortex shedding will continue without the need for any further perturbations since the flow is unstable. In order to investigate whether the same phenomena exists for the unsteady three-dimensional asymmetric flow, the computation has been first done using pseudo-time stepping until the residual error drops three orders of magnitude. The flow asymmetry,

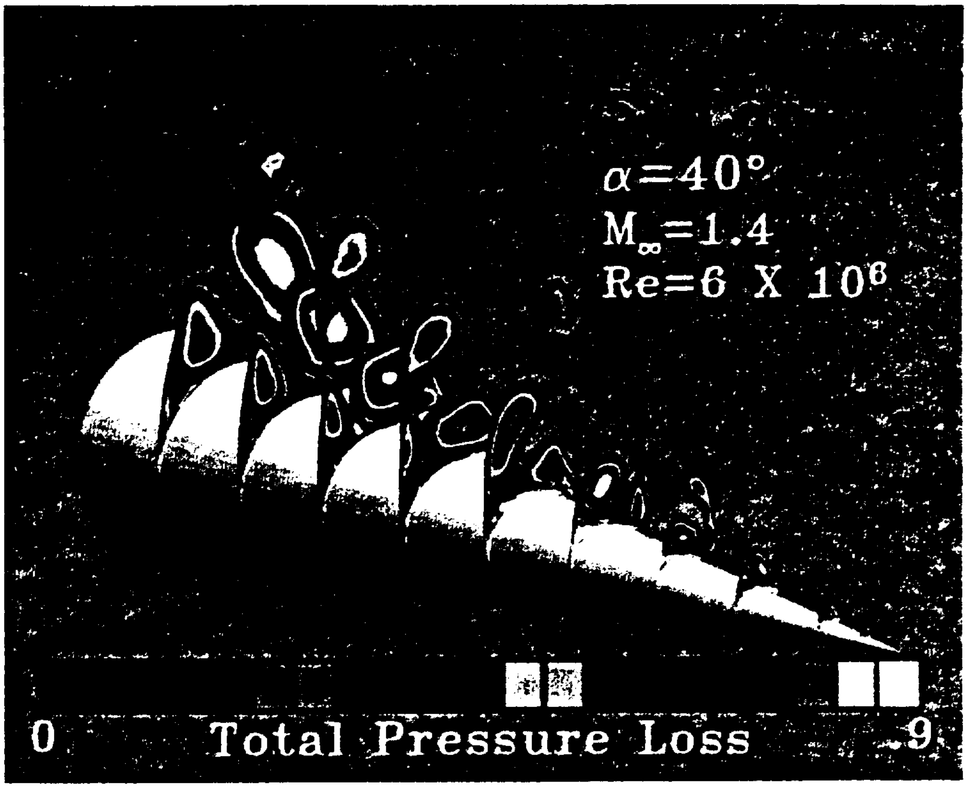

Fig. 18. Total-pressure-loss contours of flow around 5° semiapex-angle cone ($\alpha$ = 40°, $M_\infty$ = 1.4, Re = $6\times10^6$).

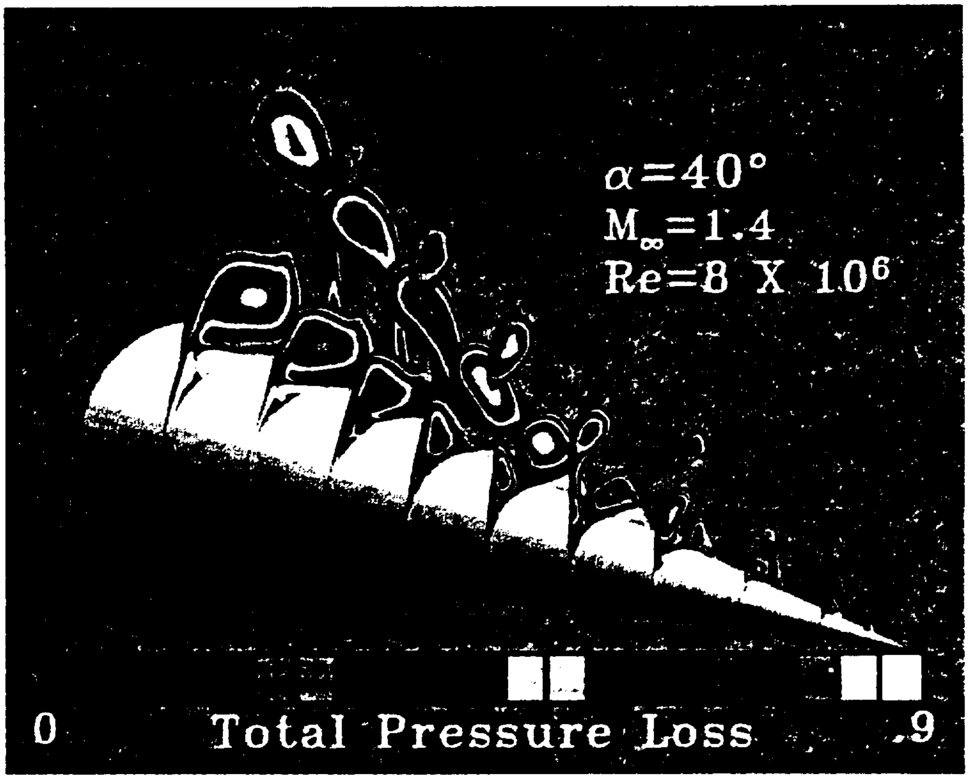

Fig. 19. Total-pressure-loss contours of flow around 5° semiapex-angle cone ($\alpha$ = 40°, $M_\infty$ = 1.4, Re = $8\times10^6$).

changing randomly from the left side to right side, has been captured by the pseudo-time stepping calculation, which indicates a possibility of unsteady vortex shedding. The computation has been continued using time-accurate calculations with a minimum global time step of $10^{-5}$. The unsteady structure of the flow at $\alpha = 50°$ is monitored at different time steps to see the mechanism of the unsteady vortex shedding and the unsteady behavior of the vortex structure. Due to the fine computational grid spacing at the nose region and the cone surface,

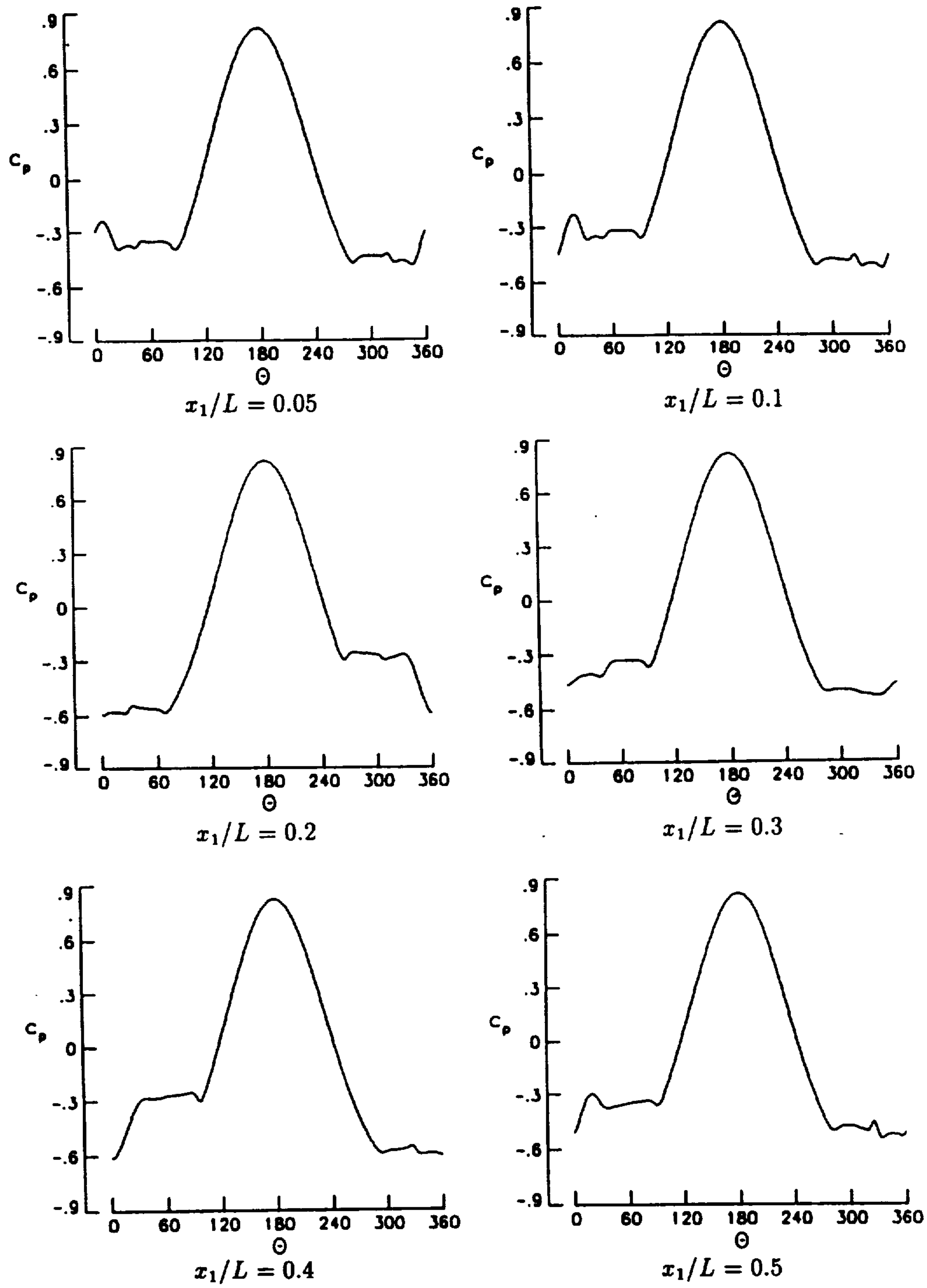

$x_1/L = 0.05$

$x_1/L = 0.1$

$x_1/L = 0.2$

$x_1/L = 0.3$

$x_1/L = 0.4$

$x_1/L = 0.5$

Fig. 20. Surface-pressure coefficient on 5° semiapex-angle cone ($\alpha = 40°$, $M_\infty = 1.4$, $\mathrm{Re} = 8 \times 10^6$).

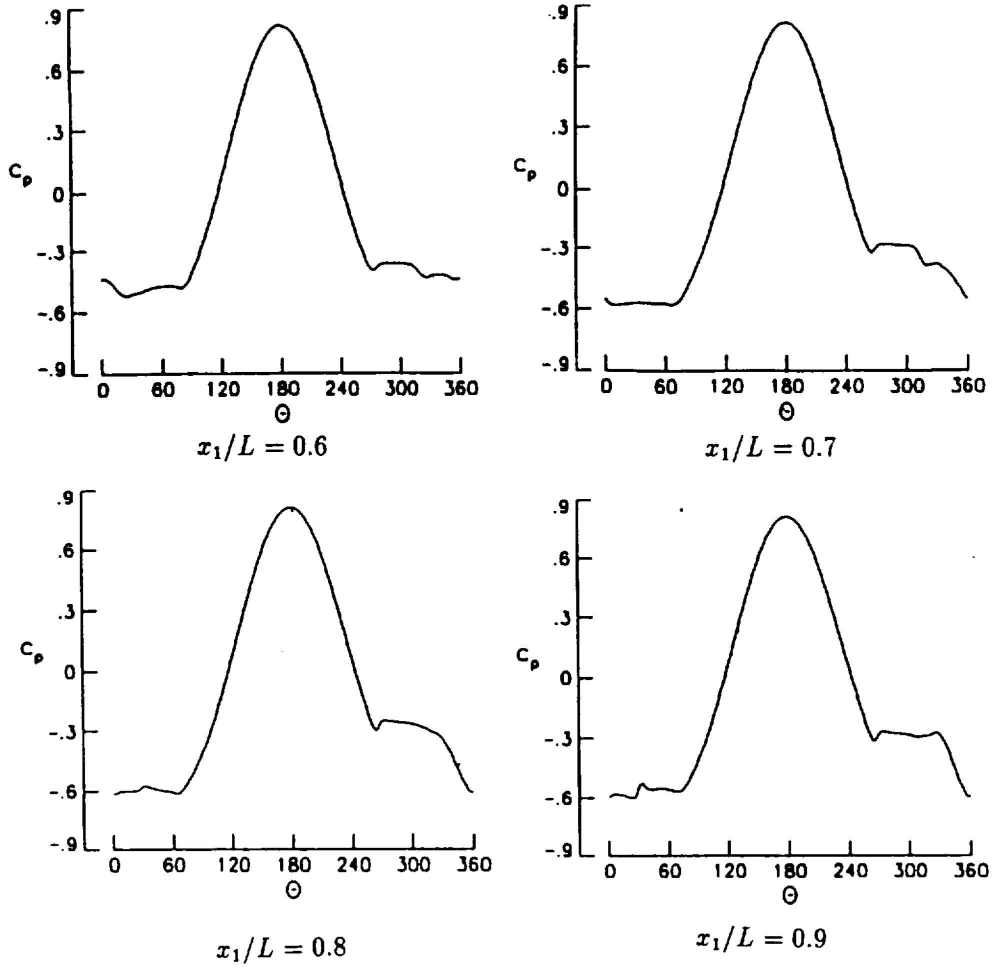

$x_1/L = 0.6$

$x_1/L = 0.7$

$x_1/L = 0.8$

$x_1/L = 0.9$

Fig. 20. (Continued).

the allowable computational time step is so small that the calculation becomes prohibitively expensive for time-marching more than a small part of a shedding cycle.

Consequently, only small changes are visible in the instantaneous snapshots of the unsteady asymmetric flow solutions presented in this section. The flow at time step 10616 is shown by the total-pressure-loss contours (fig. 21), surface-pressure coefficients (fig. 23) and enlargement of the total-pressure-loss contours (fig. 24). The same quantities for time step 11 816 are shown in figs. 22, 25, 26. Figure 21 shows a strongly asymmetric solution with vortex shedding changes little with axial location. The shear-layer thickness for each crossflow station extends about one and one half times the local diameter of the leeward plane of symmetry, as compared with the case of $\alpha = 40°$. It is evident that all of the three vortices interact with each other in a relatively small distance above of the body surface. The blow-up of total-pressure-loss contours at the time step of 11 816 (fig. 26) shows that the flow asymmetry changes side at the crossflow station of $x_1/L = 0.1$, as compared with the same crossflow section in fig. 24. Obviously, the total computed time is too short in terms of physical time to draw final conclusions for periodic vortex shedding, but the total-pressure-loss contours clearly show that the flow is unsteady asymmetric with a possibility of vortex shedding at each axial station.

All of the numerical results have been obtained using either the Cray-2 supercomputer of the NASA Langley Research center or the Cray-YMP supercomputer of the NASA Ames

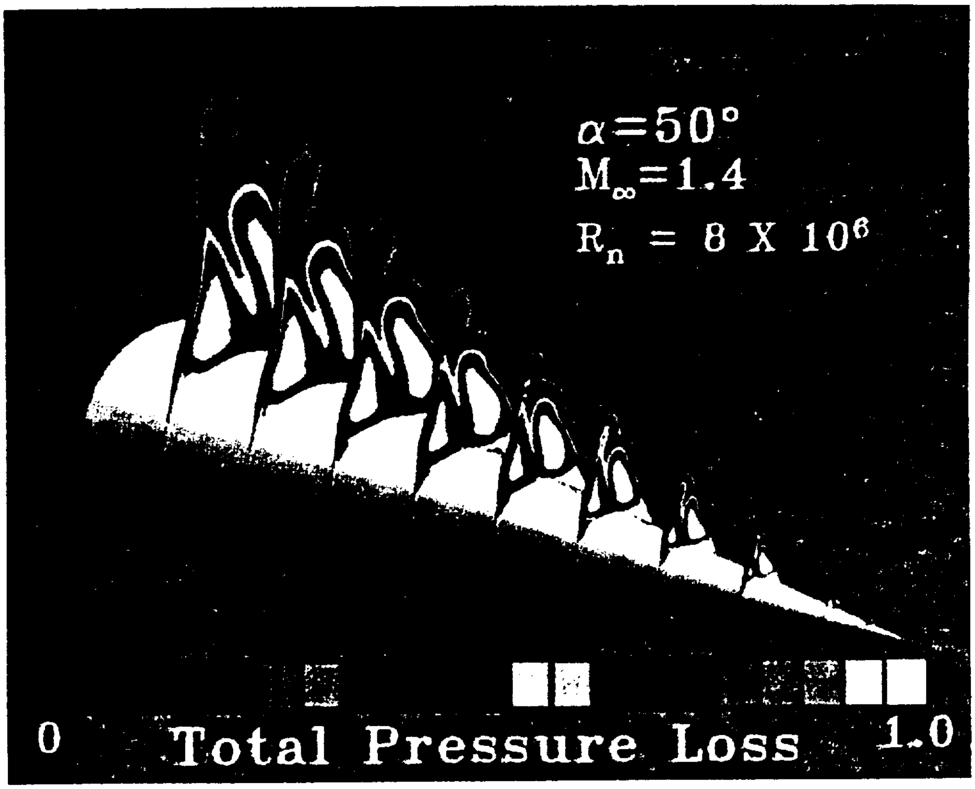

Fig. 21. Total-pressure-loss contours of flow around 5° semiapex-angle cone at time-step of 10616 ($\alpha = 50°$, $M_\infty = 1.4$, Re $= 8 \times 10^6$).

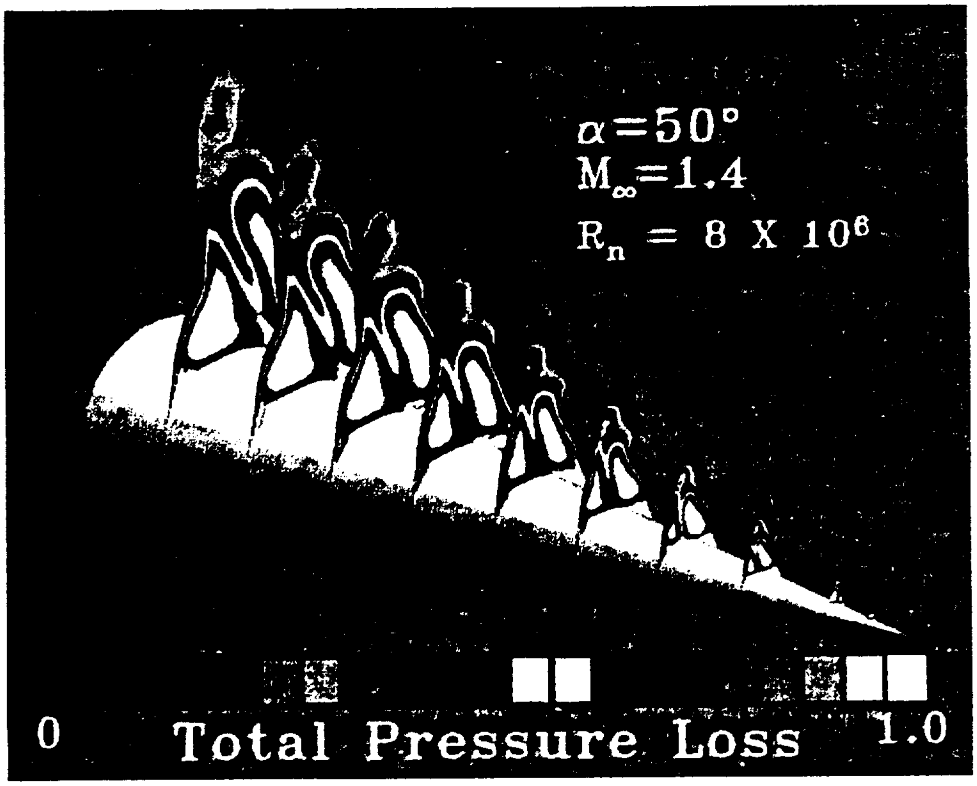

Fig. 22. Total-pressure-loss contours of flow around 5° semiapex-angle cone at time step of 11816 ($\alpha = 50°$, $M_\infty = 1.4$, Re $= 8 \times 10^6$).

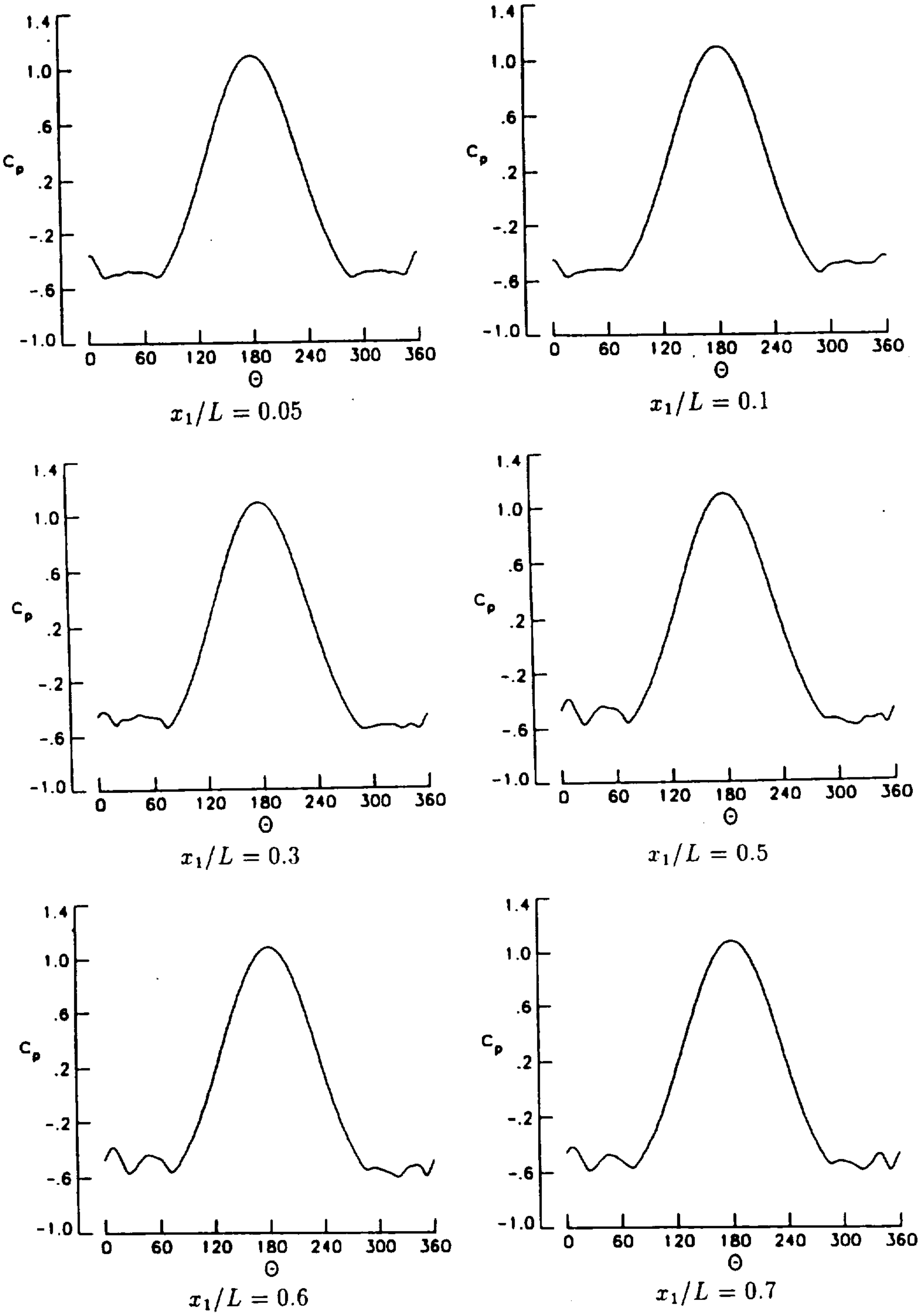

$x_1/L = 0.05$

$x_1/L = 0.1$

$x_1/L = 0.3$

$x_1/L = 0.5$

$x_1/L = 0.6$

$x_1/L = 0.7$

Fig. 23. Surface-pressure coefficient on 5° semiapex-angle cone at time step of 10616 ($\alpha = 50°$, $M_\infty = 1.4$, $\mathrm{Re} = 8 \times 10^6$).

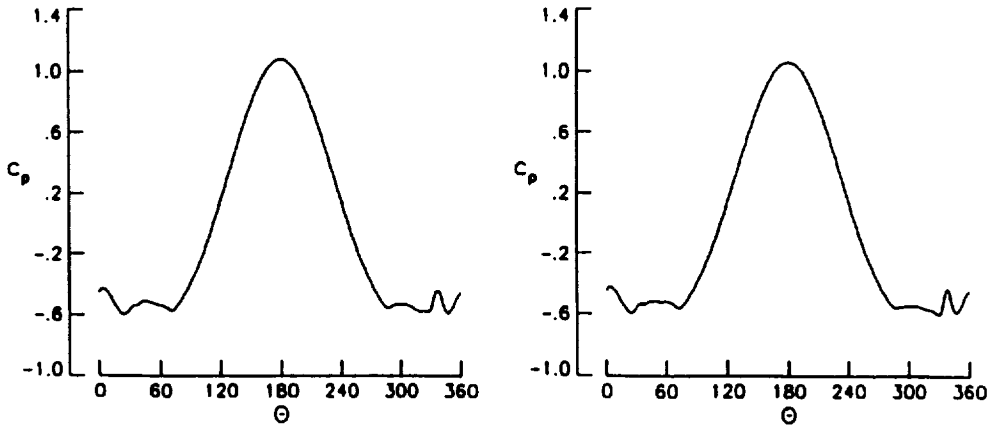

$x_1/L = 0.8$ $x_1/L = 0.9$

Fig. 23. (Continued).

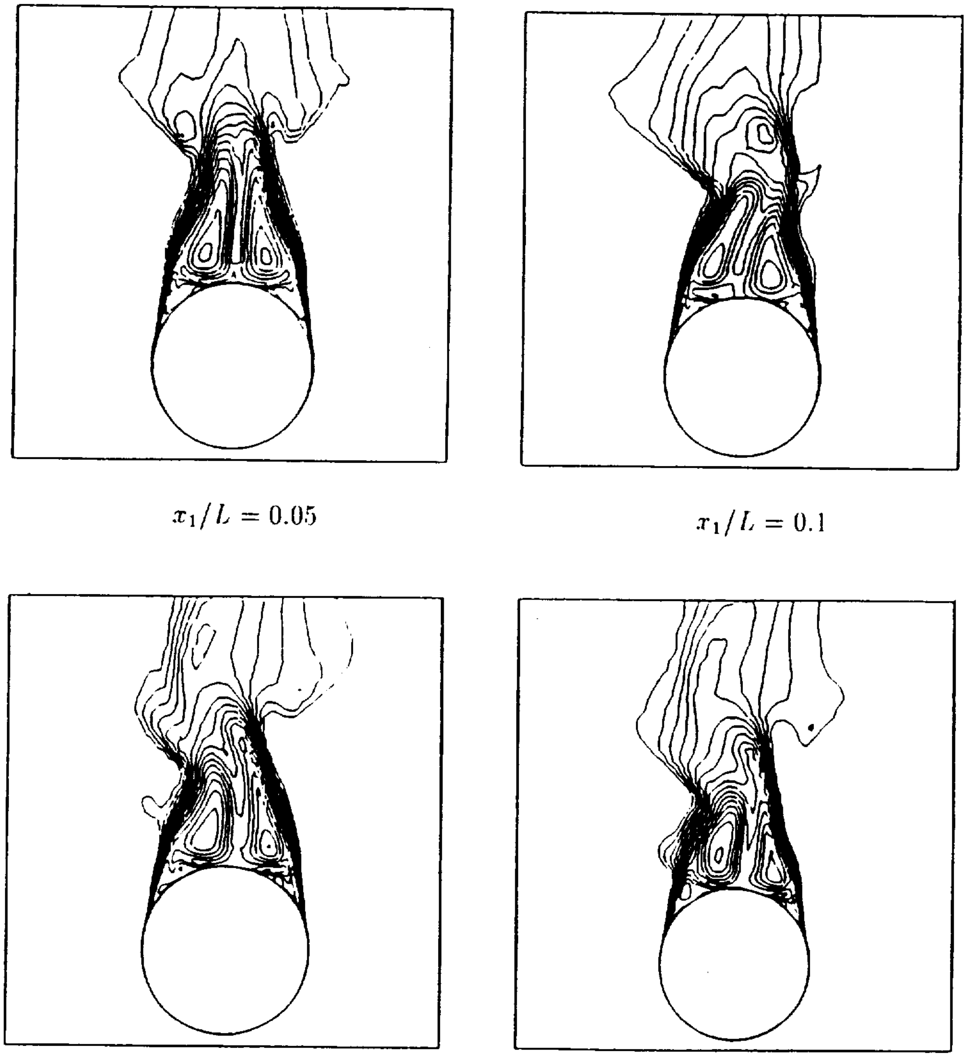

$x_1/L = 0.05$ $x_1/L = 0.1$

$x_1/L = 0.3$ $x_1/L = 0.5$

Fig. 24. Blow-up of the total-pressure-loss contours on 5° semiapex-angle cone at time step of 10616 ($\alpha = 50°$, $M_\infty = 1.4$, $\mathrm{Re} = 8 \times 10^6$).

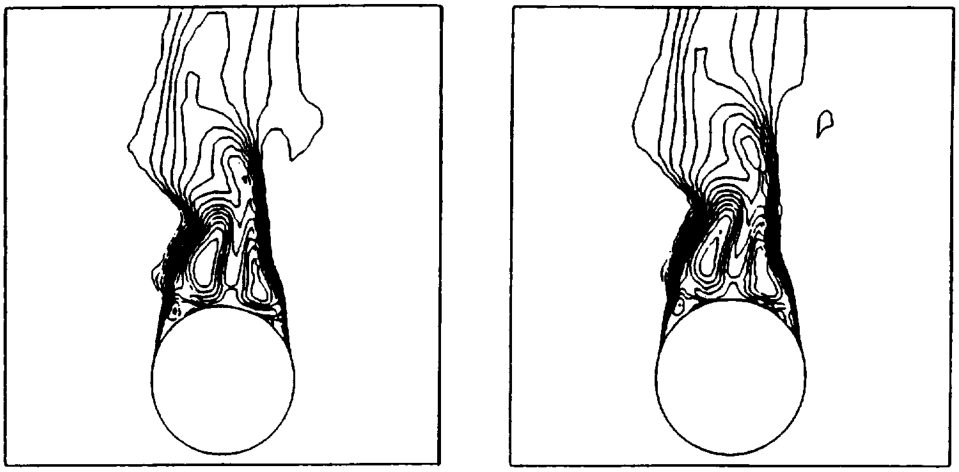

$x_1/L = 0.6$ $x_1/L = 0.7$

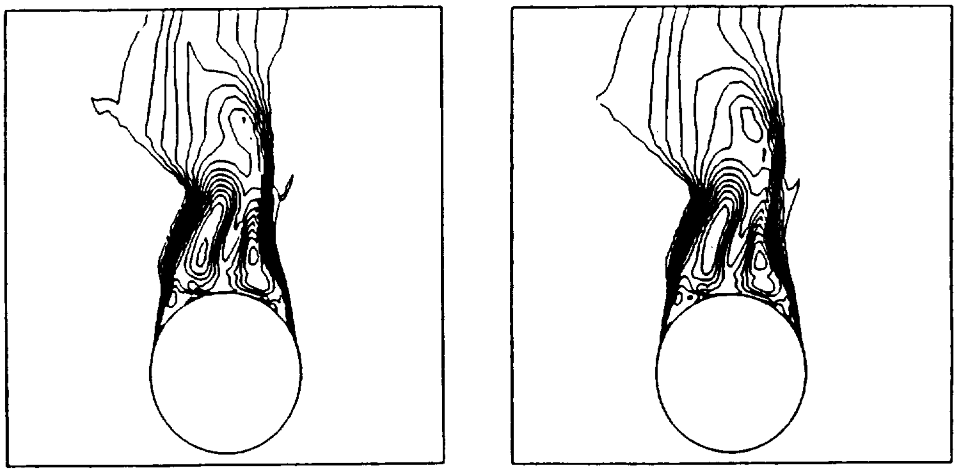

$x_1/L = 0.8$ $x_1/L = 0.9$

Fig. 24. (Continued).

Research Center. Each of the steady asymmetric flow cases takes about 100 h of CPU time on the Cray-2 and 65 h of CPU time on the Cray-YMP computer. The unsteady asymmetric flow case takes over 82 h of CPU time on the Cray-YMP computer for the 11 816 computed time steps.

#### 4.2.3. *Asymmetric flow over cone–cylinder configurations*

The effect of a cylindrical afterbody on flow asymmetry is investigated by introducing a cylindrical afterbody of unit length to the same circular cone. The flow around the resulting cone-cylinder configuration is solved with the flow conditions as for $\alpha = 40°$, $M_\infty = 1.4$, and $\mathrm{Re} = 4 \times 10^6$, which are the same flow conditions of the isolated unit-length cone shown in fig. 16. The source of disturbance is the same 2° transient sideslip. The computed total-pressure-loss contours are shown in fig. 27. It should be noted that slight flow unsteadiness has been observed during the computations. Comparing the results for fig. 16 with fig. 27, it is noticed that the flow asymmetry is stronger for the cone-cylinder configuration than that of the isolated conical forebody. It should be noted that subsonic flow region does exist inside the conical shock surrounding the cone-cylinder configuration, hence, the downstream cylindrical-afterbody boundary has an upstream effect on the flow. There are two reasons for the afterbody to increase the flow asymmetry; the first is the increase of the local angle of attack

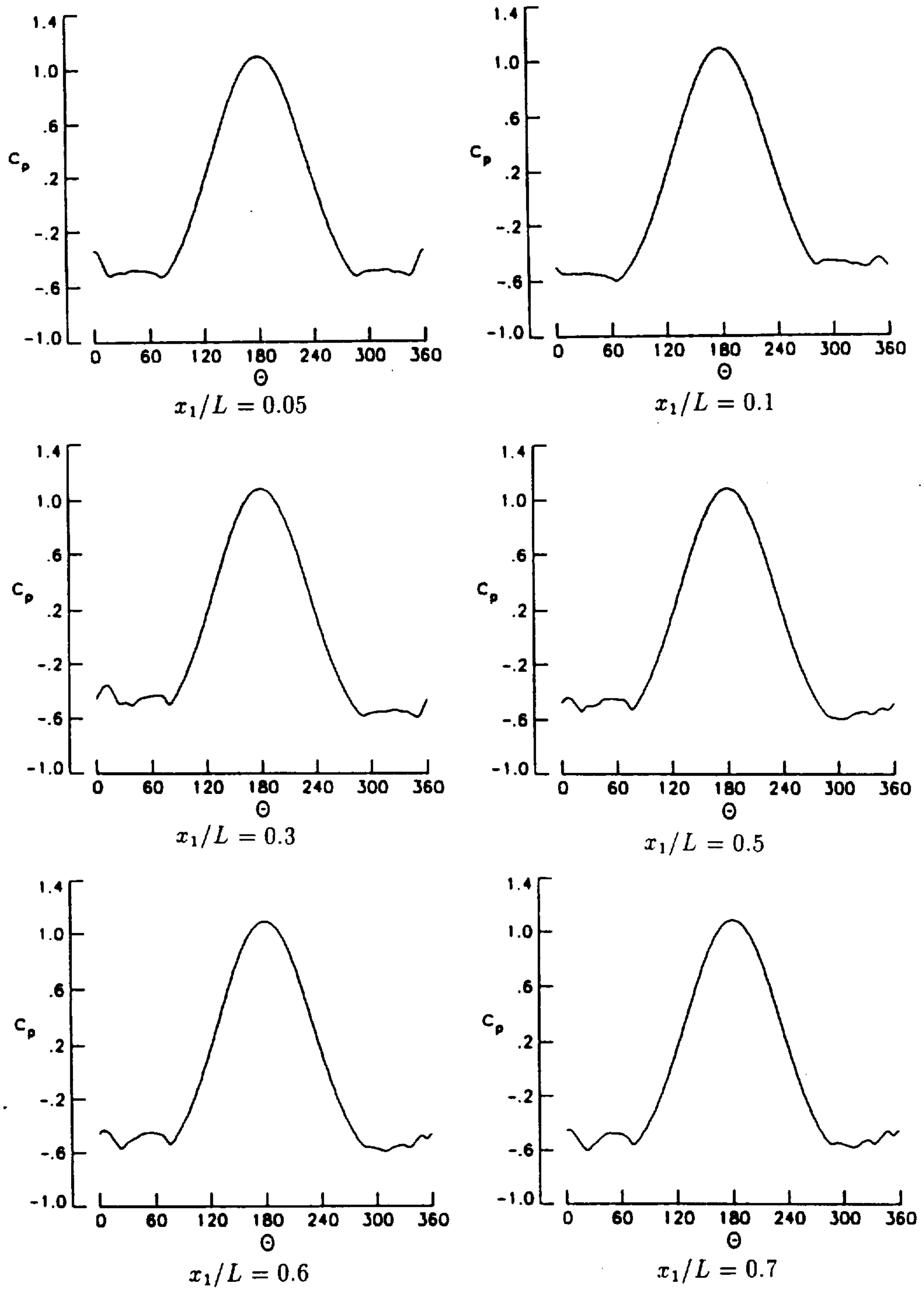

$x_1/L = 0.05$

$x_1/L = 0.1$

$x_1/L = 0.3$

$x_1/L = 0.5$

$x_1/L = 0.6$

$x_1/L = 0.7$

Fig. 25. Surface-pressure coefficient on 5° semiapex-angle cone at time step of 11816 ($\alpha = 50°$, $M_\infty = 1.4$, $Re = 8 \times 10^6$).

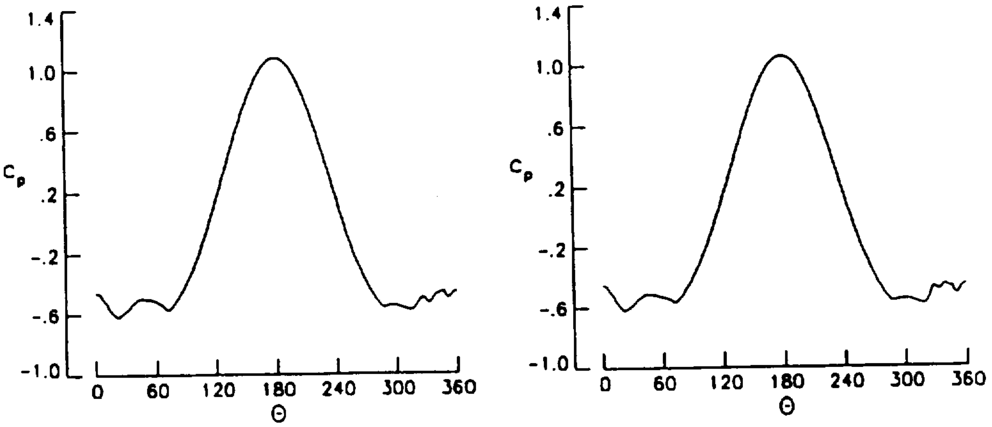

$x_1/L = 0.8$ $x_1/L = 0.9$

Fig. 25. (Continued).

of the leeward side of the cylinder, and the second is the surface discontinuity at the cone–cylinder juncture. Both of these increase the spatial growth of the flow asymmetry.

Next, a validation flow case is presented by comparing with available experimental data. For this purpose, the cone-cylinder configuration of 0.5 : 0.5 (the ratio of the conical forebody to the cylindrical afterbody) is used, which was experimentally tested by Landrum (1977). The flow conditions for this case are $\alpha = 46.1°$, $M_\infty = 1.6$, and $\mathrm{Re} = 6.6 \times 10^6$. The Reynolds number for this case is based on the total body length. The cone semiapex angle is 9.46°, and the numerical computation is assumed to be fully laminar. The problem is solved using a grid size of $65 \times 161 \times 81$, which has the same resolution in the crossflow plane as the previous cases. Figure 28 presents the computed total-pressure-loss contours, which show a relatively weak asymmetry at the nose region and a strong spatially growing asymmetry in the downstream direction. Figure 29 shows the surface-pressure coefficient along with the experimental data, and figs. 30 and 31 show the total-pressure-loss contours and the total Mach-number contours in the crossflow planes at the axial stations of 0.075, 0.225, 0.475, and 0.775. The computed (solid line) and measured (symbol) surface-pressure coefficients are in

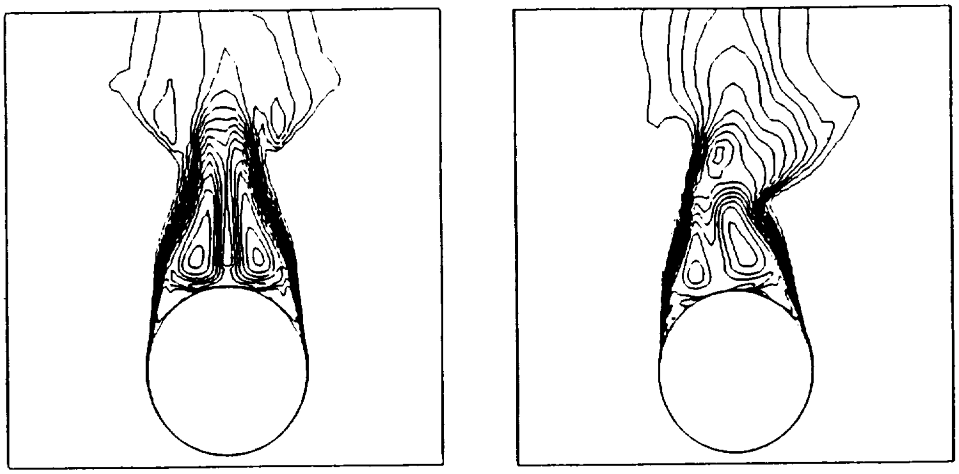

$x_1/L = 0.05$ $x_1/L = 0.1$

Fig. 26. Blow-up of the total-pressure-loss contours on 5° semiapex-angle cone at time step of 11816 ($\alpha = 50°$, $M_\infty = 1.4$, $\mathrm{Re} = 8 \times 10^6$).

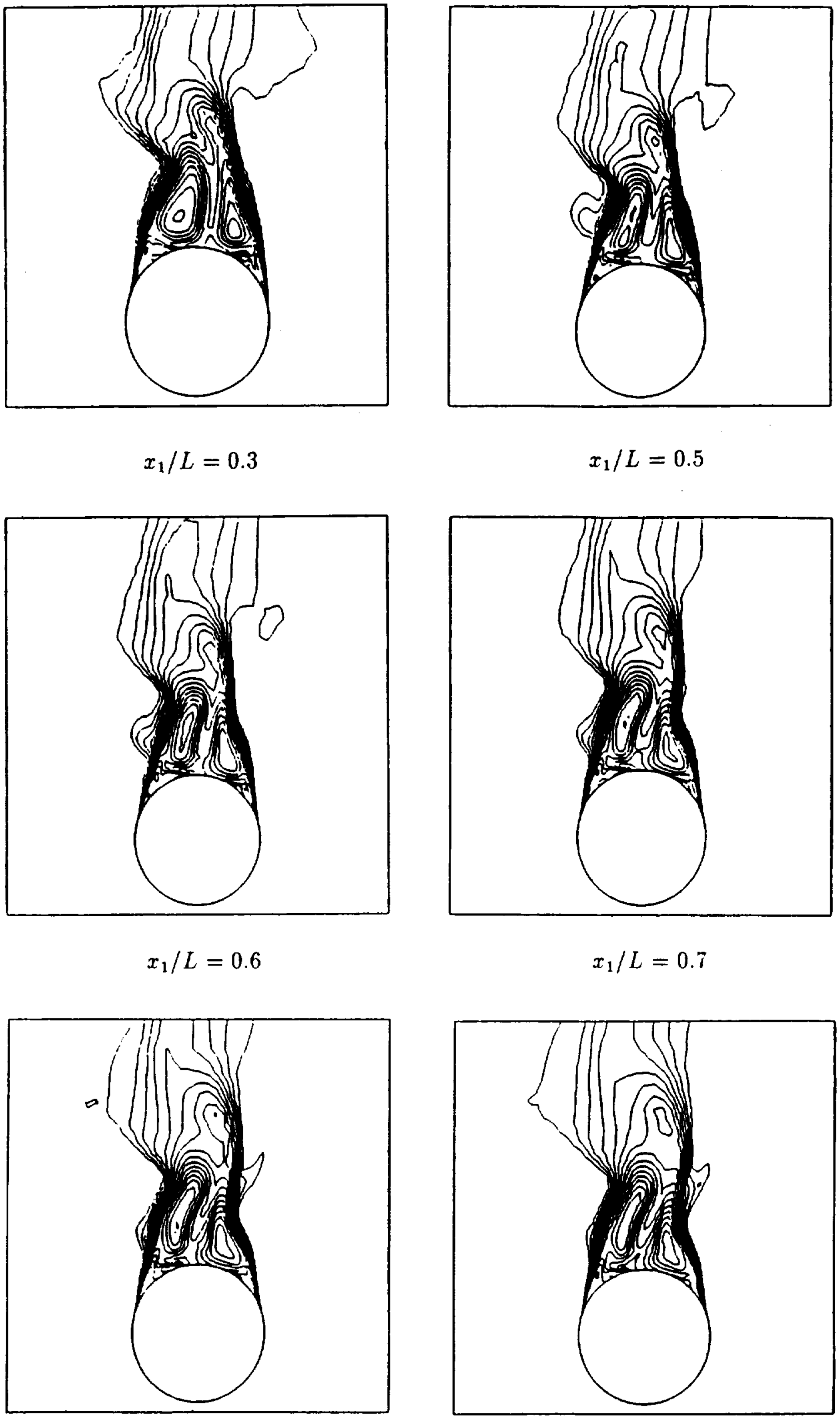

$x_1/L = 0.3$

$x_1/L = 0.5$

$x_1/L = 0.6$

$x_1/L = 0.7$

$x_1/L = 0.8$

$x_1/L = 0.9$

Fig. 26. (Continued).

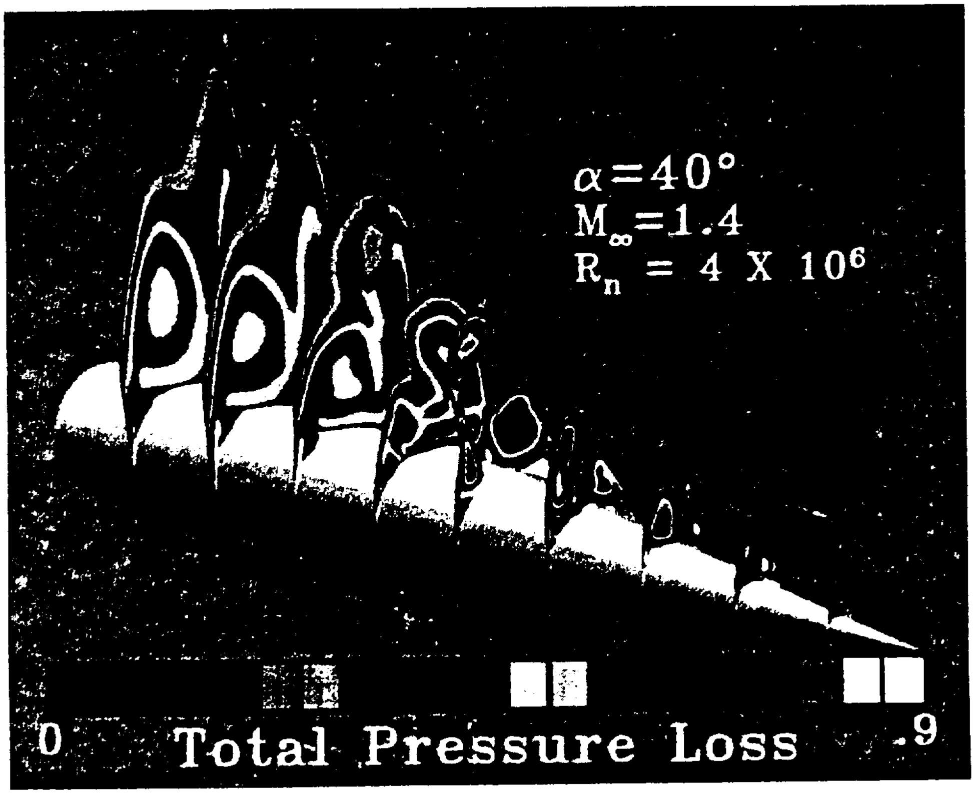

Fig. 27. Total-pressure-loss contours of flow around 5° semiapex-angle cone–cylinder configuration ($\alpha = 40°$, $M_\infty = 1.4$, $\mathrm{Re} = 4 \times 10^6$).

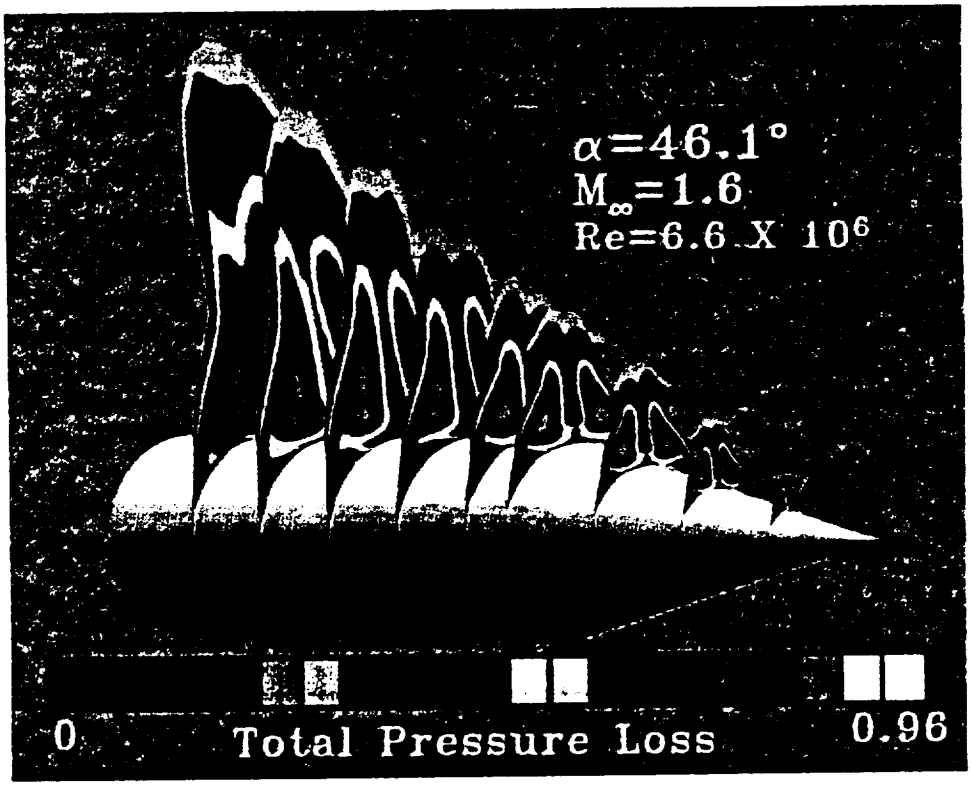

Fig. 28. Total-pressure-loss contours of flow around 9.46° semiapex-angle cone–cylinder configuration ($\alpha = 46.1°$, $M_\infty = 1.6$, $\mathrm{Re} = 6.6 \times 10^6$).

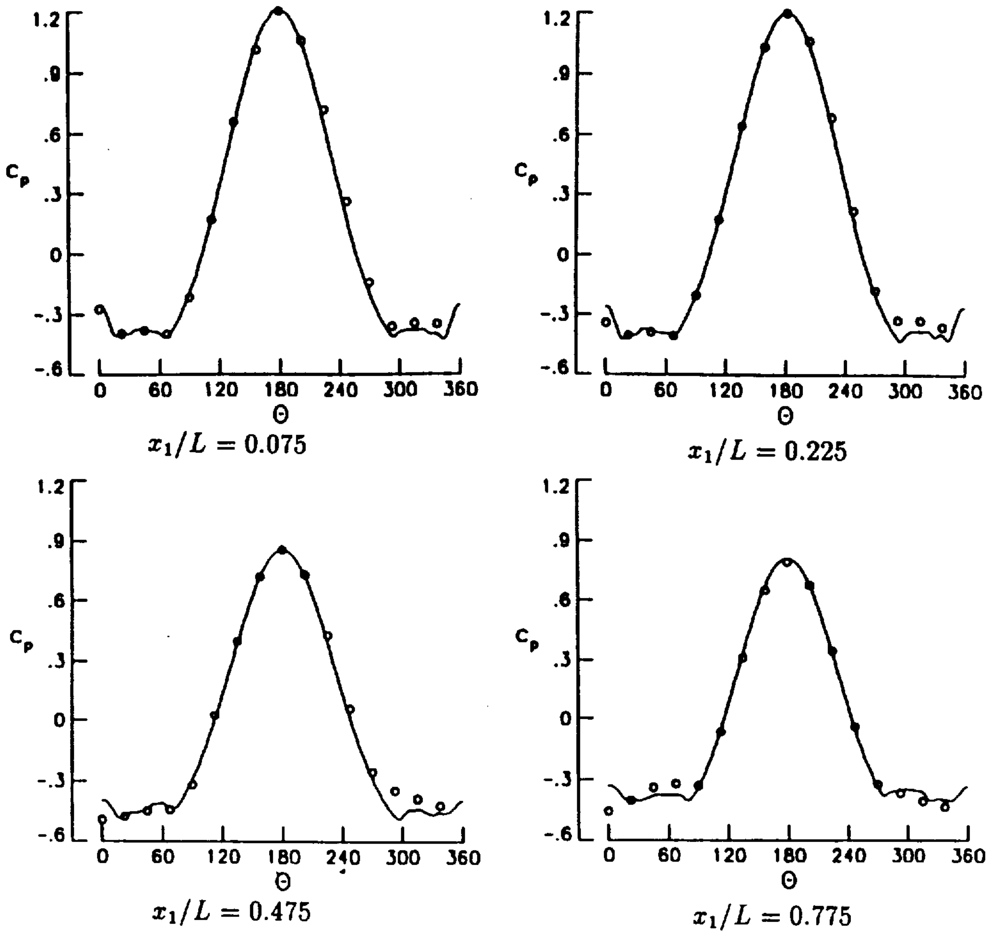

$x_1/L = 0.075$

$x_1/L = 0.225$

$x_1/L = 0.475$

$x_1/L = 0.775$

Fig. 29. Surface-pressure coefficient on 9.46° semiapex-angle cone-cylinder configuration ($\alpha = 46.1°$, $M_\infty = 1.6$, $\mathrm{Re} = 6.6 \times 10^6$) (experiment: Landrum, 1977).

good agreement, with the exception of the region close to the leeward plane of symmetry. By studying the blow-up of the total-pressure-loss contours (fig. 30), it is seen that a slight flow asymmetry starts at $x_1/L = 0.075$ and spatially grows in the downstream direction. The total Mach-number contours (fig. 31) show that the shocks on the primary vortices are asymmetric and change sides as moving downstream, as shown by the results at the axial stations of 0.475 and 0.775. It is noticed that the flow asymmetry of this case is relatively weaker than that of the 5° semiapex-angle cone-cylinder case because the relative incidence of the forebody of the former case is lower than the latter.

## 5. Conclusions

The main goal of the present work is to predict asymmetric vortex-dominated flows around slender bodies over a wide range of angles of attack, Mach numbers, and Reynolds numbers. In this section, a summary of the findings of the numerical investigation is presented. First, steady and unsteady solutions of supersonic asymmetric flows around a circular cone have been obtained using the thin-layer Navier–Stokes equations along with the locally conical flow

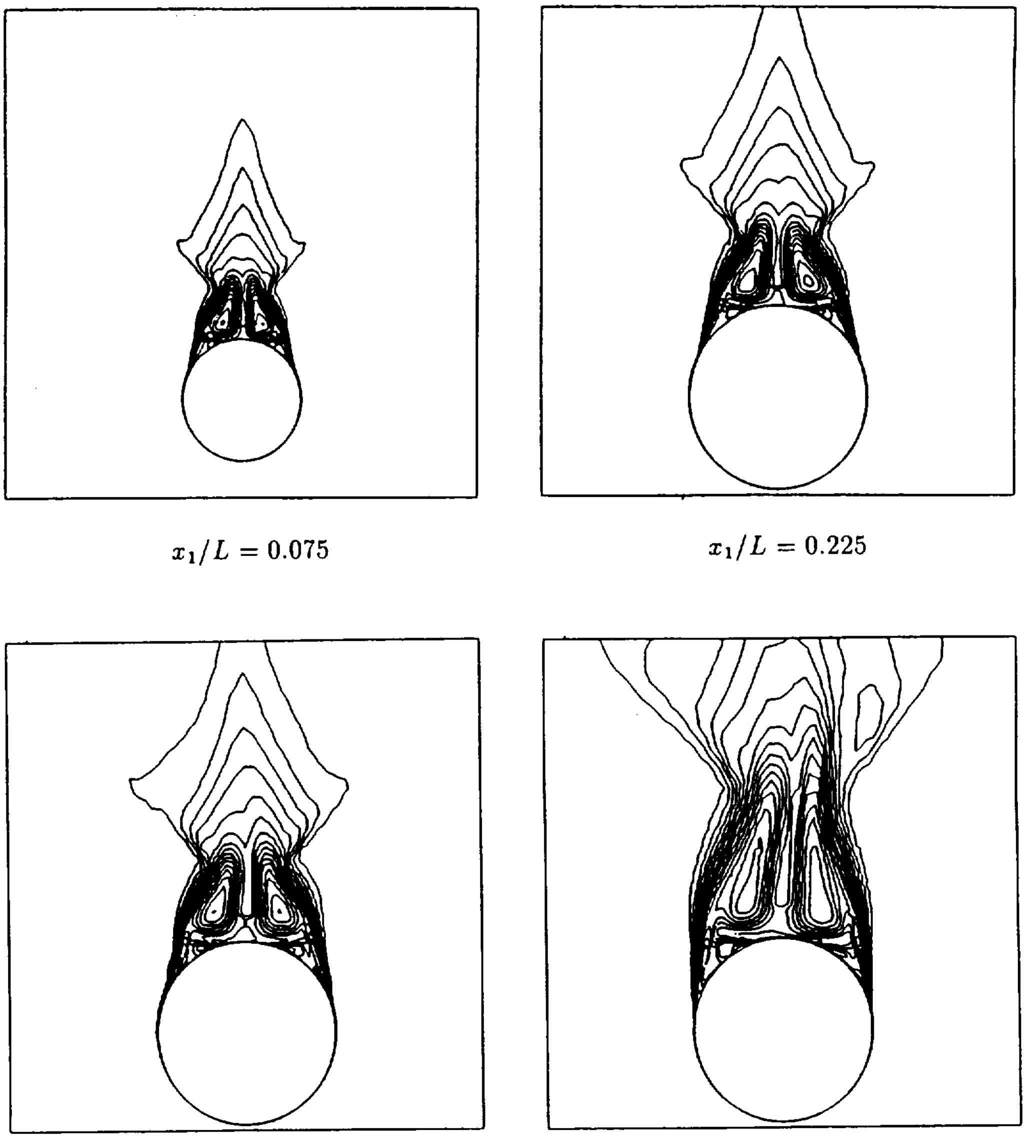

$x_1/L = 0.075$ $x_1/L = 0.225$

$x_1/L = 0.475$ $x_1/L = 0.775$

Fig. 30. Blow-up of the total-pressure-loss contours on 9.46° semiapex-angle cone–cylinder configuration ($\alpha = 46.1°$, $M_\infty = 1.6$, $\mathrm{Re} = 6.6 \times 10^6$).

assumption. The results have shown that the onset of flow asymmetry occurs when the relative incidence of cones exceeds certain critical values. At these critical values of relative incidence, asymmetric flow develops, irrespective of the sources of disturbance. Two types of flow disturbances of short duration are used to demonstrate that the asymmetric solution is unique and that the mechanism leads to flow asymmetry due to instability of the saddle point, even without the presence of any permanent disturbance. It has also been shown that as the Mach number increases, vortex flow asymmetry becomes weaker. In the high angle-of-attack regime, unsteady asymmetric flow with periodic vortex shedding has been uniquely captured.

Second, asymmetric supersonic three-dimensional flow problems have been solved using the thin-layer Navier–Stokes equations. Steady and unsteady flow solutions for asymmetric

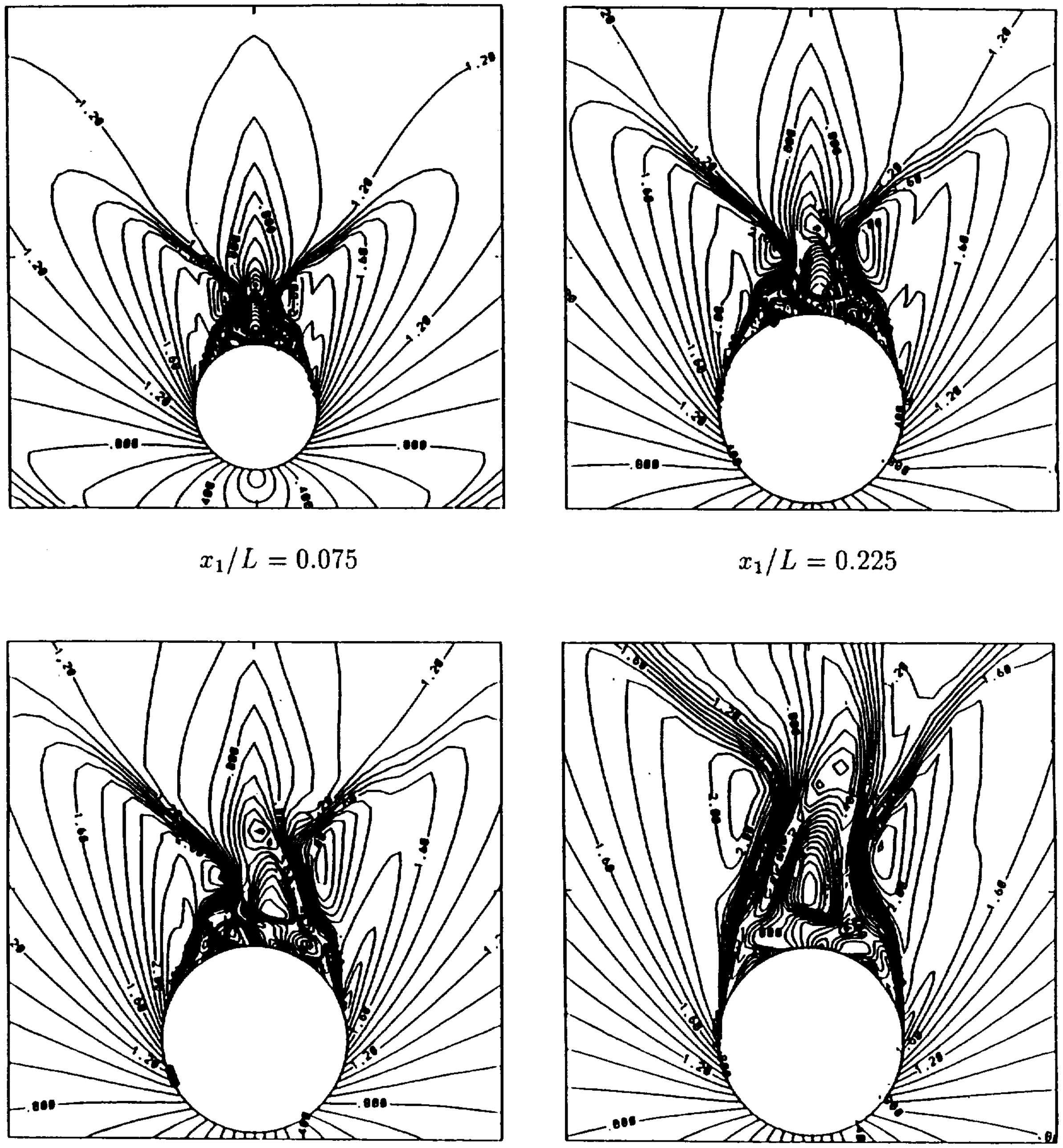

$x_1/L = 0.075$ $x_1/L = 0.225$

$x_1/L = 0.475$ $x_1/L = 0.775$

Fig. 31. Blow-up of the total-Mach-number contours on 9.46° semiapex-angle cone–cylinder configuration ($\alpha = 46.1°$, $m_\infty = 1.6$, Re $= 6.6 \times 10^6$).

supersonic flow over a circular cone and cone–cylinder configurations have been presented. However, because there is a serious lack of steady and unsteady three-dimensional detailed experimental measurements for supersonic asymmetric vortex flows, only surface-pressure coefficients from one of the cases are validated with the experiment in the present study.

It is shown that the three-dimensional flow calculation does not produce the same solution as that of the corresponding flow case under the locally conical assumption. The reason is that for the viscous flow problem the transformed equation using the locally conical flow assumption is not self similar. However, most of the characteristics and physics of the asymmetric flow can be simulated. The three-dimensional numerical results also show that the onset of steady and unsteady asymmetric flow develops due to a transient sideslip disturbance of short duration, provided that the body is at a certain critical range of Mach number, Reynolds number, and angle of attack. The steady and unsteady asymmetric flow solutions have been obtained without the need to impose any permanent type disturbance. As the free-stream Reynolds number increases for flows around a cone, the flow asymmetry becomes strong and changes sides in the downstream direction. For the high-Reynolds number flows, the spatially asymmetric flow develops in a wavy manner. The mechanism of vortex shedding is qualitatively similar to the temporal asymmetric flow of the locally conical flow solution, where the flow asymmetry develops in a periodic manner. As the angle of attack increases, the flow asymmetry becomes stronger and unsteady. The unsteady asymmetric flow case shows evidence of multiple small-scale vortices moving along the body and vortex shedding at each section.

Adding a cylindrical afterbody to the conical forebody strengths the flow asymmetry in comparison with that of the isolated cone. Finally, a comparison of the computed surface-pressure coefficients with the experimental measurement for a cone–cylinder configuration is given. The results show that a slight flow asymmetry starts close to the nose region and spatially grows moving downstream. The shocks on the top of the primary vortices show strong asymmetry and change sides in the downstream direction.

The next step for the research work is to study the control of three-dimensional asymmetric supersonic flow using a passive-control method in the form of side-strakes and/or an active-control method in the form of blowing or suction ports with various blowing rates and orientations of the ports on the body surface.

## Acknowledgement

The research work of Tin-Chee Wong and Osama A. Kandil is supported by the NASA Langley Research Center under Grant NAG-1-994.

## References

Ayoub, A. (1987) Slender delta wing at high angles of attack – a flow visualization study, *AIAA Paper No. 87-1230.*

Degani, D. (1990) Numerical investigation of the origin of vortex asymmetry, *AIAA Paper No. 90-0593.*

Degani, D. and L.B. Schiff (1989) Numerical simulation of the effect of spatial disturbances on vortex asymmetry, *AIAA Paper No. 89-0340.*

Degani, D. and G.G. Zilliac (1988) Experimental study of unsteadiness of the flow around on ogive-cylinder at incidence, *AIAA Paper no. 88-4330.*

Graham, J.E. and W.L. Hankey (1982) Computation of the asymmetric vortex pattern for bodies of revolution, *AIAA J. 23*, 1500–1504.

Hsu, C.-H. and C.H. Liu (1990) Numerical study of vortical flow over a sideslipping delta wing, *AIAA Paper No. 90-3001.*

Kandil, O.A., T.C. Wong and C.H. Liu (1990a) Prediction of steady and unsteady asymmetric flows around cones, *AIAA Paper No. 90-0598.*

Kandil, O.A., T.C. Wong and C.H. Liu (1990b) Asymmetric supersonic flow around cones with noncircular sections, in: *FDP Symp. Missile Aerodynamics, Friedrichshafen FRG*, AGARD CP-493 paper No. 16.

Kandil, O.A., T.C. Wong and C.H. Liu (1990c) Numerical simulation of steady and unsteady vortical asymmetric flows, in: *Int. Symp. Nonsteady Fluid Dynamics, Toronto, Canada*, FED-Vol. 91, pp. 99–108.

Kandil, O.A., T.C. Wong, H.A. Kandil and C.H. Liu (1991a) Thin-layer and full Navier-Stokes, locally-conical and three-dimensional asymmetric solutions, *AIAA Paper No. 91-0547.*

Kandil, O.A., T.C. Wong and C.H. Liu (1991b) Three-dimensional Navier–Stokes asymmetric solutions for cones and cone-cylinder configurations, *AIAA Paper No. 91-1732.*

Keener, E.R. and G.T. Chapman (1977) Similarity in vortex asymmetries over slender bodies and wings, *AIAA J. 15*, 1370–1372.

Lamont, P.J. (1980) Pressure measurements on an ogive-cylinder at high angles of attack with laminar, transition or turbulent separation, *AIAA Paper No. 80-1556-CP*.

Lamont, P.J. (1982) The complex asymmetric flow over a 3.5d ogive nose and cylindrical afterbody at high angles of attack, *AIAA Paper No. 82-0053*.

Landrum, E.J. (1977) Wind-tunnel pressure data at Mach numbers from 1.6 to 4.63 for a series of bodies of revolution at angles of attack from −4° to 60°, *NASA TM-X-3558*.

Liu, C.H., O.A. Kandil and T.C. Wong (1990) Computational study for passive control of supersonic asymmetric vortical flows around cones, *AIAA Paper No. 90-1581*.

Peake, D.J. and M. Tobak (1982) Three-dimensional flows about simple components at angle of attack, in: *High Angle-of-Attack Aerodynamics*, AGARD LS-121, Paper No. 2.

Rediniotis, O.K. and D.P. Telionis (1989) Periodic vortex shedding over delta wings, *AIAA Paper no. 89-1923*.

Schiff, L.B., D. Degani and S. Gavali (1989) Numerical simulation of vortex unsteadiness on slender bodies of revolution at large incidence, *AIAA Paper No. 89-0195*.

Shanks, R.E. (1963) Low subsonic measurements of static and dynamic stability derivative of six flat plate wings having leading-edge sweep angles of 70°–84°, *NASA TN D-1822*.

Siclari, M.J. (1990) Asymmetric separated flows at supersonic speeds, *AIAA Paper No. 90-0595*.

Siclari, M.J. and F. Marconi (1989) the computation of Navier–Stokes solutions exhibiting asymmetric vortices, *AIAA Paper No. 89-1817*.

Skow, A.M. and D.J. Peake (1982) Control of the forebody vortex orientation by asymmetric air-injection, (part b) – details of the flow structure, in: *High Angle-of-Attack Aerodynamics*, AGARD LS-121, Paper No. 10.

Thomson, K.D. and D.F. Morrison (1971) The spacing, position and strength of vortices in the wake of slender cylindrical bodies at large incidence, *J. Fluid Mech. 50*, 751–783.

Wong, T.C. (1991) Prediction and Control of Asymmetric Vortical Flows around Slender Bodies Using Navier–Stokes Equations. *Ph.D. Dissertation*, Old Dominion University.

Yanta, W.J. and J. Wardlaw (1982) The secondary separation region on a body at high angles of attack, *AIAA Paper No. 82-0343*.